SAPIENZA
UNIVERSITÀ DI ROMA

Facoltà di Scienze Matematiche, Fisiche e Naturali

Corso di Dottorato in Fisica XXX Ciclo

Search for new particles decaying into $Z\gamma/W\gamma$ final states in proton-proton collisions at $\sqrt{s} = 13$ TeV

Ph.D. Thesis

Supervisors

Prof. Daniele Del Re
Dr. Francesco Santanastasio

Student

Simone Gelli

October 2017

Contents

Introduction

The Standard Model of elementary particles and their fundamental interactions (SM) provides the theoretical framework for the description of particles and force intermediators that regulates matter interactions.
During the last decades many experiments have shown an excellent agreement between the theoretical expectations and experimental results for the SM. The success of this model was moreover proved with the observation of the last particle predicted but yet undiscovered: the Higgs boson. Its discovery has been announced in July 2012, when both the ATLAS and the CMS collaborations at the CERN Large Hadron Collider (LHC) of Geneva presented the discovery of a new scalar boson having a mass of 125 GeV with properties very similar to those of the Higgs boson predicted by the SM.
Despite the completeness of the SM, the search for physics Beyond the Standard Model (BSM) is nowadays carried on, as the SM theory still has some drawbacks and unsolved problems that represent a strong conceptual indication for new physics in the high energy domain; the existence of the dark matter (visible only through astrophysical observations), the matter/anti-matter asymmetry in the universe are only two examples of such unsolved problems. There are several alternative theories to the SM which try to solve these open issues. In these models, new physics, in terms of new particles and new interactions, is expected to be visible at the TeV energy scale and thus accessible at the LHC.
In this thesis, a search for new heavy particles decaying into a Z boson and a photon or a W boson and a photon is performed with data collected during 2016 by the general-purpose detector of the Compact Muon Solenoid (CMS) experiment at the LHC.
The Chapter 1 of this document is referred to the Standard Model of particle physics. The model and its properties are described in details as well as new theories beyond it. Two independent models compatible with the latest SM measurements that describe the production of new resonances decaying into a Z boson and a photon or a W boson and a photon are discussed. Neutral or charged particles of spin 0 or 1 can be sought in the $Z\gamma$ or $W\gamma$ channel, allowing for a broad search program. In the hadronic final state studied in this thesis, the Z/W decay products are collimated and therefore reconstructed as a single wide-jet. This is due to the high mass of the resonance and the correspondent large Lorentz boost of the Z/W bosons. The Z/W-jets are discriminated from background jets coming from hadronization of single quark/gluons by studying the jet substructure: in particular the large jet mass (around the Z/W mass) and the two-prong jet substructure for Z/W-jets are both exploited in the analysis.

Chapters 2 is related to the collider (LHC) that delivers proton-proton (pp) collisions analyzed by the four detectors present in the accumulation ring and the description of the interactions between partons (protons constituents).
Chapter 3 is focused on the CMS detector in all of its partitions that together are meant to the identification of particles produced in the pp collisions.
The Electromagnetic Calorimeter (ECAL) of CMS has an important role in the $Z\gamma/W\gamma$ analyses as it is responsible for the detection of photons. During the 3 years of my thesis I have been responsible for the timing intercalibration and monitoring (Appendix A) which is fundamental for the stability of the pulse-shape reconstruction of the MultiFit algorithm described in Sec. 4.1; a shift in the time of the signal coming from the detector will affect the reconstruction of the MultiFit algorithm and therefore worsen the energy resolution. I have also worked at the High Voltage (HV) system of the ECAL (the Barrel partition) for the calibration of the HV modules that power the photodetectors (Avalanche Photodiodes), and I provided assistance as on-call expert for this system. An accurate and stable HV system is required to maintain a good energy resolution of the calorimeter (to have an impact on the energy resolution constant term less than 0.2%, the HV stability has to be better than 60-65 mV per month) and providing assistance as on-call responsible.
Chapter 4 is mainly focused upon the event reconstruction in the CMS offline software which associates signals coming from the detector to particles that are used in the analysis of this thesis.
As well as photons, another physic object that has a central role in this thesis is the jet as, for the $Z\gamma$ and $W\gamma$ resonance search, I considered final states where the Z/W bosons decay to hadrons. In Sec. 4.7 the jet clustering algorithm is described and in Sec. 4.13 techniques for jet substructure identification are listed and discussed in details.
In Chapter 5 the procedure used to calibrate the jet substructure observables relevant for this analysis is presented; the jet mass scale, the jet mass resolution, and the efficiency of jet substructure requirements used to identify two-prong substructures inside a jet are studied using isolated, energetic W bosons coming from events with pair production of top-antitop quarks.
The $Z\gamma$ and $W\gamma$ analysis performed with the complete dataset of $\sim$36 fb^{-1} recorded by the CMS experiment in 2016 is presented in Chapter 6. The analysis consists in the search for a resonant peak in the invariant mass spectrum of the hadronic Z/W + photon system. In the first part of the Chapter, the $Z\gamma$ "standalone" analysis is described; it has been completed in summer 2017 and it is expected to be published in early 2018. In the second part, some improvements of the strategy are discussed; they will not be included in this publication but could be introduced in future analyses. The new analysis strategy exploits the similarities between $Z\gamma$ and $W\gamma$ final state with the Z/W bosons decaying into hadrons. Selected events are divided in independent categories depending on the jet mass, the presence of jets initiated from b-quarks, and requirements on the jet substructure. The possible signal from resonances decay is looked simultaneously in all the event categories, making the analysis sensitive to both $Z\gamma$ and $W\gamma$ signal models within the same analysis framework. Finally the conclusions of these analyses are discussed.

Chapter 1

The Standard Model of particle physics

This chapter introduces the Standard Model (SM) of elementary particle physics, which describes in its conceptual framework the elementary particles and three of the four fundamental forces of Nature. Its gauge structure, based on the $SU(3) \times SU(2) \times U(1)$ symmetry group, is exposed in general terms. Finally, the theories Beyond the Standard Model predicting new resonances decaying into a Z+photon or a W+photon signal are discussed. The signature and the analysis challenges are discussed in Sec. 1.8.

1.1 Elementary particles and forces

Despite the Greek meaning of the word, the atom is not indivisible. It consists, in fact, of smaller components: electrons, protons and eventually neutrons. While in the SM the electron is considered to be an elementary particle with no substructure, protons and neutrons are made of quarks, which are in turn believed to be elementary. In particular, the proton is made of two up quarks with an electric charge of $+2/3\ e$, where e is the Coulomb charge $e = 1.6 \times 10^{-19}$ C and one down quark with an electric charge of $+1/3\ e$. For the neutron, the numbers of up and down quarks are reversed giving a resulting charge of 0. Quarks and leptons have spin $\frac{1}{2}$ and follow the Fermi-Dirac statistic, hence they are fermions.
During the last century, the knowledge of the elementary particles have been increased thanks to both theoretical and experimental efforts: our most up-to-date insight of the elementary constituents of nature organizes both leptons and quarks into three families of particles.
Starting from the leptons, the electron e belongs to the first generation, together with the electronic neutrino ν_e[1]. The muon μ and the muonic neutrino ν_μ constitute the second generation of leptons, while the tau τ and the tau neutrino ν_τ form the third generation. The masses of the charged leptons differ by four orders of magnitude between the first and third generations. Table 1.1 summarizes the leptons and

[1]The ν_e has been introduced by Wolfgang Pauli in order to allow energy-momentum conservation in the nuclear beta decay

their properties[2].

Generation	Lepton	Charge	Mass
First	electron (e)	-e	511 MeV
	electron neutrino (ν_{e})	0	< 2 eV
Second	muon (μ)	-e	105.67 MeV
	muon neutrino (ν_{μ})	0	< 2 eV
Third	tau (τ)	-e	1776.99 MeV
	tau neutrino (ν_{τ})	0	< 2 eV

Table 1.1: Properties of the leptons in the three generations. Neutrinos are known to have a tiny mass compared to the other SM particles, but non-zero, so to allow oscillations between neutrino families, which have been experimentally observed [1]

The same organization in three families can be found also for quarks. In addition to the up and down quarks, which constitute the first generation, two further generations of quarks have been found: the charm and strange quarks are placed in the second generation and the top and bottom quarks in the third one. The charm and the top quark have the same electric charge as the up quark, while the strange and the bottom quark have the same electric charge of the down quark. Beside their electric charge, the six quarks carry also colour charge, hence they can interact via strong interaction (described later in this Section). The quarks and their properties are shown in Table 1.2. In particular, the quark masses span 5 orders of magnitude from the ≈ 2 MeV of mass of the up quark, up to the top quark, which was discovered in 1995 at the Tevatron and has a mass close to 173.2 GeV. The top quark is in fact the heaviest SM particle carrying a mass which is close to the one of a gold nucleus.

Generation	Quark	Charge	Mass
First	up (u)	2/3 e	$2.3^{+0.7}_{-0.5}$ MeV
	down (d)	-1/3 e	$4.8^{+0.5}_{-0.3}$ MeV
Second	charm (c)	2/3 e	1.275 ± 0.025 GeV
	strange (s)	-1/3 e	95 ± 5 MeV
Third	top (t)	2/3 e	$173.21 \pm 0.51 \pm 0.71$ GeV
	bottom (b)	-1/3 e	4.66 ± 0.03 GeV

Table 1.2: Quarks and their properties [1]

So, in the SM there are 12 elementary particles, 6 leptons and 6 quarks, while ordinary matter on earth is essentially composed of particles belonging to the first generations: up and down quarks in the nucleus and electrons in the electron cloud. In addition to this, it is important to notice that every particle has its own antiparticle, which is characterized by having the same mass, but opposite quantum

[2]In this thesis all masses and energies are expressed in natural units, where the speed of light c and $\hbar$ are taken as equal to 1.

numbers, as predicted by the Dirac's theory. The question whether the neutrinos are their own antiparticles (Majorana particles) or not (Dirac particles) remains still open.
In order for the elementary particles to interact with each other, forces have to act between them. Forces are mediated by particles with an integer spin that follow the Bose-Einstein statistic and are hence called bosons. There are four fundamental interactions in Nature which can act or not on a specific particle depending if this particle carries or not the corresponding charge.

- Electromagnetic force: all electrically charged particles are subject to electromagnetic interactions. The massless and chargeless photon (γ) is the carrier particle of the electromagnetic force and, owing to its masslessness, the electromagnetic force is a long range force with a $1/r$ potential. The theory describing the electromagnetic interactions is called quantum electrodynamics (QED).

- Weak force: weak interactions are usually not relevant at energies well below $\approx$ 100 GeV, since the strong or electromagnetic interactions have couplings that are orders of magnitude larger. This is not true anymore for processes where the electromagnetic interactions and the strong interactions are forbidden, for example because of a quantum number conservation law taking place. Weak interactions can involve neutrinos which have neither electric nor strong charge and, therefore, do not interact strongly or electromagnetically. Processes involving the changing of quark flavour must happen via weak interaction since this is not allowed with the other interactions. Contrary to the photon (and the gluons), the bosons which carry the weak interaction are heavy compared to most elementary particles in SM. There exists a charged ($W^{\pm}$) and a neutral version (Z) of the vector bosons that mediate the weak force. The range of the weak interactions is small (between 10^{-18} and 10^{-16} m) because of the mass of the bosons involved.

- Strong force: the strong interactions are responsible for the attracting force between quarks. It is mediated by the gluons which are massless spin one particles. Gluons exist as a colour octet: they follow the "8" representation (ad-joint) of the $SU(3)$ group. Gluons also carry colour charge, hence they can interact with themselves, unlike the electrical neutral photon. Due to the property known as confinement, it is not possible to observe quarks as free particles: they would instead undergo the hadronization process, which allows to re-arrange the colour structure from coloured quarks to colourless hadrons. The top quark is a special case since, due to its mass, the decay into a b quark (which then hadronizes) and a W boson happens before the hadronization process itself could start. The theory describing the strong interactions is called quantum chromodynamics (QCD).

- Gravitational force: all particles are affected by the gravitational force. However, even though it is the dominant force on the astronomical scale, it is negligible on a microscopic scale and, in general, when the energies involved are lower than the Planck scale (1.22×10^{19} GeV). The graviton G, a hypothetical, massless and chargeless elementary particle of spin two, would be the

carrier of the gravitational force in a quantum field theory that involves gravity. However, such theory is extremely difficult to construct.
The forces and some of their characteristics are summarized in Table 1.3.

Interaction	Range	Relative strength	Mediators
Strong	10^{-15} m	1	8 gluons (g)
Electromagnetic	∞	10^{-3}	photon (γ)
Weak	10^{-18} m	10^{-14}	W^+, W^-, Z
Gravitational	∞	10^{-43}	graviton (G) ?

Table 1.3: Range, relative strength with respect to the strong force and mediators of the four fundamental interactions. The gravitational force is not included in the SM and gravitons are hypothetical particles

Due to reasons connected to the internal symmetry of the $SU(3)\times SU(2)\times U(1)$ group (that will be treated in Sec. 1.3) to account for the observed masses of the elementary particles, a special role has to be assigned to at least an additional particle, which has to be a scalar boson. Its role is intimately connected to the spontaneous symmetry breaking mechanism which gives rise to non-zero masses for the other elementary particles (see again Sec. 1.3). A new particle, whose couplings to the massive fermions have to be proportional to the mass of the fermions themselves and proportional to the square root of the bosons' masses, was proposed in 1964 independently by Brout and Englert [2] and Higgs [3]. Such particle have been observed in 2012 by the ATLAS [4] and CMS [5] experiments and it is known as the Brout-Englert-Higgs scalar boson (denoted in literature as H or H^0), sometimes also referred to as the Higgs boson. This discovery constitutes an outstanding milestone of the modern particle physics and a tremendous success of the SM theory.
A visual summary of the elementary particles and their organization in the SM framework, as well as the force carriers and the H boson is shown in Fig. 1.1.

1.2 Role of symmetries

In quantum field theories [6], the equations of motion of the different fields are derived, exploiting the "least action principle", from the Lagrangian density $\mathcal{L}$, which after integration over space and time defines the action S. For a spin 1/2 particle with mass m, described by a spinor field ψ, the action S is written, in the simplest case of no interaction, as:

$$S = \int dx^4 \mathcal{L} = \int dx^4 (i\bar{\psi}(x)\gamma^\mu \partial_\mu \psi(x) - m\bar{\psi}(x)\psi(x)) \tag{1.1}$$

where γ^μ are the Dirac's matrices. The term in parenthesis contains only the fermionic field $\psi(x)$ and hence can be labeled as $\mathcal{L}_f = i\bar{\psi}(x)\gamma^\mu \partial_\mu \psi(x) -$

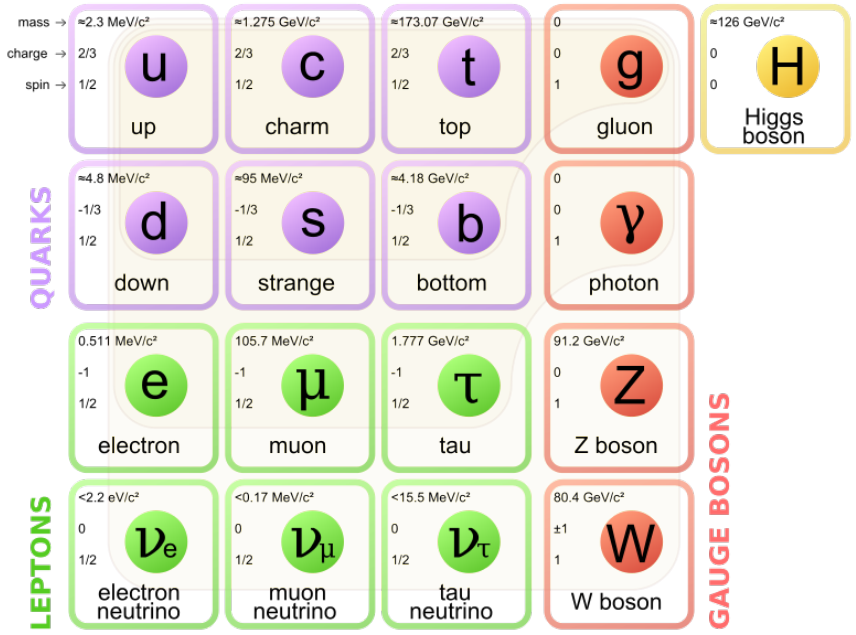

Figure 1.1: Overview of the Standard Model constituents

$m\bar{\psi}(x)\psi(x)$. The equation of motion leads to the Dirac equation:

$$i\gamma^{\mu}\partial_{\mu}\psi(x) = m\psi(x) \tag{1.2}$$

As shown by Emmy Noether in her famous theorem, symmetries play a central role in physics: every continuous symmetry in the Lagrangian gives rise to a conserved quantity during the motion. Starting from the free spinor action defined in Equation 1.1, one sees that it is invariant under the transformation:

$$\psi(x) \to e^{ie\alpha}\psi(x) \tag{1.3}$$

where α is a global, i.e. not space-time dependent, phase rotation of the field and e is the already is the already introduced Coulomb charge.
The leading "building principle" of the SM Lagrangian states that it is unnatural, in a relativistic theory, to allow a global phase transformation over the entire 4-D space, since it would be like if all the observers in the entire 4-D space agree on shifting their clocks by a certain fixed phase. In this sense, it is much more natural to allow local phase transformations, instead of global ones. The global symmetry has then to be forced to become a local one: this concept is called *symmetry gauging*[3]. If one wants to impose the invariance of the Lagrangian under the local transformation where $\alpha = \alpha(x)$:

$$\psi(x) \to e^{ie\alpha(x)}\psi(x) \tag{1.4}$$

[3]This argument gives credibility to the principle but it is not a rigorous demonstration, despite the fact that the symmetry gauging is the deepest and most profound concept of the SM.

one needs to introduce a new field $A^\mu(x)$, which must transform in the proper way under local phase transformation: the transformation of the ψ field and the A_μ field must act in a coordinate way as described by the transformation rule (Eq.1.5), so that the extra term coming from the derivates of the local phase $\alpha(x)$ compensate each other.

$$\psi(x) \to e^{ie\alpha(x)}\psi(x), \qquad A_\mu \to A_\mu - \partial_\mu\alpha(x) \tag{1.5}$$

The insertion of the new field A^μ can be achieved by replacing the partial derivative operator ∂ with the covariant derivative $\mathcal{D}$ in the Lagrangian:

$$\mathcal{D}_\mu = \partial_\mu + ieA_\mu(x) \tag{1.6}$$

The new Lagrangian is then given by:

$$\mathcal{L} = i\bar{\psi}(x)\gamma^\mu\partial_\mu\psi(x) - m\bar{\psi}(x)\psi(x) + ie\bar{\psi}(x)\gamma^\mu A_\mu\psi(x) - \frac{1}{4}(F_{\mu\nu}(x)F^{\mu\nu}(x)) = \mathcal{L}_f + \mathcal{L}_{gauge} \tag{1.7}$$

where:

$$F_{\mu\nu} = \partial_\mu A_\nu(x) - \partial_\nu A_\mu(x) \tag{1.8}$$

It can be seen that the Lagrangian (1.7) is composed of the two terms: $\mathcal{L}_f$ containing only the matter field $\psi(x)$ and $\mathcal{L}_{gauge}$ being the additional contributions containing the gauge field A_μ. It can be also shown that the Lagrangian is now invariant under coordinate local transformations of $\psi(x)$ and $A(x)$, as dictated in Eq. 1.5.

In this sense, the introduction of a new bosonic field that couples to matter fields is needed to achieve the local gauge invariance of the action: in general, in the SM all interactions are consequences to this request. Ultimately, applying the Noether theorem, this symmetry leads to the law of conservation of the electric charge Q. The QED component of the SM Lagrangian is then a U(1) subgroup[4].

Exploiting this "building principle", all the fermionic fields of Tables 1.1 and 1.2 are added by hand in the SM action, while the existence of the bosonic fields is a direct consequence of the required invariance properties of the action. Up to now the example dealt with the simplest $U(1)$ group of symmetry. The complete SM theory is based instead on the bigger group: $SU(3)_c \times SU(2)_L \times U(1)_Y$, obtained as direct product of smaller symmetry groups[5]. The Lagrangian of the electroweak theory (which treats the electromagnetic and the weak forces into a unified framework) is invariant under transformations in the $SU(2)_L \times U(1)_Y$ subgroup, while the QCD Lagrangian is invariant under $SU(3)_c$.

[4]Actually the U(1) group of the SM Lagrangian is not directly related to electric charge. The SM U(1) subgroup is instead related to the hypercharge $U(1)_Y$. The electric charge conservation rule is achieved in a more complex way: (spontaneously) breaking the bigger $SU(2)_L \times U(1)_Y$ group in the $U(1)_{em}$ group.

[5]The subscript c stands for colour, L for left and Y for hypercharge. Their meaning will be explained later in the Section

In order to explain the subscript L, one can group the fermions of the SM by their chirality, either left or right. The chirality is defined by the projection operators $\mathcal{P}_{left} = (1 - \gamma^5)/2$ and $\mathcal{P}_{right} = (1 + \gamma^5)/2$, where $\gamma^5 = i\gamma^0\gamma^2\gamma^2\gamma^3$ and γ^i being the Dirac matrices. Left-handed fermions form doublets, while right-handed fermions form singlets. The left-handed quark doublets consist of up-type and down-type quarks and the left-handed lepton doublets consist of a neutrino and the associated charged lepton (see diagram 1.9). Up to now right-handed neutrinos have never been observed. The weak interaction only acts on left-handed particles and violates parity which is the invariance under mirror operation at the origin in space: the subscript L of the $SU(2)_L$ group reflects this fact.

$$\ell_L = \begin{pmatrix} \nu_L \\ e_L \end{pmatrix}, \; e_R, q_L = \begin{pmatrix} u_L \\ d_L \end{pmatrix}, \; u_R, \; d_R. \tag{1.9}$$

The quantum number associated to the $SU(2)_L$ symmetry is the weak isospin I_w, while the $U(1)_Y$ subgroup is related to the hypercharge Y. The weak hypercharge Y carried by the matter fields is related to the electric charge Q and the third component of weak isospin I_w^3 by:

$$Y = Q - I_w^3. \tag{1.10}$$

Finally, the subscript c of the $SU(3)_c$ group stands for *colour*, which is the additional quantum number carried by the quarks[6]. Under $SU(3)_c$, quarks are colour triplets while leptons are colour singlets; quarks therefore carry a colour index ranging between one and three, whereas leptons do not take part in strong interactions.
The fermion content of the SM is summarized in Table 1.4, together with its representation under the different groups of symmetry.

As explained earlier in the chapter, to each group of symmetry there should be an associated gauge field. The gauge field associated to the symmetry group $U(1)_Y$ is usually denoted as B_μ, with the hypercharge Y as generator of the group. Three gauge fields, W_μ^1, W_μ^2 and W_μ^3 are associated to $SU(2)_L$ group, with three generators that can be expressed as half of the Pauli matrices:

$$T_1 = \frac{1}{2}\begin{pmatrix} 0 & 1 \\ 1 & 0 \end{pmatrix}, \; T_2 = \frac{1}{2}\begin{pmatrix} 0 & -i \\ i & 0 \end{pmatrix}, \text{ and } T_3 = \frac{1}{2}\begin{pmatrix} 1 & 0 \\ 0 & -1 \end{pmatrix} \tag{1.11}$$

The generators T^a satisfy the Lie algebra:

$$[T^a, T^b] = i\varepsilon^{abc}T_c \quad \text{and} \quad [T^a, Y] = 0, \tag{1.12}$$

where ε^{abc} is the antisymmetric tensor. Finally, in the $SU(3)_c$ group, the eight generators (that can be expressed in term of the Gell-Mann matrices) correspond to the eight gluon fields $G_\mu^{1\ldots8}$.

[6]The introduction of the colour as an additional quantum number was done so to realize the Pauli's exclusion principles in particles like the Δ^{++} that would have apparently violated it.

Field	$SU(3)_c$ representation	$SU(2)_L$ representation	Y	I_w^3	Q
u_{iL}	3	2	$\frac{1}{6}$	$\frac{1}{2}$	$\frac{2}{3}$
d_{iL}	3	2	$\frac{1}{6}$	$-\frac{1}{2}$	$-\frac{1}{3}$
ℓ_{iL}	1	2	$-\frac{1}{2}$	$-\frac{1}{2}$	-1
ν_{iL}	1	2	$-\frac{1}{2}$	$\frac{1}{2}$	0
u_{iR}	3	1	$\frac{2}{3}$	0	$\frac{2}{3}$
d_{iR}	3	1	$-\frac{1}{3}$	0	$-\frac{1}{3}$
ℓ_{iR}	1	1	-1	0	-1
ν_{iR}	1	1	0	0	0

Table 1.4: Fermion content of the SM, with representations under $SU(3)_c$ and $SU(2)_L$, hypercharge Y, isospin I_w^3 and electric charge Q. The index i refers to the fermion generation, while the indices L and R represent the left-handed or right-handed nature of the particle [1]

When "gauging" the $SU(3)$ and the $SU(2)$ symmetries, the same principle depicted in the simpler $U(1)$ symmetry gauging has to be implemented. A more complex algorithm is needed due to the fact that, unlike the $U(1)$ group, $SU(2)$ and $SU(3)$ are not-Abelian, i.e. not-commutating groups[7]. Apart for the complexity, the SM Lagrangian will be organized as in Eq. 1.7 so to include all the SM fermions in $\mathcal{L}_f$ while $\mathcal{L}_{gauge}$ will include the gauge fields G_μ, the W_μ and the B_μ.
Unlike the simplest $U(1)$ scenario, the striking consequence of the invariance under the $SU(3)_c \times SU(2)_L \times U(1)_Y$ group is that the SM Lagrangian cannot include any explicit mass term, neither for the fermionic field nor the bosonic fields: this is because a mass term like $m\bar{\psi}\psi$ can be simply re-written[8] as $m\bar{\psi}_R\psi_L$. Therefore, a mass term would couple right- and left-handed fields and, since the left-handed fermions transform as doublets and right-handed fermions as singlets under the SM gauge group, a term like $m\bar{\psi}_R\psi_L$ would break the invariance of the Lagrangian. On the other hand, the impossibility to have a mass term would lead to the conclusion, in clear disagreement with the experimental facts, that all particles should be massless, both the fermions and the bosons. In reality, some of the gauge bosons, photons and gluons, are indeed massless, while the weak gauge bosons must have non zero masses in order to explain the "weakness" of the weak interaction. In addition to this, all fermions have masses, including the neutrinos.
The solution to this problem is conceptually different for bosons and fermions and it's detailed in the next Section.
In general terms:

- The fact that the weak gauge bosons have a mass different from zero indicates that the vacuum of the theory, i.e. the fundamental state does not share (is not invariant under) the same symmetries of the SM La-

[7]Ultimately, it's the covariant derivative which assumes a more complex form.
[8]Any field can be written in terms of chiral fields $\psi = \psi_R + \psi_L$.

grangian: the electroweak group $SU(2)_L \times U(1)_Y$ is not a symmetry of the vacuum. On the other hand, since gluons and photons are massless the SM symmetry group of the Lagrangian must (spontaneously) break into:

$$SU(3)_c \times SU(2)_L \times U(1)_Y \rightarrow SU(3)_c \times U(1)_{em} \tag{1.13}$$

where the subscript em in $U(1)_{em}$ stands for "electromagnetic" and is used to clearly indicate its difference with respect to the $U(1)_Y$ related to the hypercharge. This breaking pattern can be achieved introducing a new complex scalar doublet field ϕ in the theory. Three of the four degrees of freedom coming from the complex doublet ϕ are "used" to give masses to the W and the Z bosons, leaving an additional degree of freedom which would correspond to a new spin-0 particle.

– Once the ϕ field is introduced, the mass of the fermions can be achieved with the interaction terms between the field ϕ and the matter field, via the so-called Yukawa terms.

1.3 Scalar sector

Given the "building principle" behind the SM, explicit mass terms are forbidden inside the SM Lagrangian. Let's now imagine to introduce a certain field[9] ϕ and let's consider its expectation value $\langle 0|\phi|0\rangle$ calculated on the fundamental state of the theory $|0\rangle$, also called the vacuum of the theory. Suppose the theory is invariant (i.e. the Lagrangian describing the theory is invariant) under a certain symmetry of the fields, for example a simple $U(1)$ symmetry $\phi \rightarrow e^{i\alpha}\phi$. If the vacuum state itself were invariant under the same symmetry, $U(1)$ in this example, meaning

$$|0\rangle = e^{i\alpha}|0\rangle$$

then the expectation value of the ϕ field must be equal to zero[10]

$$\langle 0|\phi|0\rangle = 0$$

As a consequence if $\langle 0|\phi|0\rangle \neq 0$ then the vacuum state $|0\rangle$ is not invariant under the same symmetry of the Lagrangian. This situation defines what is called spontaneous symmetry breaking in group theory.
In the SM case, an additional complex scalar (i.e. having spin 0) doublet ϕ

[9] In principle it's not mandatory for this field to be added by hand as a new field in the Lagrangian, as it goes in the SM case. There are cases, like the Cooper pair in superconductivity, i.e. a pair of electrons (or other fermions) bounded together at low temperatures, where the new field (the bound state of electron pairs) is "dynamically created" and not explicitly present in the Lagrangian [7]. The SM approach is then the simplest possible.

[10] This is because $\langle 0|\phi|0\rangle = \langle 0|(e^{-i\alpha}e^{i\alpha})\phi|0\rangle = e^{i\alpha}\langle 0|\phi|0\rangle$, given that $\langle 0|e^{-i\alpha} = \langle 0|$ because of the vacuum invariance hypothesis. Hence $\langle 0|\phi|0\rangle = e^{i\alpha}\langle 0|\phi|0\rangle$ which means $\langle 0|\phi|0\rangle = 0$.

is simply introduced by hand in the Lagrangian and makes its components explicit. It can be written as:

$$\phi = \frac{1}{\sqrt{2}} \begin{pmatrix} \varphi_1 + i\varphi_2 \\ \varphi_3 + i\varphi_4 \end{pmatrix}. \tag{1.14}$$

The corresponding additional Lagrangian density $\mathcal{L}_\phi$, associated to the scalar sector, can be written as a kinematic and a potential terms:

$$\mathcal{L}_\phi = (D^\mu \phi)^\dagger D_\mu \phi - V(\phi) \tag{1.15}$$

Where the kinetic part includes the gauge covariant derivatives for the $SU(2)_L \times U(1)_Y$ group, which is defined as:

$$D_\mu \phi = \left(\partial_\mu + ig\vec{T}.\vec{W}_\mu + \frac{ig'}{2} B_\mu \right) \phi \tag{1.16}$$

The potential $V(\phi)$ has the most general renormalizable[11] form invariant under $SU(2)_L \times U(1)_Y$ in:

$$V(\phi) = \mu^2 \phi^\dagger \phi + \lambda (\phi^\dagger \phi)^2 \tag{1.17}$$

where, in order to obtain a non-zero expectation value $\langle 0|\phi|0\rangle$ and to realize the required spontaneous breaking of the SM group of symmetry, the factor μ^2 has to be negative. Given the sign requirement for the μ^2 factor, the λ parameter has to be a positive real number in order to preserve the vacuum stability[12]. This choice for the sign of the parameters μ^2 and λ gives to the potential $V(\phi)$ the shape of a "Mexican hat", as shown in Fig. 1.2. While a

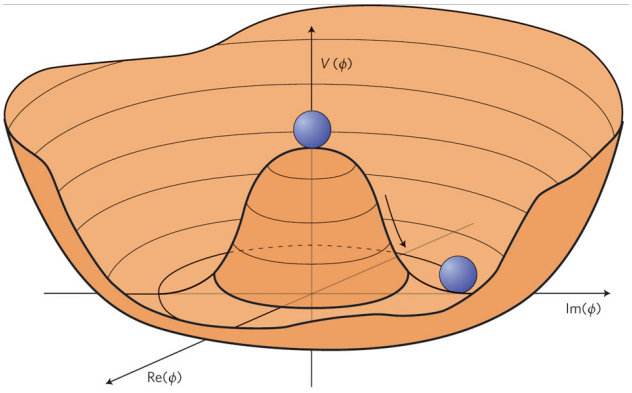

Figure 1.2: The Higgs potential in the simpler case where the ϕ field has only 2 degrees of freedom, instead of the 4 ones of a complex scalar doublet field

local maximum of the potential is found for $\phi = 0$, there is a closed surface

[11] In quantum field theories, divergences tend to arise in calculations because all particles can contribute to a process as virtual particles in loops: then a cut-off is often needed in the computation of the physical quantities. If the cut-off disappears from the final results by its absorption in a finite number of measured constants, the theory is called renormalizable (see Sec. 1.5).

[12] To avoid that the minimum of the potential goes at $-\infty$.

of minima corresponding to a non-zero field. Using the approach of the "small oscillations" in polar coordinates (perturbative expansion), the field ϕ can be developed around one of its degenerate minima. Clearly, the second derivative in the radial direction is positive, since the curvature of the potential is positive in that direction, while the second derivative in the angular coordinate is zero, since there is an entire closed circumference of degenerate minima. The radial excitations give rise to a non-zero mass particle, while the angular excitations give rise to massless particles, called Goldstone bosons, one for each broken degree of symmetry, hence, in principle, three massless particles in the SM case as $SU(2)_L \times U(1)_Y \to U(1)_{em}$. On the other hand, the presence of those additional massless particles would be the scenario of a spontaneous breaking of a global symmetry of the Lagrangian, as stated by the Goldstone theorem. The SM case appears more complex: the broken symmetry $SU(2) \times U(1)$ is not a global one, since the SM Lagrangian is defined using the leading principle of the symmetry gauging: 4 gauge fields (3 W_μ e 1 B_μ) are in fact present. The 3 massless Goldstone bosons that would appear in a global symmetry breaking are instead "re-absorbed", using the gauge invariance of the Lagrangian, by a re-definition of the gauge fields themselves, which in exchange gain mass different from zero [8]. The additional massive field corresponding to the radial excitation of the potential cannot instead be reabsorbed via a redefinition of the gauge fields and hence it becomes a prediction of the SM theory. The associated massive particle is the introduced H boson.
More specifically, the potential $V(\phi)$ has (degenerate) minima corresponding to the radial position $|\phi| = \sqrt{\frac{-\mu^2}{2\lambda}} \neq 0$. This non-zero quantity can be interpreted as the vacuum expectation value v of the field ϕ, measured to be about 246 GeV. It can be demonstrated that any scalar doublet ϕ can be written in the canonic form "down and real" using an appropriate matrix $U(x) \in SU(2) \times U(1)$, of the form $U(x) = e^{i\gamma\frac{T_2}{2}} e^{i(\alpha T_3 + \beta Y)}$. Using $U(x)$, the field ϕ can be re-written so that its non zero expectation value v is exposed:

$$\phi = \frac{1}{\sqrt{2}} \begin{pmatrix} \varphi_1 + i\varphi_2 \\ \varphi_3 + i\varphi_4 \end{pmatrix} = U(x) \begin{pmatrix} 0 \\ v + \frac{h(x)}{\sqrt{2}} \end{pmatrix} \tag{1.18}$$

where $h(x)$ is a field with zero expectation value over the vacuum. Given the local gauge invariance, the $U^{-1}(x)$ transformation can be applied to all fields without affecting in any way the form of the Lagrangian: the three degrees of freedom of $U(x)$ disappear, simply "absorbed" by the gauge fields, thus eliminating the degrees of freedom associated to the massless Goldstone bosons. In particular, applying U^{-1} transforms the ϕ field as:

$$\phi \to U^{-1}\phi = \begin{pmatrix} 0 \\ v + \frac{h(x)}{\sqrt{2}} \end{pmatrix} \tag{1.19}$$

Using (Eq. 1.19) and the perturbative approach around one arbitrary minimum, the potential

$$V = \mu^2|\phi|^2 + \lambda|\phi|^4$$

can be written in the suitable form:

$$\begin{aligned} V(\phi) &\simeq \frac{\mu^2}{2}h^2 + \lambda[v^2 + \frac{h^2}{2} + \sqrt{2}vh]^2 \\ &\simeq \frac{\mu^2}{2}h^2 + 2\lambda v^2 h^2 + \lambda v^2 h^2 + O(h^3) + O(h^4) \\ &\text{and given that } v = \sqrt{\frac{-\mu^2}{2\lambda}} \\ &= -\mu^2 h^2 + O(h^3) + O(h^4) \end{aligned} \tag{1.20}$$

where:

- No linear terms in the h field are present (since the potential is being expanding around a minimum).
- The constant terms are discarded as the equation of motions are obtained by deriving the Lagrangian.
- The cubic and quartic terms in the h fields are not detailed, but simply indicated as $O(h^3)$ and $O(h^4)$.
- The last equation gives rise to the mass of the h field:

$$m_H^2 = -2\mu^2 > 0. \tag{1.21}$$

The kinetic term of the Lagrangian $\mathcal{L}_\phi$

$$(D_\mu\phi)^\dagger D_\mu\phi = |D_\mu\phi|^2 \tag{1.22}$$

again using the perturbative expansion, leads to:

$$|D_\mu\phi|^2 \simeq \frac{1}{2}\partial_\mu h\partial^\mu h + \frac{g^2v^2}{4}\left((W_\mu^1)^2 + (W_\mu^2)^2 + (W_\mu^3 - \frac{g'}{g}B_\mu)^2\right) \tag{1.23}$$

The charged vector bosons W^1 and W^2 therefore acquire a mass, given by:

$$m_{W^1}^2 = m_{W^2}^2 = \frac{g^2v^2}{2} \tag{1.24}$$

The third term of Eq. 1.23 is a linear combination of W_μ^3 and B_μ. The relation between the W_μ and B_μ fields and the physical fields Z_μ and A_μ, associated respectively to the neutral boson Z and the photon, is expressed by the set of relations:

$$\begin{cases} Z_\mu = W_\mu^3\cos\theta_W - B_\mu\sin\theta_W \\ A_\mu = W_\mu^3\sin\theta_W + B_\mu\cos\theta_W \\ \tan\theta_W = \frac{g'}{g} \end{cases} \tag{1.25}$$

Equation 1.23 can therefore be written as:

$$|D_\mu\phi|^2 \simeq \frac{1}{2}\partial_\mu h\partial^\mu h + \frac{g^2v^2}{4}\left((W_\mu^1)^2 + (W_\mu^2)^2 + (\frac{Z_\mu}{\cos\theta_W})^2\right) \tag{1.26}$$

The mass of the Z boson is related to the mass of the charged W bosons through the Weinberg angle θ_W, which can be determined experimentally[13]:

$$\frac{m_{\mathrm{W}}}{m_{\mathrm{Z}}} = \cos\theta_W \tag{1.27}$$

There is no mass term for the A_μ field, hence the photon remains massless. Equation 1.26 solves the problem of the masses of the vector bosons and shows a kinetic term related to a new scalar field h, having a non-zero mass specified in Eq. 1.21.
To take into account the fermions' masses a different approach can be pursued: given the existence of the field doublet ϕ, one can write coupling terms, known as the Yukawa couplings, between fermions and the ϕ field. Considering the electron e, for example and indicating with l^e the $SU(2) \times U(1)$ doublet containing the left-handed electron and (electron) neutrino, one can write the following Lagrangian term

$$\mathcal{L}^e_{Yuk} = -\lambda_e \bar{l^e}_L \phi e_R + h.c. \tag{1.28}$$

which after the electroweak symmetry breaking (EWSB) procedure described earlier becomes

$$\mathcal{L}^e_{Yuk} \xrightarrow[EWSB]{} -\lambda_e v \bar{e}_{1L} e_{1R} + h.c. \tag{1.29}$$

A mass term can now be given to the electron e, where in particular:

$$m_e = \lambda_e v \tag{1.30}$$

A similar reasoning can be re-done for the down-type quark which can, like the electron, acquire a mass through Yukawa couplings to the ϕ doublet:

$$\mathcal{L}^d_{Yuk} = -\lambda_d \bar{q}_{1L} \phi d_{1R} + h.c. \xrightarrow[EWSB]{} -\lambda_d \frac{v}{\sqrt{2}} \bar{d}_{1L} d_{1R} + h.c. \tag{1.31}$$

On the other hand, the up-type quark and in general all the particles that are located in the "up-side" of the doublets detailed in Eq. 1.9, both quarks and neutrinos, cannot acquire a mass with a simple Yukawa term like the one written in Eq. 1.31, because of the canonical "down and real" form chosen for the ϕ doublet, whose non-zero component after EWSB is always in the "down-side" of the doublet. The most economical solution is to make the "up" fields couple to the other possible $SU(2) \times U(1)$ term of interaction:

$$(l^i \phi^j)\varepsilon_{ij} \tag{1.32}$$

where the indices $i, j = 1, 2$ run over the "up-side" and "down-side" components of the objects and the antisymmetric tensor ε_{ij} is used such that are now the "up" fields the ones gaining mass. The interaction term for the "up" fields can be seen as a coupling term with a transformed (rotated) ϕ field, $\tilde{\phi}$ defined as:

$$\tilde{\phi} = i\sigma_2(\phi^\dagger)^t \tag{1.33}$$

[13] $\sin^2\theta_W \simeq 0.231$

For quarks and neutrinos an additional complication is also necessary: the eigenstates produced by weak interactions are flavour eigenstates but not, at the same time, mass eigenstates. The two basis (interaction and mass) are related by the rotation matrices, known as the CKM matrix (Cabibbo-Kobayashi-Maskawa) for quarks and the PMNS matrix (Pontecorvo–Maki–Nakagawa–Sakata) for neutrinos.

1.4 Standard Model Lagrangian

Finally, the SM Lagrangian density can be decomposed as a sum of four different terms:

$$\mathcal{L}_{SM} = \mathcal{L}_f + \mathcal{L}_{gauge} + \mathcal{L}_\phi + \mathcal{L}_{Yuk} \tag{1.34}$$

which are related respectively to the fermion, gauge, scalar and Yukawa sectors. The four Lagrangian terms are detailed below.

– The fermionic part of the Lagrangian density consists of kinetic energy terms for quarks and leptons, namely:

$$\mathcal{L}_f = i\bar{q}_{iL}Dq_{iL} + i\bar{u}_{iR}Du_{iR} + i\bar{d}_{iR}Dd_{iR} + i\bar{\ell}_{iL}D\ell_{iL} + i\bar{e}_{iR}De_{iR} \tag{1.35}$$

The gauge-covariant derivatives contain the gauge tensors:

$$G^i_{\mu\nu} = \partial_\mu G^i_\nu - \partial_\nu G^i_\mu - g_s f_{ijk} G^j_\mu G^k_\nu, \text{ with } i,j,k = 1,...,8;$$

$$W^i_{\mu\nu} = \partial_\mu W^i_\nu - \partial_\nu W^i_\mu - g\varepsilon_{ijk} W^j_\mu W^k_\nu, \text{ with } i,j,k = 1,...,3;$$

$$B_{\mu\nu} = \partial_\mu B_\nu - \partial_\nu B_\mu$$

where g_S and g are the coupling constants associated to the $SU(3)_c$ and $SU(2)_L$ symmetry groups respectively.
The covariant derivatives are specified as:

$$D^\mu q_{iL} = (\partial^\mu + \frac{i}{2} g_S G^\mu_a \lambda_a + \frac{i}{2} g W^\mu_b \sigma_b + \frac{i}{6} g' B^\mu) q_{iL},$$

$$D^\mu u_{iR} = (\partial^\mu + \frac{i}{2} g_S G^\mu_a \lambda_a + \frac{2i}{3} g' B^\mu) u_{iR},$$

$$D^\mu d_{iR} = (\partial^\mu + \frac{i}{2} g_S G^\mu_a \lambda_a - \frac{i}{3} g' B^\mu) d_{iR},$$

$$D^\mu \ell_{iL} = (\partial^\mu + \frac{i}{2} g W^\mu_a \sigma_a - \frac{i}{2} g' B^\mu) \ell_{iL},$$

$$D^\mu e_{iR} = (\partial^\mu - i g' B^\mu) e_{iR}$$

where g' is the coupling constant associated to the $U(1)_Y$ symmetry group.

– The gauge Lagrangian density $\mathcal{L}_{gauge}$ regroups the gauge fields of all three symmetry groups:

$$\mathcal{L}_{gauge} = -\frac{1}{4}G^i_{\mu\nu}G^{\mu\nu i} - \frac{1}{4}W^i_{\mu\nu}W^{\mu\nu i} - \frac{1}{4}B_{\mu\nu}B^{\mu\nu} \tag{1.36}$$

– The scalar sector is composed of the kinetic term and the potential one:

$$\mathcal{L}_\phi = (D^\mu\phi)^\dagger D_\mu\phi - \mu^2\phi^\dagger\phi - \lambda(\phi^\dagger\phi)^2 \tag{1.37}$$

where the kinetic part includes the gauge covariant derivative defined as:

$$D_\mu\phi = \left(\partial_\mu + ig\vec{T}.\vec{W}_\mu + \frac{ig'}{2}B_\mu\right)\phi$$

– The last piece is the Yukawa Lagrangian density which describes the interactions between the fermions and the scalar doublet ϕ. If one notes Y^u, Y^d and Y^e three general complex 3×3 matrices of dimensionless couplings, the Yukawa Lagrangian density can be written as:

$$\mathcal{L}_{Yuk} = -Y^u_{ij}\bar{q_{iL}}u_{jR}\tilde{\phi} - Y^d_{ij}\bar{q_{iL}}d_{jR}\phi - Y^e_{ij}\bar{\ell_{iL}}e_{jR}\phi + h.c. \tag{1.38}$$

where $\tilde{\phi}$ is defined as:

$$\tilde{\phi} = i\sigma_2(\phi^\dagger)^t \tag{1.39}$$

1.5 Radiative corrections and renormalization

The SM Lagrangian in Eq. 1.34 contains all the information needed to compute physical quantities such as decay rates or cross-sections. In quantum field theory, the probability of a state $|a\rangle$ to evolve after some time to a state $|b\rangle$ is proportional to the square of the amplitude $\langle b|\hat{S}|a\rangle$, where $\hat{S}$ is the S-matrix which consists of a time ordered exponential of the interacting Hamiltonian. It is usually treated using a perturbative technique. The exponential is decomposed into a sequence of terms of increasing powers of the coupling constants. Each of its terms can be described by one or several Feynman diagrams from which an amplitude can be calculated using a finite set of rules. The leading order (LO) represents the classical amplitude and the higher orders are quantum corrections. A common issue when calculating the quantum corrections is the appearance of divergences. In the SM though, these divergences can be reabsorbed in the definition of the coupling constants at a given scale through a procedure named renormalization [9].
As an example, one can consider the action in Eq. 1.7 where the spinor field is taken massless. The leading order and the 1-loop Feynman diagrams for

the process $\psi\bar{\psi} \to \gamma \to \psi\bar{\psi}$ are shown in Fig. 1.3. The leading order amplitude, computed applying the Feynman rules and naming q the exchanged momentum, is:

$$\mathcal{M}_{LO} = ie^2\gamma^\mu \frac{\eta_{\mu\nu}}{q^2}\gamma^\nu$$

For the 1-loop contribution, one must integrate over the fermion 4-momentum

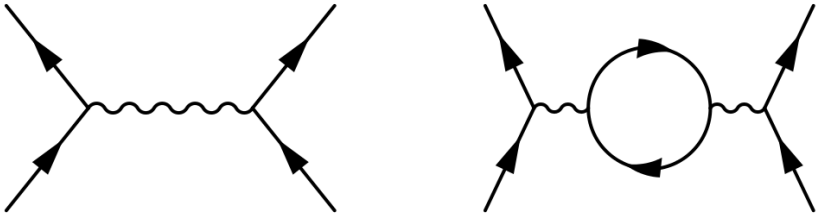

Figure 1.3: The leading order (left) and 1-loop correction (right) Feynman diagrams for the process $\psi\bar{\psi} \to \gamma \to \psi\bar{\psi}$ in QED

in the loop, k. The integral is proportional to $\int d^4k/k^4 \simeq \int dk/k \simeq ln(k)$. In order to obtain a finite result, one introduces a cut-off Λ inside the integral: $\int^\Lambda dk/k$ and the total amplitude including the 1-loop correction becomes:

$$\mathcal{M}_{1-loop} = ie^2\gamma^\mu \frac{\eta_{\mu\nu}}{q^2}\gamma^\nu(1 + \frac{e^2}{12\pi^2}\log\frac{q^2}{\Lambda^2}) \tag{1.40}$$

One can get rid of this cut-off by trading the coupling present in the action, e, for the effective coupling e_{eff} at a given scale μ. The equation then becomes:

$$\mathcal{M}_{1-loop} = ie^2_{eff}\gamma^\mu \frac{\eta_{\mu\nu}}{q^2}\gamma^\nu(1 + \frac{e^2_{eff}}{12\pi^2}\log\frac{q^2}{\mu^2}) \tag{1.41}$$

As a consequence, the coupling that should be used to calculate a physical process depends on its scale. The variation of the coupling is described by the renormalization group equation which in the present case is given, for 1-loop corrections by:

$$\frac{d}{d\log q}e(q) = \frac{e^3(q)}{12\pi^2} \tag{1.42}$$

A similar equation holds for any parameter present in the action.
In the SM, the effective couplings g_i $(i = 1, 2, 3)$ associated respectively to U(1), SU(2) and SU(3) are constrained by the equations:

$$\frac{d}{d\log q}g_i(q) = -\frac{b_i g_i^3(q)}{(4\pi)^2} \tag{1.43}$$

with [10]

$$b_1 = -\frac{4}{3}n_g - \frac{1}{10}n_h$$

$$b_2 = \frac{22}{3} - \frac{4}{3}n_g - \frac{1}{6}n_h$$

$$b_3 = 11 - \frac{4}{3}n_g$$

where n_g is the number of generations (3) and n_h the number of scalar bosons (1). One of the important consequences of these equations is the asymptotic freedom of QCD [11, 12]: because of the sign of b_3, g_3 weakens at high energy and the quarks can then be treated as free particles. This feature plays an essential role in the calculation of cross-sections in hadron collisions. Equation 1.43 can be also seen as a powerful guideline for the construction of models of new physics, since it happens to be very easy to build a theory which is not renormalizable which hence, in principle, has to be discarded.

1.6 Motivation for new theories beyond the Standard Model

Despite its success in describing a vast amount of experimental data, spanning several orders of magnitudes in energy, it is commonly known that the Standard Model only constitutes a low energy approximation of a more fundamental theory. Indeed, there are some open questions or features which cannot be explained by the SM, as explained below. Some of them come from experimental observations (dark matter [13, 14], neutrino mass [15, 16]) some others are limitations of the current theory (lack of gravity description, convergence of the coupling constants [10]) or aspects dealing with the internal consistency of the theory (hierarchy problem, free parameters of the Lagrangian [1]). In more details:

- **Gravitational interaction:** gravity, the fourth fundamental interaction which is easily visible and described in macro systems already at the beginning of physics by the Newton's laws, is not included in the SM. It is, by many aspects, very different from the three other forces and the purpose to establish a common framework describing all of them has to face several difficulties. The Einstein's General Relativity (GR) theory shows that gravity is intimately connected to the space-time geometry which is, in turn, coupled to the particles energy-momentum tensor via the Einstein's fields equations: this makes its integration inside the SM framework more difficult than simply adding a new interaction. To combine the quantum theory of the SM with the GR, a quantum theory of gravity is necessary; this would lead to a new field associated to gravity: a spin 2 particle, called graviton. It can be shown that such a theory is not renormalizable: loop corrections including gravitons induce ultraviolet divergences that cannot be reabsorbed through the renormalization procedure, which is instead adopted in electroweak and chromodynamics

theories (see Sec. 1.5). Finally, the strength of the gravitational force is much lower than the other ones. Whereas the strong, weak and electromagnetic forces have similar strengths at the electroweak scale (energies of $\mathcal{O}(100$ GeV$)$), the energy at which gravitational interactions becomes relevant is at the order of the Planck scale of $E_{Pl} = 10^{19}$ GeV, which is defined by the Planck mass, $M_{Pl} = \sqrt{\hbar c/G}$, where G is the gravitational constant. The huge difference between the electroweak scale and the Planck scale is also known as the hierarchy problem and is deeply connected to the problem of the fine-tuning of the Higgs boson mass (see the following point).

– **Hierarchy problem and fine-tuning of the Higgs boson mass:** after the discovery of the Higgs boson and the measurement of its mass of ≈ 125 GeV all the ingredients of the SM have been experimentally established. All particles in the Standard Model, including the Higgs boson, have a *bare mass* which is the mass obtained from the quantum propagator at the lowest order in perturbation theory. This is not anyway the *physical mass*, i.e. the mass that can be measured experimentally, because radiative corrections at higher orders coming from loops have to be considered. As explained in Sec. 1.5, the renormalization process relates the properties of the physical quantities (mass, charge, ...) to those of the bare particles, introducing suitable cut-off parameters in considering higher order corrections. It is known [17] that the renormalization procedure corrects the squared bare mass (m_0) of the Higgs boson (H) with an extra term, including higher order corrections, δm_{H}^2 to obtain the physical mass m_{H}:

$$m_{\mathrm{H}}^2 = m_0^2 - \delta m_{\mathrm{H}}^2 \tag{1.44}$$

where δm_{H}^2 includes all contributions from radiative corrections to the Higgs propagator. The main ones[14] are those involving top quarks, vector bosons and the scalar boson itself. The corresponding Feynman diagrams are shown in Fig. 1.4, where the Higgs boson is denoted as h [1].

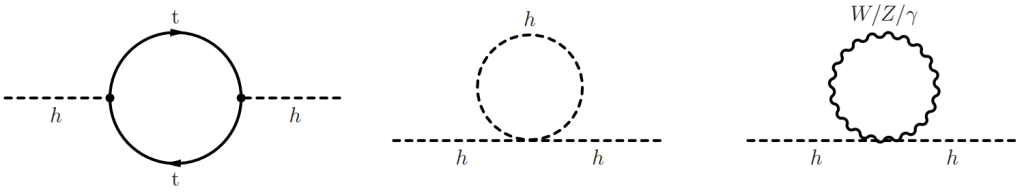

Figure 1.4: Main divergent contributions to the scalar boson mass predicted by the SM

The integrals corresponding to the amplitude of these processes are divergent, so a cut-off parameter Λ is introduced. This parameter represents the energy up to which the SM can be still considered valid. In principle, one can assume that the SM is valid up to the Planck scale at which

[14]This statement is true for any elementary spin 0 boson.

gravitational effects cannot be neglected. With this assumption Λ would be of the order of $\approx 10^{19}$ GeV. The full calculation gives that δm_{H}^2 is proportional to Λ^2:

$$\delta m_{\mathrm{H}}^2 \propto \Lambda^2 \approx 10^{38}\ \mathrm{GeV}^2 \tag{1.45}$$

Since m_{H} is ≈ 125 GeV ($\approx 10^2$), Eq. 1.44 can be rewritten as:

$$10^4\ \mathrm{GeV}^2 \approx m_0^2 - \Lambda^2 \approx m_0^2 - 10^{38}\ \mathrm{GeV}^2$$

which means that m_0^2 is of the same order of Λ^2 (10^{38}) and that these two terms cancel with a very high precision to obtain the value of the physical mass. This mathematical problem, known as *fine-tuning*, does not invalidate the theory, which is still consistent. Anyway it seems an unnatural coincidence that m_0^2 cancels all the loop contributions up to this precision.

The choice of Λ made in the previous calculation is somehow arbitrary because it is based on the assumption that the Standard Model is still valid up to the greatest possible energy, the Planck scale. If a lower Λ is chosen, the cancellation is tuned to an acceptable level. If, for instance, $\Lambda \approx$1 TeV is chosen, the hierarchy problem is completely solved since the cancellation is of the order of one over ten, which seems a natural and acceptable value. For this reason, if one accepts the fine-tuning argument, new physics phenomena at the TeV scale are expected, since at energy higher than Λ =1 TeV, the SM is not valid anymore.

– **Matter content of the universe**: astronomical observations show that the visible content of matter can only be approximately 5% of the total matter and energy content of our universe. This statement results from several recent cosmological observations. First, the measured orbital velocities of stars around their galaxy center [13, 14] is incompatible with the observed matter density in space: in other words, the stars are moving too fast. In order to reconcile the experimental data with the theory, the existence of another kind of matter that does not interact via electromagnetic or strong interactions, the dark matter, has therefore been postulated. A second major result in cosmology is the discovery that the Universe is in accelerated expansion: in average galaxies recede from each other and their escape speed increases with the distance [18, 19]. Putting together these two cosmological results, one can conclude that the matter/energy content of the universe is made of 5% ordinary matter, 25% dark matter and 70% dark energy, which is thought to be responsible for the observed accelerated expansion of the universe, by introducing a repellent force (negative pressure). The SM does not offer good candidates or explanations for the dark matter and dark energy problems.

– **Neutrino masses**: originally, SM neutrinos were assumed massless. The fact that neutrinos can change from one flavour to another implies that they must have non-zero mass differences [15, 16] and that their mass eigenstates are different from their flavour eigenstates. A mass term for

the neutrinos can, in principle, be added to the SM as described in Chapter 1, but it is not clear if the small masses that the neutrinos must have can arise from the same electroweak symmetry breaking mechanism that is in act for the other SM particles.

– **Free parameters of the SM Lagrangian**: the SM contains 19 free parameters, that have to be measured. The parameters include the charged fermion masses, the mixing angles and the charge-parity (CP) violating phase of the Cabibbo-Kobayashi-Maskawa (CKM) matrix, the coupling constants of the three forces and the mass and vacuum expectation value of the Higgs boson. However, it is widely believed that at least some of these parameters should be related to each other from a mechanism that is not described by the SM. As an example one could consider the different masses of the quark and lepton generations as arising from a common generation mechanism in a BSM theory, that has a spontaneously broken symmetry at the SM scale. The list of parameters is summarized in Tab. 1.5.

Quantity	Symbol	Value
Electron mass	m_{e}	511 keV
Muon mass	m_{μ}	105.7 MeV
Tau mass	m_{τ}	1.78 GeV
Up quark mass	m_{u}	2.3 MeV ($\mu_{\overline{\mathrm{MS}}}$=2 GeV)
Down quaky mass	m_{d}	4.8 MeV ($\mu_{\overline{\mathrm{MS}}}$=2 GeV)
Strange quake mass	m_{s}	95 MeV ($\mu_{\overline{\mathrm{MS}}}$=2 GeV)
Charm quark mass	m_{c}	1.28 GeV ($\mu_{\overline{\mathrm{MS}}} = m_{\mathrm{s}}$)
Bottom quark mass	m_{b}	4.18 GeV ($\mu_{\overline{\mathrm{MS}}} = m_{\mathrm{b}}$)
Top quark mass	m_{t}	173.5 GeV
CKM 12-mixing angle	θ_{12}	12.9°
CKM 23-mixing angle	θ_{23}	2.4°
CKM 13-mixing angle	θ_{13}	0.2°
CKM CP violating phase	δ_{13}	69°
W boson mass	m_{W}	80.4 GeV
Z boson mass	m_{Z}	91.2 GeV
Strong coupling constant	α_s	0.119 ($\mu_{\overline{\mathrm{MS}}} = m_{\mathrm{Z}}$)
QCD vacuum angle	θ_{QCD}	~ 0
Higgs boson vacuum expectation value	v	246 GeV
Higgs boson mass	m_{H}	125.09 GeV [20]

Table 1.5: SM parameters. The quark masses are presented in the renormalization scheme known as $\overline{\mathrm{MS}}$ [1]

– **Convergence of the coupling constants**: the SM coupling constants of the electromagnetic interaction, the weak interaction and the strong interaction have a similar value at an energy scale of $\mathcal{O}(10^{16}$ GeV). However, they do not converge to a single value as shown in Fig. 1.5. In

order to unify the coupling constants, an extension of the SM would be necessary in order to modify their evolution above the electroweak scale.

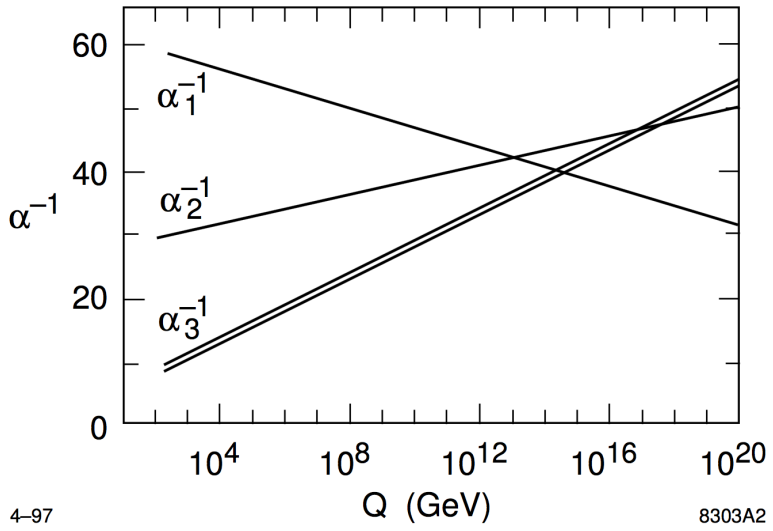

Figure 1.5: Evolution of the SM couplings $\alpha_i = \frac{g_i^2}{4\pi}$ as a function of the energy scale [10]

All these aspects indicate that there must be new physics at a scale beyond the electroweak scale. What is unknown, however, is the energy scale at which this new physics will manifest itself. Driven by the arguments given while treating the hierarchy problem, it is believed that there should be new physics at the TeV scale, at which a discovery with direct searches at the LHC could be possible.

1.7 Theory model for Vγ resonances

In general, many theories which predict new resonances decaying into boson pairs exist. Through the postulation of the existence of Higgs doublets [21], extra-dimension [22] or predicting theories [23] of physics beyond the SM that address electroweak gauge symmetry breaking (the mechanism through which W and Z bosons acquire masses).
One of this theories [24] predicts a "so called" pion triplet π_3^0 - $\pi_3^\pm$ besides other resonances reported in Fig. 1.6.
The model is an extension of minimal supersymmetry [25] which preserve gauge coupling unification and that can be included in the SM. In these theories, the confinement scale is tied to the mass scale of the superpartners. Minimal split supersymmetry places this confinement scale between ∼1-10^3 TeV, so that the composite states of the new sector lie within reach of the LHC or, at worst, a 100 TeV collider. The low energy spectra of these theories include new pseudoscalar particles and new vector mesons. If explicit chiral symmetry breaking

is small, we expect the new pseudoscalars to be the lightest new states. While the precise phenomenology, including their lifetimes, depends on the details of the UV completion. Moreover, if some of the coloured or charged pseudoscalars are collider stable, then the confinement scale is forced to be >7 TeV, provided that these new particles are sufficiently light.

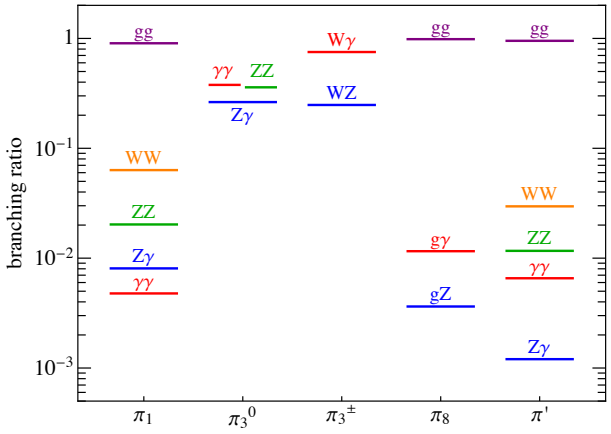

Figure 1.6: Branching ratios for different new particles prediction. The one used for the analysis described in Chapter 6 is the third column where a charged π_3 decays into a W boson and a photon (the highest signature for this particular "pion")

The predicted cross section of these spin-1 particles is shown in Fig. 1.7.

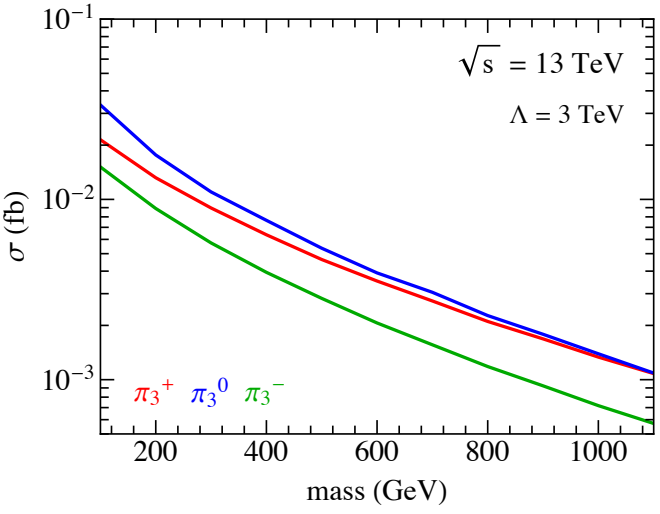

Figure 1.7: Single production cross section of pions in vector boson fusion. The red and green lines describe the cross section behaviour with respect to the resonance mass of the charged π_3 while the neutral case is described in blue

As can be seen in Fig. 1.6, many final states are predicted from this theory. The branching ratios and the production cross sections strongly depend from

the model parameters which are however unknown. In Fig. 1.6, the most probable decay of the new particles predicted by this model is the gg final state. However in this thesis the Zγ and Wγ final states are probed and are discussed in Chapter 6. It is of great importance to have a wide research program covering all the possible final states to investigate such theories as much as possible.

1.8 Experimental signature

The searches for resonances which are predicted by theories described in Sec. 1.7, need a boson (Z or W) and a photon in the final state. The final signature of these new resonances can be detected through the decay product of the boson and one photon. For what concern the Z, its decay modes are 3:

1. leptonic: 10% of the times (Z$\rightarrow$l$\bar{\text{l}}$, where l is an electron, muon or tau)
2. hadronic: 70% of the times (Z$\rightarrow$ q$\bar{\text{q}}$ where q is a quark)
3. invisible: 20% of the times (Z$\rightarrow$ $\nu\bar{\nu}$ where ν is a neutrino)

The leptonic and hadronic final states are described below in Sec. 1.8.1 - 1.8.2 and Sec. 1.8.3.
For the Wγ final state, the possible decay of the W boson are:

1. leptonic: 30% of the times (W$\rightarrow$ lν where l is an electron, muon or tau and ν is a neutrino)
2. hadronic: 70% of the times (W$\rightarrow$qq' where q is a quark)

The following final states are possible:

1) Z$\gamma \rightarrow$ ll + photon
2) Zγ/W$\gamma \rightarrow \nu\nu$/l$\nu$ + photon
3) Zγ/W$\gamma \rightarrow$ hadrons + photon

The experimental signatures and the general analysis strategies are discussed in the next sections.

1.8.1 X$\rightarrow$Z$\gamma \rightarrow$l$\bar{\text{l}}$ channel

The Z boson, coming from the interaction X $\rightarrow$ Zγ, can decay in a l^+l^- and the final state in this case will have a lepton couple and a photon. The search looks for a bump in the mass spectrum of the dilepton+photon system (whose Feynman diagram is shown in Fig. 1.8). The main background for this analysis comes from the SM Zγ production and the Drell-Yan (Fig. 1.9) processes that could mimic the signature of the analysis.
However, to minimize the background contribution, the reconstructed dilepton mass is required to be around 90 GeV (the Z mass) in order to reduce the

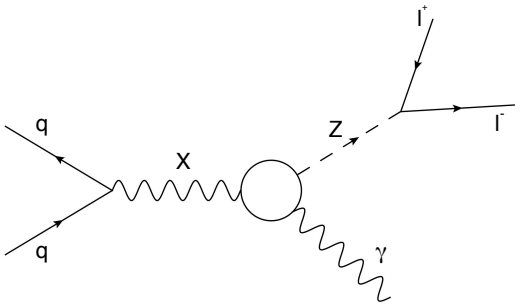

Figure 1.8: Feynman diagram representation of the Zγ decay into leptons (l stands for electron, muon or tau)

Drell-Yan contribution.

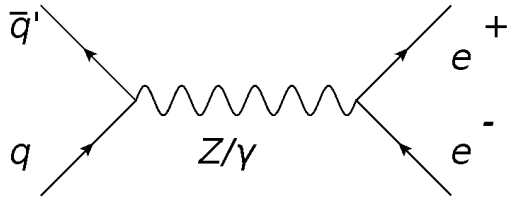

Figure 1.9: Feynman diagram representation of the Drell-Yan process

Due to the high resolution of the detector and the low contribution of the background, this particular channel is very sensitive at low mass (of the Z+photon system).

1.8.2 X→Z$\gamma \to \nu\bar{\nu}$ and X→W$\gamma \to l\bar{\nu}$ channels

In this particular signature, the product decay of the boson are made (in total or in part) by invisible particles. The Z boson can decay in a neutrino couple (see Fig. 1.10(a)) while the W boson, as seen in Sec. 1.8, can decay into a lepton and its corresponding neutrino (as showed in Fig. 1.10(b)). In this case, the Vγ (where V stands for Z or W boson) signal cannot be detected as a peak in the invariant mass of the V+photon spectrum because the invisible component of the decay cannot be detected, therefore it will appear as Missing Transverse Energy (described in Sec. 4.14). The solution is to look at another variable called "transverse mass" of the V+photon system which is obtained through the relation in Eq. 1.46 (showed in Fig. 1.11).

$$M_T = \sqrt{(E_{T,V} + E_{T,\gamma})^2 - (\overrightarrow{p}_{T,V} + \overrightarrow{p}_{T,\gamma})^2} \tag{1.46}$$

where the V and γ subscripts indicates the V boson or photon variables and the transverse energy is defined in Eq. 1.47.

$$E_T = \sqrt{m^2 + (\overrightarrow{p}_T^2)} \tag{1.47}$$

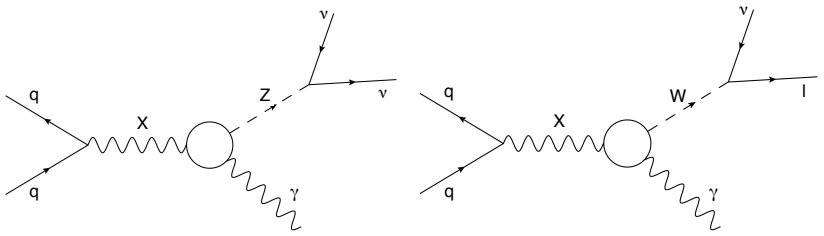

Figure 1.10: Feynman diagram representation of the Zγ invisible decay (a) and the Wγ decay (b) into leptons (l stands for electron, muon or tau and ν is the associated neutrino)

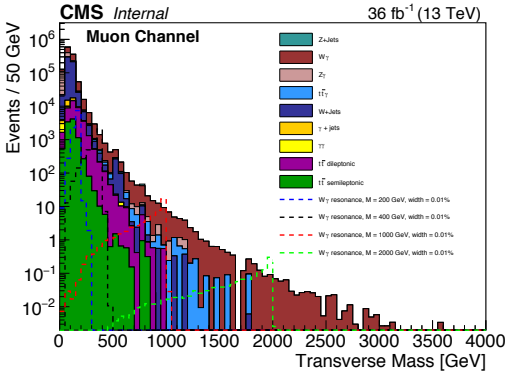

Figure 1.11: Preliminary transverse mass of MC background and signal for masses between 200 GeV and 1 TeV (dashed lines) in the leptonic channel

Due to the characteristics of the two channels, their sensitivity to new physics is different. The Wγ search will be more sensitive as half of the final state of the boson can be reconstructed with respect to the Zγ signature where the Z decays into invisible particles.

1.8.3 X→Z/Wγ →q$\bar{\text{q}}$ channel

Both Z and W bosons can decay into hadrons (detected as jets and described in Sec. 4.6) for ∼70% of the times. In the final state for both signals (showed in the diagram of Fig. 1.12) one or two jets and a photon are required. As the leptonic channel, also in this case, a bump in the invariant mass jet+photon is searched. The main backgrounds for the Zγ and Wγ analyses are the events coming from QCD interactions and γ+Jets production.

The number of jets present in the final state is determined by the mass of the new resonance produced. The higher its mass is, the higher will be the transverse momentum of the Z/W. Following the simplified equation defined in Eq. 1.48, it is possible to estimate the minimum angle separation between the two quarks coming from the boson decay.

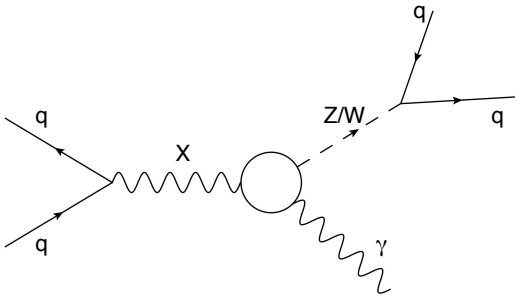

Figure 1.12: Feynman diagram representation of the Zγ/Wγ decay into hadrons (q stands for quarks)

$$\vartheta_{12} \approx 2\frac{M_V}{p_{TV}} \tag{1.48}$$

where ϑ_{12} is the angle between the two quarks of the boson decay, M_V is the boson mass and p_{TV} is its transverse momentum.
As the p_T of the boson increases, the ϑ_{12} angle decreases and the two quarks are more collimated until they are so close to be reconstructed as a single jet (for a resonance of $\sim$1 TeV the angle ϑ would be around 0.4 rad). In this case, to optimize the energy recollection, wide jets are used (with a cone of $\sim$ 1 rad).
The study carried on the Zγ/Wγ resonances presented in Chapter 6 looks for resonances with mass greater than 600 GeV where the bosons are in the boosted regime and the two jets are already merged in a single wide one. The main challenge in this channel is to discriminate jets from W/Z boson decays and jets coming from hadronization of isolated quarks and gluons.

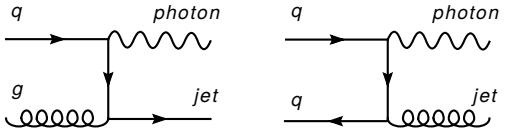

Figure 1.13: Feynman diagram representation of the Zγ/Wγ decay into hadrons (q stands for quarks)

In the search for massive resonances decaying into bosons going to hadrons, techniques for noise and background reduction are needed. In the boosted regime a dedicated selection can be arranged to discriminate between quark or gluon hadronization products and the boson hadronic decay products. The mass of the jet (which for the signal has a peak around the boson mass) and the topology of the particles inside the jet are used.
In the high mass region (for resonances heavier than 1 TeV), thanks to the high branching ratio and the low γ+jet and QCD background, this channel has better a performance compared with the leptonic ones.

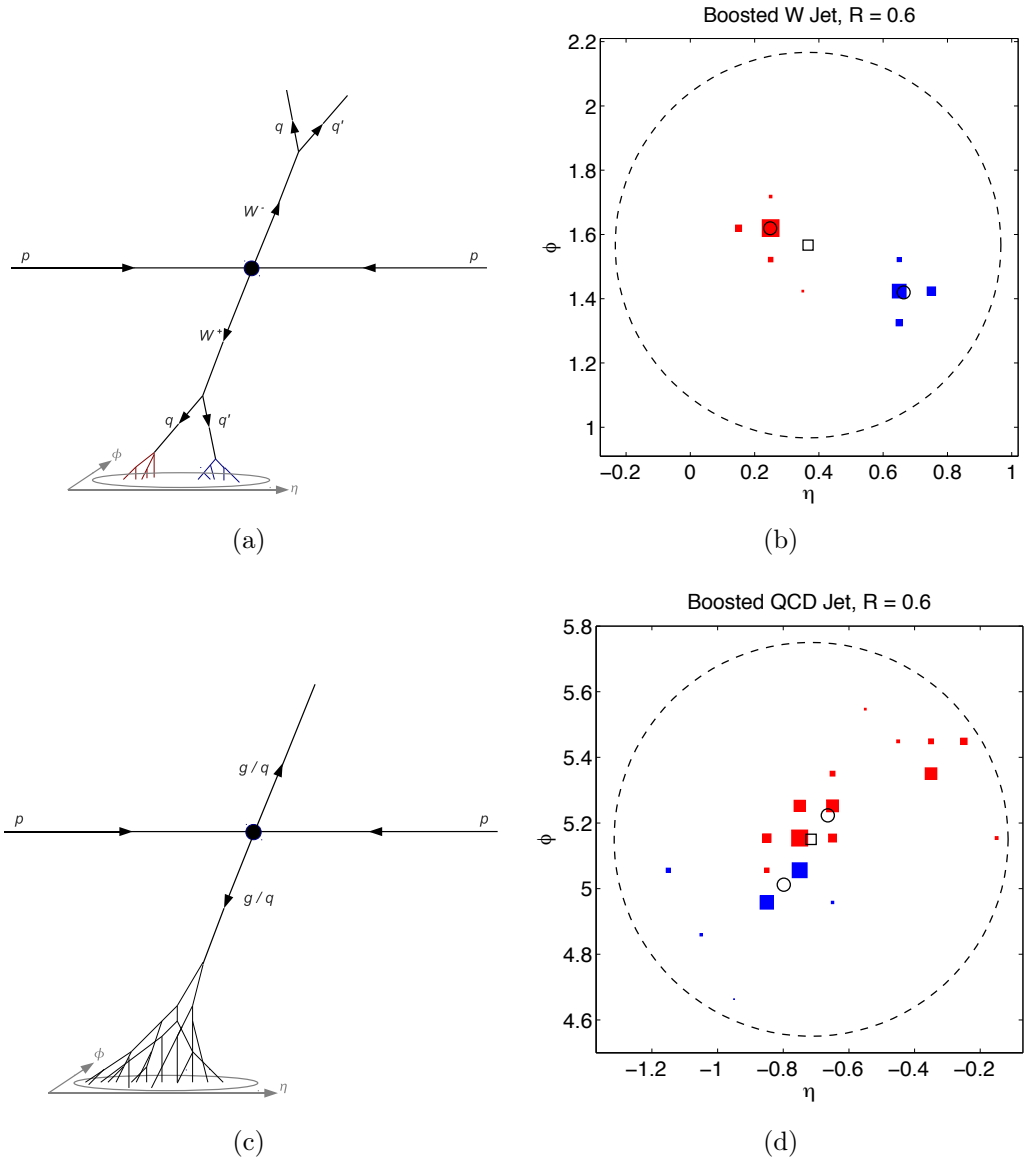

(a) (b) (c) (d)

Figure 1.14: Schematic of the fully hadronic decay sequences in (a) W^+W^- and (c) dijet QCD events. Whereas a W jet is typically composed of two distinct lobes of energy, a QCD jet acquires invariant mass through multiple splittings. Typical event displays for (b) W jets and (d) QCD jets with invariant mass near m_W

In Fig. 1.14, the topology of the jet and the decay sequence of events coming from a boson and a quark/gluon are shown. Comparing the Fig. 1.14(b) and 1.14(d) the typical 2-prong structure of the boson decay can be noted. Several observables have been proposed to identify this particular substructure (a detailed description can be found in Sec. **??**). In addition, the mass of a jet coming from boson decay is higher than the mass of a quark/gluon jet. This difference can also be exploited to distinguish the two events. In addition, grooming algorithms that clean the final jet from soft QCD radiation, are also employed as discussed in Sec. 4.7.

These jet substructure observables are studied in data and simulation in order

to evaluate their performance and derive correction factors for the simulation. This calibration procedure is one of the topics of this thesis and it is described in Chapter 5.
In the Zγ/Wγ hadronic analyses presented in this thesis, this selection is used to reduce the background component coming mainly from the γ+Jet Standard Model processes and increasing the sensitivity of the final results showed in Sec. 6.10.

1.8.4 Leptonic and Hadronic comparison

The final states in leptons and hadrons can be treated as complementary. The leptonic final states typically reach high sensitivity at low masses due to the excellent energy and momentum resolution for leptons and the relatively low background. On the other hand, the hadronic final states are characterized by larger branching ratios compared to the leptonic ones; they are more sensitive at high resonance mass when QCD and γ+jet backgrounds become small.

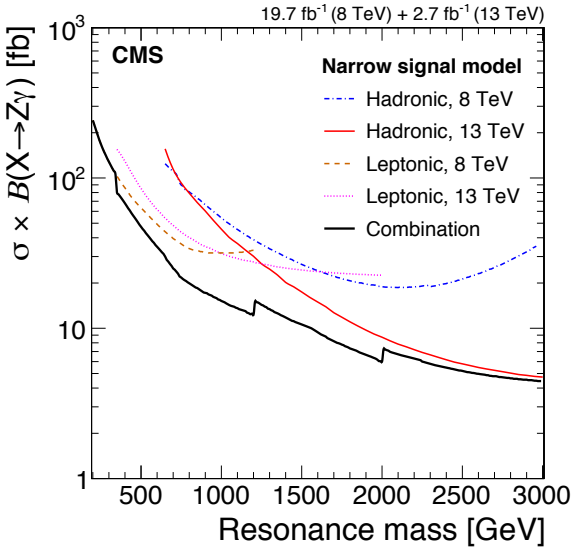

Figure 1.15: Leptonic and hadronic expected limits for RunI and RunII. In blue the hadronic limit for 8 TeV, in brown the leptonic limit for 8 TeV, in red the hadronic limit for 13 TeV while in magenta the leptonic limit for 8 TeV

Figure 1.15 shows the expected sensitivity (in terms of upper limits on the cross section of the new resonance X) for both leptonic and hadronic final states for 8 and 13 TeV. The limits have been rescaled to take into account the two different energies. This estimation refers to an analysis that uses the full dataset collected by CMS before 2016. In the Fig. 1.15 it is shown that the leptonic channel (Z$\gamma\rightarrow$ ll + γ) dominates the sensitivity to new physics at low resonance mass (<1.2 TeV) while at high resonance mass (>1.2 TeV) the hadronic channel provides better (meaning lower) limits on the cross section. Similar considerations can be made for the Wγ final states.

1.8.5 Previous results of Zγ and Wγ searches

Searches for Zγ and Wγ resonances have been performed by the ATLAS and the CMS collaborations using pp collision data collected at $\sqrt{s}$ =8 TeV (Run I) and $\sqrt{s}$ = 13 TeV (Run II, partial dataset).
For RunI at 8 TeV the analysis for Wγ signals performed by the ATLAS collaboration is reported in [26]. For RunII at 13 TeV ATLAS recently presented a result combined with the H→Zγ→ ll + γ production in [27].
In Fig. 1.16, the upper limits on the cross-section of the resonance production of RunI (X→Wγ →lνγ) and RunII (X→Zγ →llγ) for ATLAS are presented. No excesses have been found in both searches and upper limits on the resonance production cross-section have been set.

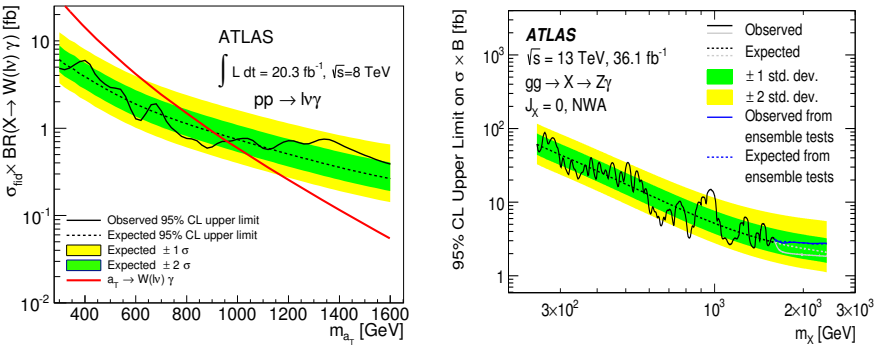

(a) (b)

Figure 1.16: ATLAS limits for Wγ resonances for RunI data (a) and Zγ resonances (b) for RunII data

For what concern the results of CMS they are reported into two different articles [28, 29], which contain the RunI and RunII (only 2015 data) datasets and are divided into hadronic and leptonic channels (Zγ → qq + γ and Zγ → ll + γ). In the leptonic analyses (showed in Fig. 1.17(a)) no significant deviation with respect to the Standard Model expectation has been found and upper limits at 95% confidence level have been set on the production cross section of resonances. The results of the combined analyses (leptonic and hadronic, at 8 TeV and 13 TeV) are shown in Fig. 1.18; they cover masses between 280 GeV and 3 TeV.

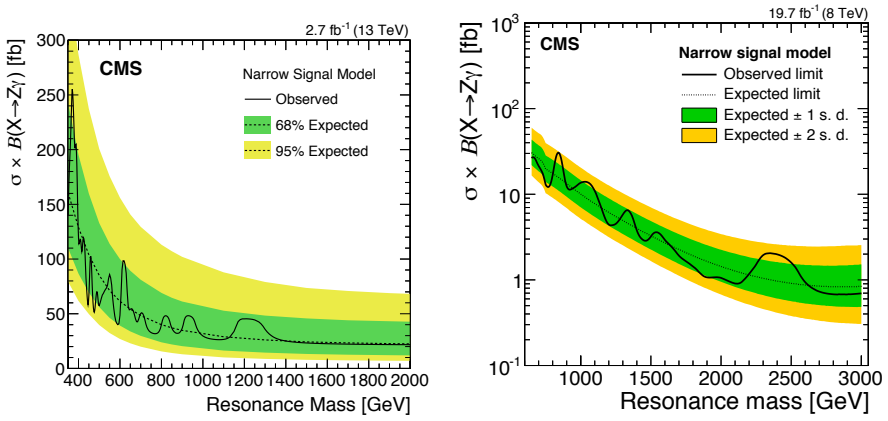

(a) (b)

Figure 1.17: CMS limits for $Z\gamma \to ll\gamma$ resonances (a) and $Z\gamma \to qq\gamma$ (b) at 13 TeV (2015 data)

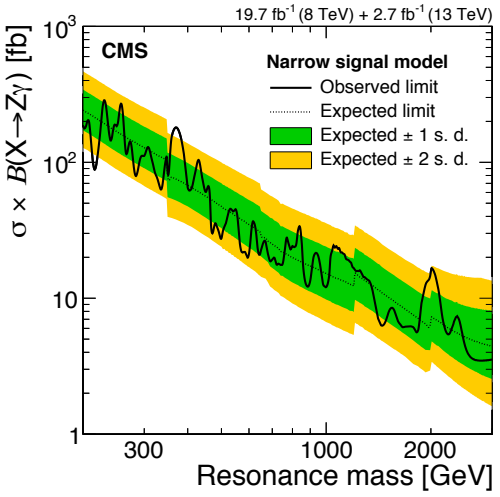

Figure 1.18: CMS limits for $Z\gamma \to qq/ll\gamma$ resonances combined for 8 TeV and 13 TeV (2015 data)

Chapter 2

Proton physics at the Large Hadron Collider

In this chapter the design of the Large Hadron Collider will be described as well as the phenomenology of the proton-proton interactions. While the Large Hadron Collider can also support lead-lead or lead-proton collisions, the following chapter will describe only the phenomenology of the proton-proton collisions as they correspond to the dataset analyzed for the physics results exposed in this thesis.

2.1 The LHC collider

The Large Hadron Collider (LHC) [30] is a proton-proton (pp) accelerator and collider installed in the same circular underground tunnel occupied until the year 2000 by the Large Electron Positron collider (LEP)[1]. The tunnel is located at approximately 100 m below the level of the ground[2], under the Geneva area and has a circumference of 26.7 km. Due to the need of achieving higher center-of-mass energy, pp proton beams replaced the electron and positron beams used for LEP. In fact, in a circular collider of radius R, the energy loss per turn due to the synchrotron radiation is proportional to $(\mathrm{E/m})^4/\mathrm{R}^2$, where E and m are respectively the energy and mass of the accelerated particles: the use of protons, due to their higher mass compared to electrons, implies a smaller energy loss from synchrotron radiation. A pp collider was preferred to a $\mathrm{p\bar{p}}$ collider because it allows to reach higher event rates. Moreover the low anti-proton production efficiency (10^5 protons are needed to create an anti-proton via the reaction $\mathrm{pp} \rightarrow \mathrm{ppp\bar{p}}$) and larger time needed to accumulate them would make almost impossible to achieve the required statistics of events needed in the search for new physics at the LHC. This in turn excludes the $\mathrm{p\bar{p}}$ collider configuration, where a common vacuum and magnet system are used for both circulating p and $\bar{\mathrm{p}}$ beams, as it was done for example at the Tevatron: to

[1] In this latter case, electrons and positrons were accelerated and brought into collisions.
[2] The closest point to the surface is at 45 m, while the deepest one is at 170 m.

collide two counter-rotating proton beams opposite magnetic dipole fields are required with separate vacuum chambers. Because of the limited size of the tunnel inherited from the LEP era, the LHC uses twin cylindrical magnets instead of two separate rings.

The LHC ring is divided in eight arcs and eight straight sections, four of them host various equipment needed for the accelerator while in the other four the two beams are brought into collision at the four interaction points (IPs), where the four main experiments of the LHC are located:

- ALICE (A Large Ion Collider Experiment) [31] is designed to address the physics of the quark-gluon plasma at extreme values of energy density and temperature in nucleus-nucleus collisions.
- ATLAS (A Toroidal LHC ApparatuS) [32] covers the same physics objectives as CMS while exploiting different technical solutions, including a large toroidal magnet;
- CMS (Compact Muon Solenoid) [33], which will be described in greater details in Chapter 3, is a general-purpose detector with a large program of physics analyses;
- LHCb (Large Hadron Collider beauty) [34] studies matter-antimatter asymmetry via CP violation, through studies involving b quarks;

ATLAS and CMS analyze completely independent datasets and, since they exploit completely different technical hardware and software implementations, their respective results can cross-check each other and be combined to increase the precision and the accuracy of the measurements.

The existing CERN infrastructure, shown in Fig. 2.1, is used for injecting the protons into the LHC.
In particular, protons are produced in a duoplasmatron source, where electrons from a heated cathode ionize a hydrogen gas. A magnetic field coupled to an electric field creates an intense ionization and the confinement of a plasma, while an electrode extracts the protons from the plasma. Protons are first accelerated in a linear accelerator, the LINAC2, until they reach an energy of about 50 MeV. They are then injected in a circular accelerator, the Proton Synchroton Booster (PSB), where they reach an energy of 1.4 GeV, before entering the Proton Synchrotron (PS). In the Super Proton Synchrotron (SPS), the proton energy increases from 26 to 450 GeV and the protons are then injected in the LHC, where they are finally accelerated to their final energy (3.5 TeV in 2011, 4 TeV in 2012, 6.5 TeV in 2015 and 2016). Three to four cycles of the PS synchrotron are needed to fill the SPS, whereas twelve cycles of the SPS are required to fill the LHC. The total injection time is about twenty minutes and about twenty additional minutes are needed to increase the beam energy from 450 GeV to 6.5 TeV. When completely filled, the LHC nominally contains 2808 bunches of approximately 10^{11} protons each.
Once inside the LHC, protons are accelerated by sixteen radio-frequency cavities, while 1232 niobium-titanium superconducting dipole magnets ensure the

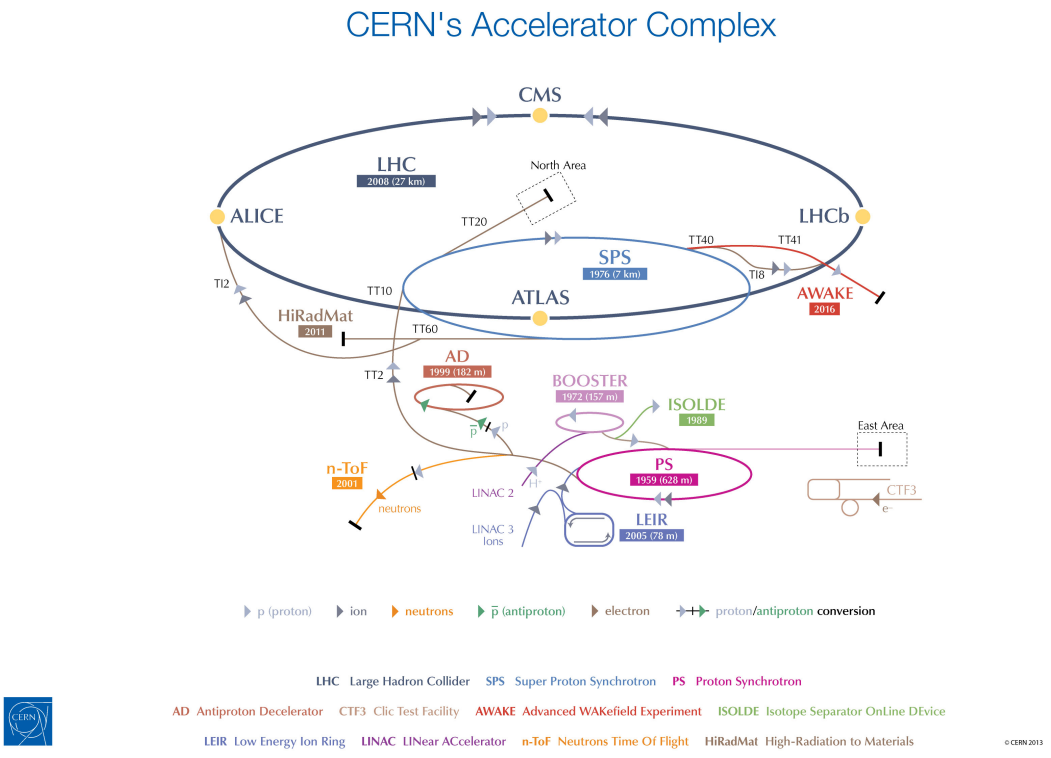

Figure 2.1: The CERN accelerator complex

deflection of the beams generating a magnetic field up to 8.3 T; quadrupole magnets are used to collimate the beams. The superconducting magnets used to bend the protons trajectory operate at a temperature below 2 K, obtained with a pressurized bath of superfluid helium at about 0.13 MPa. Three vacuum systems are also part of the LHC architecture: the beam vacuum (10^{-10} to 10^{-11} mbar at room temperature), the insulation vacuum for helium distribution (about 10^{-6} mbar) and the insulation vacuum for cryomagnets (about 10^{-6} mbar).
The machine is designed to achieve an energy per proton beam of 7 TeV, which would result in a design center-of-mass energy of $\sqrt{s} = 14$ TeV. The time between two bunch crossings in any IP is 25 ns, which means a bunch space $\approx$ 7.5 m along the beam axis. Nevertheless, not all the design parameters has been reached in the operations: in particular the center-of-mass energy of 14 TeV has not been achieved yet. In the years 2010 and 2011 the LHC operated with proton beam energies of 3.5 TeV. In 2012, the beam energy of 4 TeV was reached, resulting in a proton-proton center-of-mass energy of 8 TeV and a bunch spacing of 50 ns. This first LHC running period is called RunI and won't be considered in this thesis.
Starting from spring 2013, the LHC went through a shut down period of about 2 years to allow consolidation and upgrade of numerous machine systems. In July 2015 LHC started to collide proton beams with a center-of-mass energy of 13 TeV (LHC running period called RunII). After a short period of 50 ns operation (Run2015B), the machine collected data with a bunch spacing of 25 ns in both 2015 and 2016. The LHC will continue operate at 13 or 14 TeV center-of-mass energy until 2018. A second long shutdown (LS2) is planned in 2019 and 2020, while RunIII will extend until 2023. After the Phase-1, which includes RunI, RunII and RunIII, the Phase-2 should extend the data taking up to approximately 2037. The integrated luminosity (see next section) collected in Phase-1 is expected to reach 300 fb^{-1}, while 3000 fb^{-1} should be collected by the end of Phase-2. An overview of the LHC schedule up to 2021 is presented in Fig. 2.2.

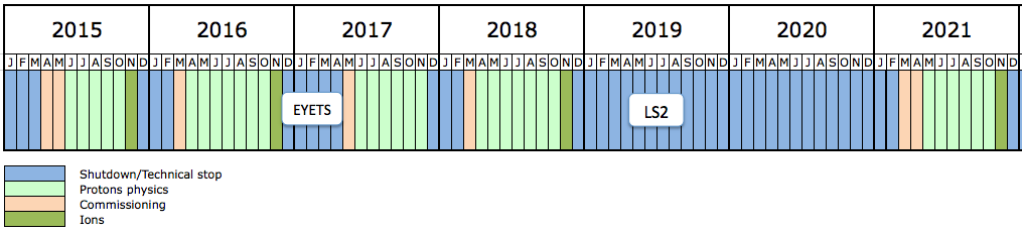

Figure 2.2: The LHC schedule up to year 2021

Luminosity

An important parameter used to quantify the performances of a collider is the instantaneous luminosity $\mathcal{L}$. Given the event rate R_i of the process i, defined

as the number of events occurring per unit of time, one can write:

$$R_i = \frac{dN_i}{dt} = \sigma_i \times \mathcal{L} \tag{2.1}$$

where σ_i is the cross section of the process i and $\mathcal{L}$ is the machine instantaneous luminosity. The instantaneous luminosity depends only on machine parameters and can be written as:

$$\mathcal{L} = \frac{N_1 N_2 n_b f_{rev}}{A} \tag{2.2}$$

where N_1 and N_2 are the number of particles in the two colliding bunches, A is the overlap area of the two bunches in the transverse plane with respect to the beam direction, n_b is the number of bunches in each beam and f_{rev} is the revolution frequency of the bunches (with a design value of 11245 Hz). At the LHC, $N_1 = N_2$ both equal to the number of protons per bunch N_p ($\approx 10^{11}$) and, since the area of overlap is difficult to be measured, for a Gaussian-shaped beam distribution $\mathcal{L}$ can be rewritten as :

$$\mathcal{L} = N_p^2 n_b f_{rev} \frac{\gamma}{4\pi\epsilon_n \beta^*} F \tag{2.3}$$

where γ is the relativistic Lorentz factor, ϵ_n is the normalized transverse beam emittance (with a design value of 3.75 μm), β^* is the so called betatron function at the IP and F is the geometric luminosity reduction factor due to the crossing angle at the IP.

The maximum number of bunches per beam and the revolution frequency are defined by the circumference of the LHC. Hence, in order to get as many events of interest as possible, on can either increase the number of particles in a bunch or focus the two beams on a smaller area.

The summary of the the design values for the LHC machine parameters can be found in Tab. 2.1. During collisions the number of particles in the bunches

	Parameter	Design
Center-of-mass energy	$\sqrt{s}$	14 [TeV]
Luminosity	$\mathcal{L}$	10^{34} [cm^{-2}s^{-1}]
Bunch spacing		25 [ns]
Number of bunches	n_b	2808
Number of protons/bunch	N_p	1.15×10^{11}
Emittance	ϵ_n	3.75 [μm]
β^* at the IP	β^*	0.55 [m]

Table 2.1: Machine parameters (design values) of the LHC

and thus also the instantaneous luminosity, decreases exponentially from the initial peak luminosity and after several hours of data dating the instantaneous luminosity $\mathcal{L}$ tends to decrease so much that it is more efficient to abort the fill and refill the machine with new beams instead of taking data at very low

luminosity. The peak luminosity of the LHC for both 2015 and 2016 is shown in Fig. 2.3. Due to the highest statistics, in the analyses discussed in Chapter 6 is the 2016 one.

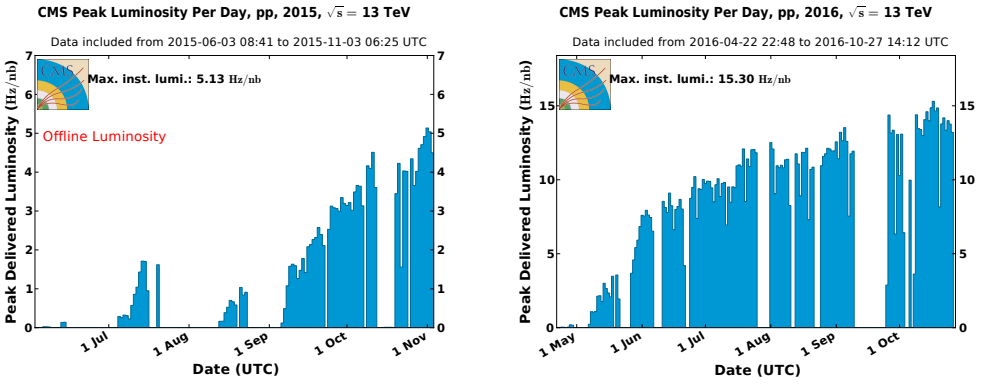

Figure 2.3: Peak luminosity delivered during day for 2015 (left) and 2016 (right) as measured by the CMS experiment [35]

If $\mathcal{L}$ is the instantaneous luminosity, L is the integrated luminosity, where $\mathcal{L}$ is integrated over time. The integrated luminosity for all the pp fills taken during 2015 ($\sim$2.7 fb^{-1}) and 2016 ($\sim$36 fb^{-1}) is shown in Fig. 2.4.

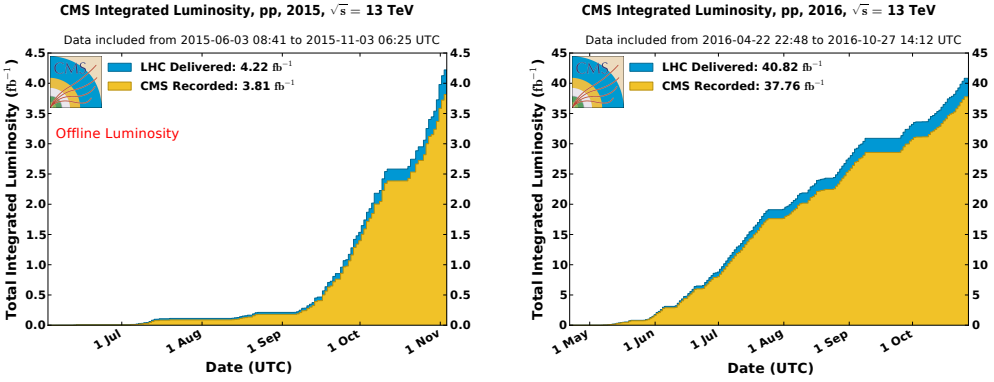

Figure 2.4: Cumulative offline luminosity versus day delivered to (blue) and recorded by CMS (orange) during stable beams for pp collisions at 13 TeV center-of-mass energy in 2015 (left) and 2016 (right) [35]

2.2 Phenomenology of proton-proton interactions

The phenomenology of proton-proton interactions have peculiar characteristics that have to be taken into account both in the machine design and at analysis level:

– The proton is a composite particle whose *valence* quarks are two up-type quarks and one down-type quark. The rest mass of the *valence* quarks added together makes up about 1% of the total proton mass of 938.3 MeV. The quarks are in fact held together inside the proton by gluons that are interacting with them and exchanging the colour charge. However, at higher loop order the gluon exchanged between two quarks can interact with other gluons in the proton or produce a quark-antiquark pair that annihilates shortly afterwards. Such quarks and antiquarks produced from gluons are called *sea* quarks. Both *valence* and *sea* quarks are generally referred to as *partons*, the inner constituents of the proton.

– There are two possible kind of proton-proton interactions: soft and hard collisions. In soft collisions only a small momentum is transferred and particle scattering at large angle is suppressed. The final state particles have small transverse momentum ($\sim 10^2$ MeV), so that most of them escape down the beam pipe. The other possible scenario is when two of the proton partons take part in the interaction (referred to as hard interaction) with high transferred transverse momentum. From now on, only hard collisions will be considered. The corresponding cross sections are several order of magnitudes smaller than those of the soft interactions, as shown in Fig. 2.5.

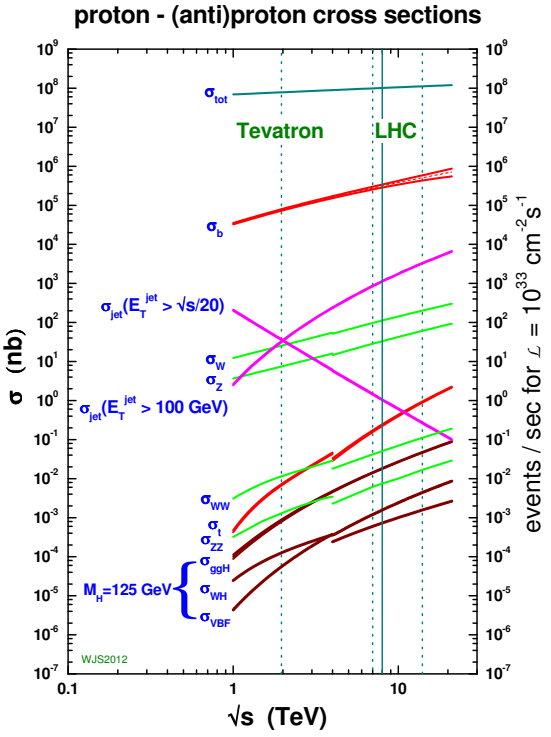

Figure 2.5: Cross section of SM processes as a function of the center-of-mass energy of proton proton collisions. The vertical lines mark the center-of-mass energies of the Tevatron and the LHC [36]

– The elementary cross section associated to a given hard interaction involving a parton a and a parton b is estimated using the QFT prescriptions described in Chapter 1. In order to estimate the total cross section of the process though, one needs to know also the probability of finding such partons in the colliding protons and their momentum distribution. For this purpose, see the description of the parton distribution functions in Sec. 2.2.1.

– Before or after the two partons interact with each other, they can radiate other partons or photons. This radiation of particles is called *initial state radiation* (ISR) when it happens before the hard interaction and *final state radiation* (FSR) if it occurs with the decay products of the hard interaction.

– All the observed hadrons are colourless, hence if the final state of a hard interaction contains particles that carry a colour charge (like e.g. quarks), they have to form new particles re-arranging their colour structure in order to become colour neutral. This process is called *hadronization* and results in showers of particles that form a cone along the initial particles direction which are called *jets*. The only exception is the top quark, which has a lifetime shorter than the timescale at which the hadronization takes place and, therefore, decays before it can hadronize. After the hard interaction, the remnants of the two protons are not colour neutral anymore and have to hadronize as well, forming jets that fly along the beam axis (underlying event, whose produced hadrons carry in general small transverse momenta). The hadronization process is currently described only phenomenologically through various models, among which the most commonly used is the Lund string model [37].

– Finally, the fact that the LHC bunches are made of many ($\approx 10^{11}$) protons leads to what is called *pile-up* in the event, due to the presence of several proton-proton interactions besides the one of interest (see Sec. 2.2.2).

.

2.2.1 Parton distribution functions

The parton distribution function (PDF) is the probability density to find a parton p carrying a fraction x of the longitudinal proton momentum of a proton. The PDF depends on the squared four-momentum Q^2 transferred in the collision and is labeled as $f_p(x_p, Q^2)$. PDFs are different for gluons, valence quarks and low-momentum sea quark-antiquark pairs of all flavours and depend on the energy scale at which the interaction between the partons takes place: in particular for interactions with "high exchanged momenta" where a shorter distance scale is probed, the contributions of gluons and sea quarks become dominant.
PDFs don't come directly from first-principles criteria, hence must be experimentally measured. Currently they are essentially extracted from the study

of lepton-hadron collisions such as those provided by HERA [38, 39]. Once the PDF have been measured at a given Q^2, it can be extrapolated at another energy using the Dokshitzer-Gribov-Lipatov-Altarelli-Parisi (DGLAP) evolution equation [40, 41, 42]. Different sets of PDF exist provided by different collaborations, such as CTEQ [43, 44], MSTW [45] or NNPDF [46]: As an example MSTW parton distribution functions are shown in Fig. 2.6 for two different values of Q^2 and superimposing the PDFs of the different quark flavors and gluons. The bump around $x = 0.1$ visible for up and down quarks in both left and right plots of Fig. 2.6 corresponds to the contribution of the valence quarks. While the total center-of-mass energy carried by the pp system is $\sqrt{s}$,

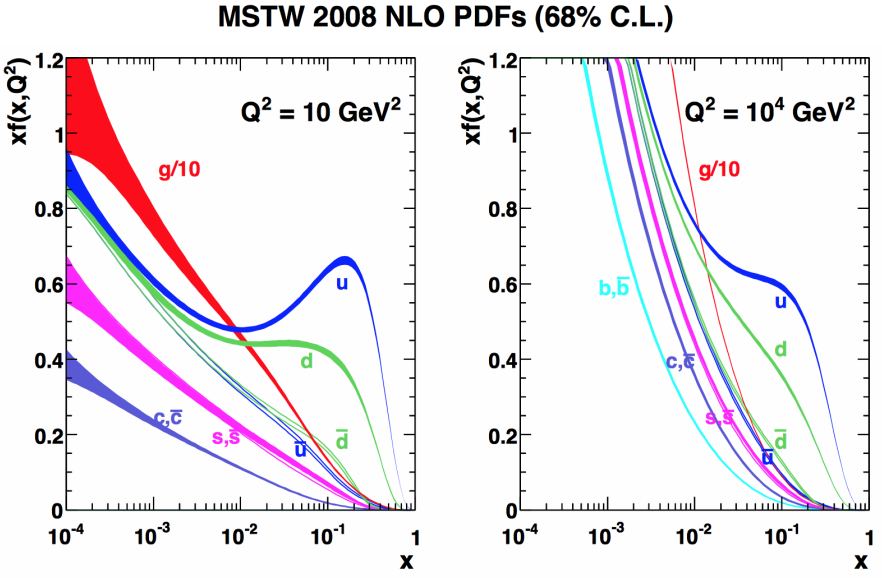

Figure 2.6: Parton density functions multiplied by the fraction of the total momentum carried by the parton ($xf(x, Q^2)$), including the 1 standard deviation uncertainty bands, for two different invariant momentum transferred Q^2=10 GeV^2 (left) and Q^2=10^4 GeV^2 (right) [45]

the effective center-of-mass energy of the hard scattering $\sqrt{\hat{s}}$ is given by the following relation:

$$\sqrt{\hat{s}} = \sqrt{x_a x_b s} \tag{2.4}$$

where x_a and x_b are the fractions of the longitudinal momentum of the proton carried by the interacting partons a and b. To probe physics at a certain energy scale, the Q^2 value has to be in the range of the squared effective center-of-mass energy ($\hat{s}$) of the hard scattering, which corresponds to the squared invariant mass M^2 of the system of the interacting particles. From Eq. 2.4, to study physics at the TeV scale with a collider reaching $\sqrt{s} = 13$ TeV, the average x of the partons has to be around 0.1. From the corresponding PDF in Fig. 2.7 (Q^2=(1000 GeV)^2) it can be seen that for such values the up quark and down quark contents show an excess over the other quarks, meaning that the interactions are dominated by the valence quarks and the gluons.

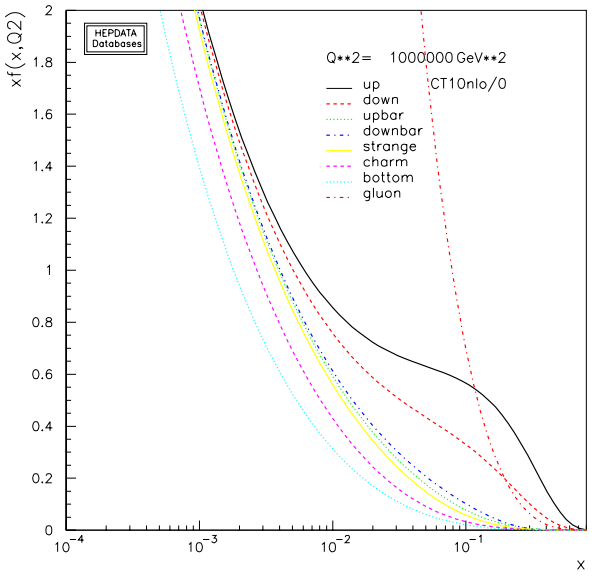

Figure 2.7: PDFs for different partons in a proton, obtained with the CT10 parametrisation [43] where the Q^2 is chosen for physics studies at the TeV scale. The plot was generated with the specific tool from the HepData project [47]

Once the PDFs are known at a given Q^2, the total proton-proton cross section is computed as the convolution of the elementary cross section and the PDFs, integrated over all the possible elementary processes (also known as *factorization theorem* [48]) giving rise to the considered final state.
The partonic cross section, describing the proton-proton collisions, is expressed in Eq. 2.5.

$$\sigma_x = \sum_{a,b} \int_0^1 dx_a dx_b f(x_a, flav_a, Q^2) f(x_b, flav_b, Q^2) \cdot \sigma_{ab\to X}(x_a, x_b, Q^2) \quad (2.5)$$

where a and b are the initial partonic states, $f(x_a, flav_a, Q^2)$ and $f(x_b, flav_b, Q^2)$ are the Parton Density Function while $\sigma_{ab\to X}(x_a, x_b, Q^2)$ is the hard scattering cross section.

2.2.2 Pile-up

More than one independent proton-proton interaction can take place simultaneously in a bunch crossing at the interaction point. The interaction of two protons forms a primary vertex, from which the particles that were created in the interaction are spread in the detector.
The number of primary vertices created on average depends on the beam parameters, e.g. the number of particles in a bunch and how small is the focusing area of the bunches. In 2012 this number has been measured by the CMS experiment and, on average, corresponded to 21 interactions per bunch crossing as shown in Fig. 2.8 [35].

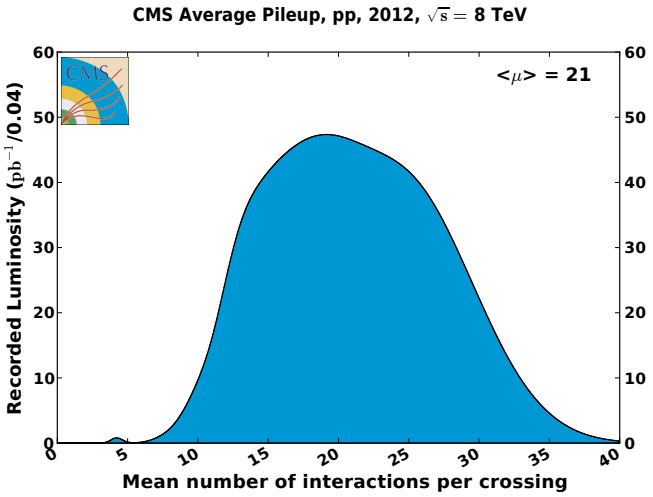

Figure 2.8: Luminosity recorded as a function of the mean number of interactions per bunch crossing in the CMS experiment in 2012 [35]

The presence of many primary vertices per bunch crossing presents a challenge for the event reconstruction, since the particles originating from different primary vertices are superimposed in the detector creating a diffuse background that can affect the physics measurements.

Chapter 3

The CMS detector

This Chapter describes the Compact Muon Solenoid (CMS) experiment purely under its hardware aspects. Its design is briefly exposed starting form the innermost region (close to LHC's beampipe) to the outermost one. Given its importance in the context of this thesis, more details are given concerning the electromagnetic calorimeter (ECAL) responsible for the detection and reconstruction of photons and electrons. My ECAL activities during this thesis are described in two Appendices of this thesis and are focused on the timing crystal-by-crystal calibration of the ECAL signal (Appendix A) and the calibration of the High Voltage system of its Barrel partitions (Appendix B).

3.1 Overall concept

The Compact Muon Solenoid (CMS) is one of the two multi-purpose experiments taking data at the LHC facility and is situated at the fifth access point (called P5 in the following) of the scientific district. The other one is ATLAS (A Toroidal LHC ApparatuS) situated at the first access point of LHC tunnel, exactly on the other side of the accelerating ring. After the discovery of the Higgs boson (see Sec. 1.3) achieved in 2012 by the ATLAS [4] and CMS [5] experiments, the main goal of the two collaborations become the search for new physics beyond the standard model, either via direct discovery or via precision measurements of already known particles and phenomena [49]. The CMS detector has a cylindrical shape with an total length of 28.7 m, 21.6 m of which make the main cylinder with a diameter of 15 m and the rest of the length coming from the forward calorimeters. The total mass is about 14000 t. CMS is made of several layers of detectors, designed to identify and detect different SM particles depending on their possible interactions with solid matter and cover most of the 4π solid angle. One of its peculiar features is the presence of a 3.8 T superconducting solenoidal magnetic field. In order to achieve good momenta and energy resolution, the tracking detector (Tracker) and the two calorimeters, both the electromagnetic (ECAL) and the hadronic one (HCAL),

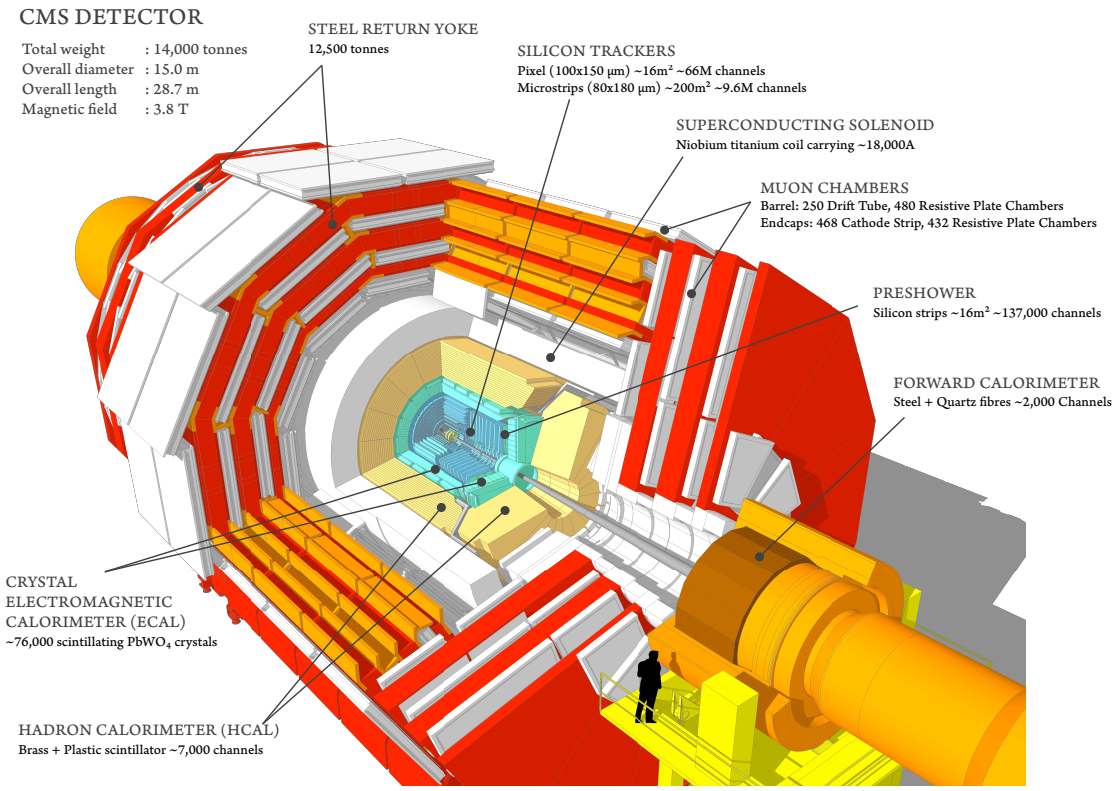

Figure 3.1: An exploded view of the CMS detector

are located inside[1] the volume of the magnetic field (13 m-long, with 5.9 m of inner diameter). The muon chambers are instead located outside the volume of the magnet (completely integrated in its return yoke), whose field is large enough to saturate 1.5 m of iron, allowing four muon stations to guarantee full geometric coverage. The overall layout of CMS is shown in Fig. 3.1.

Before moving to the description of the CMS subdectors, the coordinate conventions is described in the following section.

3.2 Coordinate conventions

The origin of the coordinate system adopted by CMS is centered at the nominal collision point inside the experiment, while the y-axis points vertically upward and the x-axis points radially inward, toward the center of the LHC ring. The coordinate system is shown in Fig. 3.2. The azimuthal angle ϕ is measured from the x-axis in the x-y plane. The polar angle θ is measured from the z-axis. Two important quantities for the physics analyses are defined in the transverse plane with respect to the beam direction: the so-called transverse momentum and transverse energy, denoted by p_T and E_T respectively. Their importance is given by the fact that the interaction between the elementary

[1] Most of the HCAL is inside the magnet, with an outer detector (HO) located outside the coil (see Sec. 3.5).

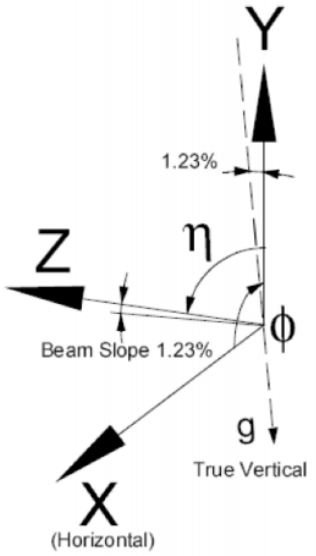

Figure 3.2: Coordinate system adopted by CMS

partons happens with unknown center-of-mass energy (see Sec. 2.2) as well as unknown is the total initial energy of the interacting partons. For this reason the energy conservation rule can be applied only in the plane transverse to the beams direction. The transverse momentum and transverse energy are computed accordingly to the following relations:

$$p_T = psin\theta \tag{3.1}$$

$$E_T = Esin\theta \tag{3.2}$$

It is also important to note that particles which escape the detection, for example neutrinos, leave an imbalance in the transverse plane total momentum, which is quantified as missing transverse energy, i.e. the negative vectorial sum of the transverse momenta of all the detected particles in the event:

$$E_T^{miss} = -\sum_i p_T^i \tag{3.3}$$

Moreover, the center-of-mass may be boosted along the beam direction. This is the reason why it is useful to use experimental quantities that are invariant under such boosts.
The rapidity is defined as:

$$y = \frac{1}{2}\ln\frac{E + p_z}{E - p_z} \tag{3.4}$$

and has the property of being additive under Lorentz boosts along the z direction, i.e. it is simply shifted by a constant when subjected to such transformations. For ultrarelativistic particles ($p \gg m$) the rapidity is approximated

by the pseudorapidity:

$$\eta = -\ln \tan \frac{\theta}{2} \tag{3.5}$$

where θ is again the angle between the particle momentum and the z axis. The pseudorapidity can be reconstructed from the measurement of the θ angle and can be also defined for particles whose mass and momentum are not measured.
The value $\eta = 0$ corresponds to the direction perpendicular to the beams direction, while the limit $\eta = \infty$ gives the direction parallel to the beams direction. Usually, the subdetectors' regions are defined according the their η value, where the central part ($\eta < 1.5$) is called *barrel* and the outer parts ($\eta > 1.5$) are denoted as *endcaps*. In the following sections, the CMS subdetectors are described from the innermost region (the closest one to the nominal interaction point) to the outermost region. The chapter ends with a short description of the trigger and data acquisition systems.

3.3 Inner tracking system

Placed within the magnetic field, the tracker [50] is the subdetector which is the closest one to the interaction point. Its purpose is to identify tracks and vertexes in a high track multiplicity environment. In order to provide good radiation hardness, high granularity and large hit redundancy to achieve good performances in pattern recognition, the silicon (Si) technology has been chosen for the whole volume of the tracker (given by a cylinder of 5.8 m length and 2.6 m diameter). A global view of the tracker layout is depicted in Fig. 3.3. The innermost tracker is made of three layers of silicon pixel detectors[2]

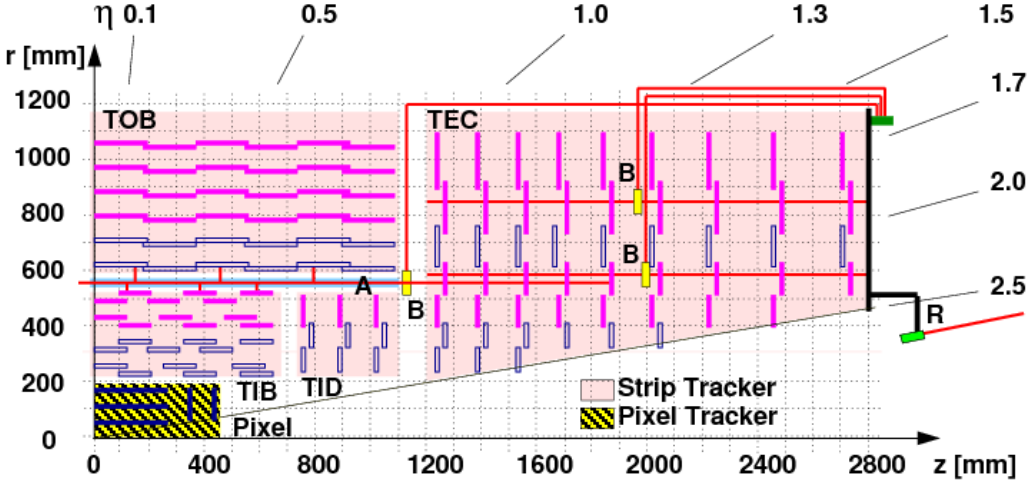

Figure 3.3: A global view of the tracker layout

[2]From February 2017 the detector has been changed with a 4-layer tracking system to achieve greater performances in terms of momentum resolution and vertexing. However, data included in this thesis have been collected with the 3-layer version of this subdetector.

named Tracker Pixel Barrel (TPB), ranging from 8.8 cm to 20.4 cm diameters and two wheels of Tracker Pixel Endcap (TPE), covering the pseudorapidity range up to $|\eta| = 2.5$. TPB and TPE contain 48 million and 18 million pixels, respectively. The pixels have a size of 100×150 μm^2.
Thanks to the large Lorentz drift angle in the magnetic field, the measured hit resolution in the TPB is 9.4 μm in the $r - \phi$ plane and 20-40 μm in the longitudinal direction. The longitudinal resolution depends on the angle of the track relative to the sensor. For longer clusters, sharing of charge among pixels improves the resolution, with optimal resolution reached for interception angles of $\pm 30°$.
The silicon strip tracker is placed outside of the pixel tracker. The barrel part of the strip tracker is divided in the 4 layers of the Tracker Inner Barrel (TIB) and the 6 layers of the Tracker Outer Barrel (TOB). Coverage in the forward region is provided by the 3 Tracker Inner Discs (TID) and the 9 disks of the tracker endcap (TEC) on each side. The dimensions of the strips varies between 80 μm in the innermost layers of the TIB and 183 μm in the outer layers of the TOB. In the disks the dimension varies between 97 μm and 184 μm. Some of the modules are composed by two detectors mounted back-to-back with the strips rotated by 100 mrad. These double-sided (stereo) modules will also provide a measurement in the coordinate orthogonal to the strips. The single point resolution that can be achieved depends strongly on the size of the cluster and on the pitch of the sensor and varies not only as a function of the cluster width, but also as a function of pseudorapidity, as the energy deposited by a charged particle in the silicon depends on the angle at which it crosses the sensor plane. The measured hit resolution in the barrel strip detector varies between $\sim$20 μm and $\sim$30 μm in the $r - \phi$ plane in the TIB and TOB. The total area of the Si detectors is around 200 m^2, providing a coverage up to $\eta = 2.5$. The material budget inside the active volume of the tracker increases from 0.4 X_0[3] at $\eta = 0$ to around 1 X_0 at $|\eta| = 1.6$, before decreasing to 0.6 X_0 at $|\eta| = 2.5$.

3.4 Electromagnetic calorimeter

The electromagnetic calorimeter [51] is the subdetector devoted to the identification of photons and electrons and the measurement of their energies. In particular photons are used in the search for new $Z\gamma/W\gamma$ resonances discussed in Chapter 6. ECAL is a homogeneous calorimeter of 75848 Lead Tungstate $PbWO_4$ scintillating crystals divided into a barrel (61200 crystals) and two endcaps (14648 crystal), with coverage in pseudorapidity up to $|\eta| < 3.0$. A preshower system is installed in front of the edges of ECAL for π^0 rejection[4].

[3] X_0 defines the so-called *radiation length*, i.e. the typical length after which the energy of an incoming electron is reduced by a factor $1/e$ only by radiative processes (bremsstrahlung).

[4] The separation angle between two photons coming from the $\pi^0 \to \gamma\gamma$ decay, in case of a boosted π^0, would be small enough for the two photons to be misidentified as only one photon, if both of them go in the same ECAL crystal. Since the energy release in the preshower is different in case

A 3D view of the barrel and endcap electromagnetic calorimeter is shown in Fig. 3.4.

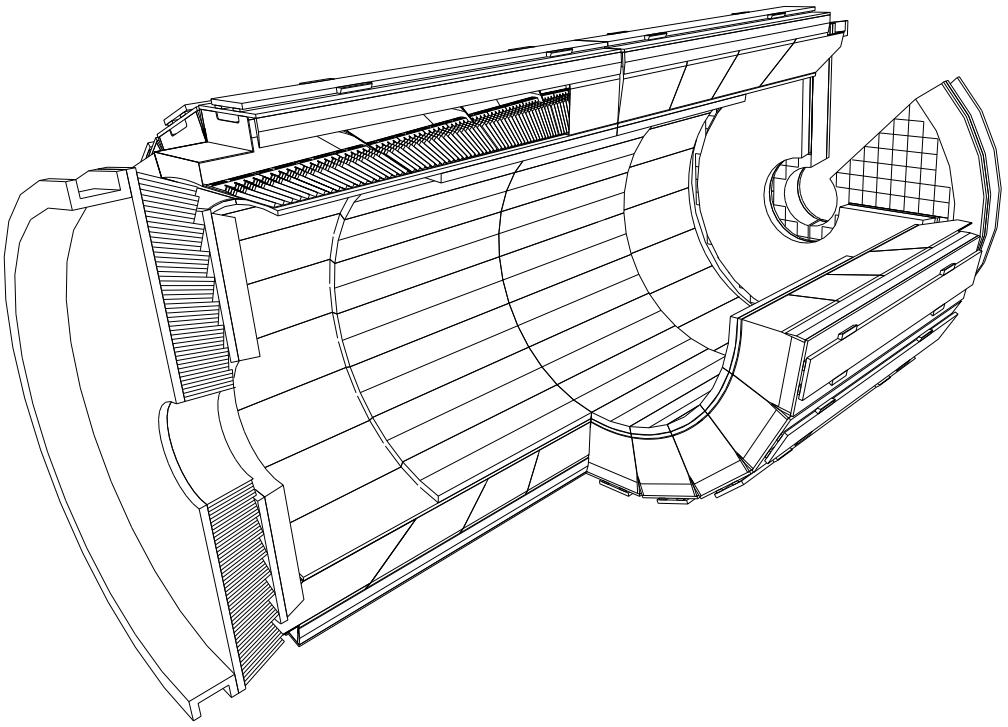

Figure 3.4: A 3D view of the electromagnetic calorimeter

3.4.1 Barrel calorimeter

The barrel part of the ECAL covers the pseudorapidity range $|\eta| < 1.479$ (see Fig. 3.5). The front face of the crystals is at a radius of 1.29 m from the nominal interaction point and each crystal face has an area of $22 \times 22\,\mathrm{mm}^2$ (given the Molière radius[5] of this material equal to 2.2 cm) and a length of 230 mm corresponding to $25.8\,\mathrm{X}_0$. The truncated pyramid-shaped crystals are mounted in a geometry which is off-pointing with respect to the mean position of the primary interaction vertex, with a 3° tilt in both ϕ and in η directions, in order to avoid the scenario in which a particle could go right along the separation between two center-pointing crystals. In terms of $\eta \times \phi$ dimensions, the crystal size corresponds to $\Delta\eta \times \Delta\phi = 0.0175 \times 0.0175$[6]. The barrel granularity is 360-fold in ϕ and $(85 \times 2$ half barrel)-fold in η, resulting in a total number of 61200 crystals. The crystal volume in the barrel amounts to $8.14\,\mathrm{m}^3$ (67.4 t). Crystals for each half-barrel are grouped in 18 supermodules, each subtending

of two collimated photons or only one photon, it offers a handle in order to solve this ambiguity.

[5]It is a characteristic constant of a material giving the scale of the transverse dimension of the fully contained electromagnetic showers started by an incident high energy electron or photon. In other words, it is the radius of a cylinder containing on average 90% of the shower's energy deposition.

[6]There are 360 crystals in the ϕ direction, which means that a crystal covers exactly 1° in ϕ.

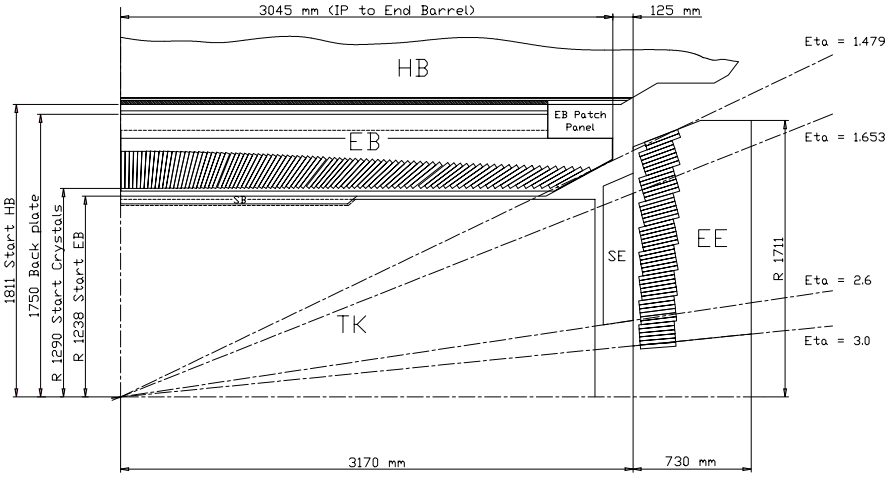

Figure 3.5: Longitudinal section of the electromagnetic calorimeter (one quadrant)

20° in ϕ. Each supermodule consists of four modules: 500 crystals are located in the first module and 400 crystals in each of the remaining three ones. During the construction and assembly, crystals have been grouped in arrays of 2×5 crystals, contained in a very thin (200 μm thick) alveolar structure. Thermal regulation is granted by two active systems: a specially regulated cooling circuit which keeps the operating temperature (ambient temperature) of the crystal array and of the APDs[7] (avalanche photodiodes) within a tight temperature spread of $\pm0.05\,^{\circ}$C, ensuring adequate thermal stability; and the power cooling circuit which antagonizes the heat generated by all power sources in the supermodule (each supermodule is designed as a separate thermal entity). The service systems such as the High Voltage power supplies (Appendix B) are located above the detector in the *Service Cavern* outside the detector cavern to protect the hardware from irradiation.

3.4.2 Endcap calorimeter

The endcap part of the ECAL covers a pseudorapidity range from 1.48 to 3.0. The design of the endcaps provides precision energy measurement up to $|\eta| = 2.5$. Crystals are however installed up to $|\eta| = 3$ in order to extend the energy-flow measurement in the forward direction. The mechanical design of the endcap calorimeter is based on an off-pointing pseudo-projective geometry using tapered crystals of the same shape and dimensions ($24.7\times24.7\times220\,\mathrm{mm}^3$) grouped together into units of 36 (called supercrystals). A total of 268 identical supercrystals is used to cover each endcap with a further 64 sectioned supercrystals used to complete the inner and outer perimeter. Each endcap contains 7324 crystals, corresponding to a volume of $1.52\,\mathrm{m}^3$ (for a total weight of 12.6 t). Both endcaps are identical and each one is constructed using the so

[7]Two photo-detectors per crystal due to the low number of photons emitted per MeV by the material.

called Dee-shaped sectors as seen in Fig. 3.6.

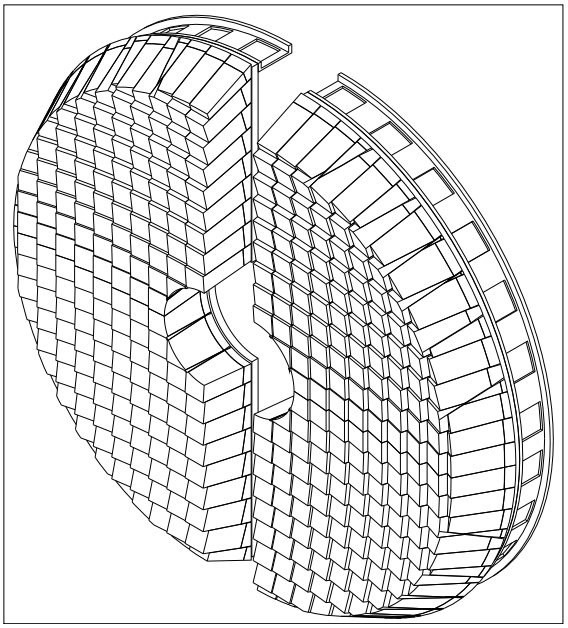

Figure 3.6: A single endcap with Dees apart

Figure 3.7 shows the total thickness (in radiation lengths) of the ECAL as a function of pseudorapidity. The endcap part also includes the preshower detector (see the specific subsection). Because of the higher radiation levels

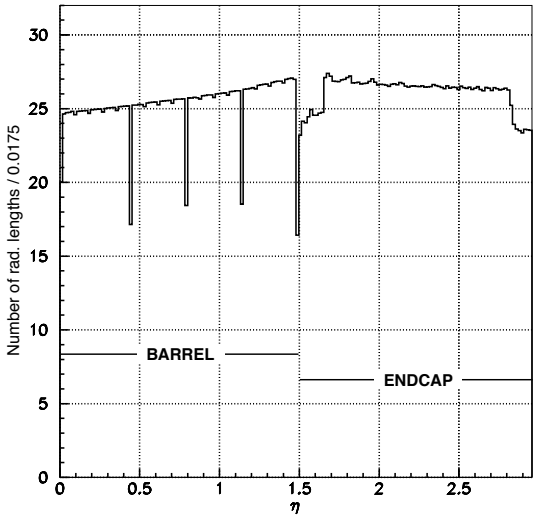

Figure 3.7: Total thickness in X_0 of the ECAL as a function of pseudorapidity, averaged over ϕ. In the endcap region, the preshower contribution is also considered [51]

in the forward region, the endcaps must tolerate very large doses and neutron fluences, hence all materials used in this region had to be chosen with higher

radiation hardness. Also the electronics is different between barrel and endcap for the same reason: avalanche photodiodes (APDs) are employed in the barrel and vacuum phototriodes (VPTs[8]) in the endcaps.

3.4.3 Preshower detector

The endcap preshower covers a pseudorapidity range from $|\eta| = 1.65$ to 2.61. Its main function is to provide π^0-γ separation. The preshower detector, placed in front of the crystals, contains two lead converters of a total thickness of $2\,X_0$ and $1\,X_0$ respectively, followed by detector planes of silicon strips with a pitch of $< 2\,\text{mm}$. The impact position of the electromagnetic shower is determined by the barycenter of the deposited energy. The accuracy is typically $300\,\mu\text{m}$ at 50 GeV. In order to correct for the energy deposited in the lead converter, the energy measured in the silicon is used to apply corrections to the energy measurement in the crystal. The fraction of energy deposited in the preshower (typically 5% at 20 GeV) decreases with increasing incident energy.
Figure 3.8 shows the layout of this sub-detector.

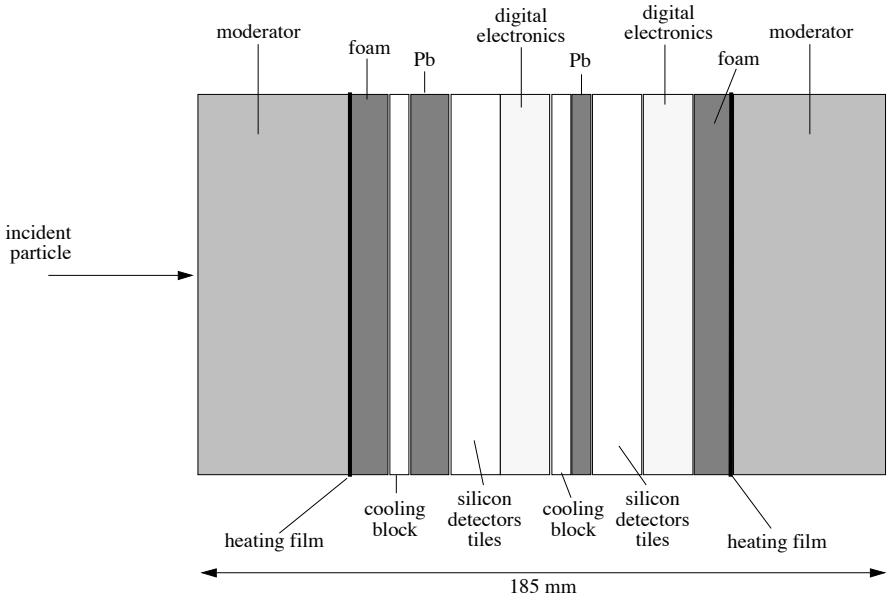

Figure 3.8: Schematic view of a section of the endcap preshower

To maintain its performance during the lifetime of the experiment, heating films and insulating foam glued on the moderators guarantee that the external surfaces are kept at the ambient temperature of the neighboring detectors.

3.4.4 Lead tungstate crystals

The lead tungstate crystals ($PbWO_4$) were chosen for operation at LHC due to their peculiar characteristics [52]. In particular, the high density ($8.3\,\text{g/cm}^3$),

[8]Only one VPT is coupled to each crystal.

short radiation length (0.89 cm) and small Molière radius (2.2 cm) results in a fine granularity and a compact calorimeter (the compactness is a very important parameter due to the fact that the calorimeters are placed inside the magnetic field and that it's technically challenging to achieve a magnetic field, both 3.8 T intense and constant inside the all internal volume). The scintillation decay time is of the same order of magnitude of the LHC bunch crossing time: about 80% of the light is emitted in 25 ns, while the light output is relatively low: about 100 scintillating photons per MeV. The electronics collect about 4.5 photoelectrons per MeV in both the avalanche photodiodes (APDs) and the vacuum phototriodes (VPTs), where the higher APD quantum efficiency[9] (75% vs 20%) is balanced by their smaller surface coverage on the back face of the crystal. The crystals emit blue-green scintillation light with a broad maximum at 420 nm [52].

3.4.5 Energy resolution

The ECAL energy resolution has been parametrized as:

$$\frac{\sigma(E)}{E} = \frac{a_{stoc}}{\sqrt{E}} \oplus \frac{b_n}{E} \oplus c \quad \text{(E in GeV)} \tag{3.6}$$

where a_{stoc} is the stochastic term, b_n the noise and c the constant term.
Figure 3.9 summarizes the different contributions expected for the energy resolution. Terms representing the degradation of the energy resolution at extremely high energies have not been included. The stochastic term includes fluctuations in the shower containment as well as a contribution from photostatistics. The noise term contains the contributions from electronic noise and pile-up energy; the former is quite important at low energy, the latter is negligible at low luminosity. The curve labeled *intrinsic* in Fig. 3.9 includes the shower containment and a constant term of 0.55%. The constant term must, in fact, be kept down to this level in order to profit from the excellent stochastic term of $PbWO_4$ in the energy range relevant for the searches for new physics. To achieve this goal, in situ calibration/monitoring using isolated high p_T electrons is performed. The parameters, measured in an electron test beam, for incident electrons of different energies from 20 to 250 GeV, with a 3x3 crystal configuration, considering E in GeV, correspond to a_{stoc}=0.028 $\sqrt{(GeV)}$, b_n=0.12 GeV and c =0.003. A detailed study of the energy resolution behavior both at low and high energy region is crucial in order to describe a reliable signal model in the searches for new physics beyond the standard model.

3.5 Hadronic calorimeter

The design of the hadronic calorimeter (HCAL) [53] is strongly influenced by the choice of the magnet parameters since most of the CMS calorimetry is

[9]The device efficiency to convert a photon in photoelectrons.

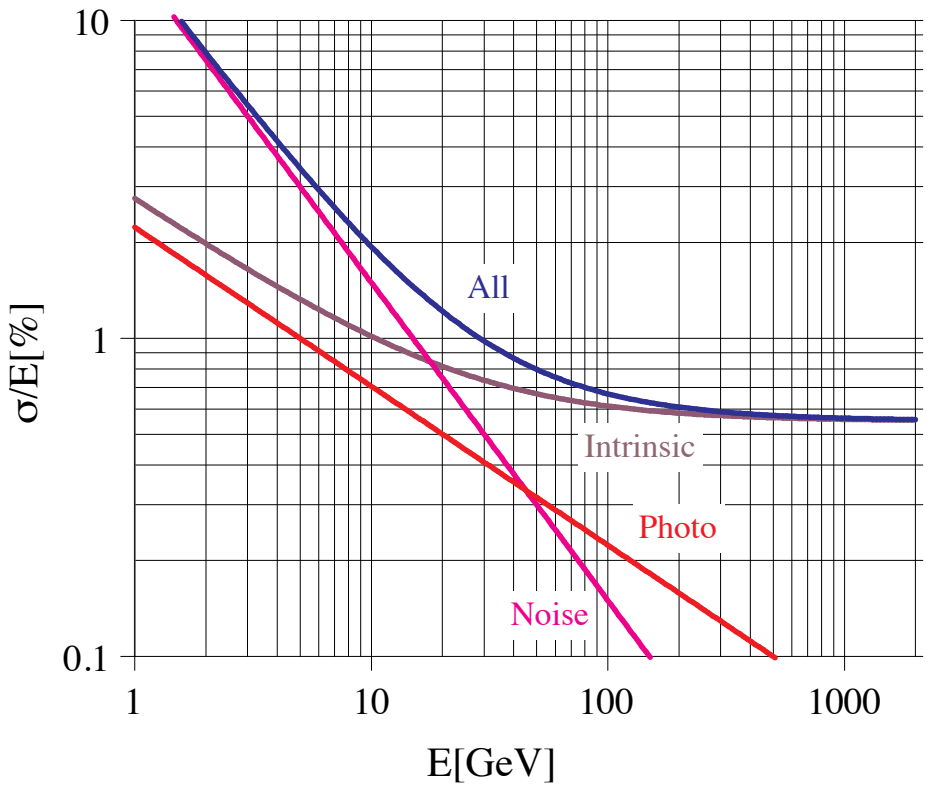

Figure 3.9: Different contributions to the energy resolution of the $PbWO_4$ calorimeter. The noise term contains the contributions from electronic noise and pile-up energy. The curve labeled "photo" describes the contribution from photostatistics, while the curve labeled "intrinsic" includes the shower containment and a constant term of 0.55%. The parametrisation given in Eq. 3.6 re-arrange the 3 contributions in a slightly different way, including the shower containment and the photostatistics contributions in the stochastic term a_{stoc} [52]

located inside the magnet coil (see Fig. 3.11). An important requirement of HCAL is to minimize the non-Gaussian tails in the energy resolution and to provide good containment and hermeticity. Hence, the HCAL design maximizes material inside the magnet coil in terms of interaction lengths[10]. This is complemented by an additional layer of scintillators, referred to as the hadron outer (HO) detector, which is installed outside the magnet. Brass has been chosen as the absorber material as it has a reasonably short interaction length (5.15 interaction length in 79 cm), it is relatively easy to mold and it is non-magnetic. Maximizing the amount of absorber before the magnet requires minimizing the amount of space devoted to the active medium. So the tile/fiber technology has hence been chosen: it consists of plastic scintillator tiles read out with embedded wavelength-shifting (WLS) fibers. The photodetection readout is based on multi-channel hybrid photodiodes (HPDs). The absorber

[10]The interaction length is the equivalent of the radiation length (X_0) for hadronic showers, modulo the fact that it's generally much bigger, with a factor between 1 to 30 depending on atomic mass number Z of the specific material considered.

structure is assembled by bolting together precisely segmented and overlapping brass plates so as to leave space to insert the scintillator plates, which have a thickness of 3.7 mm. The overall assembly enables the HCAL to be built with essentially no uninstrumented cracks or dead areas in ϕ. The gap between the barrel and the endcap of HCAL, through which the services of the ECAL and the inner tracker pass, is inclined at 53° and points away from the center of the detector. Since the identification of forward jets is very important for the rejection of many backgrounds, the barrel and the endcap parts, which cover up to $|\eta| < 3.0$, are complemented by a very forward calorimeter (HF), placed at ± 11.2 m from the interaction point, which extends the pseudorapidity range of the calorimetry up to $|\eta| < 5.2$. As the particle flux in this very forward region is extremely high, a radiation hard technology, using Cherenkov light in quartz fibers was chosen, using steel as an absorber. The HF detector is also used as a real-time monitor for the luminosity on a bunch-by-bunch basis.
The HCAL baseline single-particle energy resolution is:

$$\frac{\sigma_E}{E} = \frac{65\%}{\sqrt{E}} \oplus 5\% \tag{3.7}$$

in the barrel,

$$\frac{\sigma_E}{E} = \frac{83\%}{\sqrt{E}} \oplus 5\% \tag{3.8}$$

in the endcaps and

$$\frac{\sigma_E}{E} = \frac{100\%}{\sqrt{E}} \oplus 5\% \tag{3.9}$$

in the forward calorimeter (where E is expressed in GeV).

3.6 Magnet

The design of the CMS magnet, in particular its bending power, was driven by the required performance of the muon system. The momentum determination of charged particles is performed by measuring the particles trajectories inside the solenoid. In particular, the momentum resolution is given by the formula:

$$\frac{\Delta p}{p} = \Delta s \frac{8p}{0.3BR^2} \tag{3.10}$$

where $p = \gamma mv$ is the particle momentum, B is the magnetic induction, s is the sagitta and R is the solenoid radius. To achieve the goal of the unambiguous determination of the curvature (hence the electric charge) for muons with momentum of 1 TeV, the requirement on the momentum resolution is: $\Delta p/p \sim 10\%$ at $p = 1$ TeV. Therefore strong field and large radius are an efficient approach to reach optimal momentum resolution: CMS preferred indeed a higher field within a relatively compact space. The solenoid of the CMS detector produces uniform field in the axial direction, while the flux return is assured by an external iron yoke with three layers, in between which the muon

system is installed. The superconducting magnet has a length of 12.5 m and a diameter of the cold core of 6.3 m. It is made from a 4-layer winding of NbTi (Niobium-Titanium) cable reinforced with aluminium, weighting a total of 220 t and kept at a temperature of 4.5 K with liquid helium. It was designed to produce a field of 4 T but operate at a lower field of 3.8 T. The magnetic field is generated by a 18 kA current circulation in the cables. The magnet system stores an energy of 2.5 GJ.

The parameters of the CMS superconducting solenoid are summarized in Table 3.1.

Parameter	Value
Field	3.8 T
Inner core	5.9 m
Length	12.9 m
Number of turns	2168
Current	19.5 kA
Stored energy	2.7 GJ

Table 3.1: Parameters of the CMS superconducting solenoid

3.7 Muon system

The muon system is the outermost of the CMS subdetectors. Its main goals are the identification of muons, thanks to their high penetrating power[11], and a precise measurement of their momentum, with the help of the information coming from the tracker. The muon system also works as trigger for events which involve muons and it provides a precise time measurement of the bunch crossing. The CMS muon system [54] relies on three kinds of gaseous detectors: drift tubes (DT), cathode strip chambers (CSC) and resistive plate chambers (RPC). The DT and the CSC provide an excellent spatial resolution for the measurement of charged particle momentum; the RPC are used for trigger issues because of the very good timing. The active parts of the muon system are hosted into stations which are interleaved by the iron layers of the return yoke of the magnet. The longitudinal view of a quarter of the muon system is given in Fig. 3.10. The barrel extends up to $|\eta| < 1.4$, the endcaps up to $|\eta| < 2.4$.

A schematic view of a transverse slice of the CMS barrel is provided in Fig. 3.11, as a visual summary of what has been presented in the previous sections.

[11] Muons are, in fact, minimum ionizing particles (MIP).

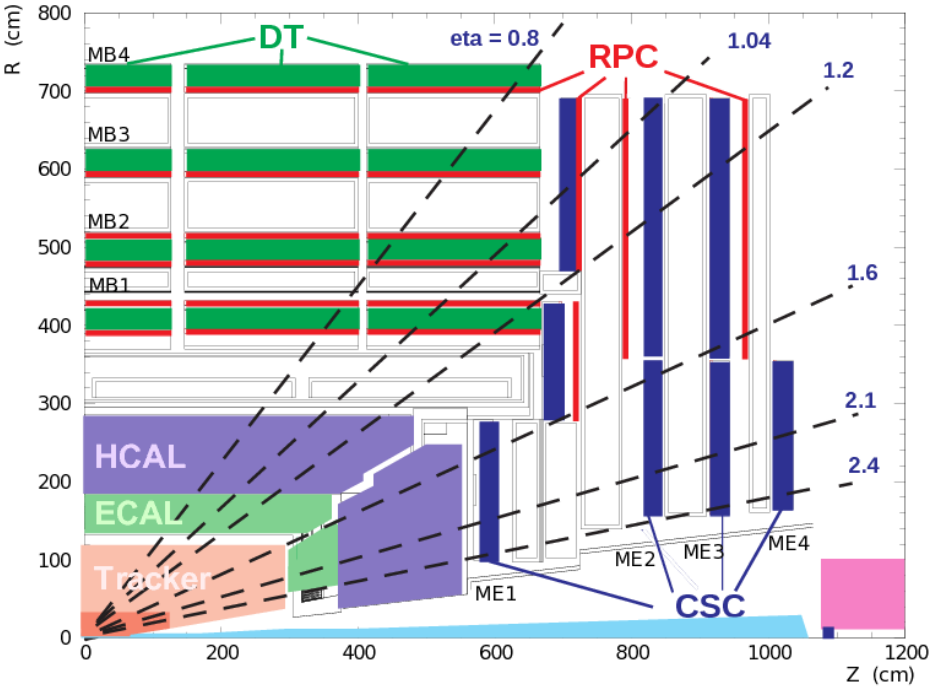

Figure 3.10: Longitudinal view of one quarter of the CMS muon system

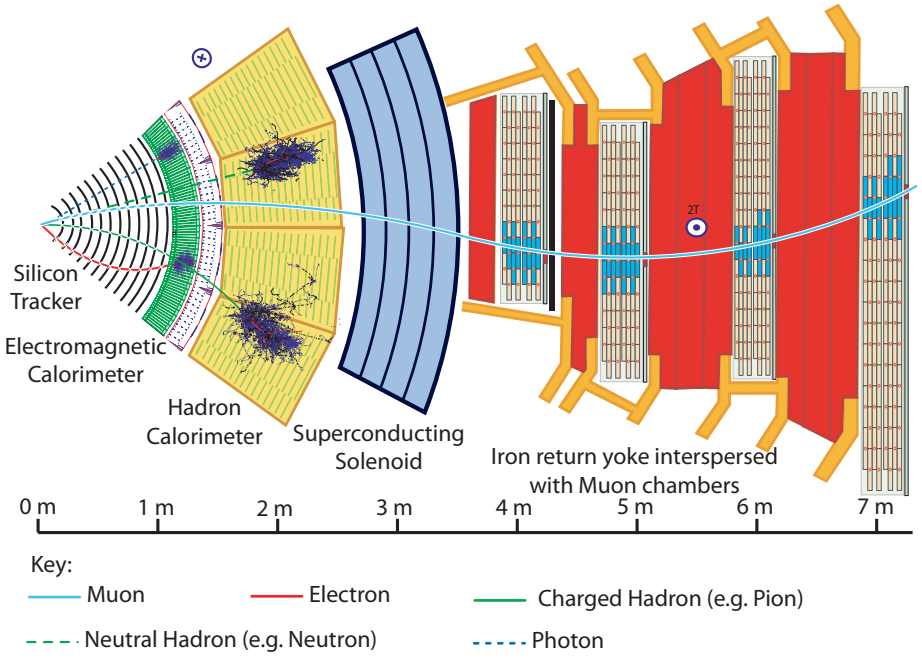

Figure 3.11: Schematic view of a transverse slice of the central part of the CMS detector

3.8 Trigger and data acquisition

The bunch crossing frequency at the CMS interaction point is 40 MHz (bunch spacing of 25 ns). Technical difficulties in handling, storing and processing extremely large amounts of data impose a limit of about 600 Hz on the rate of events that can be written to permanent storage, as the average event size is about 1 MB. At the LHC nominal luminosity the total event rate for inelastic interactions is expected to be of the order of 10^9 Hz while the rate of interesting events is rather small in comparison (see Fig. 3.12). A sophisticated trigger

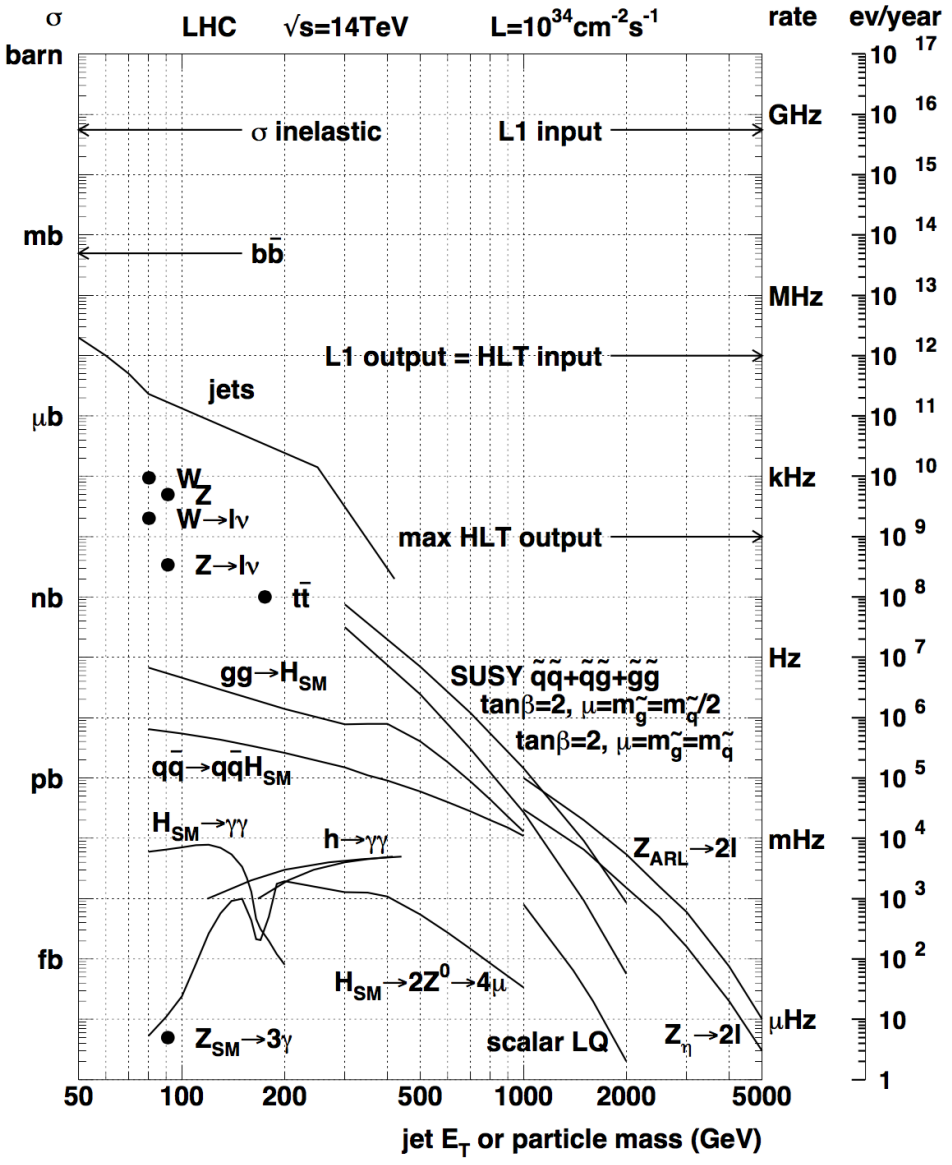

Figure 3.12: Event cross-sections and rates of selected processes for the LHC design luminosity of 10^{34} cm^{-2}s^{-1} as a function of the mass of produced objects [49]

system is then necessary to select events of interest, within a limited amount

of time available for the selection since the bunch crossing time is 25 ns. This interval of time would not be enough to read out all raw data from the detectors and for this reason CMS uses a multi-level trigger design, where each step of the selection uses only part of the available data combined with a zero suppressed readout. In this way higher trigger levels have to process fewer events and have more time available: they can go into finer detail and use more refined algorithms. The two steps of the CMS selection chain are: the first level (L1) trigger, built from custom hardware, which reduces the rate to a maximum of 100 kHz and the high level trigger (HLT), running the CMS reconstruction software on a processor farm, which performs higher level reconstruction and reduces the rate of events selected by the L1 trigger to about 600 Hz before the events are stored on disk.

3.8.1 Trigger Control and Distribution System (TCDS)

It is of vital importance that all parts of an LHC experiment are synchronized to each other and to the passage of particles in the centre of the experiment. The original CMS Timing, Trigger and Control (TTC) system made this possible during the first period of data-taking at the LHC from 2009 to 2012. Detector upgrades foreseen to be completed during 2014/2015 required a greater number of individual detector partitions to be available than were available in the TTC system. This along with the upcoming upgrade of the CMS Global Trigger (GT) system allowed us to re-define the boundary between the previous TTC and GT systems and separate the pure trigger functionality from the control and synchronization of the data-taking of CMS. The new CMS Timing and Control Distribution System (TCDS) has been designed, built and installed in CMS during the first Long Shutdown (LS1) of the LHC and is now routinely used to control CMS data-taking.
Before this installation, CMS trigger control comprised three almost separate systems. The Trigger Timing and Control (TTC) system distributes the L1A signals and synchronization commands to all front-ends. The Trigger Throttling System (TTS) collects front-end readiness information and propagates those up to the central Trigger Control System (TCS). The TCS allows or vetoes Level-1 triggers from the Global Trigger (GT) based on the TTS state and on the trigger rules. These three systems are combined in the new control and distribution system (see Fig. 3.13), separating the trigger control part from the trigger decision part of the GT (i.e., after the final decision logic). Apart from this logical reconstruction, the design allows for more trigger partitions (up to 96 instead of the current 32), as well as a dual setup of the control network. The second control and distribution tree can be used either as a hot spare or as a live commissioning test-bed for the future GT upgrade. In addition the flexibility of the new system will allow room for a test setup for future, LHC-wide, TTC developments. All TCDS hardware will be MicroTCA-based and will be developed by CERN PH-ESE in collaboration with Imperial College. The CMS DAQ group will work on software development. At the moment, the TCDS development is in the prototyping phase. After the installation readi-

ness review in early 2014, installation at P5 has been done in March/April 2014 in the shadow of the DAQ2 installation, leaving time for final commissioning in summer 2014.
In the TCDS design great care has been taken to maintain the exact current connectivity for all pre-LS1 subsystems. For these, the hardware change was transparent. HCAL, moving to a MicroTCA-based readout, still receive the TTC signals. The fully centralized architecture of the TCDS and its place in the Run Control and Monitoring System is also visible on the software side. For the most part, however, these changes build on the centralization of the TTC system in the previous years and subsystems benefit from their investments in this area.
The TCDS integration has not gone unnoticed, but all possible care has been taken to minimise the impact for all subsystems. At the same time this upgrade improved the position for long-term maintenance and operational support and it provided an invaluable live test-bed for future CMS (and beyond-CMS) upgrades.

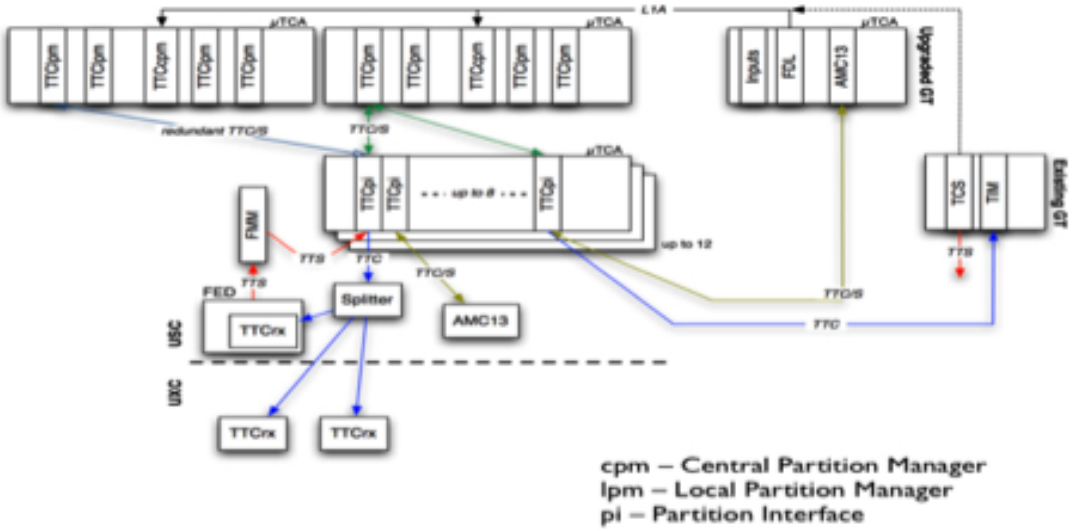

Figure 3.13: A scheme of the TDCS system

So the CMS TCDS distributes timing and control (synchronization) data flowing to the detector front-ends and receives back status information related to the readiness of the detector systems to handle more triggers. In the downstream (towards the detector) direction, this means that the clock reference that is synchronous with the particles in the LHC accelerator is distributed along with the fast control information required in order to keep the data-taking in step across the various detector systems that make up CMS. The detector systems are able to provide basic status information (TTS) regarding their readiness for accepting more triggers by sending data back to the TCDS in the upstream direction.
Physics triggers are received from the GT (existing and upgraded) system by the Central Partition Manager (CPM) module. This is the controller re-

sponsible for orchestrating global all data-taking in CMS that involves multiple sub-detectors. The system clock (received from the LHC RF systems) is also received by the CPM for further distribution. Residing in the same μTCA crate are a number of Local Partition Managers (LPMs) that are able to orchestrate local data-taking for a particular sub-detector in CMS. Each LPM contains eight identical firmware blocks that translate the generic synchronization commands emitted by the Partition Manager (Central or Local) into the sub-detector specific commands that are understood by the detector front-ends. The final module in the chain (of which there is one per detector partition) is the Partition Interface (PI). The PI serves as a fan-out for downstream clock and data (TTC) and an intelligent OR-based fan-in for the status information (TTS) coming back upstream.
An important new feature of the TCDS system is that it enables existing systems that interfaced to the pre-LS1 TTC system to be connected along with upgrading systems that are based on the new common CMS readout module (AMC13). The latter provides a bi-directional optical interface in contrast to the legacy systems where the TTC data are optical while the TTS are electrical signals.
The CMS TCDS is based on the uTCA family of standards, using full size, double width AMC modules in a 12-slot uTCA shelf with a telecom backplane and redundant power modules. In the partition manager crate, the backplane is used to distribute clock and fast timing commands from the CPM to the LPMs as well. These data are relatively low speed, being a 40 MHz clock and 160 Mb/s data. The backplane is also used to transmit control data downstream for the synchronization of the new CMS luminosity data acquisition system (LumiDAQ), this time using high-speed serial links running at 5 Gb/s. High speed serial links operating at 5 Gb/s are also used to aggregate the TTS information and send it from the LPMs to the CPM. This is where the use of the uTCA architecture is a major benefit to the TCDS project.
The CPM module reuses the same hardware as the AMC13 together with custom firmware. The LPM and PI modules are based upon the same base module, the FC7 and are differentiated by the choice of FMCs mounted on the FC7 (see Fig. 3.14).

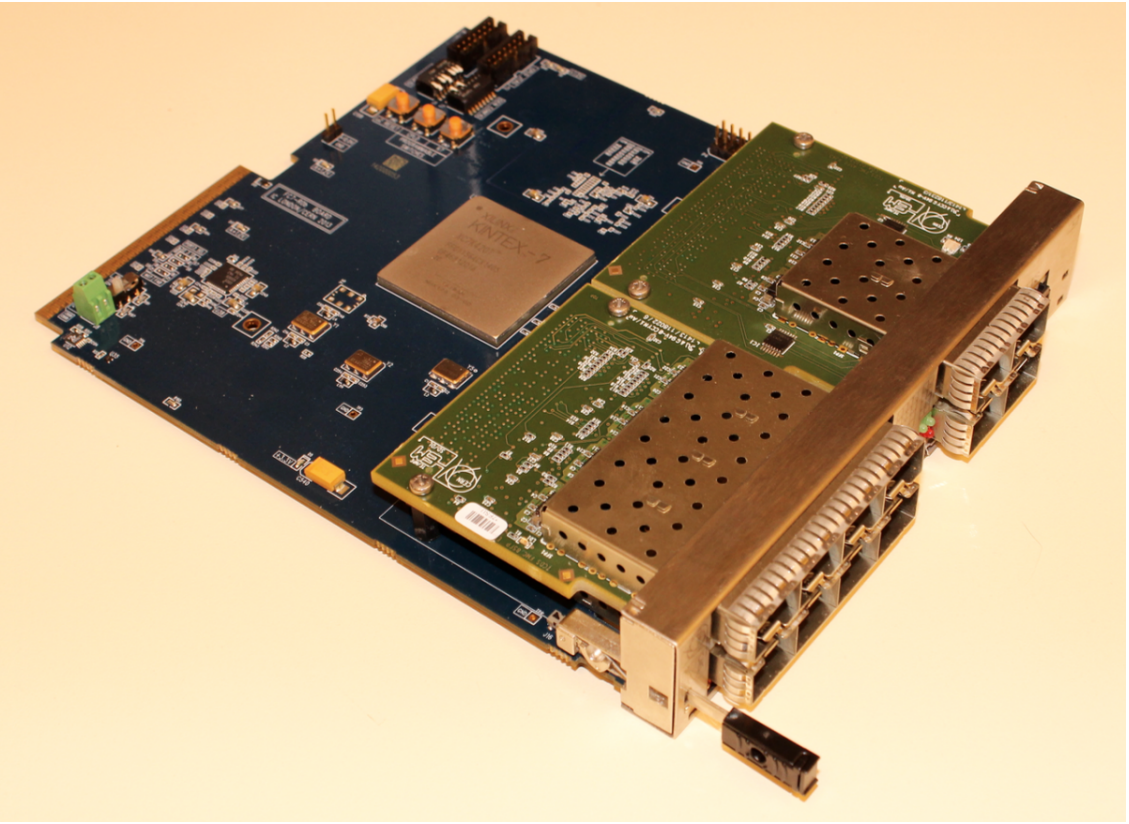

Figure 3.14: Kintex FC7 picture

The TCDS was installed in CMS in two phases: in the first phase a demonstrator was installed in parallel with the existing TTC system to allow subdetectors to become familiar with the TCDS hardware and software functionality; and in the second phase the TTC system was removed and replaced with the full TCDS at which point CMS fully switched over to TCDS. Details of the rack, powering and monitoring provided for the TCDS system will be described. This was the first time a major system in CMS installed uTCA infrastructure and thus provided a model to be copied in subsequent installations, notably for the upgrades of the CMS Trigger systems.
The TCDS system was installed in CMS six months before the LHC restart in 2015. This time was used to commission the various systems and finalize the functionality required for data-taking with particle collisions in CMS. A particularly important part of the validation of the installation was the verification of the latency added to the existing system. This has been verified to be 2 bunch crossings more than expected during initial assessment. The main reason for this has been found to be the additional interfaces necessary for the transmission of the Physics Trigger between the TCDS and the existing GT.
The TCDS system represents the first major installation of μTCA hardware in CMS and as such provides a very useful reference for future applications of this technology in particle physics applications. We have successfully applied the μTCA architecture to the design, production, installation and operation of a timing distribution system for a major particle physics experiment.

3.8.2 L1 trigger

The L1 system is built from custom designed, programmable electronics and is located underground, both in the service and the experimental caverns. Within a time budget of 3.2 μs, it has to decide if an event is kept or discarded and transfer this decision back to the subdetectors, which keep the high resolution data in memory in the meantime. The L1 is divided in a muon trigger and a calorimeter trigger, which classify and rank interesting event candidates, reconstructed from low resolution data read out from the subdetectors. The rank of a candidate is determined by energy or momentum and data quality. The calorimeter and muon triggers do not perform any selection themselves. They identify "trigger objects" of different types: e/γ (isolated and not), jets and muons. Based on the input from the muon trigger and the calorimeter trigger, the global trigger calculates the final trigger decision. Up to 128 trigger algorithms can be executed in parallel to generate a decision. The simplest triggers are in general based on the presence of one object with an E_T or p_T above a predefined threshold (single-object triggers) or based on the presence of two objects of the same type (di-object triggers) with either symmetric or asymmetric thresholds. Other requirements are those for multiple objects of the same or different types ("mixed" and multiple-object triggers). The high resolution data from the inner tracker are not used to generate the L1 decision, which means that there is no information about the vertices and no distinction between electrons and photons available at this level.

3.8.3 High level trigger

The goal of the HLT is to reduce the event rate from the maximum L1 output ($\approx$ 100 kHz) to $\sim$1 kHz which is the maximum rate for mass storage. Once the L1 trigger has accepted an event, the data of this event are transferred from the buffer memory to the surface, where they are reconstructed in the HLT. The HLT is a special part of the CMS software and runs on a farm of several thousand processors. Each processor works on the reconstruction of one event at a time, to get to a trigger decision within 100 ms on average. Since the time budget for one event is much larger than at the L1 trigger, more complicated algorithms, including tracking, can be executed at the HLT level. Once an event is accepted, it is stored on disk and fully reconstructed offline at a later time.
The use of standard software techniques and languages makes it possible to benefit from the continuous improvements in the reconstruction software. In particular the algorithms used in the HLT, which access data with full resolution and granularity from any part of the detector, is identical to those used in the off-line reconstruction. However, in order to discard uninteresting events as soon as possible, the selection is organized in a sequence of logical steps: the

Level-2 and Level-3. The Level-2 uses the full information from calorimeters and muon detectors (but not trackers) and reduces the event rate by roughly one order of magnitude. The data from the silicon tracker represents almost 80% of the event size and require complex and time consuming algorithms for the reconstruction. For this reason this information is used only during the Level-3 selection.
The HLT consists of approximately 400 trigger paths[12], which, starting from the seed of the L1 trigger, look for different objects and signatures in the event. One trigger path is built from reconstruction modules and filter modules. After some parts of the data are reconstructed, a filter module decides either the reconstructed objects pass the thresholds and the next step in reconstruction is started, or the event is not accepted by the path. In the latter case, the execution of the path is stopped and the following reconstruction steps and filter steps are not performed to save computation time.
If the acceptance rate is too high (for example in case of a trigger path with very low thresholds), the trigger path can be prescaled to lower the rate. A prescale value of 10, for example, means that the path is executed only for 1 over 10 events (randomly chosen to avoid biases) that were accepted by the L1 trigger and, consequently, the trigger rate for that path is 10 times smaller. The prescale value for one trigger path has several predefined levels, depending on the instantaneous luminosity of the LHC machine. During an LHC fill, the instantaneous luminosity decreases and the prescale values can be changed during a CMS run to keep the global trigger rate at an optimal level.

[12]In general, if an event is not accepted by a path, it can still be accepted by a different path, or even be accepted by several paths allowing a sort of redundancy that could cure some inefficiencies or issues with seeds or paths as described in Sec. 6.

Chapter 4

Event reconstruction

The aim of this chapter is to describe the way the information coming from the CMS subdetectors is combined together to reconstruct physical objects. The electron and photon reconstruction is described in Sec. 4.1, the muon reconstruction in Sec. 4.3, the jet and b-tagged jet reconstruction in Sec. 4.6 and finally the missing transverse energy reconstruction in Sec. 4.14. Jet reconstruction and topology variables are described in Sec. 4.7 and Sec. 4.13 given their importance in the topics of Chapter 5 and Chapter 6. A detailed description is reserved to jet grooming techniques (in Sec. 4.12) and pileup subtraction algorithms (in Sec. 4.8).

4.1 Electron and photon reconstruction

The strategies used in CMS to reconstruct electrons and photons have large similarities due to the similarities of the objects' signatures in the calorimeters (almost the entire energy is expected to be deposited in the ECAL in the form of an electromagnetic shower with a small lateral extension; virtually no deposit in HCAL is expected). The presence of a track matching or not the energy deposit in ECAL allows one to disentangle between the two objects. The fact that a photon can convert into electron pairs in the tracker and that electrons can radiate bremsstrahlung photons, which can in turn can convert in electron pairs, implies however that in both cases the energy of the incident particle can be distributed between several energy deposits largely spread in the ϕ direction, in reason of the bending of the electrons due to the magnetic field of CMS. In some cases, this feature also makes the electron/photon distinction more difficult and various algorithms have been developed to identify the initial particle.
This section is organized in the following way: first the common aspects of electrons and photons reconstruction are presented then the peculiarities of the individual reconstruction methods are presented.

4.1.1 Energy measurement in ECAL

The electrical signal coming from the photodetectors (APDs and VPTs) is amplified and shaped by a multi-gain preamplifier (MGPA) [55], which uses three parallel amplification stages. The output is digitized by a 12 bit Analog-to-Digital Converter (ADC) running at 40 MHz, which records ten consecutive samples and selects the gain with the highest non-saturated signal. This provides a dynamic range of about 5×10^4 from the least significant bit of 35 MeV to a saturation energy of about 1.7 (3.5) TeV in EB (EE). The data consist of a series of consecutive digitizations, corresponding to a sequence of samplings of the signal at 40 MHz. A set of 10 consecutive samplings (taken with a time distance of 25 ns) is readout and used to reconstruct the signal amplitude.
Figure 4.1 shows an example of the time sampling for a signal pulse as a function of the time difference $(T - T_{max})$, where T and T_{max} indicate the time of the generic ADC sample and the time corresponding to the maximum of the pulse shape respectively. The signal pulse is expected to start from the fourth sample and the baseline pedestal value is estimated from the first three samples.

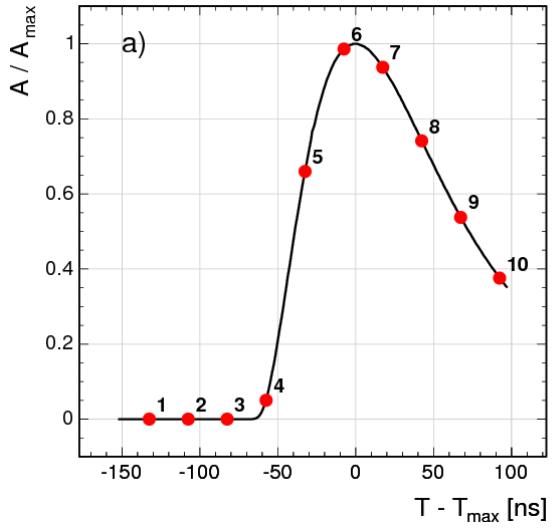

Figure 4.1: Pulse shape measured in the ECAL as a function of $(T - T_{max})$ [56]

Signal pulse reconstruction

During LHC RunI a digital filtering algorithm was used, where the signal amplitude $\mathcal{A}$ was estimated as the linear combination[1] of the $N = 10$ samples S_i:

$$\mathcal{A} = \sum_{i=1}^{N} w_i \times S_i \tag{4.1}$$

[1]The simplest method to take the sampling on the maximum as the amplitude measurement was exploited, during the RunI data-taking, for energies close to the saturation point of the three available amplifiers (see Sec. 4.1.2).

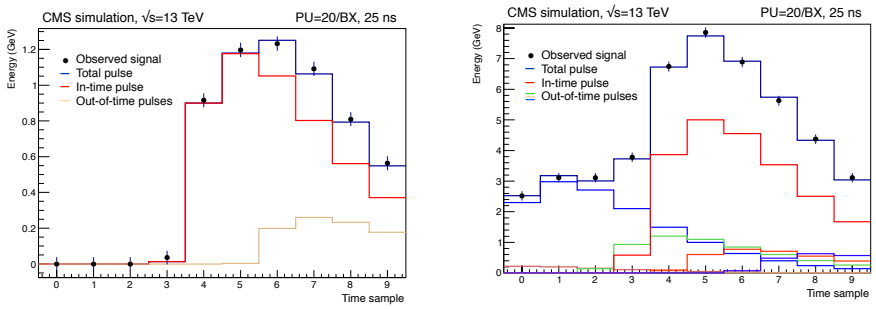

Figure 4.2: Two examples of fitted pulses for simulated events with 20 average pile-up interactions and 25 ns bunch spacing, for a signal in the barrel (left) and in the endcaps (right). Dots represent the 10 digitized samples, the red distributions (other light colours) represent the fitted in-time (out-of time) pulses with positive amplitude. The dark blue histograms represent the sum of all the fitted contributions [56]

where the weights w_i were computed in order to minimize the variance of $\mathcal{A}$. A detailed description of this method (known as "weight method") can be found in [57].

For the LHC RunII a new ECAL pulse reconstruction algorithm was developed, due to the requirements of the new data taking conditions, in particular the unprecedented pile-up conditions (see Sec. 2.2). Several methods have been investigated to mitigate the effect of pile-up, maintaining optimal noise filtering [58] and a template fit with multiple components (known as "multifit method" [56]) was chosen for the RunII data taking.

The multifit algorithm estimates the signal amplitude and up to 9 out of time amplitudes by minimization of the χ^2, given by:

$$\chi^2 = \sum_{i=1}^{N} \frac{\left((\sum_{j=1}^{M} \mathcal{A}_j p_j)_i - S_i \right)^2}{\sigma_{S_i}^2} \tag{4.2}$$

where i runs over the $N = 10$ samples and j runs over the $M \leq 10$ pulse templates p_j. As the x-axis variable (the sample time) of the template function is fixed, the pulse templates for each crystal were measured from dedicated low pile-up pp collisions data recorded by CMS and the time behaviour of the detector is constantly monitored with a dedicated analysis (Appendix A). The total electronic noise is denoted as σ_{S_i} and measured from dedicated pedestal runs, which measured the noise in all three gains of the MGPA in the absence of signal pulses.

The technique of Non-Negative-Least-Squares [59] is used to perform the χ^2 minimization of Eq. 4.2 with the constraint that the fitted amplitudes must be all positive. Examples of two fitted pulses in the barrel and in the endcaps are shown in Fig. 4.2. The fit is performed in ≈ 10 ms/event, for events with an average pile-up of 40 and for 25 ns bunch spacing. The residual contribution of out-of-time pile-up to the energy resolution has been estimated for the multifit

algorithm using simulated samples of unconverted photons. It is observed to be highly suppressed for signal pulses in both the barrel and endcaps. The improvement in energy resolution with respect the RunI reconstruction algorithm for collisions with 25 ns bunch spacing is substantial especially for low p_T photons and electrons, given the larger contribution of pile-up to the total energy estimate and is still significant for those at high p_T ($p_T > 50$ GeV).
With the amount of statistics collected in the first half of 2016 ($\sim$13) an important issue of the multifit algorithm, known as "slew rate issue", was exposed. It resulted in affecting the energy scale of electrons with high transverse momentum up to a maximal effect quantified to $\sim$4%.

4.1.2 Discussion of the ECAL slew rate issue

When converting the analogical signals coming from the ECAL crystals to digital signals, three gains are available with the different gain factors of 12, 6 and 1. When the ADC (analog-to-digital converter) count reaches its maximum with a given gain, a lower gain factor is considered (gain switch). The lowest gain factor (gain 1) corresponds to the saturation energy of $\sim$1.7 TeV in the barrel and $\sim$ 3.2 TeV in the endcaps.
The ECAL electronics showed a non-linear behavior at the end of each gain range which results in a distortion of the pulse shape in the case where the ADC switches gains during the pulse. The multifit algorithm (see previous section) did not take this effect correctly into account and, in the presence of a gain switch from sample 4 to sample 5 of the pulse shape (see Fig. 4.1), it reconstructs a lower amplitude for the pulse shape, due to an over-estimation of the out-of-time pile-up components. This issue, known as "slew rate issue" or "gain switch issue", was not simulated in the Monte Carlo samples, therefore only electrons/photons in data (and in the barrel) encountering a gain switch threshold are effected. The events with at least one electron/photon encountering gain 1 switches ($E_{\mathrm{T}} >\sim$ 300 GeV) are of course the most problematic ones given the final state (half of it) targeted in the analyses described in this thesis, but also the energy of electrons/photons affected by gain 6 switches ($E_{\mathrm{T}} >\sim$ 150 GeV) needs to be treated.
Once the problem has been understood to be due to the multifit algorithm, it was possible to overcome it simply by reconstructing the energy of the crystals encountering a gain switch as it was done with the RunI "weight" method, i.e. by simply taking the maximum sample as the estimate of the amplitude. Figure 4.3 shows the Z peak for barrel-barrel electron pairs that pass the HEEP selection (see Sec. 4.2.1) with at least one electron having a switch to gain 6 (right) or gain 1 (left) in the 5×5 crystal matrix centered on the seed crystal, with the Z mass calculated with the electron energy before and after the software fix. As can be seen from the plot, in the case without the fix and especially in the "gain 1 scenario", the Z peak is shifted from 91 GeV and a secondary tail where one of the electrons is very misreconstructed appears. With the fix applied, the Z peak position is recovered to 91 GeV, the resolution improves to expected values and the tail at 75 GeV disappears, demonstrating

the effectiveness of the fix strategy.

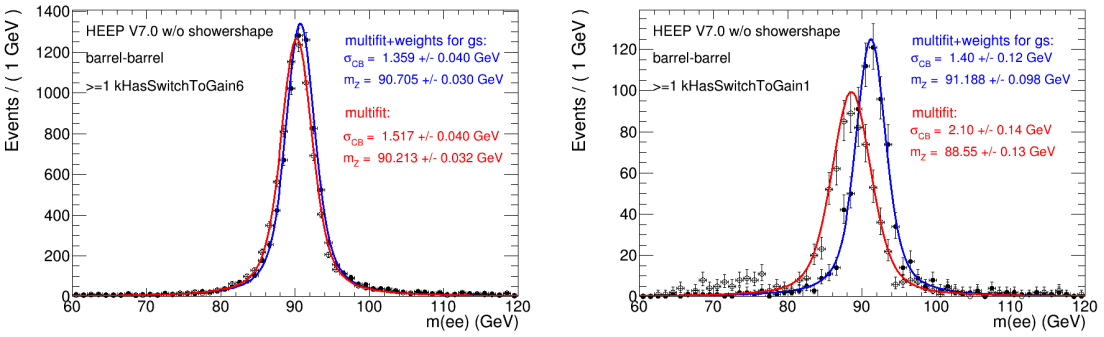

Figure 4.3: The Z peak region for barrel-barrel dielectron events where at least one electron has a gain 6 switch (left) or gain 1 switch (right). The electrons are required to pass the HEEP selection. When using the standard multifit algorithm for gain switched crystals the Z peak is shifted and the mass resolution is degraded. When using the modified multifit algorithm (standard multifit plus weight method in case of gain switches) the Z peak is restored to 91 GeV and the mass resolution is significantly improved

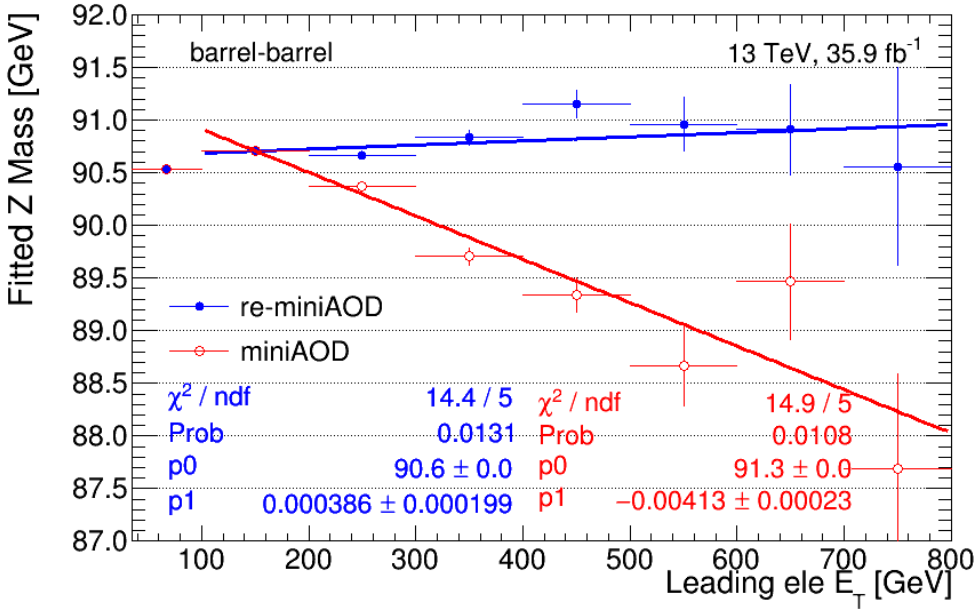

Figure 4.4: The Z peak position for barrel-barrel dielectron events as a function of leading electron E_{T} using the energy before and after the gain switch fix. The peak position after the fix (blue points and line) is clearly much more stable as a function of the leading electron E_{T} with respect to the scenario where the fix is not applied (red points and line)

4.1.3 Clustering algorithms

Electrons and photons deposit their energy over several ECAL crystals. In addition, the presence of material in front of ECAL could cause conversions of photons and bremsstrahlung from electrons and the irradiated energy is spread along ϕ by the strong magnetic field (see Sec. 3.6). Clustering algorithms are used to collect the energy deposits in ECAL, including the contributions from the irradiated energy. The clustering algorithm takes into account the correlation in the $\eta - \phi$ plane of the radiated energy due to the combined effect of the magnetic field and material budget distribution.
In fact, an electron/photon interacting in the ECAL, will deposit in average 94% (97%) of its energy in a matrix of 3×3 (5×5) crystals around the crystal with the largest energy deposit, which is denoted as the *seed* crystal. The material in front of the ECAL has a thickness between 0.4 and 2 radiation lengths. This means that at $\eta \sim 0$, on average 33% of the electron/photon energy is lost before reaching the ECAL and in the direction of the largest material budget at $|\eta| \sim 1.4$ the loss is on average 86%. The energy lost via radiative processes has to be added to the energy deposited by the electron in the ECAL. This is done by the construction of a supercluster (SC) in the two ways defined below (two different algorithms are employed for barrel and endcaps). Since the trajectory of the electron is curved in r$-\phi$ plane, the energy deposit in the ECAL barrel coming from radiated photons is mainly spread in the ϕ direction. In order to build the SC, slices of 5×1 crystals[2] in $\eta - \phi$ are produced, extending for 17 crystals (0.3 rad) in the ϕ direction around the seed crystal, which must have a transverse energy of at least 1 GeV. If the energy of the slice exceeds a threshold of 0.1 GeV it is grouped with nearby slices to form a cluster. The clusters themselves must have a seed slice that exceeds an energy of 0.35 GeV to be added to the SC. In the endcaps, the energy deposit from bremsstrahlung follows a trajectory in η and ϕ. The energy is collected in a 5×5 matrix around a seed crystal that has to exceed a transverse energy threshold of 0.18 GeV. Around this central crystal the energy is collected in 5×5 matrices along roads in η and ϕ. These roads have a range of ± 0.07 in η and ± 0.3 rad in ϕ around the seed crystal and the transverse energy of the 5×5 cluster has to exceed 1 GeV if it is to be added to the SC. The energy collected in the pre-shower detector situated in front of the 5×5 matrix is also added to the SC energy. The position of the supercluster is computed as the energy-weighted mean (barycenter) of the cluster positions, whereas its (raw) energy[3] E_{raw} is simply taken as the sum of the energy of all its constituent clusters.
The electron or photon energy is then estimated as:

$$E_{e,\gamma} = F_{e,\gamma} \left[G \times \sum_i (IC_i \times LC_i(t) \times \mathcal{A}_i) + E_{ES} \right] = F_{e,\gamma} E_{\text{raw}} \qquad (4.3)$$

[2]In order to be considered in the supercluster building procedure, the crystals must have a signal that is 2σ above the electronic noise level of 80 MeV in the barrel and up to 300 MeV in the endcaps.

[3]Also denoted as E_{SC} in literature.

where the sum is performed over all the clustered crystals. The amplitude measured in the i-th crystal is labeled by $\mathcal{A}_i$, while $LC_i(t)$ is a time dependent correction that accounts for time variation of the channel response due to changes in crystal transparency (see Sec. 4.1.4). The IC_i parameter is a relative calibration constant that takes into account differences in the crystal light yields and photodetector response (see Sec. 4.1.4) and G is a scale factor converting the digital scale into GeV. For clusters in the endcap region the corresponding energy in the preshower (E_{ES}) is added. Finally $F_{e,\gamma}$ is a particle-dependent correction, also denoted as cluster correction, applied to the SC energy. It accounts for biases in the energy reconstruction related to the geometry of the detector, the upstream material and the clustering of energy emitted by bremsstrahlung or photon conversions. The pile-up dependence of the energy scale and its correlation with the cluster shape and position is also taken into account by a multivariate algorithm trained on simulated samples of electrons and photons (giving raise to what is generally called "electron-tuned regression" and "photon-tuned regression").
In the following, the methods used to derive the parameters in Eq. 4.3 are described. They are based on in-situ measurements of copious physics processes producing electrons and photons in the final state: $\pi^0, \eta \to \gamma\gamma$, W$\to$ eν, Z$\to$ee.
Also, a definition that will be useful for the future is the ratio of the energy in a fixed array of 3×3 crystals around the seed crystal over the SC energy without the $F_{e,\gamma}$ correction of Eq. 4.3. This variable is called R_9 and defined as $R_9 = E_{3\times3}/E_{\text{raw}}$: the R_9 variable offers a convenient way to identify electrons with little radiation in the tracker or unconverted photons, for which a better energy resolution is expected.

4.1.4 Energy calibrations

The ECAL energy calibration workflow [60] exploits different methods and physics channels to measure the terms entering in the energy reconstructions expressed by Eq. 4.3. The first step consists of correcting for the single channel response time variation. Once the response of the channels is stable in time, collision events are used to derive the intercalibration corrections. As a final step of the calibration procedure, the absolute energy scale G is tuned.

Corrections for time-dependent response changes

Ionizing radiation induces loss of transparency in the ECAL crystals reducing their measured response to the deposited energy. This loss in transparency depends on the dose rate, which varies with η and a partial recovery of transparency is observed in the absence of radiation. The changes in transparency are measured and corrected using a dedicated "laser monitoring" system [61] which injects laser light ($\lambda \sim 440$ nm, close to the peak of the scintillation light spectrum for $PbWO_4$) into each crystal. One measurement point per crystal is

typically recorded every 30 minutes. The change in transparency (R/R_0) does not directly measure the change in the amount of the scintillation light (S/S_0) since the two have different spectra and the optical photons travel different paths to reach the photodetectors, but they can be related by a power law:

$$\frac{S}{S_0} = \left(\frac{R}{R_0}\right)^{\alpha} \tag{4.4}$$

where $\alpha \sim 1.5$. The history of the relative response variation measured by the laser monitoring system in the period 2011-2016 is shown in Fig. 4.5. The corrections for transparency loss, the LC (laser correction) parameters of

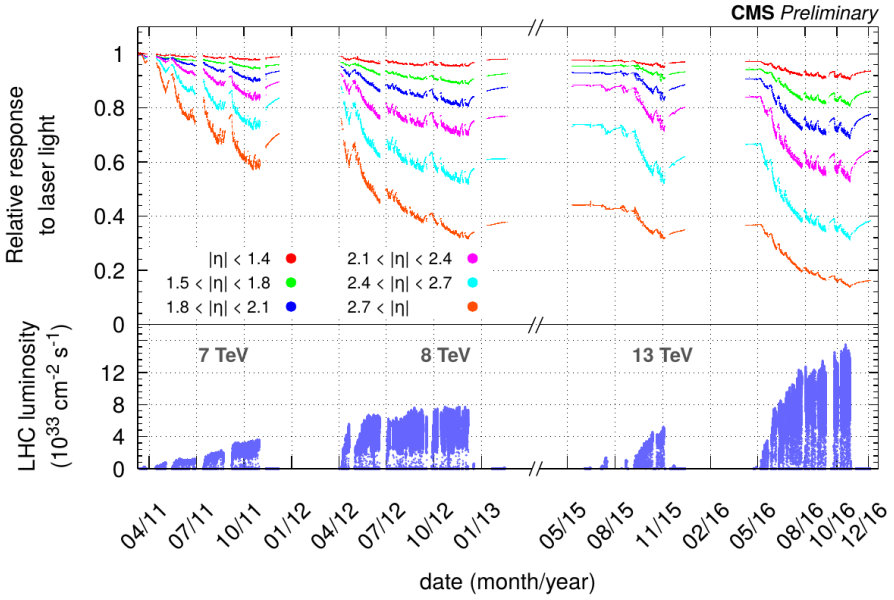

Figure 4.5: Relative response variation measured by the laser monitoring system ($\frac{S}{S_0}$) in the period 2011-2016. The response is averaged over the pseudorapidity ranges listed in the legend [56]

Eq. 4.3, are then validated with collisions data, by examining the stability of the reconstructed invariant mass of π^0 decays and using the ratio of E/p for isolated electrons from W$\rightarrow$ eν and Z$\rightarrow$ ee decays. In the ratio, E is the energy measured in the calorimeter and p is the momentum measured in the tracker. Figure 4.6 shows the stability of the E/p ratio measured from 2015 data (in barrel) before and after the LC are applied. The stability of the ratio after corrections is better than 0.1% in the barrel and 0.4% in the endcaps. Any residual imperfections in the LC (e.g. due to the dispersion in α values between crystals) are removed by applying additional time-dependent corrections, explained below.

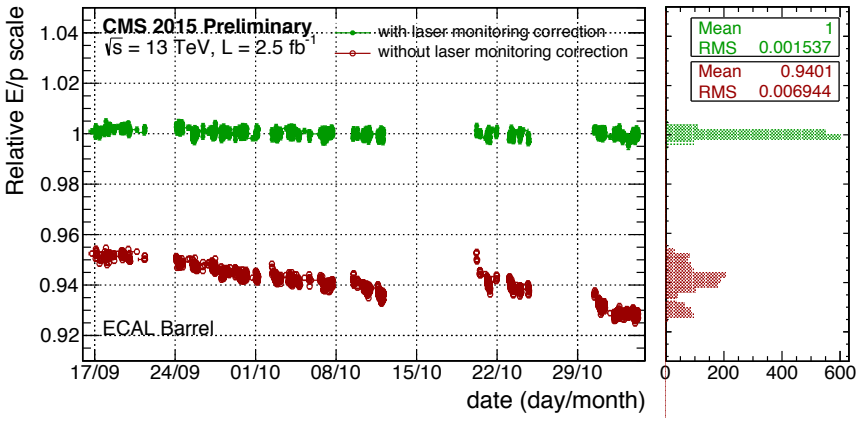

Figure 4.6: History plot for 2015 data of the ratio of electron energy E, measured in the ECAL barrel, to the electron momentum p, measured in the tracker. The electrons are selected from W$\rightarrow$ eν decays. The projections along the y-axis are shown in the histograms on the right side [56]

Intercalibrations and energy scale

Relative calibration of the crystals[4] is obtained from LHC collisions data. These intercalibration constants (IC) are calculated using several independent methods and the resulting constants are combined to provide one number per crystal. The three methods used to achieve the task are detailed below.

- The ϕ-symmetry method is based on the equalization of the average energy measured in different channels located at a constant value of $|\eta|$. This method is in fact based on the assumption that, in minimum bias events, the physics processes are ϕ-symmetric and the CMS detector is mainly ϕ-symmetric too. It employs a dedicated data stream with reduced event information. The stream records a high rate of events ($\sim$1.5 kHz) and the method achieves a statistical precision of better than 0.2% (0.4%) in EB (EE) for a typical LHC fill. The accuracy of the method is limited to few percent by systematic uncertainties in the distribution of material in front of the ECAL. Since this uncertainty does not vary with time, the method can be used to track possible time variations in the IC values. Corrections that account for these variations are propagated to the final calibration, in time intervals of approximately one month.
- The π^0 mass method is based on the reconstruction of the peak in the spectrum of the invariant mass of unconverted photon pairs from π^0 and η decays. The photons are reconstructed using the energy sum in a 3×3 matrix of crystals centered on the crystal with the highest energy deposit and an iterative method is used to determine the IC value of each crystal. It employs a dedicated data stream with high rate ($\sim$ 7 kHz) and reaches

[4]The IC_i parameters in Eq. 4.3.

a precision of 0.5% in the central barrel ($|\eta| < 0.8$). This precision is dominated by systematic uncertainties.

– The E/p method is based on the comparison of the energy measured in the ECAL to the momentum measured by the tracker for isolated electrons and an iterative procedure is used to extract the IC value for each crystal. The precision in the central barrel reaches the systematic limit of 0.5%, while for $|\eta| > 1$ the statistical contribution is the limiting factor.

The combined intercalibration was obtained from the mean of the individual intercalibration constants at a fixed value of $|\eta|$, weighted by their respective precision. In the region $|\eta| > 2.5$, beyond the tracker acceptance, the E/p method cannot be used and the high pile-up prevents the reconstruction of the invariant mass peak from π^0 or η, therefore only the IC estimate from the ϕ-symmetry are available. The precision of the different methods and of their combination is reported in Fig. 4.7 for the barrel case; it is at the level of ∼1.5% in the endcaps. The calibration of the η rings (η scale) is obtained from the

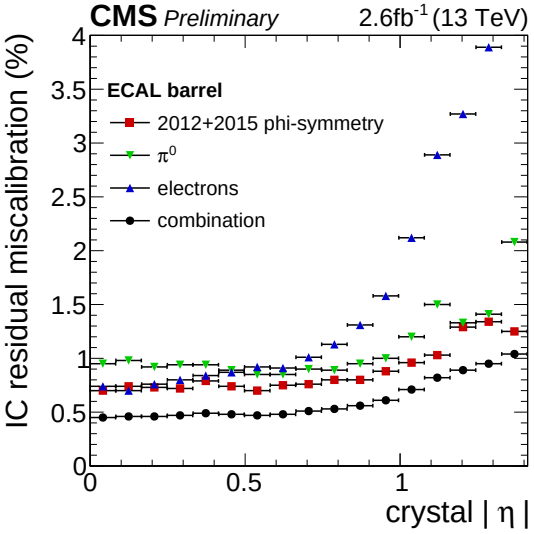

Figure 4.7: Precision of the calibration coefficients as a function of $|\eta|$, for the barrel. The precision of the different methods and of their combination are reported [56]

invariant mass of Z→ee decays, selecting a sample of non-showering electrons. The η scale is set to match the expectation from Monte Carlo simulations. Finally, the overall energy scale G is set, separately for EB and EE, such that the reconstructed Z peak in data matches what is used in the Monte Carlo datasets.

4.1.5 Energy resolution and scale

The energy resolution for electrons and photons plays a crucial role in many CMS analyses and in particular for the searches of dielectron and diphoton

resonances at high mass.
Figure 4.8 shows the measured energy resolution for electrons from Z→ee decays plotted as a function of $|\eta|$ for 2015 data. The resolution is affected by the amount of material in front of ECAL (which increases beyond $|\eta| > 1$) and the presence of cracks between modules (vertical lines in the plot). The resolution is shown for two sets of intercalibration constants: initial calibration constants derived from prompt reconstruction of 2015 data (black points) and with calibration constants derived from the re-reconstructed 2015 data (blue points).
Figure 4.8 also shows the resolution expected from Monte Carlo simulations (red points). The residual discrepancy between data and Monte Carlo is accounted for by adding in quadrature a constant Gaussian smearing to the electron and photon energies in Monte Carlo events.

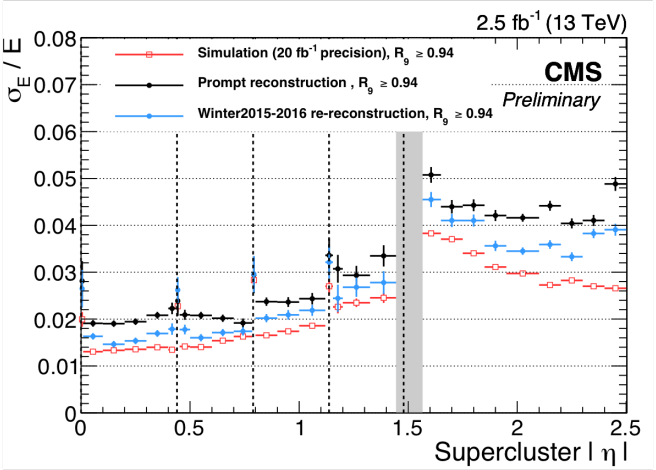

Figure 4.8: Relative electron energy resolution unfolded in bins of pseudo-rapidity $|\eta|$ for the barrel and the endcaps. Electrons from Z→ee decays are used. The resolution is shown for low bremsstrahlung electrons ($R_9 > 0.94$ with $R_9 = E_{3\times3}/E_{\text{raw}}$). All corrections from Eq. 4.3 are applied [56]

Having described the common strategies of electrons and photons energy reconstruction, in the following the peculiarities of the two objects will be presented.

4.1.6 Electron reconstruction

The peculiarity of the electron reconstruction with respect to the photon reconstruction consists in the required matching between an energy deposit in ECAL and a track in the tracker, which is of course not required for photons. More specifically, four steps are involved: the track seed selection, the track building and the track fitting (the last two are usually referred to as "tracking") and the track-supercluster matching. They are described below.

Track seeding

Track seeds for electron tracks, which are the starting point for the electron track re- construction, are built from doublets or triplets of hits in the pixel detector following two different approaches: the ECAL driven seeding and the tracker driven seeding [62].
For the ECAL driven seeding, the procedure starts from an ECAL SC, with at least 4 GeV of transverse energy and a veto of 0.15 on the ratio of hadronic energy to SC energy. The hadronic energy is calculated from the HCAL towers in a cone of $\Delta R = 0.15$ around the direction of the electron. Hits in the first pixel layer are searched by back propagating the trajectory from the barycenter of the SC, under both charge assumptions. If a pixel hit is found in a relatively wide window around the prediction from the back propagation, the track is refitted starting from the position of the hit and searching for a second hit in the next layers with a narrower window. If the first two hits are matched with the prediction from the SC, then the seed is selected.
On the other hand, tracker driven seeds are selected from tracks that were reconstructed with the Kalman filter (KF) algorithm [63]. This algorithm is not suited for electrons that emit bremsstrahlung photons as the curvature of the track changes in that case. All seeds of KF tracks that match a supercluster in the ECAL and pass a matching criterion of the ratio between SC energy and track momentum $E/p > 0.65$ (0.75), having track momenta $2 < p < 6$ GeV ($p \geq 6$ GeV), are selected.
Depending on the analysis needs, a seeding strategy could be preferred with respect to the other.

Tracking

Once the track seed has been obtained, the tracking procedure can take place. The tracking procedure consists of the "track building" outward from the seed, for which the combinatorial track finder method (CTF) [62] is used (which is an extension of the standard KF method), followed by the "track fitting" which uses a Gaussian sum filter (GSF) method [64] in a backward fit. For the track building, starting from the seed, the combinatorial track finding algorithm iteratively adds successive layers, using the Bethe–Heitler (BH) model [65] for the modeling of the electron losses. Owing to the possibility of emitted bremsstrahlung photons, a very loose requirement between the predicted hits and the found hits is applied. No more than one layer can have incompatible hit found and in case of multiple hits found up to five candidate trajectories are generated per layer. Since the distribution of the energy loss after the BH model is non-Gaussian, fitting the track with the KF algorithm that uses Gaussian distributions does not give good results. For this reason, the GSF algorithm models the BH energy loss distribution as a sum of six Gaussian distributions with different means, widths and amplitudes. After passing through a layer, six new trajectory components are generated with the weight according to the weight of the initial trajectory multiplied by the weight of the Gaus-

sian component in the BH energy loss distribution estimation. To limit the maximal number of followed trajectories to 12, the ones with low weight are dropped or merged if they are similar. Finally, the track parameters obtained have their uncertainty distributed according to the sum of Gaussian distributions from the trajectory components. For the value of the track parameter the mode of the distribution is used.

Track-supercluster matching

In order to build GSF electron candidates, a track has to be associated to a SC.
For ECAL driven tracks, the position of the SC is taken as the energy weighted position and the position of the track is the extrapolated position at the SC from the innermost track position. The difference should be smaller than 0.02 in the η direction and 0.15 rad in the ϕ direction.
For tracker driven tracks a multivariate technique, using a boosted decision tree (BDT), is used, that combines track observables and SC observables to get a global identification variable. For a successful matching, the track-SC combination should be higher than a threshold of this variable.

Charge and momentum measurement

The charge of the electron candidate is defined by three different methods.
The first method measures the charge from the curvature of the GSF track.
The second estimate comes from the curvature of the KF track associated to the GSF track if they share at least one innermost hit.
The third charge estimation comes from the comparison of the ϕ direction of the SC position as measured from the beam spot with the ϕ direction as measured from the first hit of the GSF track. Simulations predict a charge mis-identification rate of 1.2% for electrons with a transverse momentum $p_T \sim$ 35 GeV. The momentum of the electron candidates is measured by combining the momentum as measured by the tracking procedure with measurements from the ECAL. The weighting of the two measurements depends on the track parameters and the SC parameters. For electrons with high energies the precision of the energy measurement from the ECAL outweighs the one from the tracker and the transverse momentum of the electron candidate is defined by the energy measurement from the ECAL SC E_{SC} and the polar angle of the track at the interaction point θ_{track}:

$$p_T = E_{SC} \sin \theta_{track} \tag{4.5}$$

Since the transverse momentum measurement for high energy electrons is based on the energy measurement from the ECAL, it is in the following called .
A schematic view of the electron reconstruction procedure, considering also multiple bremsstrahlung emissions, is shown in Fig. 4.9.

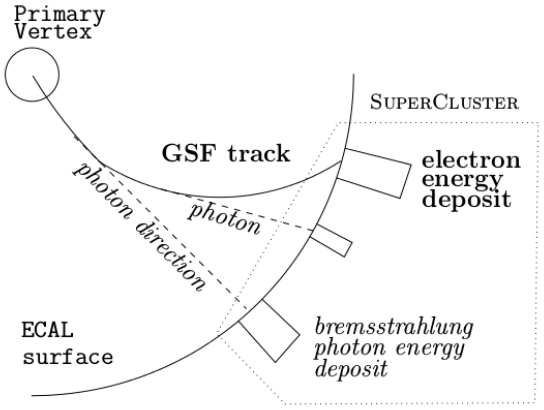

Figure 4.9: Schematic view of an electron reconstructed in CMS. The track is reconstructed by the GSF algorithm taking into account the trajectory kinks due to energetic bremsstrahlung photon emission. The energy deposits belonging to the emitted photons are collected together to the electron cluster by the clustering algorithm

4.1.7 Photon reconstruction

The photon is the simplest electromagnetic object. Any reconstructed SC with $p_T > 10$ GeV is considered as a photon candidate [66]. At this stage each electron is also reconstructed as a photon candidate since a veto with respect to reconstructed prompt electrons is applied only at final analysis level, with dedicated photon selections (see Chapter 6). Photon candidates producing an electron pair (conversion) in the material upstream ECAL are tagged using an algorithm which searches for conversion tracks matching the ECAL SC, as will be described in the following subsection.

Photon Conversions

Conversion track pairs are reconstructed starting form standard tracks reconstructed as described before and preselected with basic quality criteria[5]. Hence opposite-charge pairs are combined together and asked to satisfy the photon conversion topology. Electron conversion tracks are also required to have $p_T > 1$ GeV and requested to be matched by a SC, by requiring that ΔR between the track direction and the SC position to be smaller than 0.1. About one quarter of the events have at least one of the photon reconstructed and selected as a photon producing electron pairs.
Before concluding the section about electron and photon reconstruction at CMS, it is worth noting that the final selection of electrons or photons applied at analysis level includes various other conditions (on the shower shape, on their isolation in the detector, ...) in order to efficiently distinguish them from

[5]number of hits in the tracker layers greater than 4, $\chi^2_{track} < 10$

jets. Several variables are helpful in this task and can be combined in a set of selection criteria used by the CMS analyses.

4.2 Electron and Photon Identification

To associate almost uniquely a particular signal coming from the detector to a particular particle, selections and requirements on the signal characteristics are needed. Identification variables, called ID, are then developed to distinguish between different particles, having the best detection efficiency and trying to reject as maximum noise as possible. For the purpose of this thesis project, photons and electrons play an important role as described in Chapter 5 and 6. In the following, the identification criteria used in this thesis for electrons and photons are presented.

4.2.1 Electron HEEP ID

Depending on the physics scenario targeted by a single analysis, different IDs are developed. The HEEP (High Electron Energy Pairs) ID is meant for boosted regimes where the particles have a high transverse momentum (see Chapter 5).
The requirements for this ID are listed in Tab. 4.1.

Variable	HEEP selection	
	Barrel	Endcap
E_T [GeV]	>35	>35
$\mid \eta_{SC} \mid$	<1.4442	1.566 < - < 2.5
isEcalDriven	=1	=1
$\mid \Delta\eta_{i\eta}^{seed} \mid$	<0.004	<0.006
$\mid \Delta\Phi_{i\eta} \mid$	<0.06	<0.06
H/E	<1/E + 0.05	<5/E + 0.05
$\sigma_{i\eta i\eta}$	-	<0.03
E^{2x5}/E^{5x5}	>0.94	-
Isolation	<2+0.03E_T + 0.28ρ	<2.5 + 0.28ρ for E_T < 50
		else <2.5 + 0.03E_T − 50 + 0.28ρ
Tracker Isolation	<5	<5
Inner Layer Lost Hits	<=1	<=1
| dxy |	<0.02	<0.05

Table 4.1: HEEP Electron ID

Where E_T is the transverse energy is reported in Eq. 1.47, η_{SC} is the η coordinate of the reconstructed cluster matched to the reconstructed particle (an

electron in this case), the variable isEcalDriven is 1 if a seed is determined from the ECAL superclusters, $\Delta\eta_{i\eta}^{seed}$ is the the seed cluster η subtracted by the track η position at the point of closest approach (PCA) to the seed cluster, $\Delta\Phi_{i\eta}$ is the seed cluster ϕ - track ϕ position at the PCA to the seed cluster, H/E is the ratio between the hadronic calorimeter and electromagnetic calorimeter energy deposits, $\sigma_{i\eta i\eta}$ is the weighted cluster RMS along η and inside a 5x5 crystals matrix, E^{2x5} is the energy inside 2x5 in ϕ matrix around the seed crystal, E^{5x5} is the energy inside 5x5 in ϕ matrix around the seed crystal, while the other variables are meant to identify isolated tracks in the tracker detector.

4.2.2 Photon MultiVariate ID

The photon MultiVariate ID (MVA), employs a boosted decision tree (BDT) algorithm, trained on MC samples, to discriminate between noise signals and signals coming from photons. The input to the BDT algorithm contains shower shape variables, isolation sums computed from PF candidates in a cone of radius $\Delta R = 0.3$ around the photon candidate, as well as variables that account for the dependencies of the shower shape and isolation variables on the pileup [67]. In addition, a conversion-safe electron veto [67] is applied.

4.3 Muon reconstruction

The main characteristic of muon in term of detection is relative to their interaction with matter. They are the particles which go further in the experiment layers, therefore their detecting system is the last one.
The muon reconstruction [54] is obtained using the information coming from the muon system and the inner tracker. Muon candidates that are reconstructed only by using the information coming from the muon system are referred to as "standalone muon candidates", while muon candidates that are reconstructed by combining the information coming from the muon system inwards to the inner tracker are referred to as "global muon candidates". Finally, muon candidates reconstructed by combining the information coming from the inner tracker outward to the muon station are referred to as "tracker muon candidates". Since the global muon reconstruction algorithm starts from standalone muon tracks going inwards, it is mostly efficient for muons leaving hits in several muon stations, while the tracker muon reconstruction is more efficient for low p_T muon candidates.

4.3.1 Standalone muon reconstruction

The standalone muon reconstruction aims to reconstruct tracks only in the muon system. The reconstruction of muon tracks in the muon system starts from seeds, generated by the DT and the CSC (see Sec. 3.7), which are fitted to produce segments (called track stubs). The track stubs obtained from the

seeds are propagated to the innermost muon layer. From there a first KF pre-filter is used to find track segments in the outward direction. After the pre-filter, a filtering step, using the same technique, performs a fit in the inward direction, using the individual hits of the track segments and tighter criteria for the matching between the projected hit position[6] and the hit in the detector. A second tracking step is done in a similar way but using the hits coming from the RPC (see again Sec. 3.7) but without generating track segments in this case. The inclusion of the RPC measurements improves the reconstruction of low momentum muons and muons that pass a gap between the DT or CSC detectors.

4.3.2 Global muon reconstruction

The global muon reconstruction begins after the completion of the standalone reconstruction, by requiring that each standalone track is matched to a compatible track in the tracker. The process of identify the tracker track to combine with a given standalone muon track is referred to as track matching and consists of two steps. The first step is the definition of a region of interest (ROI) in the track parameter space that roughly corresponds to the standalone muon track and to select the subset of the tracker tracks inside this ROI. The determination of the ROI is based on the assumption that the standalone muon originates from the interaction point.
The second step is to iterate over this subset, applying more stringent spatial and momentum matching criteria to choose the best tracker track to combine with the standalone muon. The matching is performed by propagating the muon and the tracker tracks onto the same plane and looking for the best χ^2 value from the comparison of track parameters in the ROI. This outside-in algorithm is paired with an inside-out identification algorithm, where candidate tracker tracks are extrapolated to the muon system taking into account the magnetic field (and its change of direction outside the magnet), the average expected energy losses and multiple Coulomb scattering in the detector material.
If there is a suitable match between the tracker track and the standalone muon track, a final fit is performed all over the hits. However it is also possible to combine only a subset of the hits for the final fit. In particular, choosing a subset of the muon hits provides a better momentum resolution for high energy muons, when the measurements in the muon system are frequently contaminated by electromagnetic showers.
If the matching fails, the reconstruction is stopped and no global track is produced. If the matching algorithm selects more than one tracker track for a given standalone track, all matched tracks proceed in the reconstruction chain and the global track with the best χ^2 is chosen.

[6]For the propagation of the trajectory between the muon stations, energy loss from multiple scattering, ionisation and bremsstrahlung emissions are taken into account via dedicated parametrisation of these effects.

The global muon reconstruction ends with the matching of the global muon track and the energy deposits in the calorimeters.

4.3.3 Tracker muon reconstruction

Global muon track reconstruction starts from the muon system and combines standalone muon tracks with tracks reconstructed in the inner tracker. However, a large fraction of muons with transverse momentum below 6-7 GeV does not leave enough hits in the muon spectrometer to be reconstructed as standalone muons. Moreover, some muons can escape in the gap between the wheels.
A complementary approach, which starts from the tracker tracks, has therefore been designed [68] to identify off-line these muons and hence improve the muon reconstruction efficiency: it consists in considering all tracker tracks and identifying them as muons by looking for compatible signatures in the calorimeters and in the muon system.
The algorithm starts extrapolating each reconstructed tracker track outward to its most probable location within each detector of interest (ECAL, HCAL, HO, muon system). After collecting the associated signals from each detector, the algorithm determines compatibility variables corresponding to how well the observed signals fit with the hypothesis that the tracker track is produced by a muon. Based on the energy deposits in the calorimeters, a compatibility variable is determined, which describes how consistent the energies are with respect to what is expected for a muon. If the extrapolated track matches at least one muon segment in the muon system, the corresponding tracker track qualifies as a "tracker muon".
The efficiency for reconstructing a muon as global or tracker muon is very high: 99%.

Momentum assignment

The momentum assigned to the muon candidate uses the estimates coming from the final track fit performed in the global and tracker muon reconstructions. If both estimates give $p_T > 200$ GeV and the ratio of charge and momentum agrees with each other within 2σ, the estimate from the global muon reconstruction is chosen. Otherwise, the tracker muon momentum is taken.
In addition to these criteria, a specific selection has been developed for high p_T ($p_T > 200$ GeV) muons. In particular, the goodness of the global muon track fit selection, based on the χ^2 of the track is not requested, but an additional cut based on the $\sigma(p_T)/p_T$ for the track used for momentum determination is applied. The high-p_T muon selection is used to select the muon candidates in the search for high mass resonances decaying in dimuon final state, whose results are often combined with the ones obtained looking at the dielectron final state (new resonances decaying into muons could easily decay into electrons).

4.4 Muon Identification

As already done in Sec. 4.2, here is presented the selection required for this thesis to identify correctly a muon with a very high boost (a high transverse momentum) used in Chapter 5.

4.4.1 HighPt Muon ID

For the muon identification in highly boosted regimes (where the muon or the particle decaying to muons has a high transverse momentum), the so called HighPT muon ID is used. In addition, an isolation requirement is generally applied in order to suppress the background from QCD multijet events where jet constituents are identified as muons. A cone of radius $\Delta R = 0.3$, which has to be particle-free, is constructed around the muon direction.
The requirement for this ID are reported in Tab. 4.2.

Variable	HighPt selection
Global Muon	1
Valid Muon Hits	>0
Number of Muon Stations	>1
p_{Terror}/p_T	<0.3
| dxy |	<0.2
dz	<0.5
Number of Pixel Hits	>0
Number of Tracker Layers	>5

Table 4.2: High Pt Muon ID

The isolation parameter is defined as the scalar sum of the transverse momenta of all additional reconstructed tracks within the cone, divided by the muon p_T. Muon candidates with an isolation parameter less than 0.1 are considered isolated.

4.5 Particle-Flow (PF) algorithm

This algorithm [69, 70] allows to reconstruct stable particles combining, thanks to the high granularity of the CMS detector, information coming from all subdetectors under the form of calorimeter clusters and tracks (individually denoted as PF elements).
As a single physical particle can create multiple PF elements, such as a track and several calorimeter clusters, a link algorithm has been designed to fully reconstruct particles and to limit double counting computing the distance between the tracks and the calorimeter clusters to determine whether they correspond to the same physical objects. At the end of this procedure electrons,

photons, muons, charged and neutral hadrons are reconstructed as individual PF particles, which are eventually combined to form more complex objects such as hadronically decaying taus, jets, or transverse missing energy.

4.6 Jet reconstruction

A jet (Fig. 4.10), in Particle Physics, is a burst of hadronic particles coming from the hadronization of quarks or gluons (that, as already pointed out cannot be detected "alone") and that are focused in a cone.

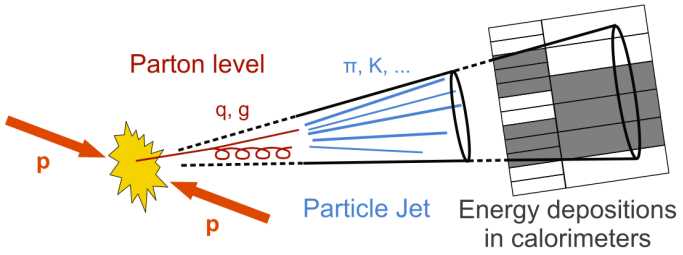

Figure 4.10: Jet graphical representation

The cross section to produce jets is by far the largest one in pp collisions at the LHC to the point that jets represent an important background for many analyses. In the event reconstruction, quark and gluon jets are built from PF objects which need to be "grouped together" into a jet. To achieve this task several algorithm can be used; the most commonly used one is the anti-k_T algorithm (which will be described in details in Sec. 4.7.1) [71]. In this analysis PF jets, which are generated by the clustering of PF candidate particles and taking the vectorial sum of their four momenta, are used.

4.7 Jet clustering

To reconstruct correctly a jet from the "particle flow candidates", which are single particles reconstructed by the CMS algorithm, a clustering procedure has to be used. It merges different particles following some criteria defined a-priori. A second step is to remove any possible noise coming from pileup, soft radiation or from closeness of two or more different jets; the clustering algorithm in those cases could merge particles which do not belong to the same jet (mainly coming from soft radiation), but that satisfy the request of the algorithm.

4.7.1 Anti-K_t algorithm

The Anti-K_t [72] algorithm is an inclusive jet finding algorithms for hadron-hadron collisions and belongs to a broader class of sequential recombination jet algorithms, parametrized by the power of the energy scale in the distance measure.
Distances d_{ij} between entities (particles, pseudojets) are introduced where i and j and d_{iB} between entity i and the beam.
The extension relative to the k_t and Cambridge/Aachen algorithms lies in our definition of the distance measures:

$$d_{ij} = min\left(k_{ti}^{2p}, k_{tj}^{2p}\right)\frac{\Delta_{ij}^2}{R^2} \tag{4.6}$$

where $d_{iB} = k_{ti}^{2p}$, $\Delta_{ij}^2 = (y_i - y_j)^2 + (\phi_i - \phi_j)^2$ and and k_{ti}, y_i and ϕ_i are respectively the transverse momentum, rapidity and azimuth of particle i. For p=-1, we obtain the anti-k_t algorithm.
If the smallest distance is of d_{ij}-type, the entities i and j are combined into a new single entity, while if it is of d_{iB}-type, the i entity is considered as a jet and removed from the list of entities. The procedure continues until the entity list is empty. Unlike other jet clustering algorithms, the anti-k_T algorithm produces jets with a conical shape, clustered around the hardest particles and with boundaries resilient with respect to soft radiation.
The performance of this particular algorithm is compared with respect to previously used algorithms such as the Cambridge/Aachen (p=0) or the k_t (p=1) in Fig. 4.11.

In the analysis (new resonances decaying into $Z\gamma/W\gamma \rightarrow qq\gamma$ signals) presented in Chapter 6, two jet collections:

- AK08: anti-kT algorithm with cone parameter R = 0.8
- AK04: anti-kT algorithm with cone parameter R = 0.4

4.8 Pileup Subtraction

To remove contribution originated by pileup events from the particles inside a jet, particular algorithms have to be used. In the CMS collaboration the standard algorithm is the Charged Hadron Subtraction; since 2016, some analyses already started using an alternative algorithm which is called PileUp Per Particle Identification. Both algorithms are presented in the following.

4.8.1 Charged Hadron Subtraction (CHS)

The In-Time pileup from charged particles is reduced by identifying which vertex the charged PF candidates originate from and removing those unam-

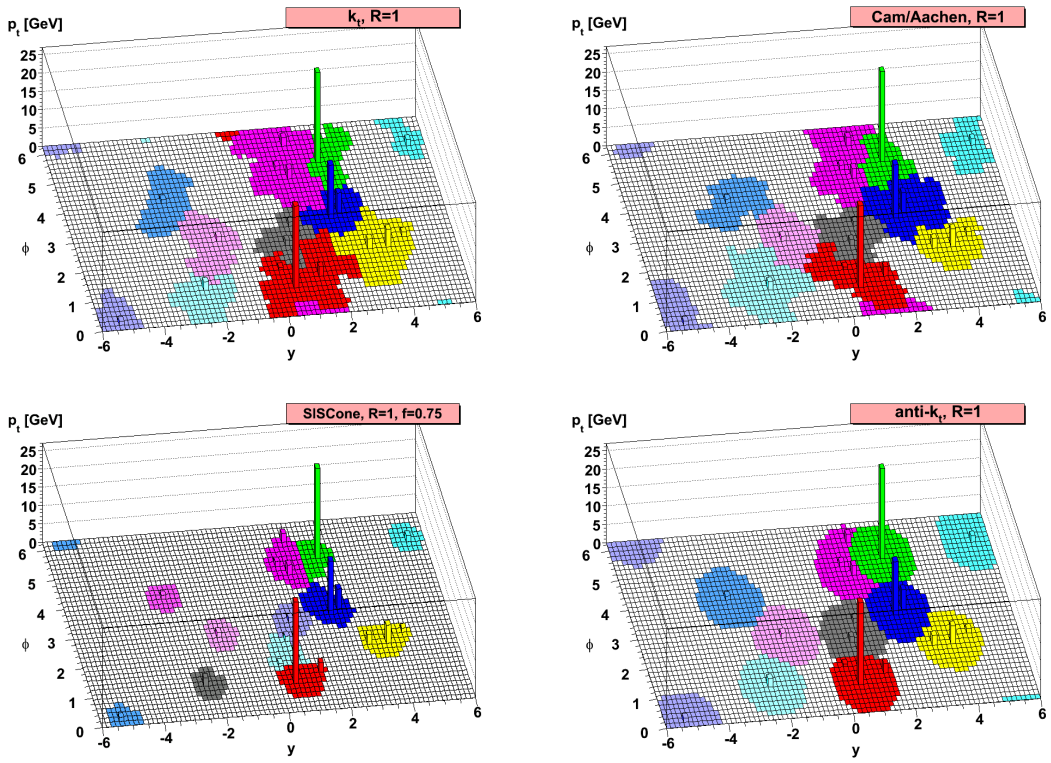

Figure 4.11: A sample parton-level event, together with many random soft "ghosts", clustered with four different jets algorithms

biguously associated with pileup vertices before clustering jets and $\overrightarrow{p}_{\mathrm{T}}^{\mathrm{miss}}$. This method is referred to as Charged-Hadron Subtraction (CHS).
The leading primary vertex is chosen based on the largest sum of squares of the tracks transverse momenta ($\sum \mid \mathrm{p}_{\mathrm{T}}^{\mathrm{track}} \mid^2$) associated with the vertex. Subleading Primary Vertex's (PV), classified as pileup vertices, are required to pass further quality criteria on the compatibility with the luminous region and on their minimum number of degrees of freedom ($\mathrm{N}_{\mathrm{dof}}$. The minimum requirement $\mathrm{N}_{\mathrm{dof}}$ >4 corresponds to at least four tracks. Tracks are matched to vertices based on their chi-squared per degree of freedom ($\chi^2/\mathrm{N}_{\mathrm{dof}}$). If $\chi^2/\mathrm{N}_{\mathrm{dof}}$ <20 for a vertex, then the track is associated with only this vertex. If the track from a charged hadron is associated with a pileup PV, passing the above quality requirements, it is considered a pileup track and removed in the CHS procedure. All other tracks, including those not associated with any PV, are kept. The CHS can remove approximately 50% of PU within the tracker coverage. The remaining unassociated charged hadrons are either not pointing to any reconstructed vertex, or are associated with a vertex that did not pass all the quality requirements, or have too large $\chi^2/\mathrm{N}_{\mathrm{dof}}$ for robust vertex association. The vertex reconstruction and identification inefficiency is about 30% for pileup vertices and it is responsible for a large proportion of the unassociated tracks from pileup.

4.8.2 Pile Up Per Particle Identification (PUPPI)

The aim of this particular algorithm [73] is to give a weight to each particle reconstructed before merging them into a cleaned jet. The value of this weight will identify the particle as pile up (not merged) or hadronic radiation (merged into the final jet). Using different steps:

1. a shape (called α) is selected. It attempts to locally distinguish parton shower-like radiation from pileup-like radiation and it is computed for each particle in an event. A basic handle to distinguish pileup and leading vertex particles is given by the p_T spectrum, with the pileup spectrum falling much faster. The shape α attempts to exploit additional and complementary information with respect to the p_T of a single particle
2. a weight to each particle is assigned by comparing its α value to the median of the charged pileup distribution. The weight takes values between zero and one and indicates how much a particle is allowed to contribute to an event. Ideally, particles from the hard scatter would get a weight of one and pileup particles would get a weight of zero
3. at last, the weights are applied to rescale the particle's four-momentum. Particles with a very small weight or with a very small rescaled p_T are discarded

The shape is defined for each particle following the function:

$$\alpha_i = log \sum_{j \in events} \zeta_{ij}\, x\Theta\left(R_{min} \leq \Delta R_{ij} \leq R_0\right) \tag{4.7}$$

where:

$$\zeta_{ij} = \frac{p_{Tj}}{\Delta R_{ij}} \tag{4.8}$$

and $\Theta\left(R_{min} \leq \Delta R_{ij} \leq R_0\right) = \Theta\left(\Delta R_{ij} - R_{min}\right) - \Theta\left(R_0 - \Delta R_{ij}\right)$ where Θ is the Heavyside step function and ΔR_{ij} is the distance between particles i and j in $\eta\phi$-space and p_{Tj} is the transverse momentum of particle j measured in units of GeV while R_0 is the cone around each particle i, so that only particles within the cone enter the calculation of α_i. Particles closer to i than R_{min} are discarded from the sum, with R_{min} effectively serving as a regulator for collinear splittings of particle i.
The α and weight (Eq. 4.10) distribution for a sample of dijet events is reported in Fig. 4.12.

As mentioned before, ideally, the weight is one for leading vertex particles and zero for pileup particle.
In order to define weights, we first introduce the following quantity:

$$\chi_i^2 = \Theta\left(\alpha_i - \alpha_{\bar{PU}}\right) \times \frac{\left(\alpha_i - \alpha_{\bar{PU}}\right)^2}{\sigma_{PU}^2} \tag{4.9}$$

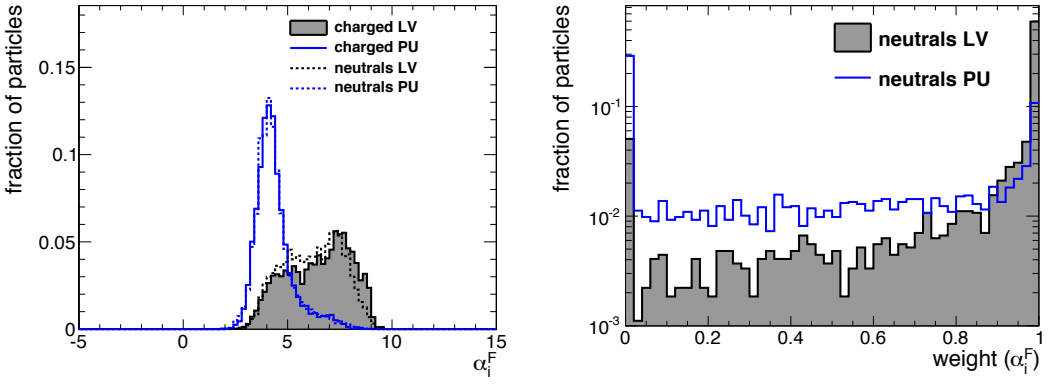

(a) (b)

Figure 4.12: Distribution for a MC dijet sample of α (a) and the weight used in the PUPPI algorithm (b) for leading (LV) and pileup (PV) vertices

Fluctuations below the median are considered to be pileup and are assigned a weight equal to zero, as defined below. On the contrary, large fluctuations above the median are very uncharacteristic of pileup and appropriately receive a weight close to 1. Any intermediate fluctuation above the median is assigned a fractional weight between zero and one.
Lastly, the weight is defined as:

$$w_i = F_{\chi^2,NDF=1}\left(\chi_i^2\right) \tag{4.10}$$

where F_{χ^2} is the cumulative distribution of the χ^2 distribution. To take into account the different construction and behaviour of the particles and the detector in the central (barrel) and forward (endcap) regions, two different α are computed. The slight difference depends on the lack of tracking information in some regions of the detector.
Therefore, the complete chain of this algorithm is:

- The values of α are computed for all charged pileup in the event
- All charged pileup particles are assigned a weight $w_i = 0$ and all charged leading vertex particles are assigned a weight $w_i = 1$
- The weights of all other particles are calculated using Eq. 4.10
- The four-momentum of each particle is rescaled by its weight $p_i^\mu \rightarrow w_i \, x \, p_i^\mu$
- Particles with small weights $w_i < w_{cut}$ or with low (rescaled) transverse momentum $p_{Ti} < p_{T,cut}$ are discarded
- The remaining set of rescaled particles is considered the pileup-corrected event

4.9 Jet Calibration

The raw jet energies are corrected to ensure a uniform response in η and an absolute calibration in p_T. The target of the calibration is that the reconstructed jet energy matches the energy of the generated jet. The correction to the raw p_T of the jet can be decomposed in four multiplicative terms [71]:

- An offset correction, to remove the energy due to particles not involved in the hard-scattering process (pile-up, detector noise);
- A MC calibration factor, which corrects the reconstructed energy to match the generated MC particle jet energy, based on simulations;
- A residual calibration for the relative energy scale, to correct the energy response as a function of the pseudorapidity;
- A residual calibration for the absolute energy scale, to make the energy response uniform as a function of the transverse momentum.

These corrections are derived from simulation and are confirmed with in situ measurements using the energy balance in dijet, multijet, γ+jet, and leptonically decaying Z+jet events.
The final energy resolution for a jet of 100 GeV of p_T is around 10%.

4.10 Jet Identification

Jets play an important role in the Z/Wγ analysis, as the vector bosons decay hadronically into a single widejet. Requirements on jets, called ID, are meant to remove any noise or anomalous deposit of energy that could be mismatched for a jet.
The less stringent requirement for jets is obtained with the loose jet ID with charged hadron subtraction to reduce contamination from pileup.
Moreover any jet used in the analyses presented in this thesis are selected to with an additional isolation requirement. Any AK08 jets within DR < 1.0 of any electron or muon are not used in the analysis. For additional jets in the event, we select AK04 jets within ΔR < 0.3 of any electron or muon, or ΔR < 0.8 of any AK08 jets.

To reject more efficiently noise and to avoid any confusion between mismeasured jets and leptons reconstructed as jets, the so called TightLepVeto ID is used. The complete list of selections for this particular ID is reported inTab. 4.4. (see Chapter 6)

Variable	loose selection
Neutral Hadronic Fraction	<0.99
Neutral EM Fraction	<0.99
Number of Constituents	>1
Charged Hadron Fraction	>0
Charged Multiplicity	>0
Charged EM Fraction	<0.99

Table 4.3: Loose Jet ID

Variable	Tight Lep Veto selection
Neutral Hadronic Fraction	<0.90
Neutral EM Fraction	<0.90
Number of Constituents	>1
Charged Hadron Fraction	>0
Charged Multiplicity	>0
Charged EM Fraction	<0.90
Muon fraction	< 0.80

Table 4.4: Tight Lep Veto Jet ID

4.11 b-jet reconstruction

Except for the top quark, which decays before hadronizing, all the quarks will generate a jet. However jets originating from b quark hadronization (b-jets), can be distinguished from other jets coming from gluons, light-flavor quarks (u, d, s) and c quark fragmentation using track, vertex and identified lepton information. Different algorithms to tag b-jets exist but only the Combined Secondary Vertex (CSV) algorithm is described here as it is the most commonly used in the CMS analyses. Since B hadrons typically have a lifetime of $c\tau \simeq 450$ μm, a powerful handle to discriminate between b-jets and other jets is the existence of a secondary vertex. A secondary vertex is defined as a vertex sharing less than 65% of its tracks with the primary vertex and separated radially from the primary vertex with a significance at least 3σ. In addition, if the radial distance exceeds 2.5 cm and if the mass is compatible with a K^0 or greater than 6.5 GeV, the secondary vertex is rejected. The last condition for secondary vertices is that the flight direction of each candidate is in a cone with $\Delta R = 0.5$ around the jet direction. When no secondary vertex is found, in about 35% of cases for real b-jets, the CSV algorithm can use so-called "pseudo-vertices", from tracks whose impact parameter is more than 2σ away. If no pseudo-vertex is found, the CSV algorithm proceeds from simple track variables. The information used by the CSV algorithm to identify b-jets are summarized as follows [74]:

- The presence of a secondary vertex, a pseudo-vertex or none of them;
- The flight distance significance between the primary and the secondary (or pseudo-) vertex in the transverse plane;
- The number of tracks at the secondary or pseudo-vertex;
- The ratio of the energy carried by tracks at the vertex with respect to all tracks in the jet;
- The pseudorapidities of the tracks at the vertex with respect to the jet axis;
- The number of tracks in the jet.

A likelihood ratio to reject c-jets and another one to reject light-parton jets are combined to form the final CSV discriminator. The efficiency of the CSV algorithm in data and simulations for the medium working point is close to 70% with a mistagging rate of about 1.5%.

4.12 Jet grooming

As the mass of the Z/W boson (V boson in the following) is larger than the mass of a typical QCD jet, the jet mass is the primary observable that distinguishes a V jet from a QCD jet. The bulk of the V jet mass arises from the kinematics of the two subjets that correspond to the two decay quarks. In contrast, the QCD jet mass arises mostly from soft gluon radiation. For this reason, the use of jet grooming methods such as filtering, trimming , or pruning, improves discrimination by removing the softer radiation, as this shifts the jet mass of QCD jets to smaller values, while maintaining the jet mass for V jets close to the V mass.

4.12.1 Pruning

The procedure of this particular grooming technique, operates by rerunning the algorithm and vetoing on these recombinations, i.e., removing, or pruning, them from the substructure of the jet. It is algorithmically similar to others, which also modify the jet substructure to improve heavy particle identification. The key distinction is that pruning is applied to an entire jet from the bottom up, with no goal of finding a particular number of "subjets". The pruning procedure is:

1) Rerun the jet algorithm on the set of initial proto-jets from the original jet, checking for the following condition in each recombination 1,2→p with the two conditions: $z<z_{cut}$ and $\Delta R_{12} > D_{cut}$

2) if this condition is met, do not merge the two proto-jets 1 and 2 into p. Instead, discard the softer proto-jet and proceed with the algorithm. The resulting jet is the pruned jet.

having $z=\min(p_{iT}, p_{jT}/p_{pT})$ where p_{iT} and p_{jT} are the p_T of the two protojets to be combined and p_{pT} is the p_T of the combination of the two protojets.
As can be seen from above, the pruning procedure involves two parameters, z_{cut}, $z=\min(p_{iT}, p_{jT}/p_{pT})$ and D_{cut}, which determine how small z must be and the minimum angle ΔR of the recombination for it to be pruned. $D_{cut}=m_J/p_{tj}$ is used for both k_T and CA, where m_j is the mass of the originally identified jet and p_{tj} is its transverse momentum. This choice is both adaptive to the properties of the individual jet and IR safe. Pruning with a smaller D_{cut} degrades the mass resolution by significantly pruning the QCD shower of daughter partons of the heavy particle decay and pruning with a larger D_{cut} does not take full advantage of the procedure. For the CA algorithm, $z_{cut} = 0.10$ is used. Because the k_T algorithm orders recombinations partly in z, very small z recombinations are not expected at the end of the algorithm. This implies a more aggressive pruning procedure is needed for the k_T algorithm [75].
Pruned jet mass is obtained by removing the softest components of a jet. The CA8 jet is reclustered from its original jet constituents, however the CA clustering sequence is modified to remove soft and wide-angle protojets (single particles, or groups of particles already combined in the previous steps). As said, the protojet with the lower p_{iT} is ignored if $z<z_{cut}=0.1$ and if it forms an angle ΔR wider than $\Delta_{cut}=m_{orig}/p_{origT}$ relative to the axis of the combination of the two protojets, where m_{orig} and p_{origT} are the mass and p_T of the original CA8 jet.
The pruned jet mass distributions for W jets and QCD jets are shown in Fig. 4.13 at generator level and detector level with pileup. Comparing the generator level predictions for the pruned jet mass of W jets with those at detector level with pileup, the widening of the peak due to detector resolution can be observed.

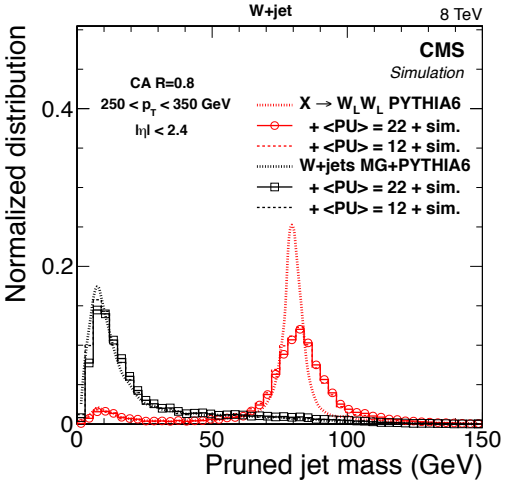

Figure 4.13: Distributions of pruning mass in simulated samples of highly boosted and longitudinally polarized W bosons and inclusive QCD jets expected in the W+jet topology

4.12.2 Soft Drop

Like any grooming method, soft drop [76] declustering removes wide-angle soft radiation from a jet in order to mitigate the effects of contamination from initial state radiation (ISR), underlying event (UE) and multiple hadron scattering (pileup). Given a jet of radius R_0 with only two constituents, the soft drop procedure removes the softer constituent unless:

$$\frac{min(p_{T1}, p_{T2})}{p_{T1} + p_{T2}} > z_{cut} \left(\frac{\Delta R_{12}}{R_0} \right)^{\beta} \tag{4.11}$$

where p_{Ti} are the transverse momenta of the constituents with respect to the beam, ΔR_{12} is their distance in the rapidity-azimuth plane, z_{cut} is the soft drop threshold and β is an angular positive exponent.
The starting point for soft drop declustering is a jet with a characteristic radius R_0. For definiteness, we will always consider jets defined with the anti-k_t algorithm, but other jet algorithms would work equally well. The jet constituents are then reclustered using the Cambridge-Aachen (C/A) algorithm to form a pairwise clustering tree with an angular-ordered structure. The soft drop declustering procedure depends on two parameters, a soft threshold z_{cut} and an angular exponent β and is implemented as:

1) Break the jet j into two subjets by undoing the last stage of C/A clustering. Label the resulting two subjets as j_1 and j_2
2) If the subjets pass the soft drop condition (Eq. 4.11), deem j to be the final soft-drop jet
3) Otherwise, redefine j to be equal to subjet with larger p_T and iterate the procedure
4) If j is a singleton and can no longer be declustered, then one can either remove j from consideration ("tagging mode") or leave j as the final soft-drop jet ("grooming mode")

The effect on a MC sample of W events and QCD events is reported in Fig. 4.14. As can be noticed, the algorithm "shifts" the QCD peak towards lower values and tightens the W peak with respect to the scenario where the algorithm is not applied.

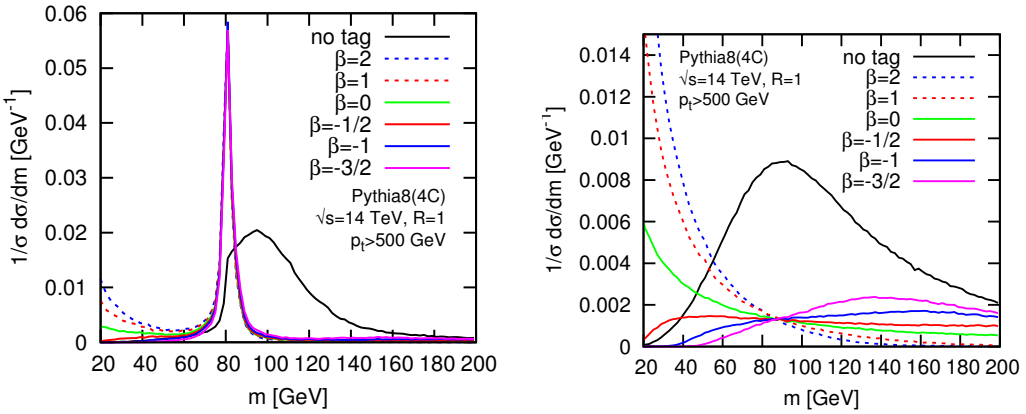

(a) (b)

Figure 4.14: Distributions of W boson (to jets) (a) and QCD (b) events using different β value for the Soft Drop algorithm and without using the Soft Drop algorithm (in black)

4.12.3 Puppi+Softdrop jet mass correction

In order to have a p_T and η independent W-jet mass when using the Puppi+Softdrop algorithm, with a mean around the W mass, corrections have to be derived. The shift in generated softdrop mass at lower p_T is of the order of 2-3% while the difference between reconstructed and generated softdrop mass is a 5-10% effect.
The result of the correction can be observed in Figure 4.15 where are shown the AK08 Puppi+Softdrop jet mass distributions taken from a $t\bar{t}$ dataset sample.

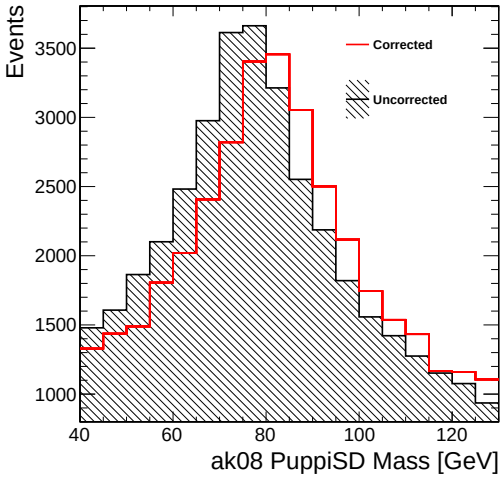

Figure 4.15: AK08 Puppi+Softdrop mass before (black) and after (red) the correction

4.12.4 Puppi+Softdrop algorithm performance at high pile up

The stability of an algorithm is an important parameter to evaluate its strength and usability. In Fig. 4.16 are reported the efficiency curves (using a set of W'→WW signal samples) as a function of the number of reconstructed vertices (taking into account also the pile up contribution). As can be seen, two combination of algorithm are tested: charged hadron subtraction + pruning and puppi + softdrop. They are also compared for two different approaches; one is simply studying a hypothetical cut on the mass of the jet, while the other one adds another cut on the N-Subjettiness (τ_{21} defined in Sec. 4.13) which is widely used among the CMS collaboration in high mass searches for new resonances decaying into boosted bosons.

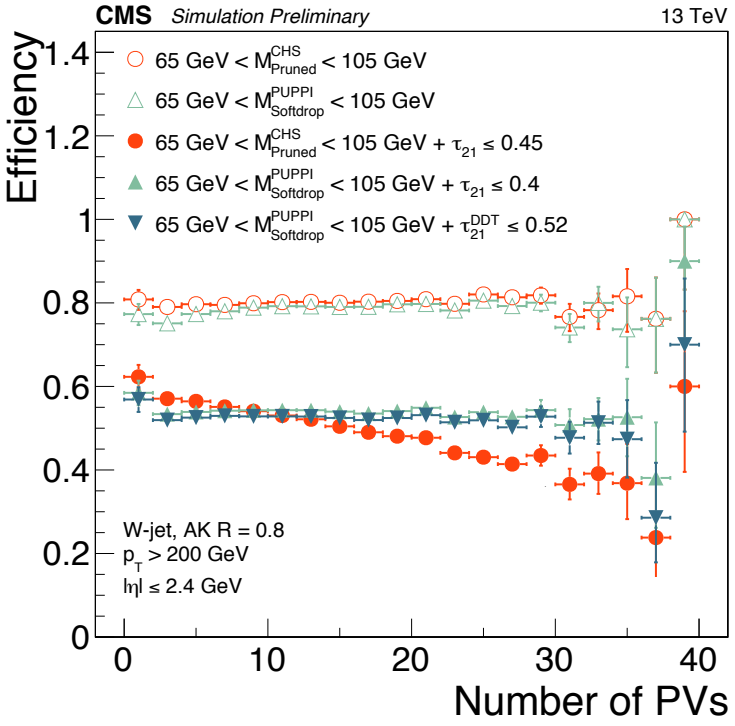

Figure 4.16: Different algorithms efficiency studied as a function of the number of primary vertices

As can be seen, adding a request on τ_{21}, introduces an inefficiency that worsen the performance of the chs+pruning algorithm increasing the number of vertices. The behaviour of the PUPPI+Softdrop algorithm (filled triangles) is completely flat. Therefore it can provide a better stability of the response also at high pileup. This can be translated in a better response of the jet mass scale (JMS, which in this case is the W mass peak) and the jet mass resolution (JMR, which is the W mass width), permitting to mantain harder cuts also in high pile up regimes without loosing any efficiency in the data analyzed.

4.13 N-Subjettiness

N-subjettiness τ_N is a generalized jet shape observable. It is computed under the assumption that the jet has N subjets and it is the p_T-weighted ΔR distance between each jet constituent and its nearest subjet axis:

$$\tau_N = \frac{1}{d_0} \sum_k p_{T,k} \cdot min(\Delta R_{1,k}, \Delta R_{2,k}, ..., \Delta R_{N,k}) \tag{4.12}$$

with the normalization factor d_0:

$$d_0 = \sum_k p_{T,k} \cdot R_0 \tag{4.13}$$

where R_0 is the radius of the cone used in the clustering process, $p_{T,k}$ is the transverse momentum of the k-constituent of the jet and:

$$\Delta R_{n,k} = \sqrt{(\Delta\eta)^2 + (\Delta\phi)^2} \tag{4.14}$$

It estimates the dispersion of the constituents of the jet in the reclustering cone.

In particular, the ratio between τ_2 and τ_1 (Fig. 4.17) has excellent capability in

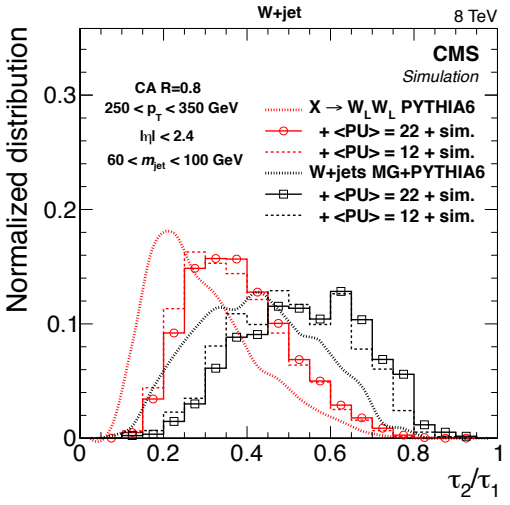

Figure 4.17: Distributions of τ_{21} variable in simulated samples of highly boosted and longitudinally polarized W bosons and inclusive QCD jets expected in the W+jet topology

separating jets with dipolar structures, originating from boosted vector bosons and jets coming from quarks and gluons hadronization. It's formula is:

$$\tau_{21} = \frac{\sum_k p_{T,k} \cdot min(\Delta R_{1,k}, \Delta R_{2,k})}{\sum_k p_{T,k} \cdot \Delta R_{1,k}} \tag{4.15}$$

The τ_{N} observable has a small value if the jet is consistent with having N or fewer subjets, as almost every jet constituent will be close in ΔR to its own true subjet. The calibration of this particular variable is described in Chapter 5.

4.14 Transverse missing energy ($\mathbf{E}_{\mathrm{TMiss}}$)

Neutrinos and other hypothetical neutral weakly interacting particles cannot be detected by CMS. However, some information about their presence can be gathered from the detection of a momentum imbalance in the transverse plane to the beam axis. The missing transverse energy is noted $\vec{E}_{TMiss}$, while its magnitude is referred to as E_T.
The most widely used type of $\vec{E}_{TMiss}$ in CMS is the particle-flow (PF) $\vec{E}_{TMiss}$, which is the negative vectorial sum over the transverse momenta of all PF particles. A bias in the E_{TMiss} measurement can be introduced for several reasons, such as the non-linearity of the response of the calorimeter for hadronic particles, or the minimum energy thresholds in the calorimeters. As pointed out before, the $\vec{E}_{TMiss}$ measurement [77] strongly relies on the reconstruction of all other physics objects and is sensitive to a wide range of effects. Large E_{TMiss} can be measured because of spurious detector signals. Sources of fake E_{TMiss} are:

- Dead cells in the ECAL;
- Beam-halo particles;
- Particles striking sensors in the ECAL barrel detector;
- Noise from HCAL hybrid photodiode;
- Direct particle interactions with light guides and photomultipliers tubes in the forward calorimeter;
- High-amplitude anomalous pulses in the ECAL endcaps;
- A misfire of the HCAL laser calibration system;
- A defective track reconstruction, from coherent noise in the silicon strip tracker.

Chapter 5

Calibration of jet mass and jet substructure observables

The hadronic decay products of energetic W/Z bosons ($p_T > 200$ GeV) can be separated by small angles ($\Delta R < 1$) and be reconstructed as a single wide-jet. Techniques to discriminate boson-jets from jets produced by hadronization of single quarks/gluons have been described previously in Sec. 4.7 and 4.13. In this Chapter, the procedure used to measure in data the W-jet mass scale, resolution and the selection efficiency of a jet substructure requirement to identify two-prong decays of W bosons (N-subjettiness) is described. The same quantities are computed for MC simulation samples and data/MC correction factors (scale factors in the following) are extracted. The first part of this Chapter is focused upon the description of the method, while in the second part, the fits and the final results are presented. The scale factors derived, allow to correct the simulation in order to match the performance measured in data of these jet substructure observables. The scale factors are used by searches for new physics involving energetic W/Z/H bosons decaying to hadrons, such as the $Z\gamma$ and $W\gamma$ analyses discussed in Chapter 6.

5.1 Analysis strategy

The main target of this analysis is to isolate a pure sample of bosons decaying into hadrons to calibrate the jet substructure observables. W bosons from semi-leptonic $t\bar{t}$ events (shown in Fig. 5.1) are used.
The W (hadronic) candidate, from which the mass scale, resolution and N-Subjettiness efficiency scale factors are measured, is the AK08 jet (see Sec. 4.7) with the highest transverse momentum in the event.

5.2 Data and MC samples

In this Section the dataset used are listed and described.

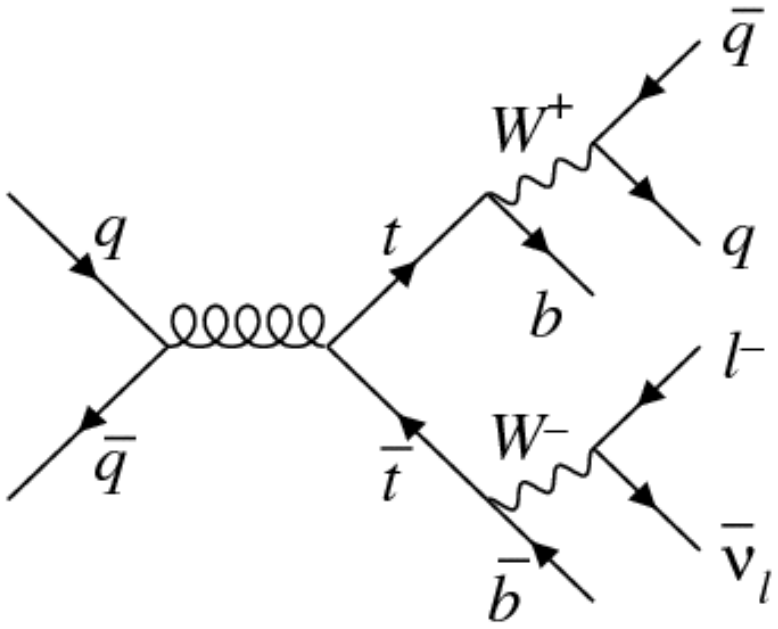

Figure 5.1: Feynman diagram of the $t\bar{t}$ semileptonic decay

5.2.1 Data samples

This analysis uses the whole 2016 data recorded by the CMS experiment, which corresponds to an integrated luminosity of about 36 fb^{-1} with an average pileup of 27 vertices per bunch crossing.

5.2.2 MC samples

The Monte-Carlo samples used are reported in Tab. 5.1 and are updated with the latest pileup prescriptions and conditions to simulate the same scenario of the data recorded. The $t\bar{t}$ Herwig sample is used to derive the uncertainties related to the showering parametrisation of Pythia described in Sec. 5.7.

Process	Generator	σ[pb]
$T\bar{T}$ inclusive sample	Powheg+Pythia	831.76
$T\bar{T}_{\text{Herwig}}$ inclusive sample	Powheg+Herwig	831.76
Single Top (s-channel) inclusive sample	AMC@NLO+Pythia	47.13
Single Top inclusive sample	Powheg+Pythia	24.6
Single Anti-Top inclusive sample	Powheg+Pythia	24.6
W+Jets with momentum in [100 GeV, 200 GeV]	MadgraphMLM+Pythia	1629.87
W+Jets with momentum in [200 GeV, 400 GeV]	MadgraphMLM+Pythia	435.6
W+Jets with momentum in [400 GeV, 600 GeV]	MadgraphMLM+Pythia	59.17
W+Jets with momentum in [600 GeV, 800 GeV]	MadgraphMLM+Pythia	14.61
W+Jets with momentum in [800 GeV, 1200 GeV]	MadgraphMLM+Pythia	6.36
W+Jets with momentum in [1200 GeV, 2500 GeV]	MadgraphMLM+Pythia	1.61
W+Jets with momentum in [2500 GeV, Inf GeV]	MadgraphMLM+Pythia	0.037
WW inclusive sample	Powheg+Pythia	118.7
WZ inclusive sample	AMC@NLO+Pythia	16.5
ZZ inclusive sample	AMC@NLO+Pythia	47.13

Table 5.1: MC dataset used in the analysis

5.3 Event Selection

As anticipated, the main goal of the kinematic requirements is to select boosted hadronic Ws from $t\bar{t}$ events. For this purpose, we require the presence of one energetic and isolated lepton (electron or muon), large E_{Tmiss} and one AK08 in the final state. The lepton and E_{Tmiss} come from the leptonic W decay, while the AK08 contains the hadronization products of the two quarks coming from the other boosted W boson.

5.3.1 Final event selection

The final event selection for both muon and electron channels are:

1. exactly one charged lepton (described in Sec. 4.1) in the final state; muon kinematic requirements with $p_T > 53$ GeV and $| \eta | < 2.1$ while for the electron the requirements are pT > 120 GeV and $| \eta | < 1.442$ or $1.56 < | \eta | < 2.5$. Additional selections are made on the ID for each particle (see Sec. 4.4.1 for muons and Sec. 4.2 for electrons)
2. missing transverse energy (see Sec. 4.14): events are required to have $E_{Tmiss} > 80$ GeV for the electron channel and $E_{Tmiss} > 40$ GeV for the muon channel to suppress contribution from QCD multijet background. The selection is tighter for electrons due to the larger QCD multijet background in this channel
3. W_{leptonic} p_T: the W_{leptonic} is the vectorial sum of the E_{Tmiss} and the lepton passing the selection in 1). The p_T of the reconstructed leptonic W must

be greater than 200 GeV. This cut is required to select the boosted W topology

4. $W_{hadronic}$: the p_T of the reconstructed hadronic W (AK08 leading jet) must be greater than 200 GeV. This cut is required to select the boosted W topology. Another requirement for the AK08 is $\mid \eta \mid < 2.0$
5. b-tag: the event is required to have one b-tagged (see Sec. 4.11) AK04 jet far from the AK08 (with > 0.8) as the signal comes from top decay
6. angular selections to select a diboson-like topology:
   - $\Delta R(lepton, W_{hadronic}) > \pi/2$
   - $\Delta\Phi(W_{hadronic}, E_{Tmiss}) > 2$
   - $\Delta\Phi(W_{hadronic}, W_{leptonic}) > 2$

All the requirement on the jet are made on the CHS (see Sec. 4.8.1) variables.

5.4 Comparison between data and MC

In this section we report data to MC comparisons for basic distributions, for both muon and electron channel passing the selection described in the previous Section.
The number of MC events are normalized taking into account the integrated luminosity of the data sample and the relative cross sections of the various samples. Additional scale factors of about 0.9 are applied to the whole MC background, in order to correct residual discrepancies in normalization between data and simulation.
From Fig. 5.2(a) to 5.3(b) the transverse momentum (p_T) and η of the leading AK8 jet and muons are shown. In the shape of these kinematic distributions, an overall good agreement is observed.From Fig. 5.4(a) to Fig. 5.5, the N-Subjettiness for the CHS and Puppi algorithm as well as the mass obtained with the pruning and PUPPI algorithms described in Sec. 4.7) used in the analysis selection are reported. The events shown in Fig. 5.5(b) are selected using the CHS kinematic variables and plotting the PUPPI+SoftDrop mass.
As can be noted in Fig. 5.5 and Fig. 5.5(b), the W peak is clearly visible together with a resonant background mainly due to bad reconstruction of the jet or failures in the grooming algorithm (e.g. the merged jet do not belong only to the W and also the b-jet is merged). Therefore a fit to extract the signal and background components of the spectrum is used.
The events under the mass peak of the W constitute the signal of this analysis and the majority of them corresponds to jets with low value of τ_{21} in Fig. 5.4. There are some discrepancies in the shape of these topology distributions between data and MC and therefore, data/MC corrections are needed. In the following Sections the procedure to extract the correction factors on these jet substructure observables for the simulation will be described.

τ_{21} in Fig. 5.4.

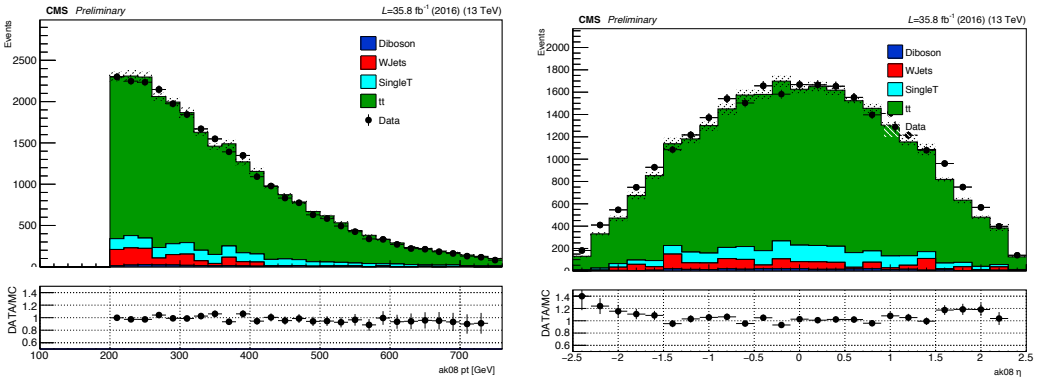

(a) (b)

Figure 5.2: AK08 transverse momentum (a) and AK08 η (b)

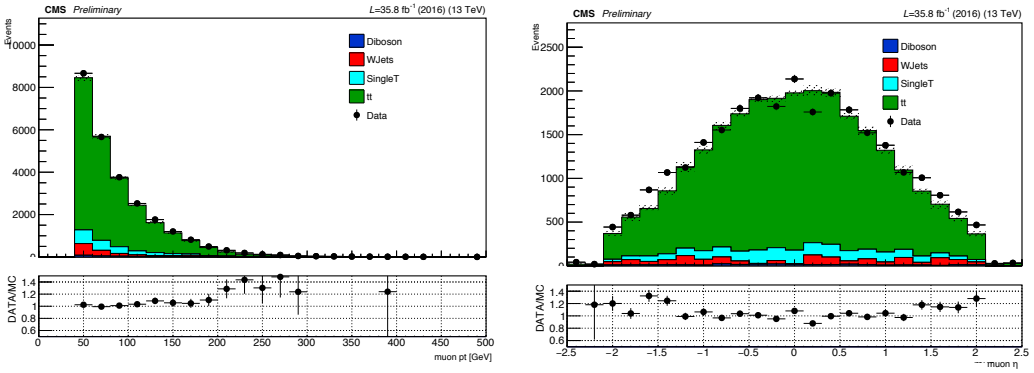

(a) (b)

Figure 5.3: Muon transverse momentum (a) and Muon η (b)

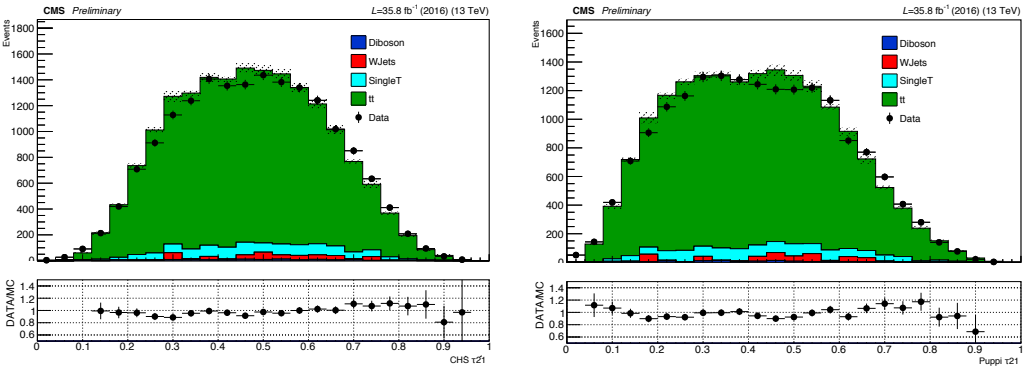

(a) (b)

Figure 5.4: AK08 τ_{21} (a) and AK08 Puppi τ_{21} (b)

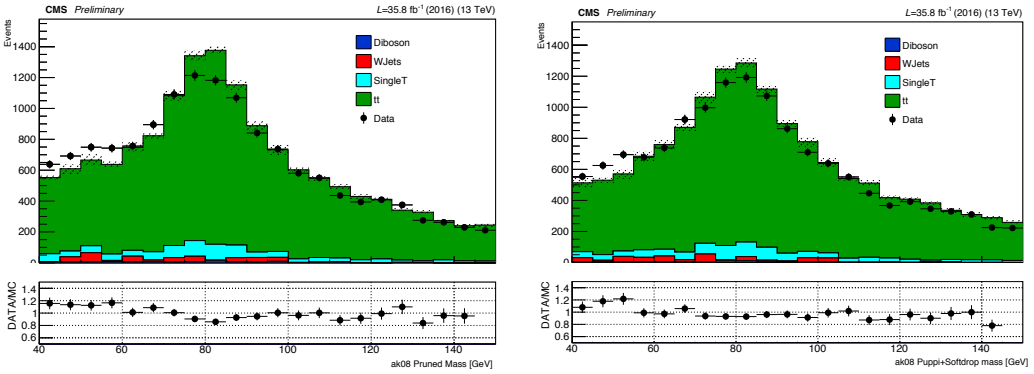

(a) (b)

Figure 5.5: AK08 Pruned Mass (a) and AK08 SoftDrop Puppi mass (b)

5.5 Fit method for data/MC scale factor extraction

This Section describes the method used to extract the data/MC Scale Factors for the τ_{21} efficiency[1], the jet mass resolution and the jet mass scale. By repeating the same study in data and simulation, for different selections for two types of τ_{21} variables (CHS and PUPPI), it is possible to derive data/MC scale factors.
The W signal is extracted from a simultaneous fit to of the jet mass distribution two categories of events, which in the following will be called High Purity (W-enriched events with $\tau_{21} < x$) and Low Purity (W-depleted events with $\tau_{21} > x$).
Two Likelihoods functions are used for the two different categories. For the High Purity (HP) we use:

$$L_{HP} = \prod_{i}^{evts} \left[N_W \cdot \varepsilon_{HP} \cdot f_{sig}^{HP}(m_i) + N_1 \cdot f_{bkg}^{HP}(m_i) \right] \tag{5.1}$$

while for the Low Purity (LP):

$$L_{LP} = \prod_{i}^{evts} \left[N_W \cdot (1 - \varepsilon_{HP}) \cdot f_{sig}^{LP}(m_i) + N_2 \cdot f_{bkg}^{LP}(m_i) \right] \tag{5.2}$$

where N_W is the number of all the W bosons in the HP and LP event categories, ε_{HP} is efficiency the of the substructure requirements, N_1 is the number of background events in the HP sample, N_2 is the number of background events in the LP one while m_i is the mass (after jet grooming) of the AK08 jet.

[1] in the jet mass region between 40 GeV and 130 GeV

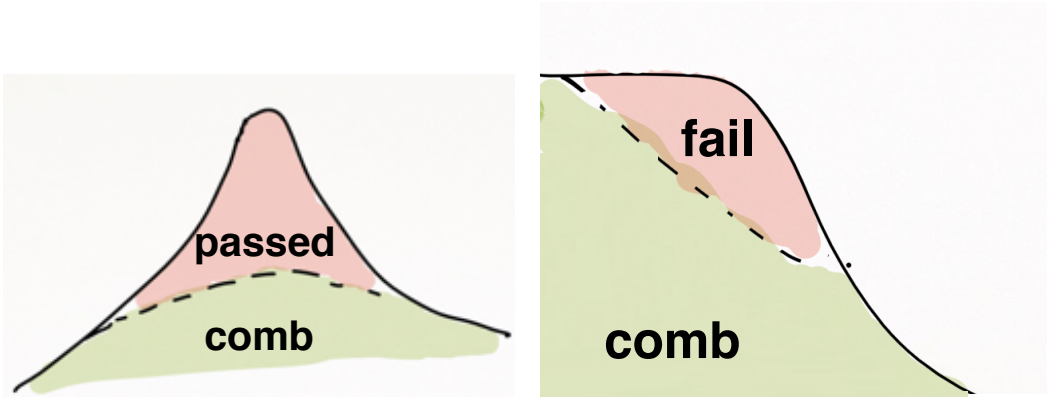

(a) (b)

Figure 5.6: High Purity (a) and Low Purity (b) graphical representation. In both categories, the signal called "passed" (in red) and the background called "comb" (in green) are reported

The signal function f_{sig} is a parametric function optimized to describe the signal mass distribution and which has been determined with generator-level studies in Sec. 5.5.2. The function presents a gaussian core (defined by a mean value μ and a standard deviation σ) and non-gaussian tails on both sides.
The background function f_{bkg} describe the background of the analysis coming from diboson (ZZ or WW) events or single-top production as well as the combinatorial background coming from the $t\bar{t}$ process itself where the hadronic W is not well reconstructed. As the signal function, f_{bkg} is further discussed in Sec. 5.5.2.
Compared to previous results in the CMS collaboration, in this analysis we introduce a new procedure for the extraction of the parameters of interest (jet mass scale μ, jet mass resolution σ and the efficiency of substructure requirement on τ_{21} ε) divided into two steps:

1. fit to W-enriched category (HP) to extract μ and σ of the W mass distribution
2. simultaneous fit to both categories (HP and LP), after fixing μ and σ parameters to the values found in first fit to extract only the efficiency of the τ_{21} requirement

the procedure can be performed for any value of the τ_{21} selection.
This two-step fitting method, has been proved to be more stable with respect a single simultaneous fit in which μ and σ of the mass distribution and the efficiency of the τ_{21} selection are extracted in a single step. A check on the method stability is shown in Sec. 5.6.
The two-step fit is performed for two different values of the τ_{21} observable and five different values of x as reported in Tab. 5.2. These corresponds to different jet substructure selections ("working points" or WP in the following) used by various searches for new physics in CMS which have boosted Z/W bosons in the final state.

Variable	Jet Mass	Working Point
CHS τ_{21}	Pruned	0.45
CHS τ_{21}	Pruned	0.6
Puppi τ_{21}	Puppi+Softdrop	0.35
Puppi τ_{21}	Puppi+Softdrop	0.4
Puppi τ_{21}	Puppi+Softdrop	0.55

Table 5.2: Working Point for τ_{21} selection used in various CMS analyses

5.5.1 Generator level matching for signal and background events

The composition of the final events selected can be divided into two types. Events coming from $t\bar{t}$ production, with an isolated, boosted, fully reconstructed hadronic W and events in which the leading AK8 jet is not the W-signal or badly reconstructed (b-jet contamination, grooming reconstruction failure, ...).
We define signal events, W bosons decaying to hadrons, isolated from other jet activity in the event. We therefore use the MC truth information to identify the reconstructed W boson candidates which are associated with a generator level W that decays into quarks (called "matched" in the following). The selection used to identify "matched" events is reported in Tab. 5.3.

	Selection
W matching	$\Delta R(W_{gen}, AK08_{reco}) < 0.1$
b cleaning	$\Delta R(bquark_{gen}, AK08_{reco}) > 0.8$

Table 5.3: Generator Selection

The jet mass distributions for all events and events passing the matching conditions are shown in Fig. 5.7(a), 5.7(b). As can be seen, the distribution of reconstructed Ws "matched" with a generated W have less tails with respect to the distribution without any generator matching requirements.

The events that we want to study at generator level, from which we will extract important parameters for the fit, will need to be cleaned from any other jet in the event, like the b-tagged one. So, the reconstructed AK08 is not only associated with a real generated W, but also away from other contributions of the event.

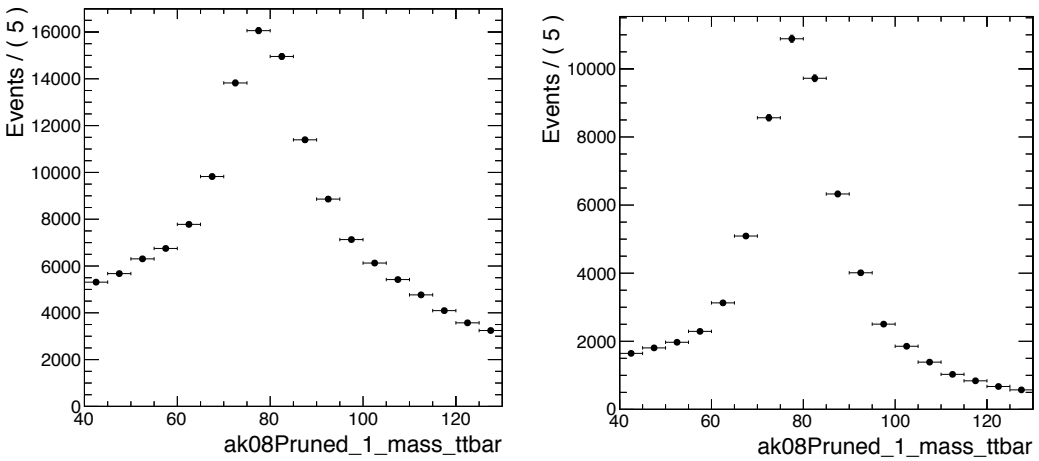

(a) (b)

Figure 5.7: Pruned jet mass distribution of leading AK8 jets passing the full selection (a) and matched with an isolated generator level W (b)

5.5.2 Fit functions definition

In the previous Section we identified the mass distributions for the signal and the background components. Here we study a parametrisation to describe them.
In this method a single function is used to describe the signal and another one to describe the background (both the combinatorial and the one coming from other processes).
The empirical functions used to fit the signal and the whole background component are listed in the following.

Signal Template We model the signal with a Double Crystal Ball. The functional form is the same for HP and LP categories (although the fitted parameters can be different) and is reported below:

$$f_{sig}(m) = \left(\frac{n}{\alpha}\right)^n e^{-\frac{\alpha^2}{2}} \left(\frac{n}{\alpha} - \alpha - \alpha\right)^{-n} \tag{5.3}$$

with $\alpha = (x - \mu)/\sigma$. In Fig. 5.8(a) - 5.9(b), the Double Crystal Ball for "matched" events (of two different WPs) are shown. For the final fit, its tails are kept constant and fixed to the MC truth value. Similar fits are performed for all the τ_{21} working points considered.
To reduce the number of fit parameters for the double crystal ball functions in the simultaneous fit, the μ and σ variables of the Low Purity function are constrained to the High Purity ones following this equation:

$$z_{LP} = k_{HP-LP} \cdot z_{HP} \tag{5.4}$$

where z stands for μ or σ and the k_{HP-LP} is obtained fitting the MC events distribution for AK08 associated with generated W.

All the values of the k_{HP-LP} are listed in Tab. 5.4.

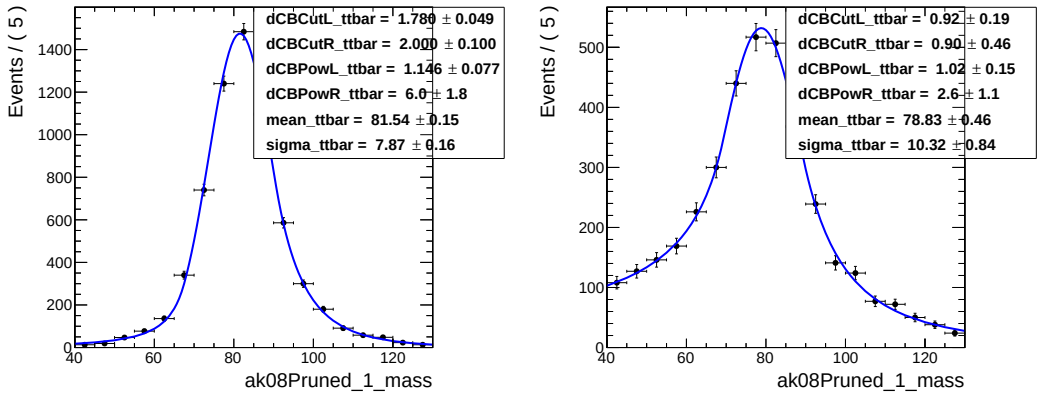

(a) (b)

Figure 5.8: Pruned jet mass distribution of HP (a) and LP (b) matched events (CHS WP 0.45)

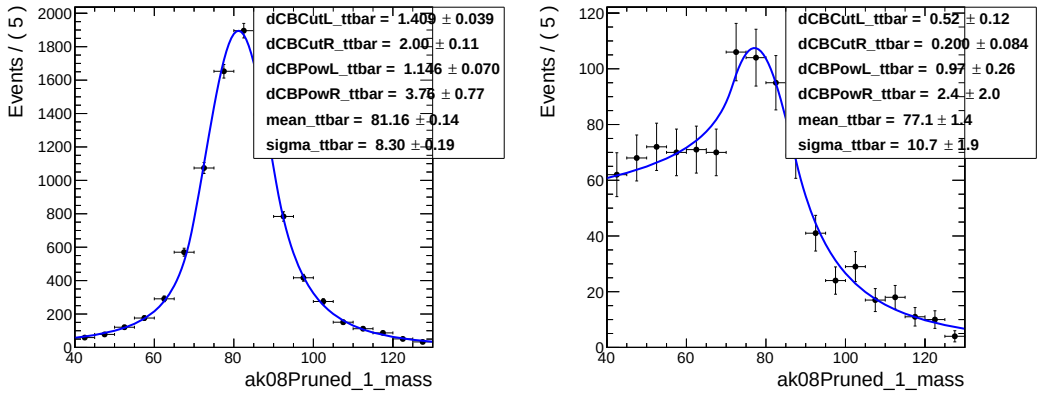

(a) (b)

Figure 5.9: Pruned jet mass distribution of HP (a) and LP (b) matched events (CHS WP 0.6)

From the fit to the matched MC distribution we not only extract the tails of the Double Crystal Ball distribution, but also the ratio for μ and σ between the High Purity and Low Purity fit result. The values extracted are summarized in Table 5.4 while the fits from which the parameters are obtained are shown in Figure 5.8(a) − 5.9(b) for two example of τ_{21} working points..

Background Template For the High Purity categories, the function used to fit the background component is always a Chebyshev of the second order. For high WPs (meaning 0.6 for CHS τ_{21} and 0.55 for PUPPI τ_{21}), the function

Working Point	Variable	k_{HP-LP}
CHS (0.45)	μ	0.96
CHS (0.45)	σ	1.31
CHS (0.6)	μ	0.94
CHS (0.6)	σ	1.28
Puppi (0.35)	μ	0.95
Puppi (0.35)	σ	1.36
Puppi (0.4)	μ	0.94
Puppi (0.4)	σ	1.28
Puppi (0.55)	μ	0.94
Puppi (0.55)	σ	1.36

Table 5.4: μ and σ Ratio Results

used to describe the background in the LP region is:

$$f_{bkg}^{LP}(x) = e^{c_0 x} \tag{5.5}$$

In the low WP, the shape of the background is very deformed and presents a turn-on behaviour (as shown in the Fig. 5.10(a)). In this case, a simple descending exponential function cannot be used. For low WPs (meaning 0.45 for CHS τ_{21} and 0.35/0.4 for PUPPIτ_{21}), the function that describes better the background is:

$$f_{bkg}^{LP}(x) = e^{c_0 x} \cdot \frac{1 + Erf\left(\frac{(x-a)}{b}\right)}{2} \tag{5.6}$$

where "Erf" is the known *Error Function*.
The background (meaning the unmatched part of the events coming from the $t\bar{t}$ and single top samples and the events coming from the other MC datasets) distributions for the LP categories, are reported in Figure 5.10(a), 5.10(b).

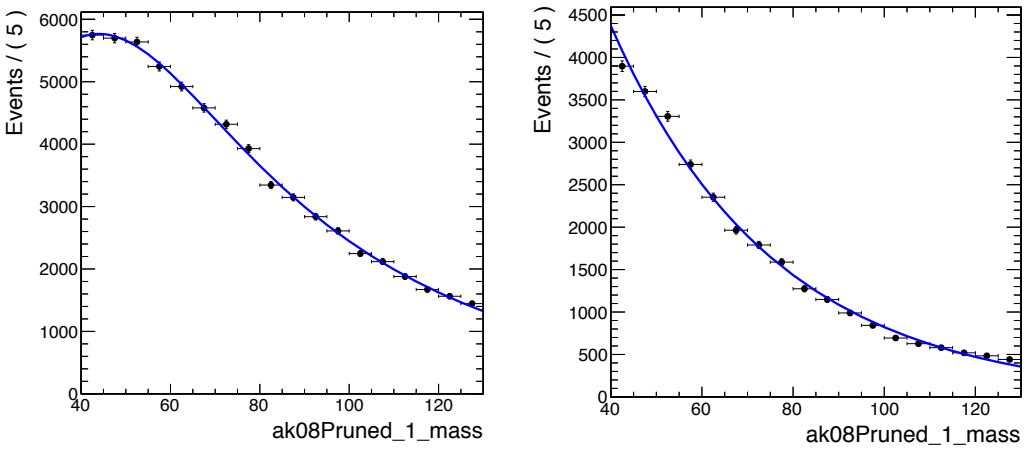

(a) (b)

Figure 5.10: Pruned jet mass distribution of LP (CHS WP 0.45) (a) and LP (CHS WP 0.6) (b) unmatched events

5.6 Validation of the fit method with toy MC datasets

In this Section we describe a study performed to verify the stability of the fit method with the usage of toy MC datasets.
The toys have been generated from the function obtained fitting the MC distributions for different Working Points (the dashed line in Fig. 5.12(a) – 5.13(b)). For each toy distribution, the two-step fit procedure procedure has been performed and the values for μ, σ and N-Subjettiness efficiency have been extracted from independent fits.
In order to test the presence of a bias in the extraction of fit parameters, we define for each toy the pull variable as:

$$pull_z = \frac{fit_z - ref_z}{fitError_z} \tag{5.7}$$

where z is one of the parameters of interest , the fit_z is the fitted value of the variable while the *reference* is the value obtained from the function used to generate the toys. The ref$_z$ represents the "true" value in this test to which the fitted values have been compared.
In Fig. 5.11(a) - 5.11(c) are reported the pull distributions for μ, σ and the N-Subjettiness efficiency calculated with Eq. 5.7 and a gaussian fit superimposed. As can be seen, the results confirm that the method is robust and describe well the toy MC datasets. The pull distributions are centered in 0 with a standard deviation of about 1 (meaning that no biases are present in the fit).

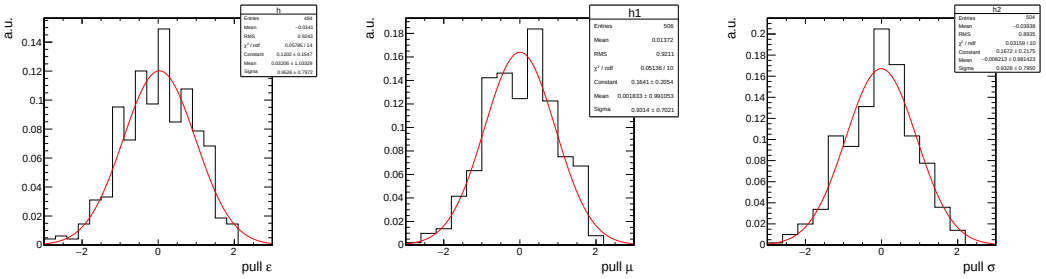

(a) (b) (c)

Figure 5.11: Pull distribution for the efficiency (a), μ (b) and σ (c) value

5.7 Systematic Uncertainties

The final results (discussed in Sec. 5.8 of this study consists in a set of scale factors for τ_{21} efficiency, jet mass scale and jet mass resolution. The systematic uncertainties on each measurement takes into account the differences in the signal shape introduced by the MC generator used (in this case POWHEG+PYTHIA) and the choice of the signal fit function. Leading systematic effects are due to the simulation of the parton showering (which is handled differently by other MC generator such as HERWIG) used to derive the data/MC scale factors. To evaluate this component we compared the scale factors obtained from the $t\bar{t}$ PYTHIA dataset with the ones obtained using the HERWIG dataset for each Working Point. They quantify the discrepancy between the jet substructure modeling of PYTHIA and HERWIG. The second source of systematics is connected to the choice of the signal fit model. Although, after the generator level studies, the Double Crystal Ball distribution seems to describe well the jet mass signal peak, we repeat the fit with two different signal template models. In the default model, the signal is described by a Double Crystal Ball. In the alternative model, the signal is described by a single Gaussian distribution with the background function absorbing the signal component of the tails. Systematic uncertainties associated to lepton identification, b-tagging and E_{Tmiss} scale are negligible.

5.8 Results

For each working point the two-step fit procedure is performed and the fitted values of jet mass scale, jet mass resolution and N-Subjettiness efficiency are obtained. The data-MC scale factors are computed from the ratio of the fitted values derived from data and simulation.
In Fig. 5.12(a)-5.13(b), the functions describing data are shown in continuous line while the dashed style is used for the MC. The green lines are referred to the background contribution, the red ones are the signal (the Double Crystal Ball function fitting the signal core) while the blue distributions are the sum of the red and the green ones. The coloured histograms represents the different

MC background components.

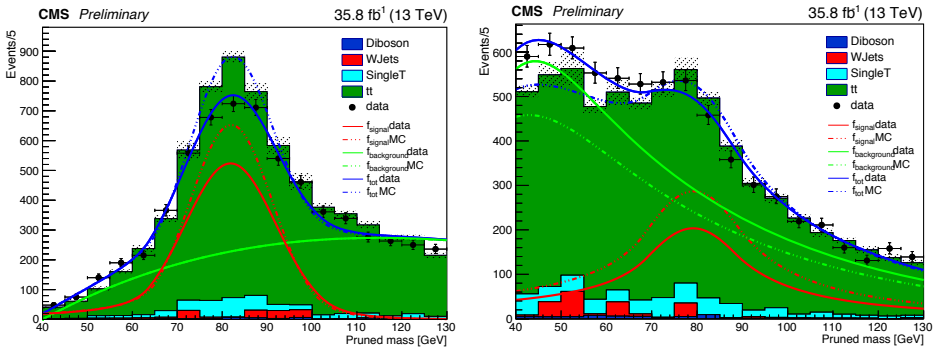

(a) (b)

Figure 5.12: CHS fit results for WP=0.45 High Purity (a) and Low Purity (b) categories

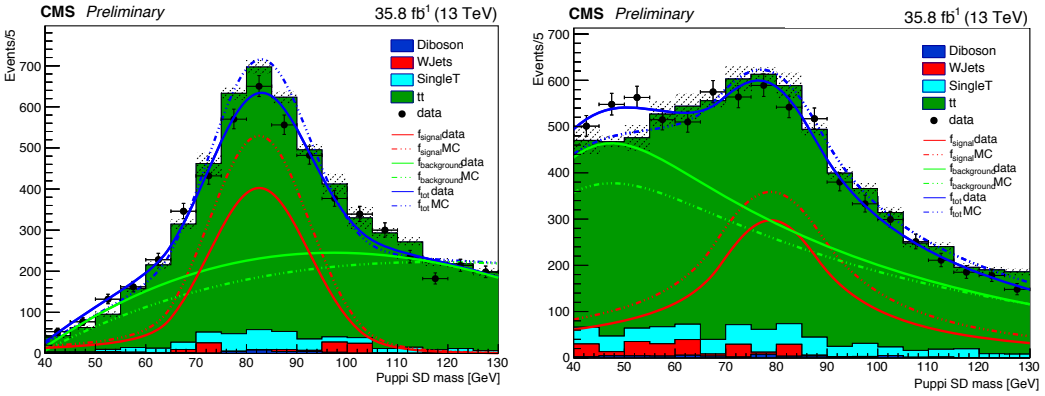

(a) (b)

Figure 5.13: Puppi fit results for WP=0.35 High Purity (a) and Low Purity (b) categories

The results for all the Working Points are reported in Tab. 5.5 (for the CHS+pruning selections) and Tab. 5.6 (for the PUPPI+softdrop selections). The central value is taken from the results of the fit while the uncertainties quoted are referred to the statistical fit error, to the MC showering program (PYTHIA or HERWIG) uncertainties and to the signal fitting function (Double Crystal Ball or Gauss) uncertainties.

For the first time in the CMS collaboration, these SF have been extracted for the PUPPI+Softdrop algorithm.
The τ_{21} efficiency SF and the μ SF are close to 1, while the jet mass resolution (σ) is $\sim$10% worst in data with respect to MC. The uncertainties on the τ_{21} efficiency are still dominated by the statistics and are of the order of 5-10%.

Variable	Data/MC Scale Factor
τ_{21} WP = 0.45	
ε	1.00 ± 0.06 (stat) ± 0.06 (syst) ± 0.03 (syst)
μ	1.007 ± 0.009 (stat) ± 0.005 (syst) ± 0.002 (syst)
σ	1.15 ± 0.04 (stat) ± 0.03 (syst) ± 0.02 (syst)
τ_{21} WP = 0.6	
ε	1.08 ± 0.06 (stat) ± 0.05 (syst) ± 0.05 (syst)
μ	1.005 ± 0.005 (stat) ± 0.006 (syst) ± 0.005 (syst)
σ	1.12 ± 0.03 (stat) ± 0.02 (syst) ± 0.04 (syst)

Table 5.5: Data/MC scale factors results for CHS (central value ± stat.err. ± MC showering systematics ± signal shape systematics)

Variable	Data/MC Scale Factor
Puppi τ_{21} WP = 0.35	
ε	0.99 ± 0.05 (stat) ± 0.03 (syst) ± 0.04 (syst)
μ	0.999 ± 0.009 (stat) ± 0.03 (syst) ± 0.02 (syst)
σ	1.06 ± 0.03 (stat) ± 0.09 (syst) ± 0.08 (syst)
Puppi τ_{21} WP = 0.4	
ε	1.01 ± 0.06 (stat) ± 0.02 (syst) ± 0.04 (syst)
ε_{LP}	0.97 ± 0.07 (stat) ± 0.02 (syst) ± 0.04 (syst)
μ	0.998 ± 0.007 (stat) ± 0.006 (syst) ± 0.001 (syst)
σ	1.08 ± 0.02 (stat) ± 0.03 (syst) ± 0.08 (syst)
Puppi τ_{21} WP = 0.55	
ε	1.04 ± 0.02 (stat) ± 0.03 (syst) ± 0.02 (syst)
μ	0.996 ± 0.004 (stat) ± 0.009 (syst) ± 0.002 (syst)
σ	1.08 ± 0.02 (stat) ± 0.03 (syst) ± 0.08 (syst)

Table 5.6: Data/MC scale factors results for Puppi (central value ± stat.err. ± MC showering systematics ± signal shape systematics)

Chapter 6

Zγ/Wγ Analysis

This Chapter is focused on the search for new resonances decaying to $Z\gamma$ and $W\gamma$ in the final state with one reconstructed jet from the boosted Z/W decay and one isolated photon. In Sec 6.1, the description of the general analysis strategy used to search for a peak in the jet+γ invariant mass spectrum is presented. In the Sec. 6.1 - 6.8 the $Z\gamma$ analysis which has been completed in summer 2017 is described; it is expected to be published in early 2018. In Sec. 6.1, 6.3 and 6.4 the data and MC samples used, the trigger and the event selection are discussed. This part is in common with the $W\gamma$ search. The background estimation for the analysis which is obtained from a fit to the jet-photon mass spectrum of data is presented in Sec. 6.5 while in Sec. 6.6 the $Z\gamma$ signal shapes and efficiencies are introduced. Section 6.7 is focused upon the systematic uncertainties of this analysis. Finally the results of the search for $Z\gamma$ resonances are presented in Sec. 6.8. In the last part of this Chapter an extension of the baseline $Z\gamma$ analysis is discussed. The new analysis strategy exploits the similarities between $Z\gamma$ and $W\gamma$ final state with the Z/W bosons decaying into hadrons. Selected events are divided in independent categories depending on the jet mass, the presence of jets originated from b-quarks and requirements on the jet sub-structure. The possible signal from resonances decay is looked simultaneously in all the event categories, making the analysis sensitive to both $Z\gamma$ and $W\gamma$ signal models within the same analysis framework. Finally the results of $Z\gamma$ and $W\gamma$ searches obtained with the new combined fit to all categories are presented.

6.1 Analysis Strategy

We search for both Zγ and Wγ resonances in final states with a wide jet (coming from the decay of the boson) and an isolated photon. The Z/W boson, coming from a high-mass resonance decay is highly boosted, thus its decay products are close in $\eta - \phi$ space and can be reconstructed as a single entity. In this analysis wide jets reconstructed with the anti-kt algorithm with distance parameter R=0.8 (indicated in the following as AK08 jets) are used

to collect the hadronization products of the quarks coming from the boson decay. Due to this merging process, the interesting AK08 jets for this analysis have an internal structure that can be used to discriminate them from the hadronization products of gluons or quarks which represent the background. The τ_{21} observable (described in Sec. 4.13) is used to identify the two-prong structure of a boson-jet (a jet coming from the boson decay) and the pruned jet mass is used to select jets compatible with the the Z/W mass.
The presence of a resonance signal is determined by searching for a narrow peak in the invariant mass distribution of the jet and the photon, corresponding to the resonance mass. The background is estimated directly on data by fitting the jet-photon mass spectrum with a smooth parametrisation which describe well the main SM backgrounds coming from γ+jet and QCD multijet events.

6.2 Analysis Samples Zγ

The focus of this analysis is to isolate a sample of γ+Jets events from the single photon dataset recorded by the CMS detector.

6.2.1 Data samples

The data used in this search correspond to an integrated luminosity of almost 36 fb^{-1} recorded by the CMS experiment at $\sqrt{s}$=13 TeV in 2016. The high instantaneous luminosity delivered by the LHC resulted in a large number of additional interactions in the same or neighboring bunch crossings (pileup) as the hard-scattering interaction. The average number of pileup interactions in the 2016 data was 27.

6.2.2 MC samples

Simulated background samples do not enter in the analysis directly, as the background is obtained from a fit to data, but have been used to assess the accuracy of the background model and to optimize the event selection. The dominant γ+jets and QCD multijet, as well as sub-dominant hadronically decaying W/Z+jets backgrounds have been generated at LO with MADGRAPH5 AMC@NLO 2.3.3 generator [78, 79]. All background samples are interfaced with PYTHIA for the description of fragmentation and hadronization.
All simulated samples were produced using NNPDF3.0 [80] parton distribution functions (PDFs), processed with the full CMS detector model based on GEANT4 [81] and reconstructed with the same suite of programs as used for collision data. The pileup effects are taken into account by superimposing minimum bias events on the hard scattering interaction, with the multiplicity distribution matching that in data.
Due to the way the samples are generated, there is an overlap between events

of the inclusive QCD and γ+Jets samples. It is dividing the sample in events with "prompt photons" and "direct prompt photons" following:

- prompt γ: photons coming directly from the proton-proton interaction. The remaining photons are classified as "non-prompt"
- direct prompt γ: are defined as prompt photons with $\Delta R > 0.4$ with respect to any quarks or gluons in the event coming from the main interaction. The remaining prompt photons are classified as "fragmentation"
- from the γ+Jets samples, only events with direct prompt γ are taken, while from the QCD samples, events with direct prompt γ are rejected, therefore, in the latter samples, only events with non-prompt or fragmentation γ are accepted

The γ+jets events are then corrected using NLO/LO k-factors extracted by the generator level distribution of the same process computed with the two different loop order.
Moreover, Pile Up-reweighting is also to be taken into account and it is done with a Minimum Bias data sample which has a cross-section of $\sigma_{\text{MinBias}} = 65$ mb as the Pile Up profile of the generated sample is slightly different with respect to the LHC one.

Dataset	Generator	Cross section σ x $k^{\frac{\text{NLO}}{\text{LO}}}$[pb]
γ+Jets with momentum in [100 GeV, 200 GeV]	MadgraphMLM+Pythia	9201
γ+Jets with momentum in [200 GeV, 400 GeV]	MadgraphMLM+Pythia	2300
γ+Jets with momentum in [400 GeV, 600 GeV]	MadgraphMLM+Pythia	277.4
γ+Jets with momentum in [600 GeV, Inf GeV]	MadgraphMLM+Pythia	93.38
QCD with momentum in [300 GeV, 500 GeV]	MadgraphMLM+Pythia	347700
QCD with momentum in [500 GeV, 700 GeV]	MadgraphMLM+Pythia	32100
QCD with momentum in [700 GeV, 1000 GeV]	MadgraphMLM+Pythia	6831
QCD with momentum in [1000 GeV, 1500 GeV]	MadgraphMLM+Pythia	1207
QCD with momentum in [1500 GeV, 2000 GeV]	MadgraphMLM+Pythia	119.9
QCD with momentum in [2000 GeV, Inf GeV]	MadgraphMLM+Pythia	25.24
W+Jets→QQ+Jets inclusive sample	MadgraphMLM+Pythia	3373
DYJets→QQ+Jets inclusive sample	MadgraphMLM+Pythia	1460

Table 6.1: MC datasets used in the analysis

6.2.3 Signal samples

Simulated signal samples of spin-0 resonances decaying to $Z\gamma \to qq + \gamma$ are generated at leading order (LO) using PYTHIA 8.205 [82] with the CUETP8M1 [83, 84] underlying event tune with masses ranging up to 4 TeV and a width of 0.014% of the resonance mass which is much less than the detector resolution. For the $W\gamma \to qq + \gamma$ the Madgraph package has been used as it has been found to describe better the process. The mass range covers up to 4 TeV and

the samples have been tuned with the CUETP8M1 as the Zγ samples with a width of 0.014% of the resonance mass.

6.3 Trigger

The analysis is carried out with events recorded by logical OR of several triggers that impose requirements on either the scalar sum of transverse energies of all reconstructed jets in an event (HT), with HT > 800–900 GeV or a photon candidate with p_T > 165–175 GeV and $|\eta| < 2.5$.
The complete list is reported below:

- HLT_Photon175: at least one photon with $p_T > 175$ GeV and $|\eta| < 2.5$
- HLT_Photon165 at least one photon with $p_T > 165$ GeV and $|\eta| < 2.5$
- PFHT800: scalar sum of transverse energies of all reconstructed jets in an event, with HT > 800 GeV
- PFHT900: scalar sum of transverse energies of all reconstructed jets in an event, with HT > 900 GeV

The trigger efficiency for the OR of the single photon triggers as function of the γ-jet invariant mass is shown in Fig. 6.1. The efficiency numerator is defined as the number of events passing the selection (reported in Sec. 6.4, but without the requirements on the jet mass) and the trigger under study, while the denominator is defined as the number of events passing the same selection and a looser trigger requirement. As can be seen in Fig. 6.1, the trigger efficiency has a significant drop at high p_T in one of the data taking period. This has been caused by a mis-configuration of L1EG (level-1 trigger for photons and electrons) that affects the first 4 fb^{-1} data of 2016 dataset (labelled as RunB in the figure).

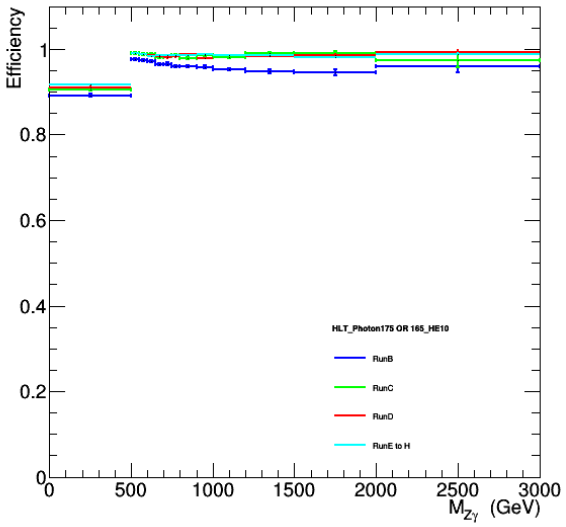

Figure 6.1: Single photon triggers efficiency divided per era

In order to avoid this issue with L1 electromagnetic triggers, jet trigger are then used together with the photon trigger to recover this inefficiency at high mass/high photon p_T.
In Fig. 6.2(a), the turn on curves of the three jet trigger is shown; it relies on different L1 seeds compared to the photon triggers. In this case, no inefficiency is observed at high mass.

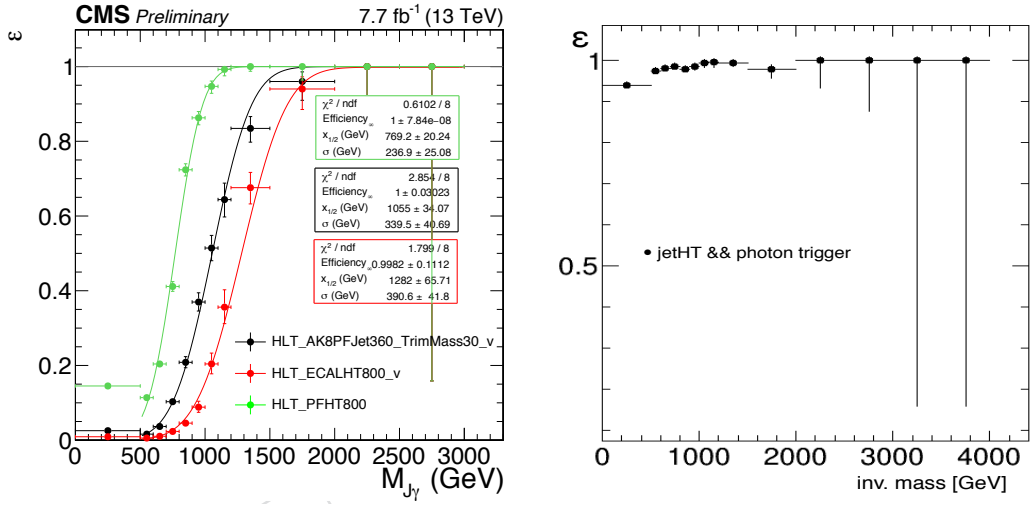

(a) (b)

Figure 6.2: Jet triggers efficiency ε (a) and trigger efficiency ε of the combined Jet+Photon bits (b) as a function of the jet+photon invariant mass

The efficiency loss, is recovered by PFHT800 triggers for mass above 1 TeV as expected and shown in Fig. 6.2(b).
The trigger is considered fully efficient from 650 GeV (of the jet+γ invariant mass) where the analysis begins.

6.4 Physics Objects and Event Selection

The events are required to contain at least one reconstructed primary vertex with at least four associated tracks and its transverse (longitudinal) coordinates are required to be within 2 (24) cm of the nominal collision point. The reconstructed vertex with the largest value of summed physics object p_T^2 is taken to be the hard-scattering (leading) vertex. The physics objects are the objects returned by a jet finding algorithm applied to all charged tracks associated with the vertex, plus the corresponding associated missing transverse momentum.

Photon identification is based on a multivariate analysis (described in Sec. 4.2.2). Photon candidates are required to pass a working point that corresponds to a typical photon reconstruction and identification efficiency of 90% in the photon p_T range used in the analysis.

Large-cone jets are used to reconstruct hadronically decaying Lorentz-boosted V boson (where V stands for Z or W) candidates in the event. Jets are reconstructed from PF candidates clustered using the anti-kT algorithm (described in Sec. 4.7.1) with a distance parameter of 0.8. Charged hadrons not originating from the primary vertex are not considered in the jet clustering. Corrections based on the jet area are applied to remove the energy contribution of neutral hadrons from pileup interactions. The energies of the jets are further corrected for the response function of the calorimeter (see Sec. 4.9).

Additional quality criteria are applied to jets (described in Sec. 4.10) in order to remove rare spurious noise patterns in the calorimeters and also to suppress leptons misidentified as jets. Jets are required to have $p_T > 200$ GeV and $|\eta| < 2.0$. The requirement on the jet η suppresses the background from γ+jets and QCD multijet events and ensures that the core of the jet is within the tracker volume of the CMS detector ($|\eta| < 2.5$). The latter requirement is important for subsequent b quark jet tagging.

On the other hand, the photon candidates are required to have $p_T > 200$ GeV, to be within the barrel fiducial region of the detector ($|\eta| < 1.44$) and pass the MVA photon ID requirements (discussed in Sec. 4.2.2). Events with a photon reconstructed in the endcap region suffer from high γ+jet background and do not add to the sensitivity of the analysis; therefore they are not considered. Photon candidates in the event are required to be separated from large-radius jets by a distance of $\Delta R > 1.1$.

To identify the V boson candidates, the reconstructed large-radius jet mass, evaluated after applying a jet pruning algorithm (described in Sec. 4.12.1), is used. The jet pruning reclusters the jet constituents and eliminates soft, large-angle QCD radiation, which increases the mass of the jet. The pruned jet mass (M_{pruned}) is corrected with the same factor as the one used to correct the jet momentum. For the Zγ signal selection, a pruned jet mass[1] for a Z candidate to be between 65 and 105 GeV is required.

Finally, a requirement on the photon p_T with respect to a reconstructed Vγ

[1] A different selection will be made in Sec. 6.10 when the combined Wγ and Zγ analysis is described

mass is imposed: $p_T/M_{V\gamma} > 0.34$. Here $M_{V\gamma}$ is defined as the invariant mass of the massive jet and the photon. The search starts from 650 GeV in the $M_{V\gamma}$ spectrum due to trigger requirements.
To further discriminate against the QCD multijet and direct photon backgrounds, the events are categorized according to the likelihood of a large-radius jet to contain b quark fragmentation products. In order to do so, in the analysis a subjet b-tagging selection is implemented and is used as well as the N-subjettiness selection. The N-subjettiness observable measures the distribution of jet constituents relative to candidate subjet axes in order to quantify how well the jet can be divided into N subjets. Subjet axes are determined by a one-pass optimization procedure, which minimizes N-subjettiness. As already mentioned in Sec. 4.13, $\tau_{21} = \tau_2/\tau_1$ offers an excellent separation between the QCD jets and jets from vector boson decays, which tend to have lower τ_{21} values than the former.
If an event contains a b-jet candidate, it is classified as "b tagged" (the study for the optimal cut is reported in Appendix D.5). For the rest of the events, if the large-radius jet has $\tau_{21} < 0.45$, we classify the event as "τ_{21} tagged". Otherwise the event is assigned to the "anti-τ_{21}" category. These three categories are mutually exclusive and are statistically combined at the end.

6.4.1 Data/MC distributions

In this analysis, the final result is completely disentangled from the MC distributions and uses only the data recorded by the experiment. However, in this Section, the comparison between data and background MC is reported. This exercise has been carried to ensure that no particular errors has been done through the analysis and that the data behaviour are comparable with the MC expectation (unless resonances are present).
Figures 6.3 and 6.4 show the distributions of AK08 jet p_T an η and γ p_T, η after the selection requirements described in Sec. 6.4 (without the jet mass requirements). This test is common for the $Z\gamma$ and the $W\gamma$ analyses. In all cases a good agreement is observed between data and MC prediction.

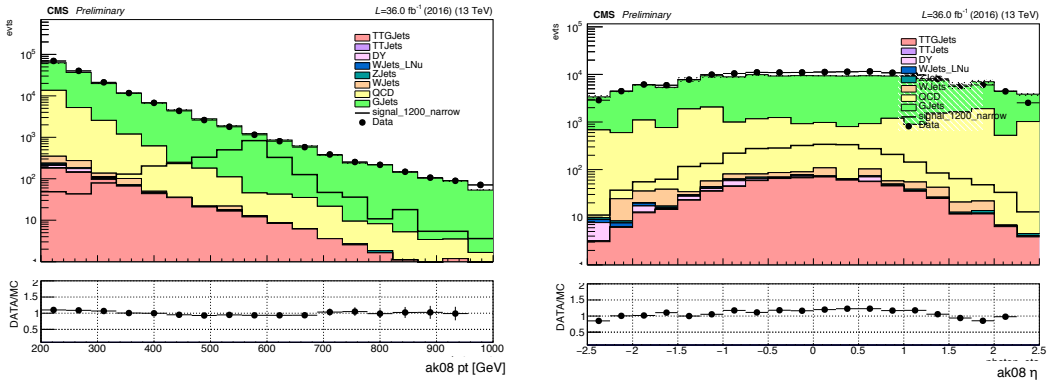

(a) AK8 jet p_T (b) AK8 jet η

Figure 6.3: Data/MC comparison in the preselection for the AK8 jet kinematic variables with a 1.2 TeV Wγ signal superimposed. The p_T has been already reweighted for the γ+Jets scale factors

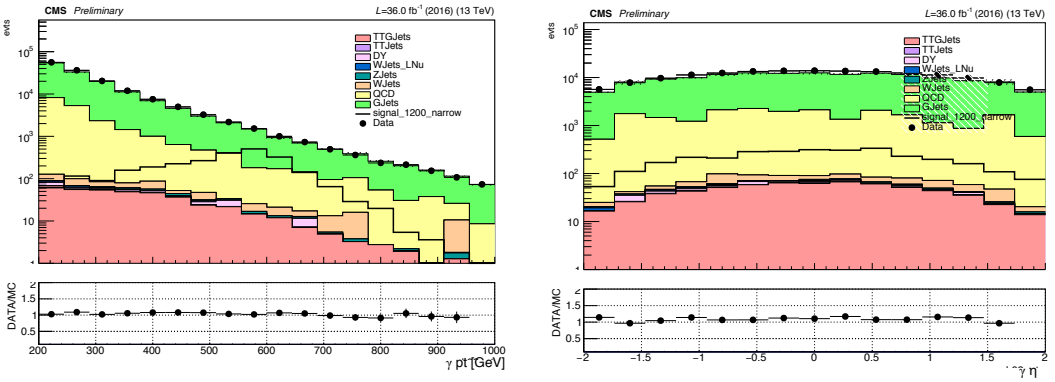

(a) γ p_T (b) γ η

Figure 6.4: Data/MC comparison in the preselection for the γ kinematic variables with a 1.2 TeV Wγ signal superimposed. The p_T has been already reweighted for the γ+Jets scale factors

6.5 Background modeling

This Section is focused on the Zγ analysis but the same considerations are also valid for Wγ discussed later.
The background is measured directly in data, through an unbinned maximum-likelihood fit to the observed $M_{Z\gamma}$ distributions, separately in each category. The background is parametrized with an empirical function. Before looking at the data in the signal region, various families of functions to model the background shape have been tested using the lower jet mass sideband. The

optimal function used is:

$$\frac{dN}{dM_{Z\gamma}} = P_0 \times \left(M_{Z\gamma}/\sqrt{s}\right)^{P_1+P_2 log\left(M_{Z\gamma}/\sqrt{s}\right)} \tag{6.1}$$

where $\sqrt{s}$ is the center of mass energy of 13 TeV, P_0 is the normalization parameter while P_1 and P_2 describe the shape of the invariant mass spectrum.

6.5.1 Bias test for background fit

To evaluate the accuracy and performance of the function used to fit the background data a bias test has been done in the sideband of the Vγ mass spectrum using the three categorization model and the Z signals.
The M_{pruned} sideband in data is: 50 GeV $< M_{pruned} <$ 70 GeV. The sideband definition has been chosen so that it closely resembles the behavior of kinematic variables in the signal region and the yield obtained in the sideband is normalized to the one in the signal region, preventing any introduction of biases from using the signal region to test the fit functions.
The mass shape of the continuum background is fitted with the dijet mass function of the second order reported in Eq. 6.1. The fit function has been chosen among others (Eq. 6.2, 6.3, called "atlas" and "vvdijet" in the following plots).

$$\frac{dN}{dM_{Z\gamma}} = P_0 \times \frac{\left(1-(M_{Z\gamma}/\sqrt{s})^{\frac{1}{3}}\right)^{P_1}}{(M_{Z\gamma}/\sqrt{s})^{P_2}} \tag{6.2}$$

$$\frac{dN}{dM_{Z\gamma}} = P_0 \times \frac{\left(1-(M_{Z\gamma}/\sqrt{s})^{P_1}\right.}{(M_{Z\gamma}/\sqrt{s})^{P_2}} \tag{6.3}$$

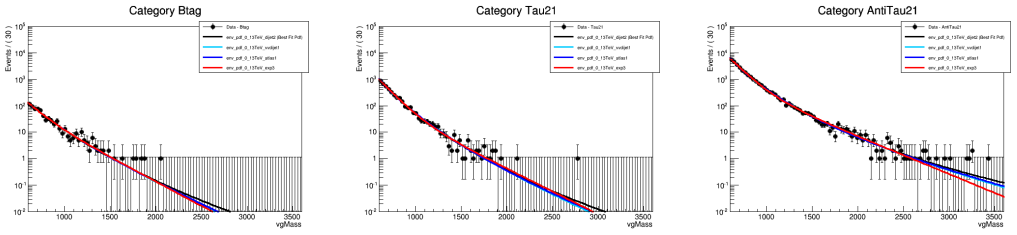

(a) b-tag category (b) τ_{21} category (c) anti-τ_{21} category

Figure 6.5: Fits in the sideband region performed for the bias test in the three categories

The test has been performed in order to check for a presence of a possible systematic bias introduced by the choice of the functional form. In this case, the mass spectra from three sideband regions (50 GeV $< M_{pruned} <$ 70 GeV

sideband divided into the three analysis categories) is fitted with alternate functions. The shapes obtained in these fits are used to generate pseudo-datasets with a total number of events derived from a Poisson distribution with the mean equal to the yields observed in data. Additionally, in a set of pseudo-experiments, a signal with a cross section close to the expected sensitivity is injected. The full spectrum is fitted with the chosen background function plus a signal model, and the signal cross section is extracted. To check the performance for each function, pull distributions for the obtained signal cross sections are constructed. The behaviour of the function in Eq. 6.1 is flat for the all masses studied indicating that no bias is introduced using this particular function.

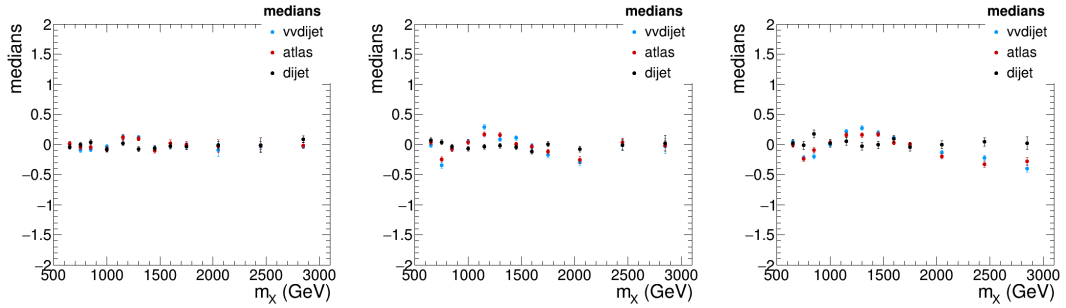

(a) b-tag category (b) τ_{21} category (c) anti-τ_{21} category

Figure 6.6: Bias pulls of the three functions used for different resonance masses

The mass spectra in the three analysis categories with the fit of the three functions superimposed are shown in Fig. 6.5.

6.5.2 Background fit (Zγ analysis)

As first test, we check if the $M_{Z\gamma}$ spectrum in data can be fitted well with a background-only function. The fits for all the 3 categories to the invariant mass of the jet+γ system are reported in Fig. 6.7.

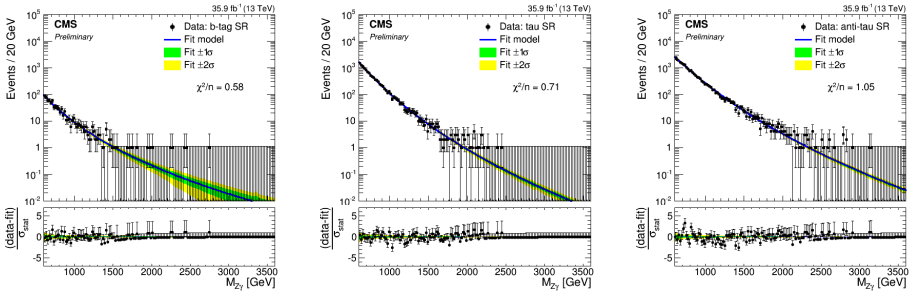

(a) b-tag signal region (b) τ_{21} signal region (c) anti-τ_{21} signal region

Figure 6.7: Observed Z+γ invariant mass spectra for the three categories. The results are shown using the function reported in Eq. 6.1

As can be seen from the plots in Fig. 6.7, no significant excess of data over expected backgrounds is observed.

6.6 Signal shape and efficiency (Zγ analysis)

In this Section the studies of the signal shape and the signal efficiency are described.

6.6.1 Signal shapes

The signal distribution in $M_{Z\gamma}$ is obtained from the generated events that pass the full selection. The signal shape is parametrized with a Gaussian core and two power-law tails, an extended form of the Crystal Ball function.

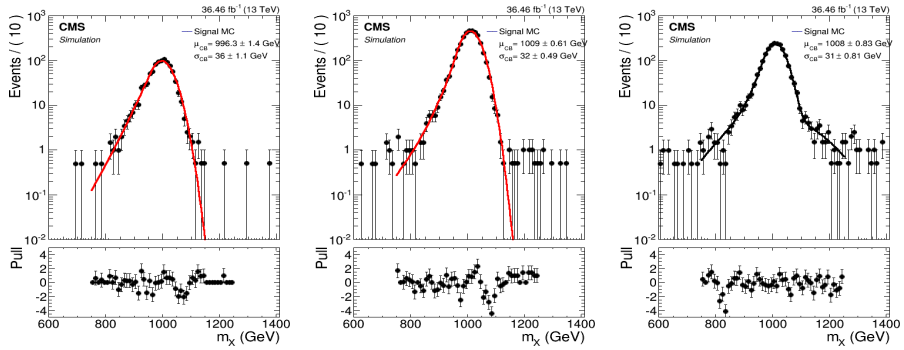

(a) b-tag category (b) τ_{21} category (c) anti-τ_{21} category

Figure 6.8: Fits of signal shape for mass hypotheses 1000 GeV in all categories

Figures 6.8 and 6.9 show the invariant mass of an AK8 jet and a photon for a

mass of 1000 GeV and 2050 GeV. The visible high mass tail cannot be described by a crystal ball function only, but it is well managed by an additional Gaussian function.
To derive the signal shapes for the intermediate mass values where simulation points are not available, a linear morphing of the shapes obtained from the simulation is used.

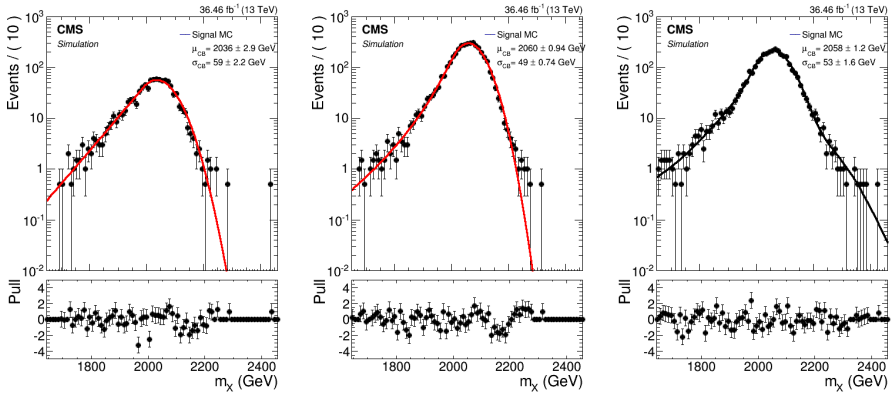

(a) b-tag category (b) τ_{21} category (c) anti-τ_{21} category

Figure 6.9: Fits of signal shape for mass hypotheses 2050 GeV in all categories

6.6.2 Signal efficiency

The signal Acceptance×efficiency (A×ε), defined as the number of signal events passing the full event selection divided by the generated ones, is obtained for all the available signal MC samples and fitted by a third or fourth order polynomial in order to ensure smooth transition between the different mass points. This is shown for the 3 categories in Fig. 6.10.

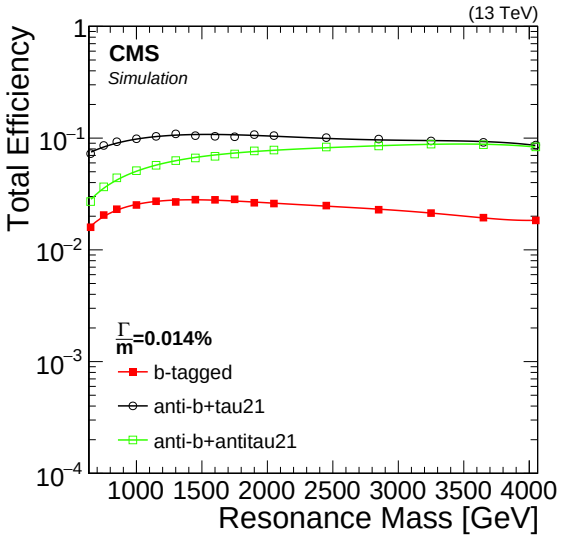

Figure 6.10: Full selection and reconstruction A$\times\varepsilon$ of three analysis categories as a function of the resonance mass

6.7 Systematic uncertainties

The background uncertainty in all channels is dominated by the statistical uncertainty of the background function fit to data.
The following systematic uncertainties in the signal yield are considered:

- integrated luminosity: the uncertainty in the CMS integrated luminosity is based on the cluster counting in the silicon pixel detector and amounts to 2.5%
- PDFs: a 1–3.5% uncertainty in the signal efficiency that takes into account the variation in the kinematic acceptance of the analysis is estimated using replicas of the NNPDF3.0 set
- pileup: the uncertainty due to the pileup description in the signal simulation is evaluated by changing the total inelastic cross section governing the average multiplicity of pileup interactions by ±5% and translates to a 1% uncertainty in the signal acceptance in all channels
- trigger: the uncertainty due to the trigger efficiency differences in data and simulation is about 2% uncertainty covers the variation of the trigger efficiency across the mass range probed in the analysis
- photon efficiency: the systematic uncertainty due to the differences in the photon identification efficiency between data and simulation is evaluated with Z $\rightarrow$ ee events in which the electrons are used as proxies for photons and amounts to 1.5%
- photon energy scale: the photon energy scale is estimated to be known with 1% precision. This takes into account the knowledge of the energy

scale at the Z peak and its extrapolation to higher masses and translates into a 0.1– 2.3% correlated uncertainty in the $M_{V\gamma}$ scale in all six categories

- b tagging efficiency: the uncertainty due to the difference in the b tagging efficiency in data and simulation is estimated from control samples in data and simulation enriched in b quarks and translates into 15–32% uncertainty in the signal yield. It is anticorrelated between the b-tagged and the other two categories, as it induces signal migration between the categories
- τ_{21} tagging efficiency: to account for the difference between the τ_{21} distributions in data and simulation, a scale factor of 0.97 ± 0.06 is introduced for simulated signal samples. This translates into an uncertainty of 10–12% in the signal yield in the τ_{21}-tagged category and is anticorrelated with that in the untagged category.
- jet energy scale (JES), jet mass scale (JMS), jet energy resolution (JER) and jet mass resolution (JMR): the uncertainties are propagated to all the relevant quantities and affect both the signal yield and its shape. The overall effect of these uncertainties added in quadrature corresponds to approximately 5% uncertainty in the signal yield, as determined by changing the four-momenta of the jets accordingly and carrying out the full analysis with the modified quantities.

All the systematic sources are listed in Tab. 6.2.

Systematic source	b-tag	τ_{21}	anti-τ_{21}
Int. luminosity	2.5%	2.5%	2.5%
PDFs	1-3.5%	1-3.5%	1-3.5%
Pileup	1%	1%	1%
Trigger	2%	2%	2%
Photon efficiency	1.5%	1.5%	1.5%
γ scale	2.3%	2.3%	2.3%
b tagging efficiency	15-32%	anticorr.	anticorr.
τ_{21} efficiency	-	10-12%	anticorr.
JES and JER	3.2%	3.2%	3.2%
JMS and JMR	4.1%	4.1%	4.1%

Table 6.2: Summary of the systematics

6.8 Zγ limit results

The observed and expected 95% CL upper limits on the product of signal cross section and branching fraction in the Z channel, $\sigma(X \to Z\gamma)$ for new particles (with a width of 0.014% of the mass of the resonance) in the b-tagged, τ_{21}-tagged and untagged categories are presented in Fig. 6.11. The results based on the combination of the three categories are instead shown in Fig. 6.12. They have been obtained using the combination tool described in [86].

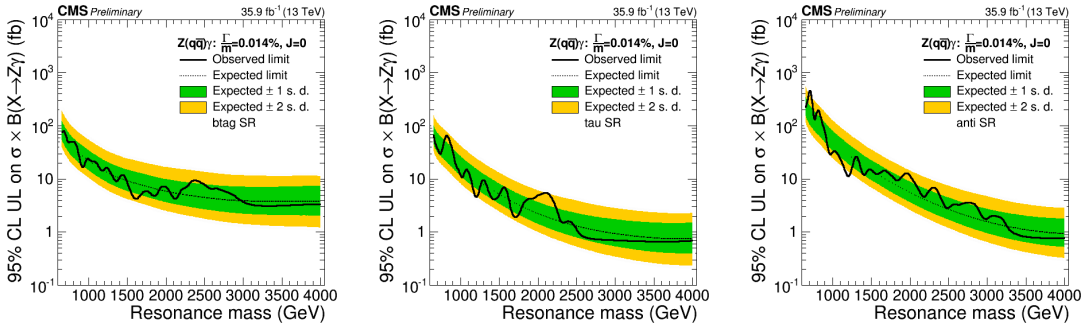

(a) b-tag category (b) τ_{21} category (c) anti-τ_{21} category

Figure 6.11: Expected limits on the narrow spin-0 resonance production cross section times branching fraction $X \to Z\gamma$ for the three categories used in the analysis

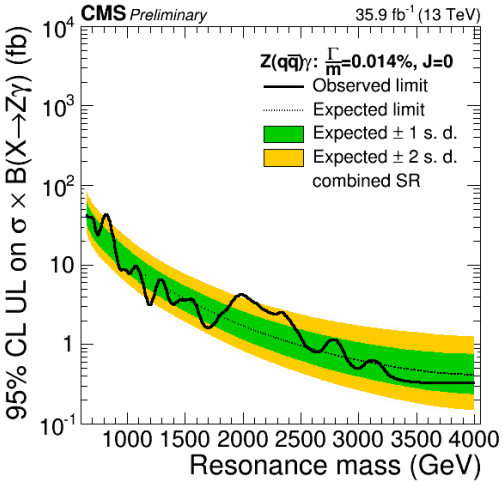

Figure 6.12: Expected limits on the production cross section times branching fraction $X \to Z\gamma$ obtained with the combination of the three categories

6.9 Zγ/Wγ common analysis

The new element introduced in this thesis, compared to previous searches in Zγ/Wγ final states, is a common framework that could be used to analyze separately a Zγ and a Wγ signal (called both in the following Vγ where V stands for a Z or a W boson that decays into hadrons). The selections on the object of this analysis (the jet and the photon) are the same of the Zγ standalone analysis and have already been described in Sec. 6.4 while here, only only the additional requirements and the final division of the events in categories are discussed.
The mass of the two bosons is very close; the Z peak is around 90 GeV, while the W is about 10 GeV lighter (as shown in Fig. 6.13). Introducing a mass selection between these two peaks will permits to discriminate between a signal coming from a Zγ resonance and a signal coming from a Wγ resonance. Therefore, the three categories presented in Sec. 6.4 are splitted into two mass regions having a total of 6 categories which are reported in Tab. 6.3. The same

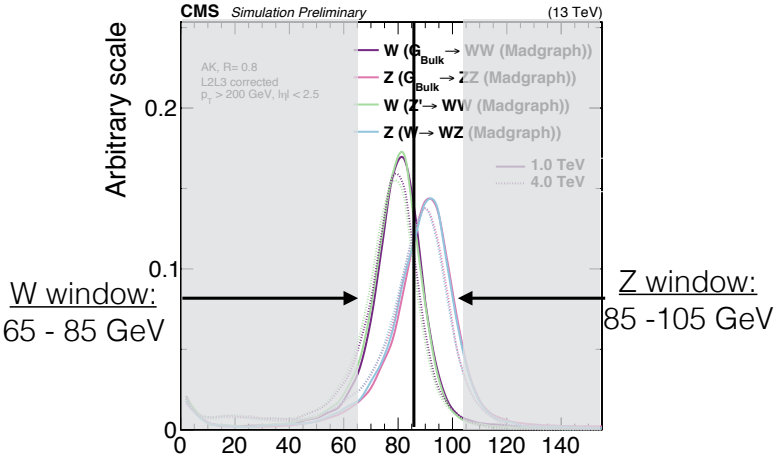

Figure 6.13: Z and W jet mass peaks for new diboson resonances simulation

schema is applied to the search for Zγ resonances and for Wγ resonances. In the latter case the b-tag categories are less motivated since W bosons do not decay to b quarks and will have a minor impact on the sensitivity of the whole analysis. On the other hand keeping the same categorization allows to use only one framework for two different searches with minimal changes in the analysis procedures, which was the initial goal of this work.
The mass categorization is the following:

a. $65 < M_{pruned} < 85$: W "enriched", Z "depleted" - called "low mass region" in the following
b. $85 < M_{pruned} < 105$: W "depleted", Z "enriched" - called "high mass region" in the following

The "low mass region" and "high mass region" results are then combined in a single outcome for both analyses.

The final selection must be chosen to be applied to both the Vγ signal taking into account the signature of the AK08 jet + an isolated photon. We decided to divide the data into 6 independent categories of events to exploit the characteristics of the final state thus using the mass differences between the two bosons, the b-tagging information and the N-Subjettiness selection already mentioned in the previous Chapter. In Tab. 6.3 all the categories are summarized.

Category Mass [GeV]	low mass region 65 ÷ 85	high mass region 85 ÷ 105
btag	loose WP	loose WP
anti-btag + τ_{21}	!loose WP btag + τ_{21} <0.45	!loose WP btag + τ_{21} <0.45
anti-btag + anti-τ_{21}	!loose WP btag + τ_{21} ∈[0.45;0.75]	!loose WP btag + τ_{21} ∈[0.45;0.75]

Table 6.3: Description of the 6 categories used in the Z/Wγ analysis

The requirements on the b-tag category differs with respect to the previously described in Sec. 6.4; as discussed in Appendix D.3, the requirement used previously (2 subjets of the AK08 jet generated by a b quark) has been found to tight and the selection has been changed; in this case, the b-tag category contains events with an AK08 jet flagged by the b-tag CSV algorithm. The change is visible also in the Acceptance×efficiency distribution described in Sec. 6.9.2.
In Appendix D.4 the difference between a 3 and a 6 categories analysis is reported.
Potential Vγ resonance signals contribute to all event categories although some regions are more enriched in Zγ or Wγ events thanks to the jet mass requirements.

6.9.1 Signal shape Zγ/Wγ

The signal function used to describe the mass of the boson+photon system ($M_{V\gamma}$) is the same used in Sec. 6.6; the signal shape is again parametrized with a Gaussian core and two power-law tails, an extended form of the Crystal Ball function. The only different in this case is the further division in mass categories as reported in Tab. 6.3.
Figures 6.14 and 6.15 show the invariant mass of an AK8 jet and a photon for a mass of 1000 GeV in all the 6 categories for a Zγ signal.

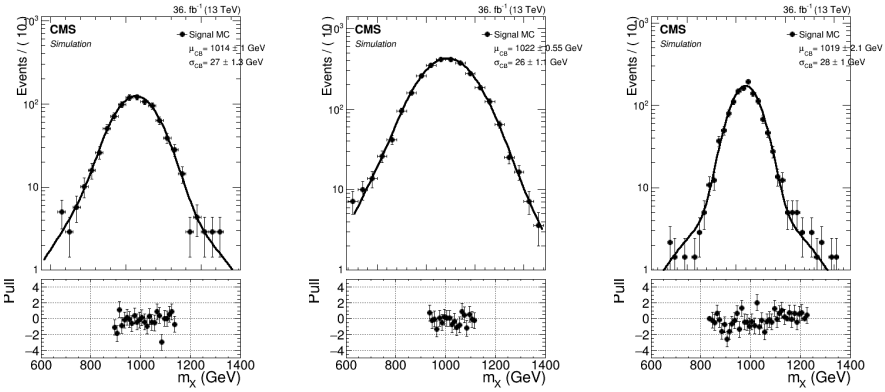

(a) b-tag category (b) τ_{21} category (c) anti-τ_{21} category

Figure 6.14: Fits of signal shape for mass hypotheses 1000 GeV for "high mass region" events in all categories for a Zγ resonance

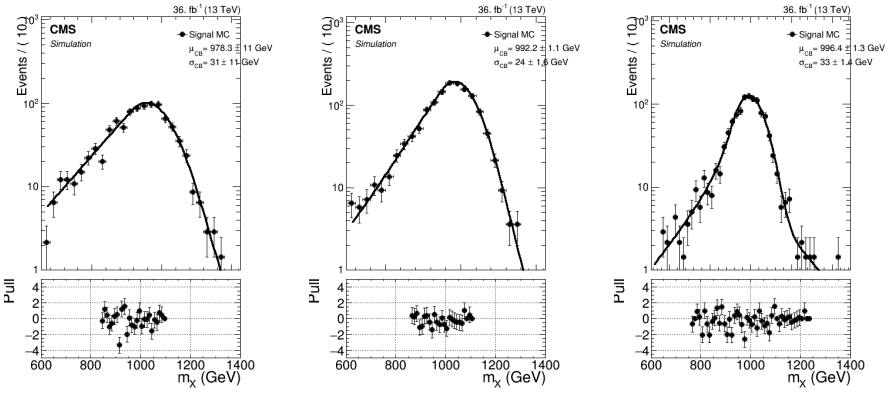

(a) b-tag category (b) τ_{21} category (c) anti-τ_{21} category

Figure 6.15: Fits of signal shape for mass hypotheses 1000 GeV for "low mass region" events in all categories for a Zγ resonance

Figures 6.16 and 6.17 show the invariant mass of an AK8 jet and a photon for a mass of 1000 GeV in all the 6 categories for a Wγ signal.

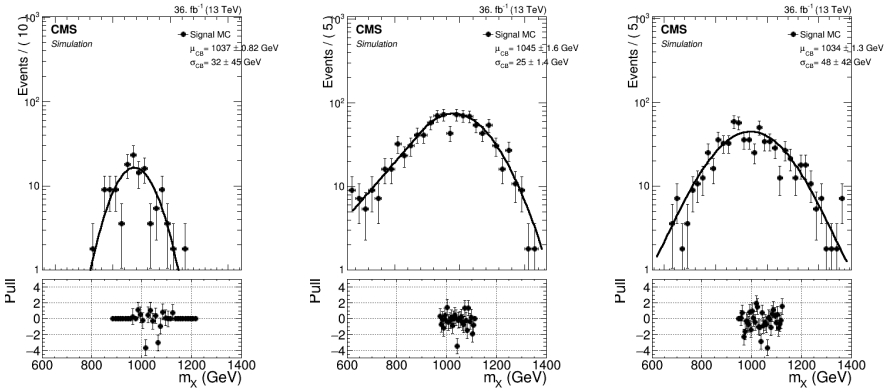

(a) b-tag category (b) τ_{21} category (c) anti-τ_{21} category

Figure 6.16: Fits of signal shape for mass hypotheses 1000 GeV for "low mass region" events in all categories for a Wγ resonance

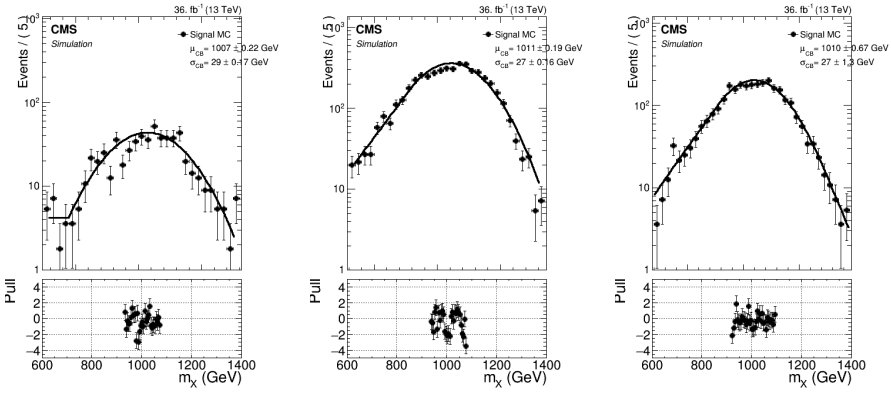

(a) b-tag category (b) τ_{21} category (c) anti-τ_{21} category

Figure 6.17: Fits of signal shape for mass hypotheses 1000 GeV for "high mass region" events in all categories for a Wγ resonance

6.9.2 Signal efficiency Zγ/Wγ

Signal efficiencies have been computed for both signals in the 6 categories. In Fig. 6.18 and Fig. 6.19 the efficiencies for the six categories are shown within $\pm 5\sigma$ of the signal mass peak for Zγ and Wγ signals respectively.

If the points of Fig. 6.18 are compared with Fig. 6.10, the response of the b-tag category have an higher efficiency using the single CSV requirement (used in Fig. 6.18) with respect to the subjet b-tag requirement of Fig. 6.10.

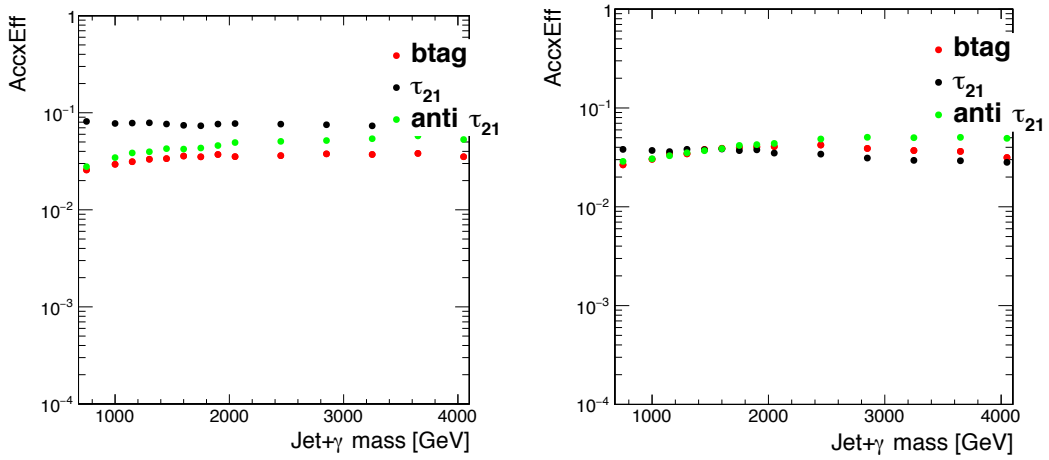

(a) Enrich category (b) Not enrich category

Figure 6.18: Signal shape efficiencies for the Z+γ signal samples in the six categories

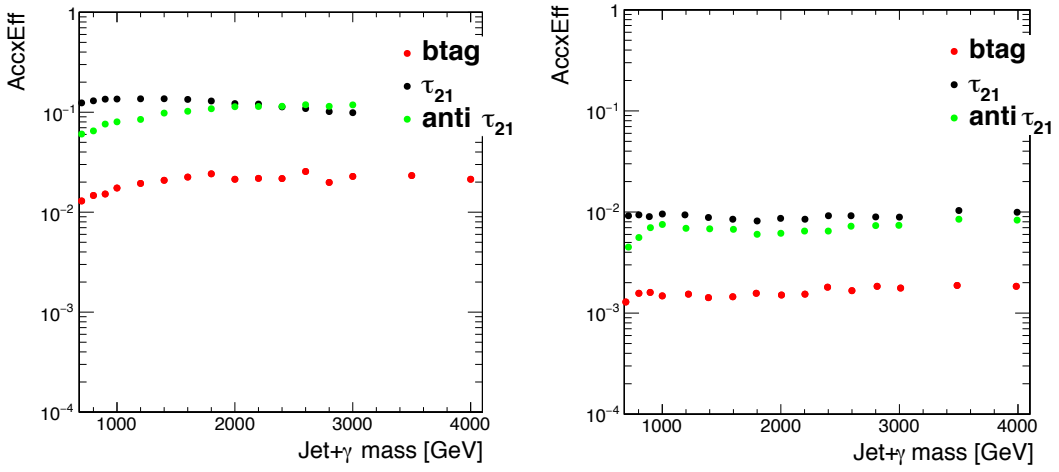

(a) Enrich category (b) Not enrich category

Figure 6.19: Signal shape efficiencies for the W+γ signal samples in the six categories

6.9.3 Background modeling Zγ/Wγ

The functional form used to fit data events in the invariant mass spectrum of the AK08+γ system in all the 6 categories is the same used in the Zγ standalone analysis (Eq. 6.1). No additional bias test has been performed as the spectrum is the same already tested.
In Fig. 6.20, all the 6 spectra are shown with the fit superimposed. No excesses are visible.

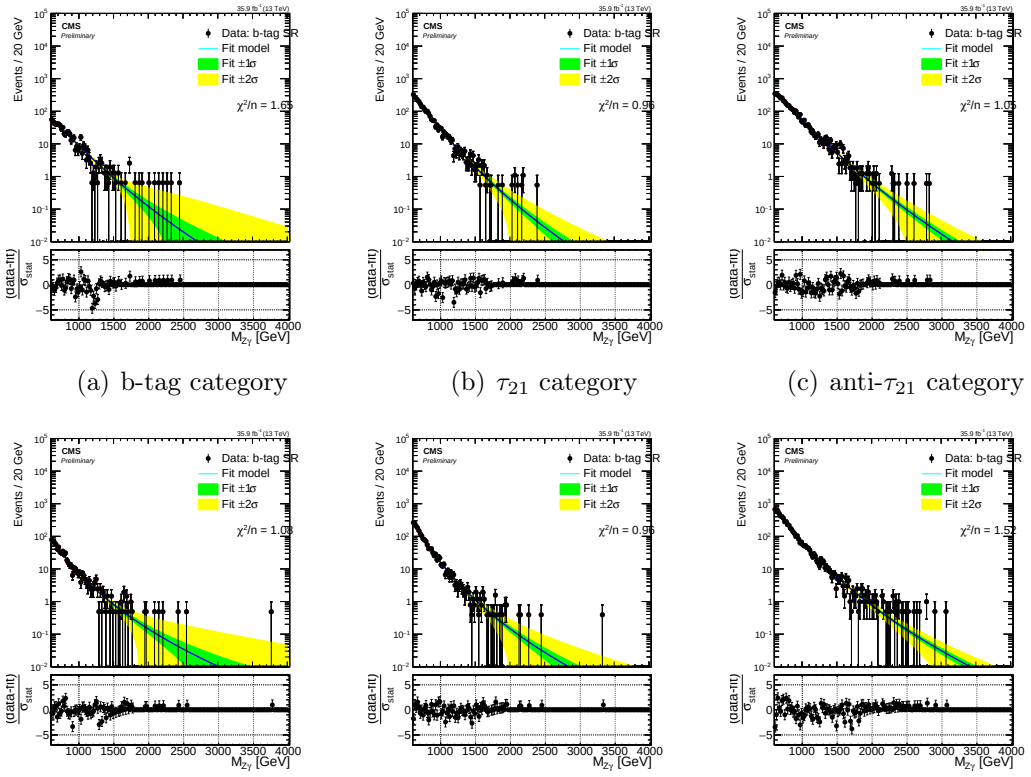

(a) b-tag category (b) τ_{21} category (c) anti-τ_{21} category

(d) b-tag category (e) τ_{21} category (f) anti-τ_{21} category

Figure 6.20: Fits of data point for "high mass region" (a-c) and "low mass region" (d-f) categories

6.10 Zγ/Wγ analysis results

The data are consistent with the background-only fit in all channels as shown in Fig. 6.20. We set upper limits on the production cross section of heavy resonances decaying into a Z boson and a photon or a W boson and a photon using the asymptotic approximation of the modified frequentist CLs method. The likelihood ratio is used as a test statistic and the uncertainties are incorporated as nuisance parameters with log-normal (normalization) or Gaussian (shape) priors. The limits are set in the mass range between 650 GeV and 4 TeV for both signals.

6.10.1 Zγ limit results

The upper limits on the product of signal cross section and branching fraction in the Zγ channel, $\sigma(\mathrm{X} \to \mathrm{Z}\gamma)$ for 0.014 % wide resonances in the b-tagged, τ_{21}-tagged and anti-τ_{21}-tagged categories are presented in Fig. 6.21 for the "high mass region" category and in Fig. 6.22 "low mass region" category. The

results based on the combination of all the categories is shown in Fig. 6.23.

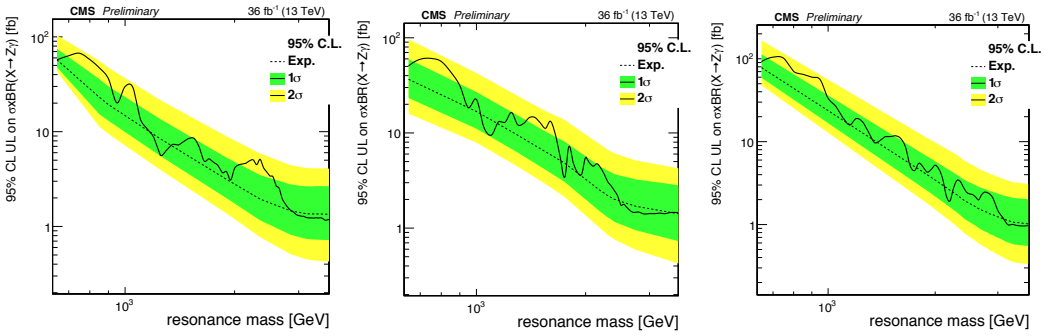

(a) b-tag category (b) τ_{21} category (c) anti-τ_{21} category

Figure 6.21: Zγ "high mass region" category limits for the three categories

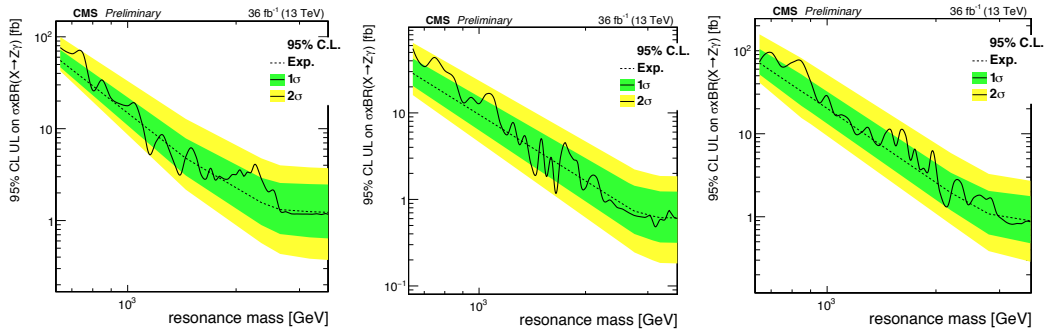

(a) b-tag category (b) τ_{21} category (c) anti-τ_{21} category

Figure 6.22: Zγ "low mass region" category limits for the three categories

In the Figures 6.21-6.23, the observed (solid) and expected (dashed) 95% CL upper limits on $\sigma(\mathrm{X} \to \mathrm{Z}\gamma)$, as a function of signal mass, together with the 68% (green) and 95% (yellow) CL ranges of the expected limit in the background-only hypothesis for the: b-tagged category ("enriched" and "depleted"); τ_{21}-tagged category ("high mass region" and "low mass region"); anti-τ_{21} category ("high mass region" and "low mass region"); for the combined "high mass region" category and the combined "low mass region" category and the combination of the two are shown.
The final expected limits on the cross section start from ∼10 fb (for a resonance of 650 GeV) to ∼0.2 fb (for a resonance of 3600 GeV).

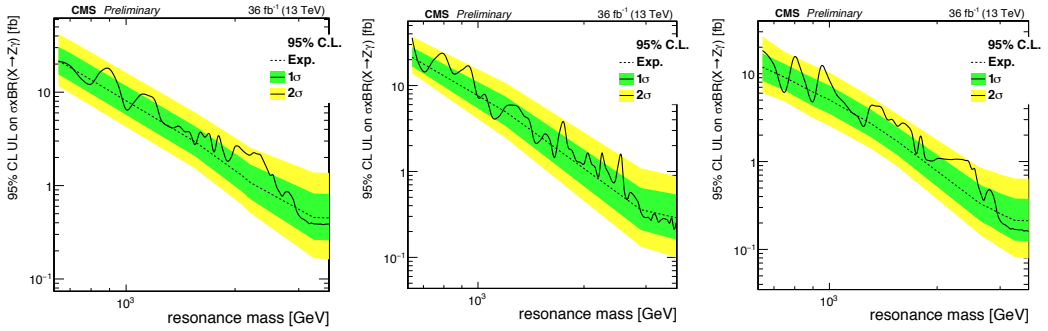

(a) "high mass region" category (b) "low mass region" category (c) "high mass region" and "low mass region" category

Figure 6.23: Zγ combination limits

6.10.2 Wγ limit results

The same machinery has been run to obtain the upper limits on the product of signal cross section and branching fraction in the Wγ channel ($\sigma(\mathrm{X} \to \mathrm{W}\gamma)$). The results are presented in Fig. 6.24 for the "low mass region" category and in Fig. 6.25 the "high mass region" category. The combination of all the categories is shown in Fig. 6.26.

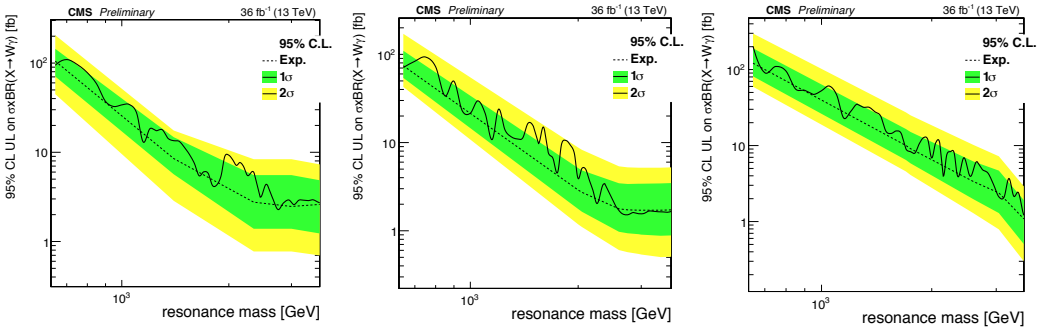

(a) b-tag category (b) τ_{21} category (c) anti-τ_{21} category

Figure 6.24: Wγ "low mass region" category limits for the three categories

The final expected limits on the cross section for the Wγ resonance production start from ∼20 fb (for a resonance of 650 GeV) to ∼0.6 fb (for a resonance of 3600 GeV).

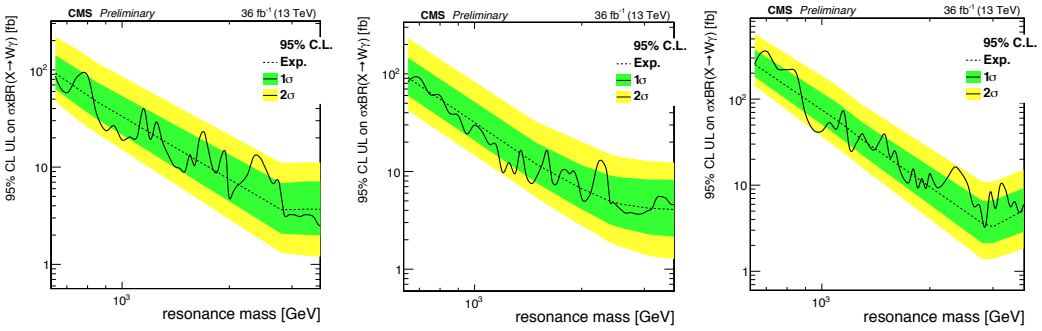

(a) b-tag category (b) τ_{21} category (c) anti-τ_{21} category

Figure 6.25: Wγ "high mass region" category limits for the three categories

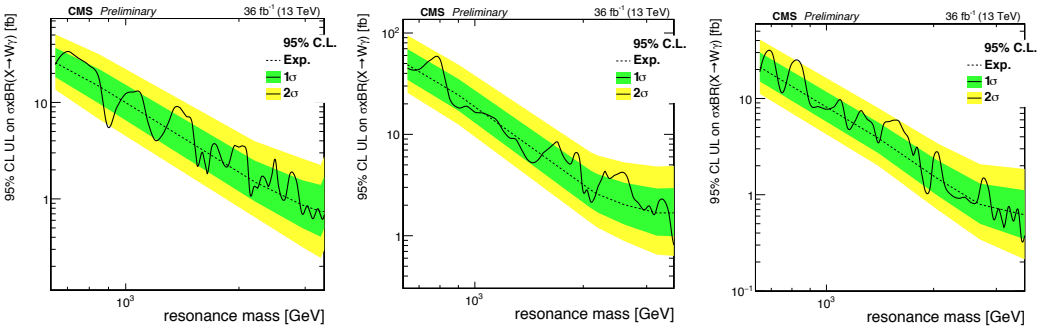

(a) "low mass region" category (b) "high mass region" category (c) "low mass region" and "high mass region" category

Figure 6.26: Wγ combination limits

6.10.3 Results comparison

In Tab. 6.4, the latest limits obtained from the ATLAS collaboration (at different masses) are compared with the three and six categories analyses presented in this thesis.
The results of these analyses are reported in the second/third columns of the Zγ comparison and in the second column of the Wγ comparison.
To compare the last two columns, the limits obtained at 8 TeV have to be rescaled by the parton lumi ratio[2]. The hadronic limits start to be comparable with respect to the leptonic ones around 1.5 TeV.
Comparing the three categories and the six categories analyses of the Zγ search presented in this thesis (third and fourth columns of Tab. 6.4) the latter presents an improvement in terms of better (lower) limits across the whole mass range used. This is explained by the different requirements on the b-tag category described in Sec. 6.9.

[2]That can be found in the parton lumi ratio website

Mass [GeV]	Leptonic Zγ Limits [fb]	Hadronic Zγ Limits [fb]		Leptonic Wγ Limits [fb]	Hadronic Wγ Limits [fb]
	ATLAS	3 categories	6 categories	ATLAS	6 categories
	13 TeV	13 TeV	13 TeV	8 TeV	13 TeV
400	30(23)		-	4(6)	-
700	10(8)	40(38)	10(12)	1.5(2)	20(30)
1000	5(12)	10(11)	5(14)	0.78(0.78)	8.7(8)
1500	3.6(3.6)	3.2(3)	2(3)	0.3(0.5)	2.8(6)
2000	-	1.7(3.9)	0.8(1)	-	1.8(1)
3000	-	0.7(0.6)	0.3(0.2)	-	0.72(0.53)
3600	-	0.3(0.2)	0.21(0.18)	-	0.6(0.32)

Table 6.4: Expected (observed) limits comparison between the latest results of ATLAS and the analyses discussed in this thesis

Conclusions

A search for TeV-mass resonances decaying to a Z or W and a photon have been presented. The analyses focus on final states where the Z/W bosons decay hadronically.
Photons are detected by the Electromagnetic Calorimeter (ECAL) of CMS which is described in Sec. 3.4. In the Appendices of this thesis, my work on the ECAL of CMS is discussed. In Appendix A, the timing monitoring and intercalibration extraction for all the ECAL crystals is described. This study permits to take under control any time shift of the detector and to maintain stable the energy resolution (as the reconstruction algorithm performance degrades with timing shifts). The Appendix B is focused on the work performed on the High Voltage (HV) system of the Barrel partition of the ECAL. All the HV channels of this system power the photodetectors glued to the crystals of the ECAL (only the Barrel) and their stability is fundamental to maintain a great energy resolution (as it contribute to its constant term).
The other important reconstructed object for the two analyses is the jet. Hadronic boosted bosons (reconstructed as single jets) can be discriminated from quark or gluon jets using grooming techniques (described in Sec. 4.7) and jet substructure observable (described in Sec. 4.13).
In Chapter 5 the calibration of jet variables such as jet mass, jet resolution and τ_{21} efficiency is described. A sample of $t\bar{t}$ is used to isolate a pure sample of W events. The variables to be calibrated are measured in data and in MC independently; then the ratio between the two is performed and corrections (called Scale Factors) are extracted. These Scale Factors are used in many analyses in the CMS collaboration which include boosted Z/W bosons in the final state.
In Chapter 6 the $Z\gamma$ analysis and the study of a new analysis framework to search for $Z\gamma$ and $W\gamma$ resonances are discussed. The analyzed dataset comprises about 36 fb^{-1} of proton-proton collisions delivered by the LHC at the center-of-mass energy of 13 TeV and recorded by the CMS detector. All the events are required to contain one energetic and isolated reconstructed photon and one energetic jet reconstructed with a distance parameter of 0.8 (see Sec. 4.7.1).
The $Z\gamma$ analysis is described in the first parts of the Chapter; new resonances ($X \to Z\gamma \to qq\gamma$) are searched. All the events are divided into three categories; events where the jet originates from a b quark (btag category), events that do not have a btagged jet and passing the τ_{21} selection and events which do not

pass the previous requirements.
In the second part of Chapter 6, the $Z\gamma/W\gamma$ analyses. The goal is to obtain a single framework capable of analyzing these two different signals making the framework sensitive to both $Z\gamma$ and $W\gamma$ signal models. The events are categorized following the $Z\gamma$ standalone selection; in addition, to discriminate between a Z and W, a new category for the jet mass is added (for a total of 6 categories).
The results have been presented in Sec. 6.10.1 and Sec. 6.10.2. No sign of new resonances has been detected and upper limits at 95% of CL on the product of the cross section times branching ratio of the process $X \to Z\gamma/W\gamma \to qq + \gamma$ have been set. The expected limits range from $\sim$10 fb (for a resonance of 650 GeV) to $\sim$0.2 fb (for a resonance of 3600 GeV) for the $Z\gamma$ resonance while $\sim$20 fb (for a resonance of 650 GeV) to $\sim$0.6 fb (for a resonance of 3600 GeV) for the $W\gamma$ resonance.
The analysis presented in this thesis shows an improvement in the $Z\gamma$ channel for the 6 categories analysis with respect to the 3 categories one due to the introduction of a new selection and the increased statistics used. The biggest improvement is in the low mass spectrum where the ratio between the expected limits obtained with the three and the six categories analysis is $\sim$3.
The results obtained by the $W\gamma$ analysis is the first search of this particular decay channel in the CMS collaboration and it extends the invariant mass spectrum probed with respect to the ATLAS analysis performed in RunI.

Appendix A

Timing Calibration

The aim of this chapter is to describe how the timing information is obtained from ECAL subdetector and its importance for the energy resolution of the calorimeter. The monitoring and the calibration (crystal per crystal) of this variable is also presented introduced by results and studies performed during the first datataking period of CMS. The definition of Interval Of Interest and how the monitoring of time can help the correct reconstruction of the pulse shape of ECAL are also shown. Moreover three brief studies regarding new possibilities for the calibration conclude this chapter.

A.1 Timing Definition in ECAL

In addition to the energy measurement, the combination of the scintillation timescale of $PbWO_4$, the electronic pulse shaping and the sampling rate allow excellent time resolution to be obtained with the ECAL sub-detector. This is very important in CMS under many aspects. The better the precision of time measurement and synchronization, the larger the rejection of backgrounds with a broad time distribution. Such backgrounds are cosmic rays, beam halo muons, electronic noise and out-of-time (OOT) proton-proton interactions. Precise time measurement also makes it possible to identify particles predicted by different models beyond the Standard Model. Slow heavy charged R-hadrons [87], which travel through the calorimeter and interact before decaying and photons from the decay of long-lived new particles reach the calorimeter later (out-of-time) with respect to particles travelling at the speed of light from the interaction point. As an example, to identify neutralinos decaying into photons with decay lengths comparable to the ECAL radial size, a time measurement resolution better than 1 ns is necessary. To achieve these goals the time measurement performance both at low energy (1 GeV or less) and high energy (several tens of GeV for showering photons) becomes relevant. In addition, amplitude reconstruction of ECAL energy deposits benefits greatly if all ECAL channels are synchronized within 1 ns [88]. Moreover previous experiments have shown that it is possible to measure time with elec-

tromagnetic calorimeters with a resolution better than 1 ns [89].

A.1.1 Timing Extraction

The front-end electronics of ECAL amplifies and shapes the signal from the photodetectors [90]. Figure 4.1 shows the time structure of the signal pulse measured after amplification (solid line). The amplitude of the pulse, A, is shown as a function of the time difference T-T_{max}, where T_{max} is defined as the time when the pulse reaches its maximum value, A_{max}. The pulse shape is defined by the analog part of the front-end electronics. For a given electronic channel, the same pulse shape is obtained, to a very good approximation, for all types of particles and for all momenta. The pulse is then digitized at 40 MHz by a 12-bit voltage-sampling analog-to-digital converter on the front-end, providing a discrete set of amplitude measurements. These samples are stored in a buffer until a Level-1 trigger is received. At that time the ten consecutive samples corresponding to the selected event are transmitted to the off-detector electronics for insertion into the CMS data stream. In this document, ECAL time reconstruction is defined as the measurement of T_{max} using the ten available samples of the pulse amplitude. For each ECAL channel, the amplitudes of these samples depend on three factors: the value of A_{max}; the relative position of T_{max} between time samples, which will be referred to as a "T_{max} phase"; and the pulse shape itself.
An alternative representation of the pulse shape is provided by a ratio variable, defined as R(T) = A(T)/A(T + 25 ns). Figure A.1.1 shows the measured pulse shape using the variable T-T_{max}, as a function of R(T). In view of the universal character of the pulse shape, this representation is, of course, independent of A_{max}. It can be described well with a simple polynomial parametrisation. The corresponding parameters have been determined in an electron test beam for a representative set of EB and EE crystals and are subsequently used for the full ECAL.

Each pair of consecutive samples gives a measurement of the ratio Ri = Ai/Ai+1, from which an estimate of $T_{max,i}$ can be extracted, with $T_{max,i}$ = T_i -T(R_i). Here T_i is the time when the sample i was taken and T(R_i) is the time corresponding to the amplitude ratio Ri, as given by the parametrisation corresponding to Fig. A.1.1. The uncertainty on each $T_{max,i}$ measurement, σ_{max}, is the product of the derivative of the T(R) function and the uncertainty on the value of R_i. The latter has three independent contributions, which are added in quadrature. The first contribution is due to noise fluctuations in each sample. The second contribution is due to the uncertainty on the estimation of the pedestal value subtracted from the measured amplitudes [88]. The last contribution is due to truncation during 12-bit digitization.
The number of available ratios depends on the absolute timing of a pulse with respect to the trigger. Ratios corresponding to large derivatives of the T(R)

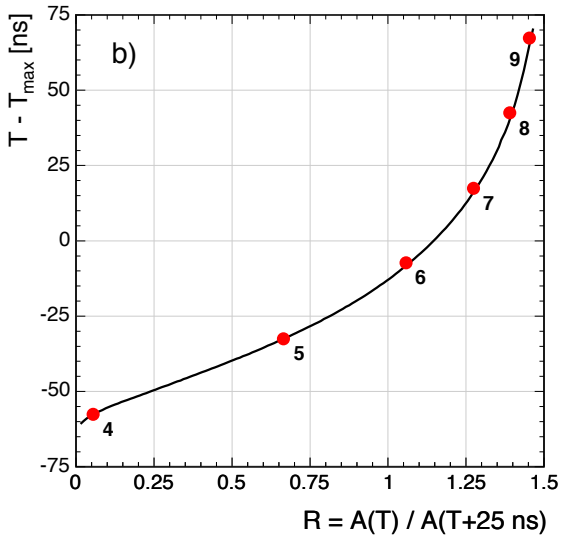

Figure A.1.1: Pulse shape points timing distribution

function and to very small amplitudes are not used. Pulses from particles arriving in-time with the LHC bunch crossing typically have 4 or 5 available ratios. The time of the pulse maximum, T_{max} and its error are then evaluated from the weighted average of the estimated $T_{max,i}$.

$$T_{max} = \frac{\sum_i \frac{T_{max,i}}{\sigma_i^2}}{\sum_i \frac{1}{\sigma_i^2}} \qquad \text{(A.1)} \qquad\qquad \frac{1}{\sigma_T^2} = \sum_i \frac{1}{\sigma_i^2} \qquad \text{(A.2)}$$

The values of $T_{max,i}$ and their errors σ_i are combined as if they were uncorrelated. Adjacent R_i ratios, however, share a common amplitude measurement value and are thus anti-correlated. Monte Carlo studies show that the uncertainty estimated using Eq. A.1 and A.2 is, on average, about 20% too large because of the anti-correlation and that the averaging of individual time measurements results in a bias of about 10% of the statistical uncertainty of T_{max}, which is negligible. The different R_i ratios are also correlated because there are correlations in the noise contributions to the samples (see Fig. 3 of Ref. [88]). This has no impact on the average and a very small effect on the estimated uncertainty of T_{max}, corresponding to $< 10\%$ of the statistical uncertainty.

A.2 Time Resolution Measurement

The time resolution can be expressed as the sum in quadrature of three terms accounting for different sources of uncertainty and may be parametrized as follows:

$$\sigma^2(t) = \left(\frac{N\sigma_n}{A}\right)^2 + C^2 \qquad \text{(A.3)}$$

Here A is the measured amplitude, σ_{n} is related to the noise level in individual samples and N, S and C represent the noise, stochastic and constant term coefficients, respectively. The noise term contains the three uncertainties mentioned above, in the discussion of the uncertainty on $\mathrm{T_{max,i}}$. Monte Carlo simulation studies give N = 33 ns, when the electronic noise in the barrel and endcaps is $\sigma_{\mathrm{n}} \sim 42$ MeV and $\sigma_{\mathrm{n}} \sim 140$ MeV, respectively. The stochastic term comes from fluctuations in photon collection times, associated with the finite time of scintillation emission. It is estimated to be negligible and it has not been considered in the study. The constant term has several contributions: effects correlated with the point of shower initiation within the crystal and systematic effects in the time extraction, such as those due to small differences in pulse shapes for different channels.

To study the pulse shape and determine the intrinsic time resolution of the ECAL detector, electrons from a test beam are used. Several fully equipped barrel and endcap sectors were exposed to electrons at the H2 and H4 test beam facilities at CERN, prior to their installation into the CMS detector [91]. The beam lines delivered electrons with energies between 15 GeV and 250 GeV. In the test beam, sectors were mounted on a rotating table that allowed the beam to be directed onto each crystal of the supermodule. The 2-D profile of the electron beam was almost Gaussian, with a spread comparable to the crystal size. As a consequence, in a single run, electrons hit the crystal in different positions and the fraction of energy deposited by an electron in a given crystal varied from event to event.

The time resolution is extracted from the distribution of the time difference between adjacent crystals that share the same electromagnetic shower and measure similar energies. This approach is less sensitive to the constant term C, since effects due to synchronization do not affect the spread but only the average of the time difference. As electrons enter the crystal from the front face and there is the requirement of depositing a similar energy in both crystals, the uncertainty due to the variation of the point of shower initiation is also negligible. In addition, the T - $\mathrm{T_{max}}$ vs R polynomial parametrisation is determined individually for every crystal to avoid systematic effects due to pulse shape parametrisation. The distribution of the time difference is well described by a Gaussian function with negligible tails for all amplitudes. The spread is defined as the sigma of the Gaussian fit to the distribution and is parametrized, following Eq. A.3, as:

$$\sigma^2(t_1 - t_2) = \left(\frac{N\sigma_n}{A_{eff}}^2\right) + 2\bar{C}^2 \tag{A.4}$$

where $\mathrm{A_{eff}} = \mathrm{A_1 A_2}/\sqrt{\mathrm{A_1^2 + A_2^2}}$ with $\mathrm{t_{1,2}}$ and $\mathrm{A_{1,2}}$ corresponding to the times and amplitudes measured in the two crystals and $\bar{C}$ being the residual contribution from the constant terms. The extracted width is presented in Fig. A.2.1 as a function of the variable $\mathrm{A_{eff}}/\sigma_{\mathrm{n}}$. The fitted noise term corresponds to N = (35.1 ± 0.2) ns. $\bar{C}$ is very small, $\bar{C}$ = (20 ± 4) ps. For values of $\mathrm{A_{eff}}/\sigma_{\mathrm{n}}$ greater than 400, σ(t) is less than 100 ps, demonstrating that, with a carefully calibrated and synchronized detector, it is possible to reach a time resolution

better than 100 ps for large energy deposits (E >10-20 GeV in the barrel). As a crosscheck, the stochastic component was left free in the fit and found to be S $<$ 7.9 ns MeV$^{\frac{1}{2}}$ (90% C.L.), confirming that this term is negligible.

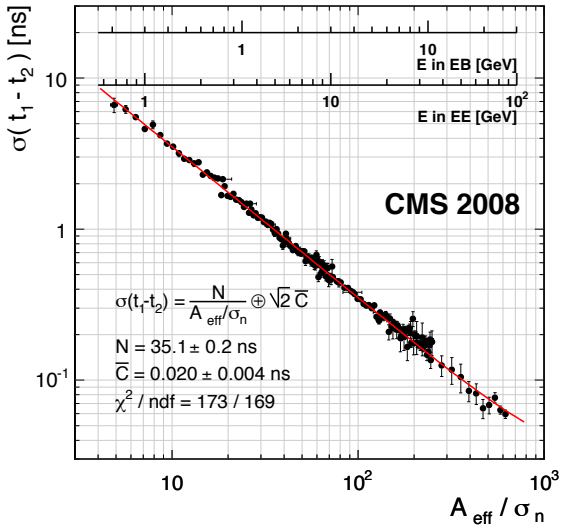

Figure A.2.1: Gaussian width of the time difference between two neighbour crystals

A.2.1 Synchronization between crystals

For each individual ECAL channel, the signals generated by particles originating from the interaction point (IP) are registered with approximately the same value of T_{max}, because their flight times to the crystal do not change (up to small differences related to the precise position of the IP). Because the time of flight varies across the ECAL by a few nanoseconds and there are different intrinsic delays among channels, a crystal-to-crystal synchronization of the ECAL must be performed.
The ECAL Front-End Electronics (FEE) allows adjustment of T_{max} for groups of 5x5 channels in steps of 1.04 ns. The determination of values for these adjustments is called hardware synchronization. To take full advantage of the high precision of the ECAL time reconstruction, the value of T_{max} corresponding to particles coming from the IP must be determined for each ECAL channel with an accuracy exceeding the typical time resolution. These additional corrections, called software synchronizations, can be extracted offline with physics collision events. Minimum bias events, which have a typical energy scale of 500 MeV/channel, can be used for this purpose. With the trigger menus planned for early data taking, they will have yield about 1000 events/channel/day. A synchronization precision on the order of 100 ps is estimated to be achievable using data from a single day of running at the start of the LHC.

Beam-produced muons, collected by CMS with the first beams circulating in the LHC in September 2008, were used to synchronize the detector. The beams

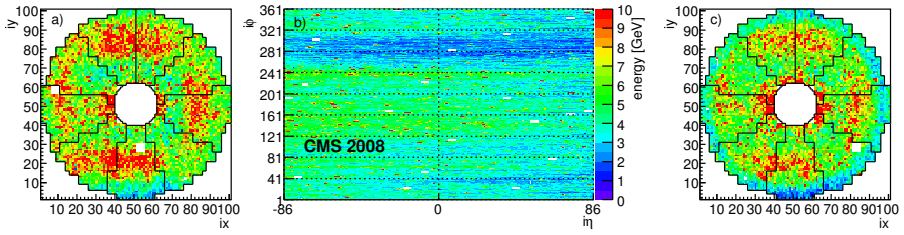

Figure A.2.2: ECAL average energy deposit per-crystal for a typical "beamsplash" event with muons coming from the minus side

were dumped on collimators located approximately 150 m upstream of CMS, producing so-called "beam splash" events. The proton bunch length along the direction of propagation was about 6 cm, corresponding to about 200 ps spread in time. The resulting pions and kaons decayed into a very large number of muons, moving horizontally along the beam direction, corresponding to the z axis, at close to the speed of light. The arrival time of these muons at each crystal depends on the crystal position and can be precisely predicted. In Fig. A.2.2 the ECAL energy deposits in each crystal for a typical "beam splash" event are shown. Several muons cross each crystal, resulting in energy deposits between 2 and 10 GeV. It may be noted that almost every crystal registered a significant energy.

As stated above, it is important to synchronize the calorimeter such that particles travelling from the interaction region appear in-time. Since muons from "beam splash" events travel as a plane wave and do not come from the interaction region, a correction using the predicted time of flight is applied. In order to compare times obtained from different events, the average times in the barrel and each endcap are used as references. It should be noted that, because of the time of flight of muons, the "T_{max} phase" depends on the position of the crystal and muon direction. Crystals with the same pseudorapidity η, forming a ring in ϕ, have a common "T_{max} phase".

Two independent samples of "beam splash" events are used to synchronize ECAL channels: about 20 events containing a large number of muons travelling in the negative direction of the z axis ("minus" beam, moving clockwise in the LHC) and about 35 events with muons travelling in the opposite direction ("plus" beam). For every individual channel, an average of time measurements weighted by their uncertainties is calculated, resulting in the time intercalibration coefficient. This procedure is applied separately for "plus" and "minus" beam events. Comparison of the "plus" and "minus" calibrations yields an estimate of the statistical and systematic uncertainties of the calibration and time reconstruction algorithms, while the sum of the two samples is used to extract the intercalibration coefficients.

Figure A.2.3a shows the difference between "plus" and "minus" calibrations for the 360 barrel channels in which muons arrived at the same time delay with respect to the trigger in both "plus" and "minus" runs. These channels, forming a ring in ϕ, have the unique property of sharing the same "T_{max} phase" for

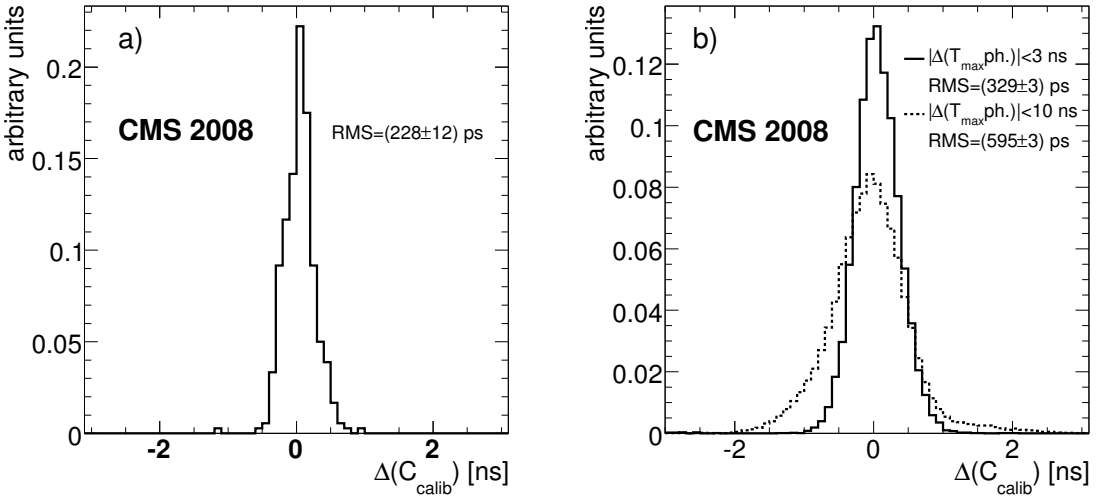

Figure A.2.3: Distributions of the differences between the calibration coefficients obtained using muons from the "plus" beam and muons from the "minus" beam

both "plus" and "minus" muons. Thus channels in this ring experience conditions similar to those in normal LHC operation i.e. the energy deposits are synchronous. The Gaussian spread of the distribution is about 230 ps, which is in good agreement with the expected statistical uncertainty. Summing the event samples from both "plus" and "minus" beams results in a synchronization of ECAL channels with a statistical uncertainty of about 85 ps in the barrel and 105 ps in the endcaps.

Figure A.2.3b shows a distribution similar to that in Fig. A.2.3a, except that muons in these channels need not arrive at the same time in both "plus" and "minus" splashes. This has the effect of including many more crystals in the selection and introduces sensitivity to any "T_{max} phase" - dependent effects. The solid line represents the distribution of channels fulfilling the requirement that the difference in "T_{max} phase" between "plus" and "minus" muons is within a 3 ns time range, which includes about 43% of the barrel channels. The dotted line is the distribution conditioned by requiring a "T_{max} phase" difference of less than 10 ns, selecting about 70% of the barrel channels. The widths of these distributions are (329 $\pm$ 3) ps and (595 $\pm$ 3) ps, respectively, both of which are significantly larger than the expected statistical uncertainty, indicating the presence of systematic effects correlated with the uncertainties in the pulse shape. The time reconstruction method assumes the same pulse shape for all ECAL channels, but the real pulse shapes slightly differ from channel to channel (see Fig. 10 of Ref. [88]). Detailed Monte Carlo simulation studies and measurements with electrons from a test beam show that these differences in shape pose no problem for in-time signals, while out-of-time signals are reconstructed with a systematic uncertainty ranging from tens to hundreds of picoseconds. The effect is proportional to the size of the range in "T_{max} phase". The results shown in Fig. A.2.3b confirm these studies. In LHC collisions, the time range will not have a wide spread since events will be synchronous and

the accumulated bias in the time reconstruction will be minimal. Thus the systematic error on the synchronization is expected to be negligible when using collision events.
It can be concluded that the overall uncertainty in the determination of the synchronization coefficients, which is the quadratic sum of the statistical and systematic uncertainties, is about 300–600 ps. This was the time resolution expected at the start-up of the LHC, when these synchronization coefficients were used.

A.2.2 Resolution and linearity checks using cosmic ray muons

The resolution and the linearity of time measurements were determined with a sample of cosmic ray muons collected during summer 2008, when the ECAL was already inserted into its final position in CMS. Samples used for this analysis were taken from runs without magnetic field. Muon tracks are reconstructed in the muon system and, where possible, in the inner tracker. Muons typically deposit energy in several ECAL crystals, which are then grouped to form clusters. The purity of the sample is increased by requiring the extrapolated muon track to point towards the barycenter of the ECAL cluster. This is done by requiring that the distance between the calorimeter deposit and the position of entrance of the muon track in the η-ϕ plane is consistent with zero within the experimental resolution [92]. The selection is restricted to the barrel region, resulting in a sample of about 2 x 10^5 muons. The associated clusters correspond to muons that lose energy in the calorimeter by ionization, with very little background contamination. The synchronization constants obtained from "beam splash" events are then applied.
The approach to extract the resolution is similar to that described in section 3, but in this case the crystal with the maximum amplitude is compared with the other crystals in the cluster. Since different pairs of crystals are used, covering the entire barrel, a constant term comparable to the systematic uncertainty of the synchronization is expected.
The results on the resolution are presented in Fig. A.2.4a. The noise term is found to be N = (31.5 $\pm$ 0.7) ns and is very similar to that obtained from test beam data. The constant term is measured to be C = (380 $\pm$ 10) ps, which is consistent with the expected systematic uncertainty from "beam splash" synchronization.

The same sample of cosmic ray muons is used to test the linearity of the time measurement. For muons which traverse the ECAL barrel from top to bottom, the times of respective clusters are taken to be the times of the crystals with the largest amplitudes. The difference in time between the two crystals is then compared with the corresponding time of flight of a relativistic muon travelling over the distance between the two crystals. The crystals are ordered

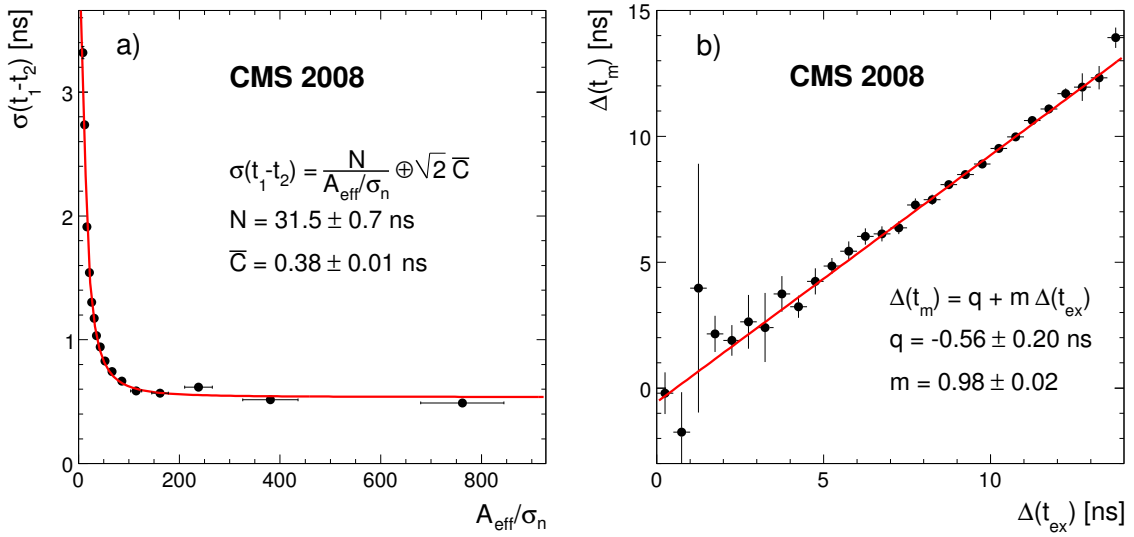

Figure A.2.4: Spread of the time difference between crystal of the same cluster (left plot), Measured time difference between top and bottom muon clusters (right plot)

depending on their vertical position, assuming that all muons are coming from the top of the detector. The distance is calculated taking into account the fact that, on average, cosmic ray muons enter crystals at the center of the lateral edge. The time of flight ranges from about 0 ns, which corresponds to muons almost tangential to the ECAL surface, to about 14 ns. In Fig. A.2.4b the correlation between expected and measured times is shown. The distribution is fitted with a straight line, resulting in a slope (m) compatible with unity. The offset (q) is compatible with zero within the systematic uncertainty on the synchronization, which is of the order of 300–600 ps (as expected).

A.3 Time Monitoring and Calibration in Run II

As already explained in Sec. A.1, the time variable is important for new physics' signatures predicted by some theory models.
Moreover, the energy reconstruction in ECAL, which uses the Multi-Fit method, is extremely connected to the timing variable of each recHit of each crystal as the fit is a template one with the x variable (the pulse shape time) fixed. If the shape is shifted (for any reason from CMS clock changes to the TCDS, crystal ageing or other hardware effects), having a wrong value of time injected in the template fit, the energy resolution can suffer and be worse as shown in Table A.3.1.

As can be seen in Fig. A.3.1, the Multi-fit can describe a pulse shape coming from a crystal also if it is shifted or in presence of high pile-up. However the shift has to be less than 200 ps to prevent any loss in the calorimeter energy resolution. Any shift greater than 200 ps will trigger the creation of a new

Time shift	EB reso diff.	EE reso diff.
± 250 ps	∼0.25%	∼0.8%
± 500 ps	∼0.5%	∼1.5%
± 2 ns	∼3.5%	∼7%

Table A.3.1: Energy resolution difference with respect to the correct value using a wrong time variable

Interval Of Interest (IOV) of the timing and the pulse shape.

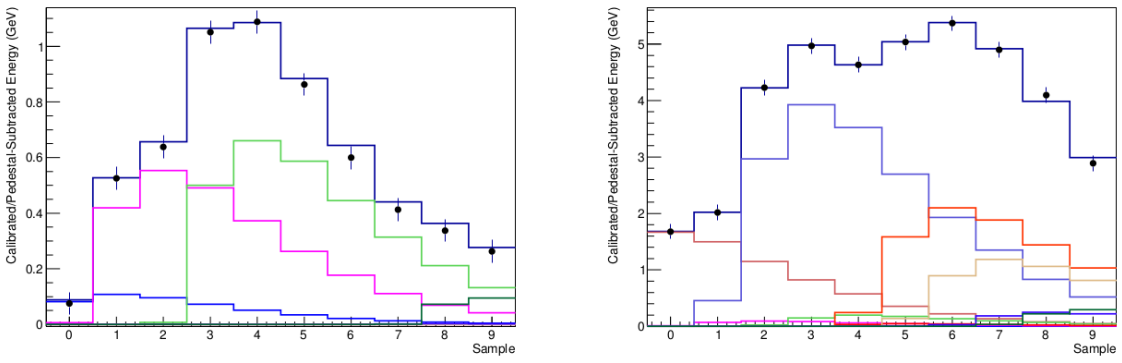

(a) EB (b) EE

Figure A.3.1: Pulse shape reconstruction with a different time shift for EB (a) and EE (b)

A.3.1 Time monitoring

Time has to be monitored closely. Every run is analyzed as soon as it is available in the storage system of CMS (48 hours after the run has been taken and registered).
In Fig. A.3.2, the time monitoring of 2016 is reported for each of the four partitions of ECAL: Barrel Plus (EB+), Barrel Minus (EB-), Endcap Plus (EE+) and Endcap Minus (EE-).

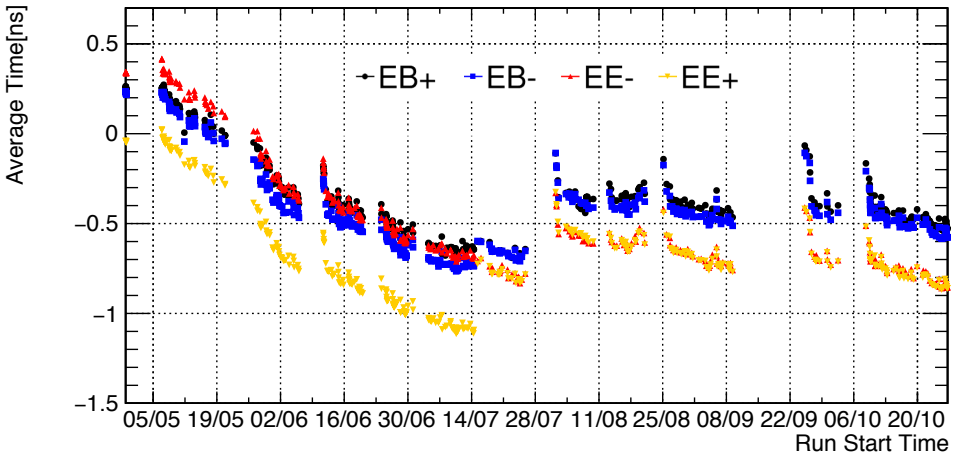

Figure A.3.2: Time behaviour of 2016 data

To do an accurate and complete monitoring of ECAL's timing, we use data coming from the *PhiSymmetry* physics stream, meaning low p_t charged particles (mainly electrons and charged pions) to maximize the statistics in the number of events per crystal.
A very important role in this study is related to the energy threshold of the recHit that can be treated as interesting signal. As the energy of the particle is very low, a compromise between negligible loss in statistics and purity of the events selected is needed. The cut on the recHit energy value prevent any selection of noise values (the cut value is 5σ above the noise peak) and has been studied in details during the first data taking of CMS in 2016. Furthermore, the energy cut should not introduce any bias on the measurement. The most important part (giving Eq. A.1) of the pulse shape in term of time response is made by the first 6 points (counting the noise ones), as they are located on the rising edge of the signal; a low signal will have an almost flat rising edge compared to very high signal. This has been taken into account for the choice of the energy requirement for both Barrel and Endcap signals. In Fig. A.3.3 and A.3.4, the profile distributions of the difference between each η ring (reported on the x axis of each plot) using two different thresholds is shown.

The error bars depend only from the statistics for each η ring and reflect the distribution expected of PhySymmetry particles inside the Barrel part of ECAL (Fig. A.3.5); higher at high η (towards the Endcap).
We chose 2.5 GeV as final threshold for Barrel's events. In fact, as can be seen, after a cut of 2.5 GeV the bias related to the selection disappears. We decided not to go further in energy to mantain reasonable values of event per-crystal and obtain an accurate measurement in term of statistics of the time variable.

For what concern the Endcap, the approach has been guided by the ageing of the crystals and sensors in the forward region. The Endcaps are more affected by the irradiation damage, as they receive an higher flux of particles when

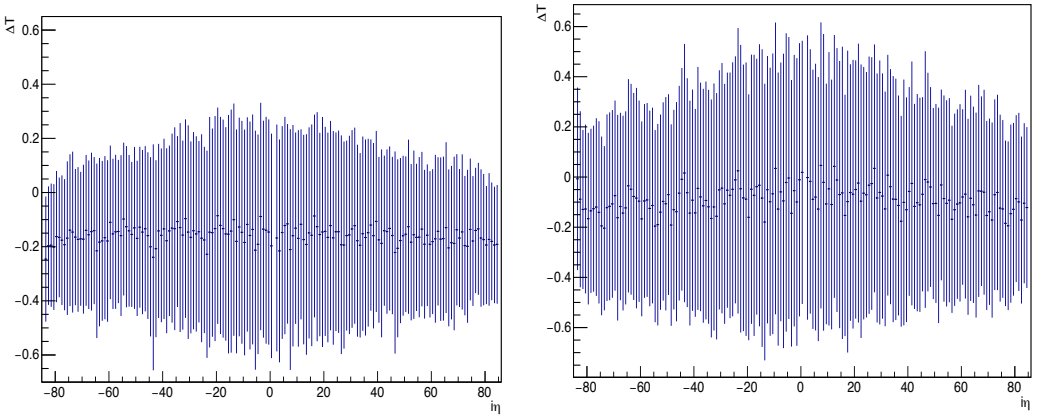

(a) (b)

Figure A.3.3: Profile difference between a cut of 1 GeV and a cut of 0.5 GeV (a) and between a cut of 1.5 GeV and a cut of 1 GeV (b)

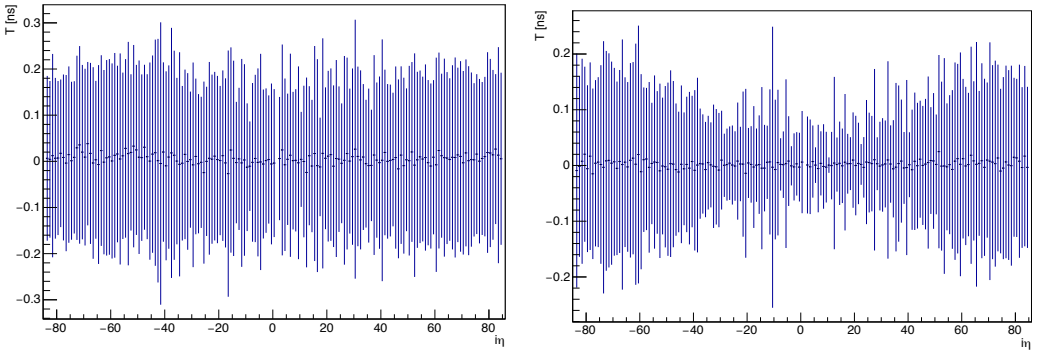

(a) (b)

Figure A.3.4: Profile difference between a cut of 2.5 GeV and a cut of 2 GeV (a) and between a cut of 3 GeV and a cut of 2.5 GeV (b)

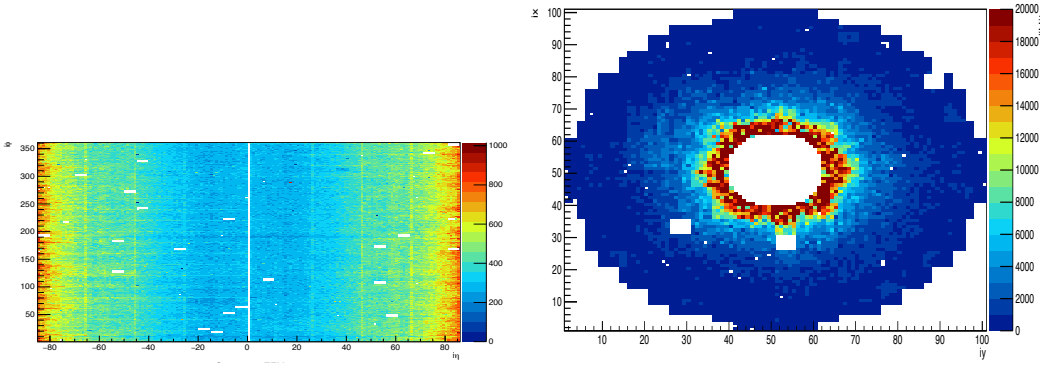

(a) (b)

Figure A.3.5: Occupancy distribution for Barrel (a) and Endcap (b)

LHC provide collisions to the experiment. In Fig. A.3.6 is reported a MC study meant to predict the ageing of the VPT+crystal system, determining a raise in the noise value given by the photodetector.

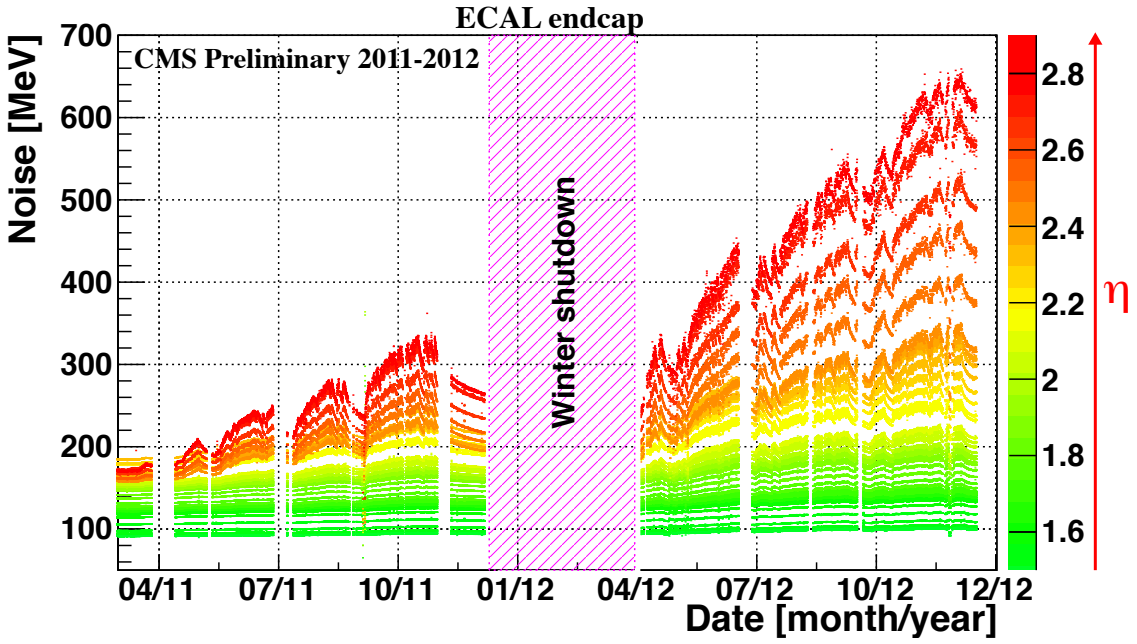

Figure A.3.6: VPT noise behaviour vs time

In this case a dynamic cut has been chosen instead of the flat cut used in the Barrel following the equation:

$$threshold_{VPT} = \frac{20 \cdot (79.29 - 4.148 \cdot iRing + 0.2442 \cdot iRing^2)}{1000} + Offset \tag{A.5}$$

where *iRing* is the η ring and *Offset* is the initial value of the selection (set to 1.5 GeV). This can be translated in a 2D map as shown in Fig. A.3.7.

A.3.2 Time calibration

To take into account the shift in time observed during 2016 data and shown in Fig. A.3.2, an accurate and minute monitoring has to be performed. Every run recorded by CMS has to be analyzed and checked for any unexpected behaviour or shift. Moreover, for each run Intercalibration Constants (IC) are calculated using the average (for each crystal) of all the events of each crystal. An IC is a value that is used to correct the shift and bring it back to 0 via software.
In fact, time can be corrected using two approaches:

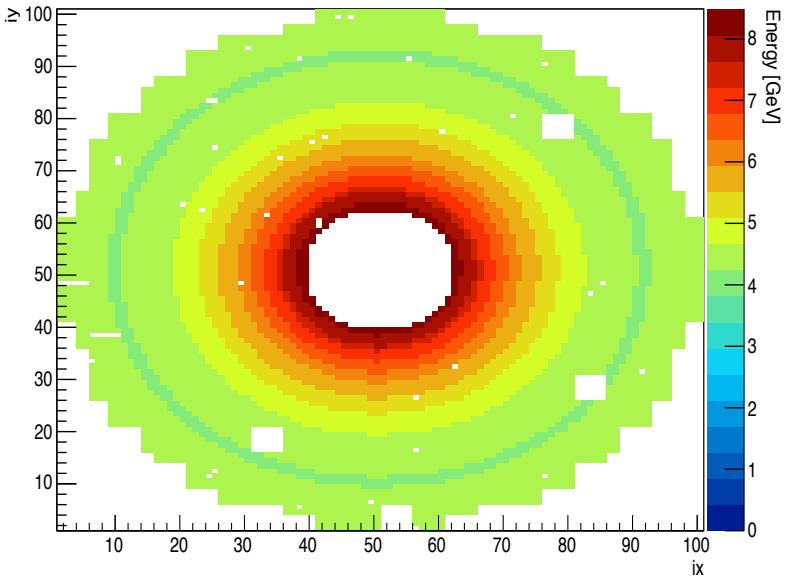

Figure A.3.7: Energy threshold [GeV] for the Endcap

1. via hardware. One SuperModule (about 1700 crystals) at a time with steps of 1.024 ns
2. via software. For each crystal an IC is derived and then applied in the IOV.

Although IC are calculated for every run, only few are used to correct the response of ECAL and depend by the definition of the IOV. An IOV is a period during data taking where there has not been any drastic changes in the time response (from the beginning to the end of the IOV the ΔT of the time has to be less than 200 ps) of ECAL or no TCDS interventions have been performed as they usually shift the whole detector in time (as can be seen in the big jumps of Fig. A.3.2).
In Fig. A.3.8, an example of three 2D maps of the IC respectively for the Barrel, Endcap Plus and Endcap Minus is reported. White dots are channels broken or that do not have more than 10 events.

After the definition of an IOV, a run, whose IC will be used, has to be chosen. There isn't a strict behaviour for this choice, but the main guidelines regard the statistics of the run (the more events are collected the best, otherwise it is better to combine different subsequent runs) and preferably it has to be registered in the middle of the IOV to give the best performance through the whole period.
A first validation of IOVs has been done during the first part of 2016 and is shown in Fig. A.3.9. In that plot are shown the average of the time values for each partition of ECAL after the application of the IC (written in the database and used for the reconstruction of data) taken from the run underlined in green. The behaviour of the four distributions recalls a "saw tooth shape" and it is connected to the choice of the run for the IC. Before that run

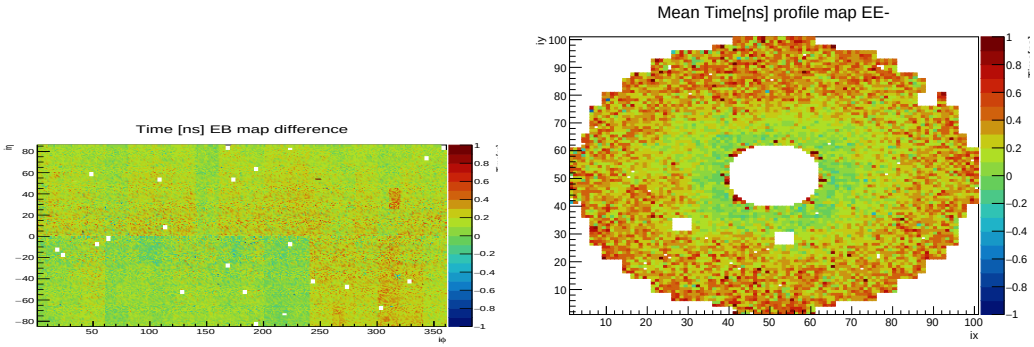

(a) (b)

Figure A.3.8: IC distribution for EB (a) and EE (b) during the first stages of 2016 data taking where all the partitions where above 0 ns

the time values are a bit in advance while afterward they are "late" and appear below the line of 0 ns.

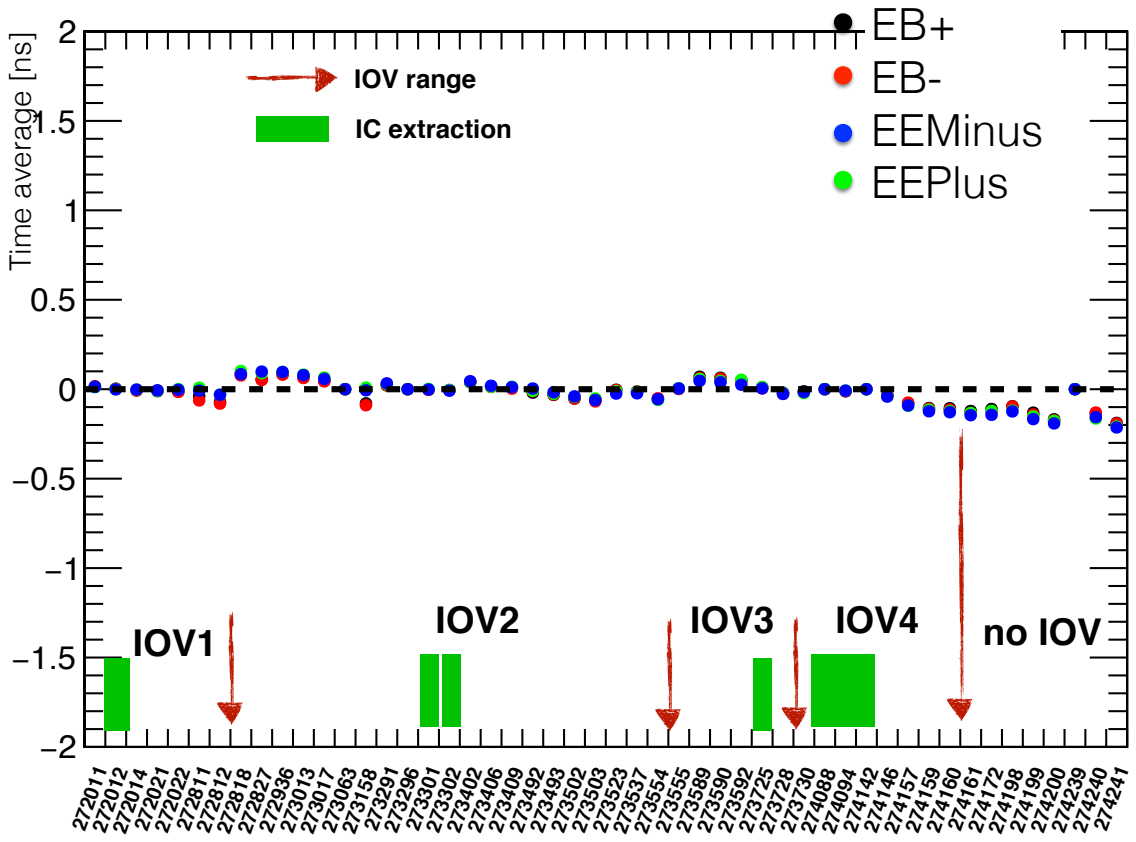

Figure A.3.9: Time IOV closure test for first 2016 data

The validation of new IOVs can also be seen separately for each partition of ECAL looking at the 2D distribution before and after the application of the IOV. In Fig. A.3.10 there is an example for the Endcap Plus side.

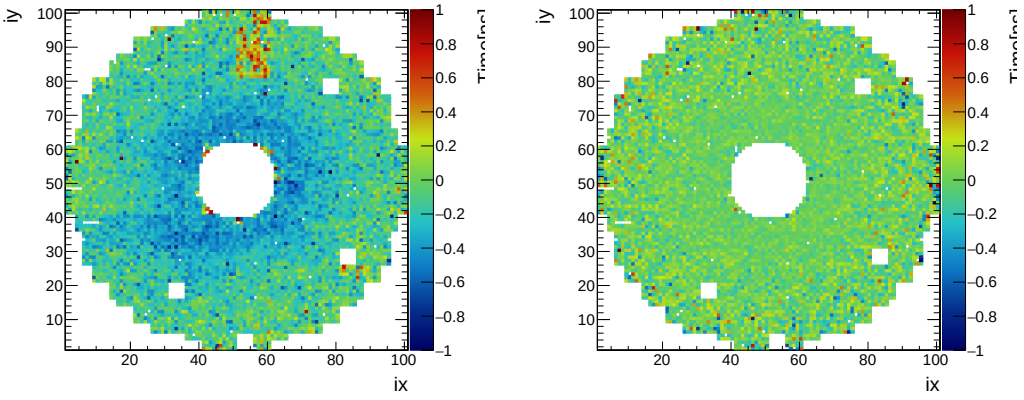

(a) (b)

Figure A.3.10: Timing distribution in EE+ before (a) and after (b) the validation. As can be seen the partition average return toward 0 ns in the right plot

A.3.3 Time calibration study using the LoneBunch trigger

Timing measurements can be affected by pile-up (the superimposition of many simultaneous events). To asses this possible difference and quantify its magnitude, we used a particular trigger developed and used by LHC since the end of 2015 called LoneBunch (Fig. A.3.11). In this case, in the experiment two single bunches collide with nothing before or ahead of them giving a more clear signal without pile-up.

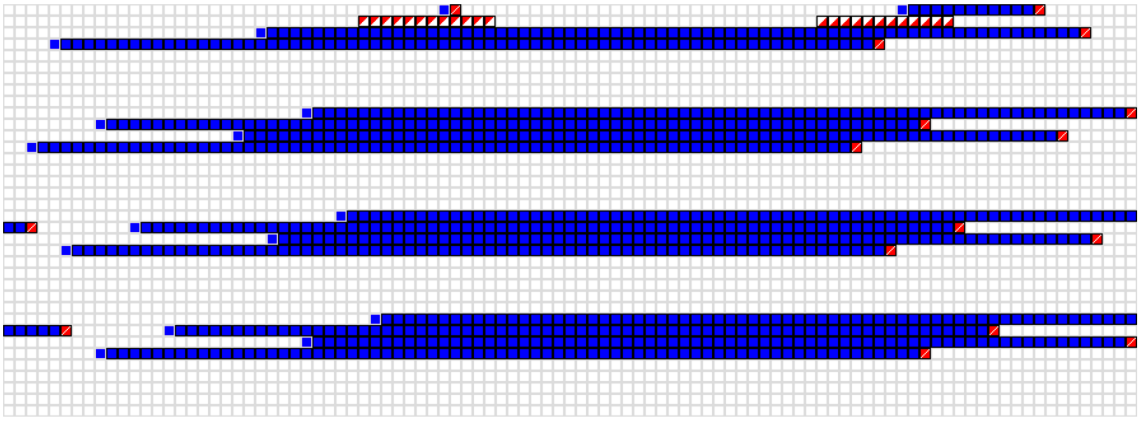

Figure A.3.11: LoneBunch configuration. The lone bunch is the blue square before the red one in the first row of the scheme

Thanks to this particular trigger, it can be possible to asses the difference in a single run between events triggered by the LoneBunch trigger and the rest.

In Fig. A.3.12 and A.3.13, the comparison shows little differences in the two sets of events. The difference in this case is simply calculated as:

$$\Delta T = time_{xtal} - time_{xtal}^{loneB} \tag{A.6}$$

However, the mean of the distribution is comparable with 0 and the σ of 100 ps is negligible with respect to the intrinsic resolution of the crystals and the electronic of the electromagnetic calorimeter (which is around 200 ps).

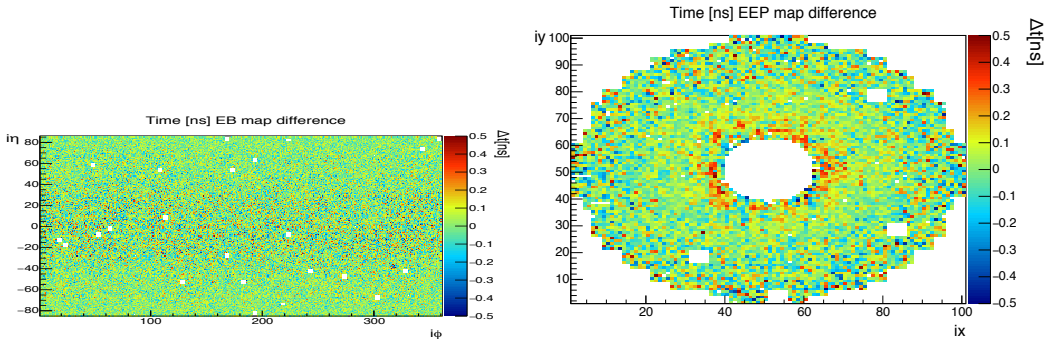

(a) (b)

Figure A.3.12: Timing difference 2D distribution in EB (a) and EE Plus (b)

As shown in Fig. A.3.13, for the Barrel the μ of the distribution is 5 ps, while for the Endcap Plus the μ is 10 ps (given the fact that in the Endcap the role of pile-up is more important and has higher effect with respect to the Barrel, although still negligible for this study and detector). For both the partitions (the statement can be extended also to the Endcap Minus) the width of the distribution is around 100 ps (a possible jitter due to the electronics that does not affect the time resolution).

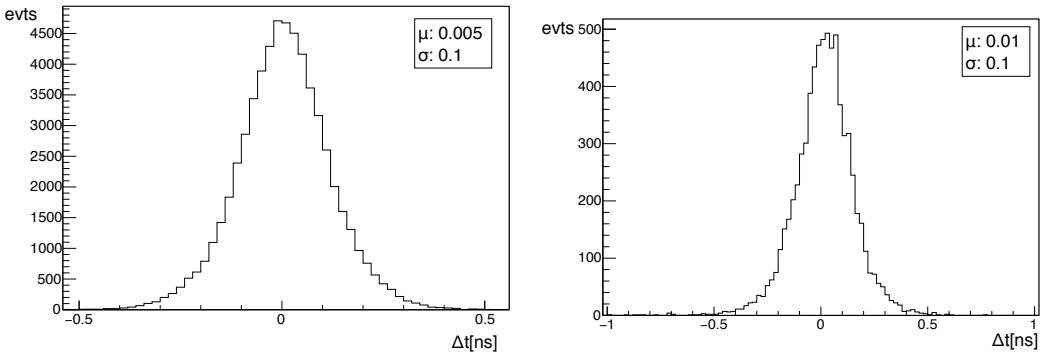

(a) (b)

Figure A.3.13: Timing difference 1D distribution in EB (a) and EE Plus (b)

A.3.4 Time calibration vs instantaneous luminosity study

LHC working period is scheduled by *Fills*. A *Fill* is a set of proton bunches that are injected in the machine and collides in the four experiments. As long as the *Fill* is stable[1] is kept circulating in the accumulation ring. At each turn, each bunch loses some protons (destroyed through collisions) until it is no more efficient to mantain the *Fill* in LHC ring. The number of interactions per bunch crossing can be measured using the Instantaneous Luminosity [$cm^{-2}s^{-1}$] and its behaviour (in this case, degradation) can be described by a descending exponential function as shown in Fig. A.14(a). As can be seen in Fig. A.14(b), it is proportional to the pile-up delivered by the machine and recorded by each experiment.

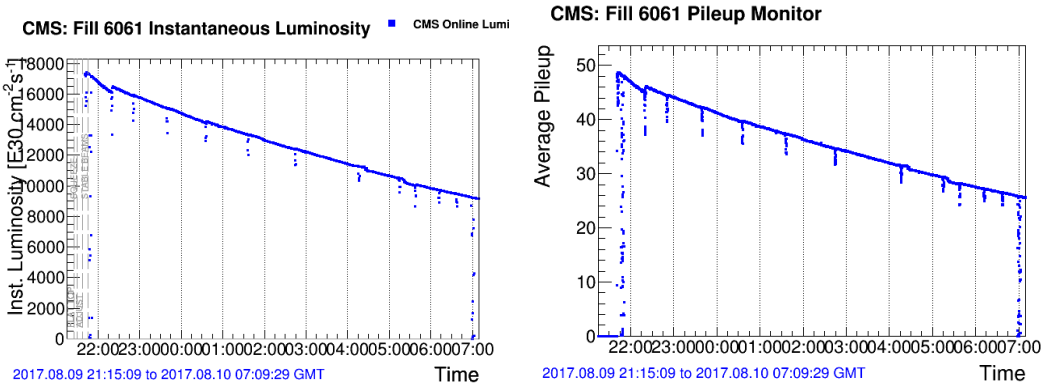

(a) (b)

Figure A.3.14: Instantaneous luminosity (a) and pile-up (b) for *Fill* 6061

As there is a connection (also if little), between pile-up and the time variable of this study, our aim in this case is to check any possible correlation between the time response and the beam degradation. To do so, we analyzed the time variable for runs which lasted for more than 12 hours trying to show its trend.

In Fig. A.3.15, two plots are reported. One (Fig. A.15(a)) that contains the subdetector timing response for three different long runs for all the events (except the ones contained in the single bunch) and another (Fig. A.15(b)) with the events selected by the LoneBunch trigger as a function of the Lumi Section[2] of the *Fill*. As already showed in Sec. A.3.3, the difference between the LoneBunch data and the rest is negligible, but it is interesting to see if the possible change of the time variable, related to the degradation of the beam, can affect both events with pile up and events of single crossing bunch.

[1] in a regime called: **STABLE BEAMS**

[2] A Lumi Section (LS) is a variable used to measure time during a *Fill* and is correlated to the luminosity delivered by the machine; it is a sub-section of a run during which time the instantaneous luminosity is unchanging, which corresponds to about 220 orbits ($\sim$ 93 seconds)

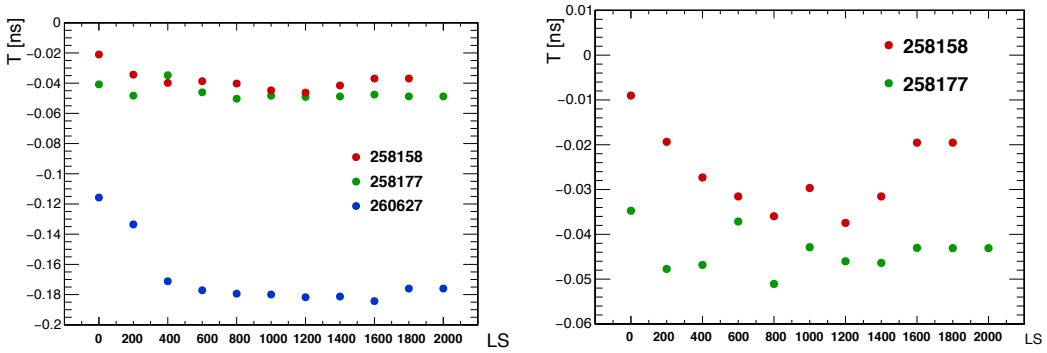

(a) (b)

Figure A.3.15: Time distribution vs lumi section for events without (a) and with (b) the LoneBunch trigger

In Fig. A.15(a), three runs are plotted. Actually, a change in time is visible, with a steep variation in the first 400 Lumi Sections. However, as the previous study on the LoneBunch effect, its magnitude is comparable to less than 200 ps and therefore is negligible. The results obtained in Fig. A.15(b), are not conclusive; an overall improvement in the stability of the time variable trend is visible, but the statistics (also if three of the longest *Fills* taken during 2016 data taking were used) is too small to give a definitive answer to the problem. Moreover only in two out of three runs analyzed the LoneBunch trigger was available.

A.3.5 Time calibration study using π_0

While for the official timing calibration extraction only charged particles of the PhiSymmetry also neutral particles as photons could be used. To evaluate possible differences and the performance of this method, the Pi0 (π_0) physics stream, mainly constituted by photons, has been used. The comparison has been made using the same run recorded by CMS and the PhiSymmetry events have been used as benchmark.
In Fig. A.3.16 the difference for the Barrel partition is showed. The difference in this case is:

$$\Delta T = time_{PhiSym} - time_{\pi_0} \tag{A.7}$$

Although in Fig. A.16(a), there is no clear bias that could affect the measurement of the IC with the π_0 dataset, in Fig. A.16(b), the difference is visible. The peak at 400 ps; a non negligible difference that cannot be underestimated.

The difference shown, depends mainly on the current method used to calculate the time variable in the ECAL reconstruction algorithm. The only difference

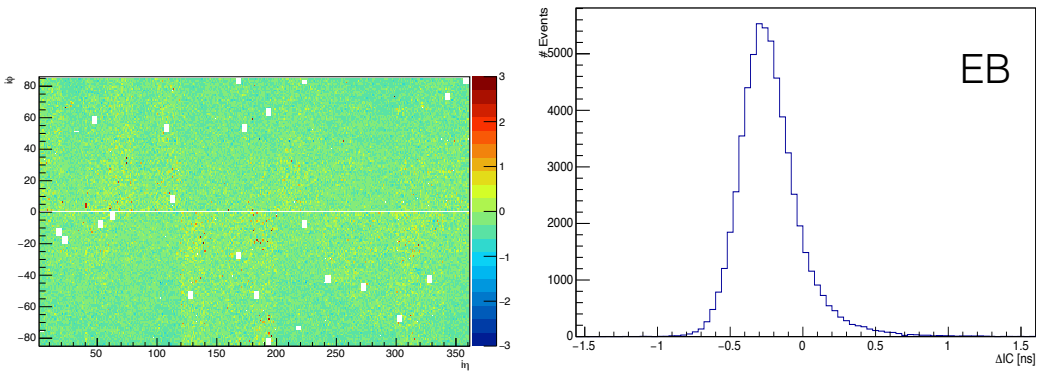

(a) (b)

Figure A.3.16: Time 2D distribution (a) and 1D distribution (b) of the difference between the PhiSymmetry and the π_0 stream

between the two datasets is the average energy of the signals (higher for the π_0 stream) and this can bring to big differences if the method and the selection of good events is maintained equal to the one used for the PhiSymmetry stream.

Appendix B

ECAL Barrel High Voltage Calibration and Monitoring

The barrel part of the electromagnetic calorimeter of CMS consists in 61200 crystals each read by two APD (Avalanche PhotoDiodes photodetectors) that need an efficient and accurate power supply to operate correctly. A new calibration system was deployed at the end of 2015 that reduce the time to be performed from about 1 month to about 1 week with half manpower improving precision and accuracy.

B.1 High Voltage System

The Electromagnetic Calorimeter of the Compact Muon Solenoid (CMS) [93] detector at the Large Hadron Collider at CERN is a hermetic homogeneous calorimeter [90] made of 61200 lead tungstate ($PbWO_4$) crystals mounted in the barrel part, closed by 7324 crystals in each of the two end-caps. The calorimeter is designed to perform precision measurements aiming to reach 0.5% energy resolution at high energy. The relatively low light yield of $PbWO_4$ (about 100 photons/MeV at 18°C) and the presence of a very intense magnetic field inside CMS (3.8 Tesla) have led to the choice of APDs (Avalanche Photo-Diodes) as photon sensors in the Barrel and VPTs (Vacuum Phototriodes) in the Endcaps.
The CMS APDs [94], produced by Hamamatsu Photonics, are silicon photodiodes with internal amplification. Two APDs are attached to each $PbWO_4$ crystal. They operate at gain M=50. Since the gain has a quite high dependence on the bias voltage ($\alpha V = 1/M \cdot dM/dV \simeq 3.1$ %/V at gain 50 as shown in Fig. B.1.1), the APDs require a very stable power supply system, as gain fluctuations directly contribute to the constant term of the energy resolution already described in this document. A custom high voltage (HV) power supply system has been designed for the CMS ECAL in collaboration with the CAEN Company. This chapter describes this HV system, its performances and its monitoring procedures as measured in laboratory tests, during test beam

operations of the calorimeter and after its installation at Point5 during daily ordinary operations.

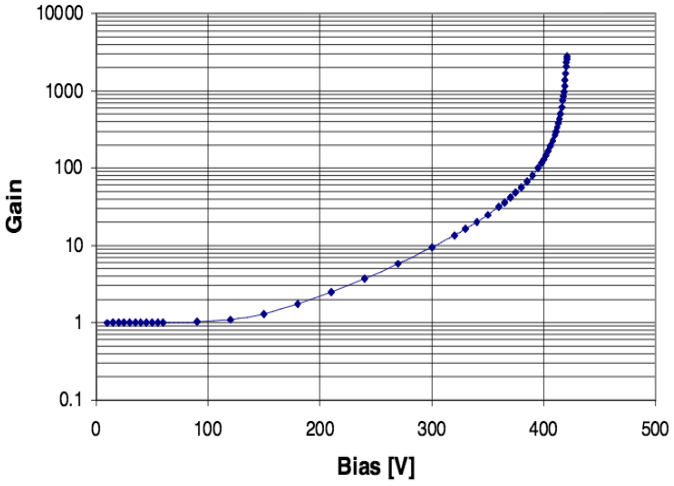

Figure B.1.1: Gain behaviour as a function of the APD's bias voltage

The APDs are Hamamatsu type S8148 reverse structure (i.e., with the bulk n-type silicon behind the p-n junction in order to reduce the nuclear counter effect) especially developed for the CMS ECAL. Each APD has an active area of 5x5 mm^2 and two of them are organized in a support (capsule) and glued to the back of each crystal. In total there are 122400 APDs. The operation at gain 50 requires a voltage between 340 and 430 V. The main electrical properties of the APDs at M = 50 and T = 18°C are reported in Table B.1.1.

Variable	value
Operating voltage [V]	380-430
Difference between breakdown voltage and operating voltage	45 ± 5
Voltage sensitivity of the gain (1/M·dM/dV)	3.1 ± 0.1%/V
Temperature sensitivity of the gain (1/M·dM/dT)	-2.4 ± 0.2%/°C
Maximum dark current (start of experiment) [nA]	< 50
Typical dark current (start of experiment) [nA]	3
Typical dark current after 2×10^{13} n/cm^2 [μA]	5

Table B.1.1: APD parameters

The stability of the bias voltage seen by the APDs, directly affects the constant term of the ECAL energy resolution through the voltage gain sensitivity. The design goal for the constant term is 0.5%, including all the contributions (e.g. channel intercalibration, light collection uniformity of the crystals, energy leakage). The contribution to the constant term, due to the HV stability, should not exceed 0.2%. To satisfy this request, the voltage stability has to be

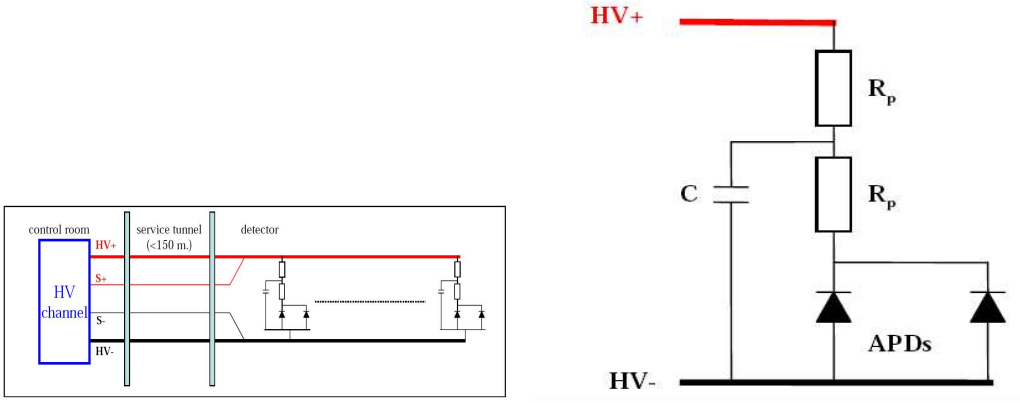

(a) (b)

Figure B.1.2: HV system scheme (a) and circuit scheme of the HV channels (b)

of the order of 60-65 mV (at M = 50 with 1/M·dM/dV = 3.1 m 0.1%/V). This requirement is applied to the combination of electrical system characteristics: noise, ripple, voltage regulation and absolute precision, for short and long term periods. This lead to a tolerance of ± 20 mV on each contribution.
To avoid the power supply radiation damage during LHC operation, the HV system is located in the CMS service cavern, around 120 m away from the detector. Logistic requirements (such as cabling or space in the patch panel) force to feed many APD pairs with the same HV source. The number of APD capsules sharing the same HV channel was then fixed to 50 (meaning 100 APDs). The APDs are sorted according to their operating voltage into bins 5 V wide; then the APDs of the same bin are paired into capsules, so that each pair has a mean gain of 50. As shown in Fig. B.2(b), each capsule receives the bias voltage through an RC filter network and two protection resistors (R_p = 68 k) to limit the bias current to 3 mA in case of APD breakdown. The HV channels must be floating; they use sense wire to correct for variations in the voltage drop on the leads. The architecture is shown in Fig. B.2(a).

The system developed by CAEN for CMS ECAL is based on a standard control crate (SY1527) hosting 8 boards A1520E expressly designed for this application. The SY1527 contains a micro-computer capable to communicate with the board controller via an internal bus and different interfaces are available to integrate the SY1527 on the ECAL detector control system (DCS). The board design is based on a modular concept so that each HV channel is implemented as a separate module and up to 9 channels can be hosted on a single HV board, thus permitting a major flexibility in case of channel failure. In total, the system is composed of 18 crates SY1527 and 144 boards A1520E. Each channel is designed to give a bias voltage to 50 capsules from 0 to 500 V with maximum current of 15 mA; this value allows an HV channel to work even in the case of short circuit of some of its APDs (four is the maximum, considering the maximal current over the protection resistors R_p).

The ECAL barrel consist of 2x18 mechanical units, called supermodules. All the connections are done through a patch panel at the outer end of the supermodule. As each supermodule of the calorimeter contains 1700 crystals, requiring 34 HV channels, taken from 4 boards (one spare channel out of two boards is left). The connection from the board (sitting in the service cavern) to the patch panel is made by custom 9-channel multiwire cables, produced on ECAL specifications by the firm Pansystem. On the other side of the patch panel, 4 bundles of 8 or 9 multiwire cables go to the so called motherboards, hosting the bias distribution circuits shown in Fig. B.2(b) and the connections to the Very Front End electronics (VFE). The motherboards are placed immediately outside the aluminium grid supporting the crystals. Each motherboard feeds through kapton cables a matrix of 5x5 crystals, corresponding to a trigger tower. Two motherboards are then connected in parallel to the same HV channel.

B.1.1 HV Boards

All the boards at P5 used as power supply for the APDs are *SY4527 Board A1520E* by CAEN^{TM}.

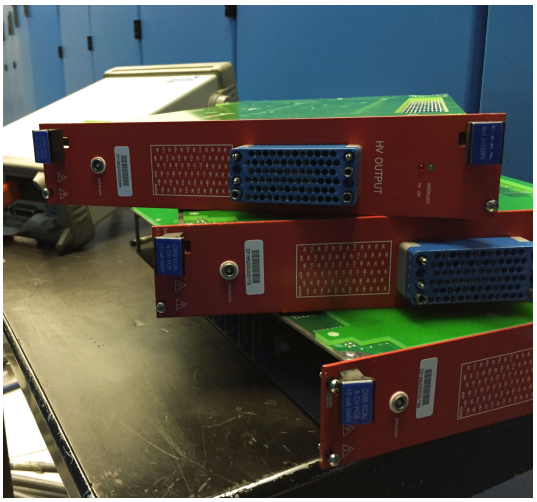

Figure B.1.3: HV board SY4527

Each board, can namely hosts a maximum of 9 channels. As already said, one SM contains 68 TTs, meaning 34 channels, half of the boards have 8 channels. The lemo cable for the interlock inhibition is plugged in the front-panel of the board and is connected also to the next board (to have a chain of lemo connectors plugged in all the crates' board and terminated with a 50 Ω resistor to close the circuit).
The blue female connector visible in Fig. B.1.3, is now connected to the Multi-Boxes: a new tool that will be described later in Sec. B.2.7 and shown in Fig. B.2.6.

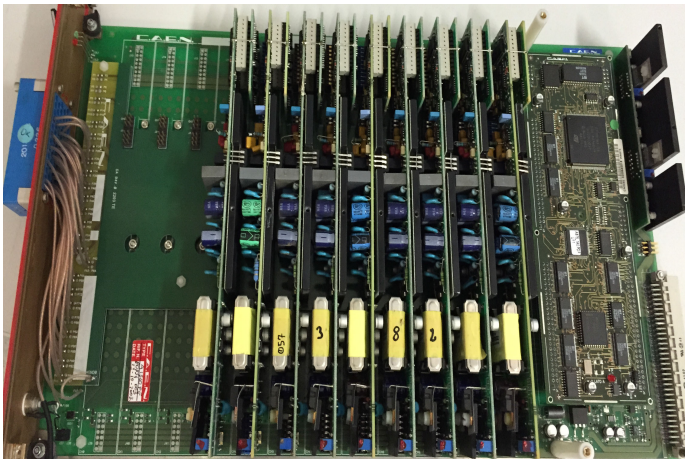

Figure B.1.4: HV board SY4527 - inside details

B.1.2 HV Channels

The HV channels are the main part of the APD Power Supply system of the CMS Ecal Barrel. Their location inside the board is shown in Fig. B.1.4. We start counting (from channel n° 0) from the left. So, the first channel is the closest to the board front-panel. In the example is shown a board completely full (9 channels), without the side-panel coverage. If a channel needs some intervention (or has to be replaced), the board has to be unscrewed from the crate and then opened as the one in the example.
The ground connection is the metallic ring with a thick black cable visible in the low left side of the Fig. B.1.5. It has been introduced to reduce the noise caused by the hardware itself during the first installation of the HV system and it is connected directly to the HV board frame with a screw.

B.1.3 Integration in the ECAL DCS system

The ECAL detector control system (DCS) [91] comprises the monitoring of the detector status, in particular various kinds of environmental parameters, as well as the detector safety system (DSS), which will generate alarms and hardwired interlocks in case of situations which could lead to damaging the detector hardware. The whole DCS software is based on the commercial SCADA package PVSS II [95]. A distributed system is built out of several applications dedicated to the DCS sub-systems. Every application is implemented as a Finite State Machine (FSM) and linked to a supervisory level, which summarizes the overall ECAL DCS status and itself incorporates a FSM. Finally, this ECAL DCS supervisor is linked to the general CMS DCS supervisory node, in

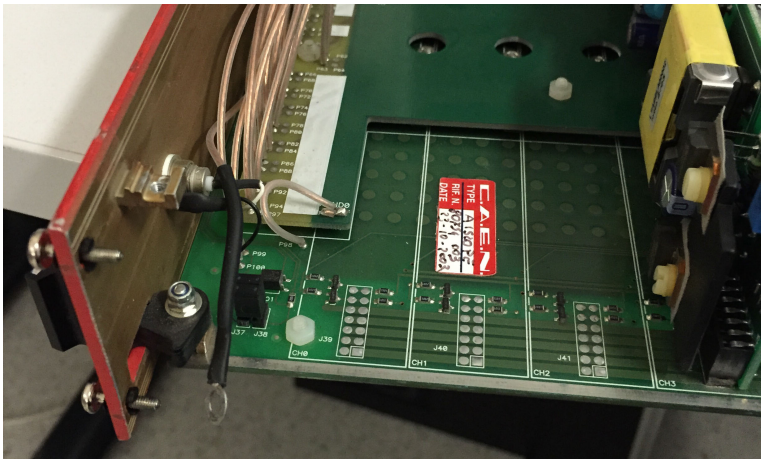

Figure B.1.5: HV board SY4527 - ground connection

order to communicate the status and alarms and to receive commands which are propagated down to the relevant sub-systems.
The HV is controlled by one of these applications, with a dedicated FSM. The PVSS application communicates with the crate via the CAEN OPC server using the TCP/IP connection. The functionalities of this application allow part of or the whole detector to be turned on and off, the monitoring of the currents and voltages of each channel, displaying plots of their history and the configuration of the HV channels with various sets of voltages. The ECAL PVSS application uses a configuration database to store the values of the high voltages for various configurations and a condition database to store the monitored values of the currents and voltages and the actual HV sets used.
The ECAL Safety System in case of need can switch off the HV system either via the crate interlock located in the front panel or via the individual board interlocks. The latter solution allows the flexibility to turn off all the channels of the same supermodules at a time and has been adopted for this experiment.

B.1.4 Stability Test

An acceptance test on the long term stability is performed on each A1520E board on reception. The test foresees setting a voltage (V_{set}) of 380 Volt with a load of 33 kΩ; the corresponding output voltages of the 9 channels are measured every 10 minutes, for around 30 days. Two examples of the output, measured as a function of time, are shown in Fig. B.1.6: on the left a stable channel, while on the right the channel presents a drift during the test. In both cases the day-night variations are clearly visible. The temperature in the laboratory is measured by 5 sensors located around the crate. Day-night variation and voltage-temperature correlation are shown in Fig. B.1.7; in the right plot, a temperature sensitivity of the voltage well inside the specifications is observable (slope of the fit: dV/dT → 3 mV/°C).

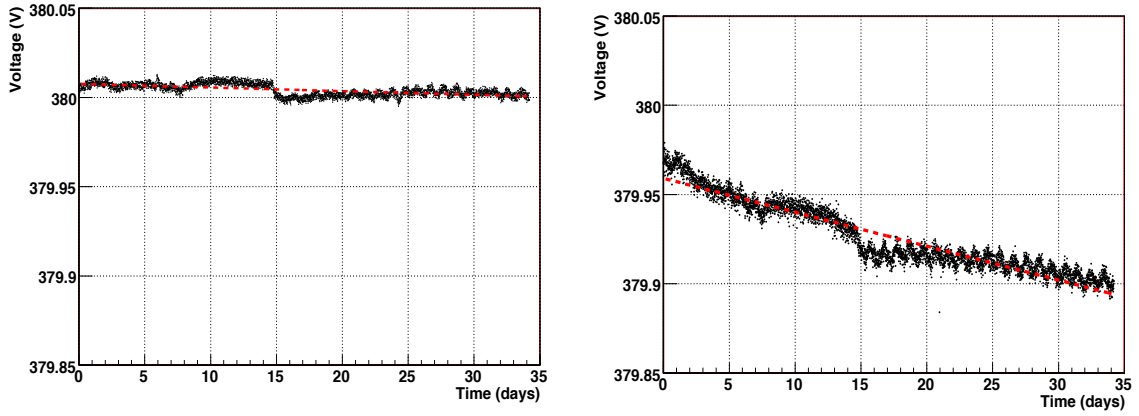

Figure B.1.6: Stability tests for two different channels (stable on the left plot, unstable on the right plot)

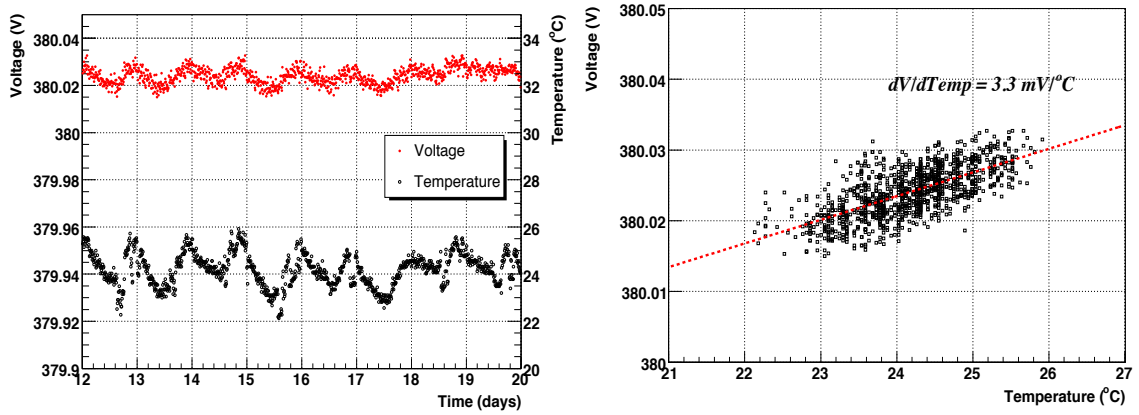

Figure B.1.7: Average of the 5 temperature measurements obtained by the temperature sensors located in the laboratory and voltage measurements on the left, while on the right voltage values vs temperatures are shown

With the APD working at gain 50, a variation of the bias voltage of 65 mV corresponds to 0.2% variation in the gain, going directly in the constant term of the ECAL energy resolution. In almost all the channels which present a variation greater than 65 mV, the voltage measurements show a clear drift upwards or downwards and not a gaussian-like behaviour; this is due to a drifting component in the channel. A channel is accepted if, after the fit of V(t) with a first order polynomial, the following conditions are satisfied:

1. V_{max} = max(|V (t) - 380.0|) < 65 mV
2. fit slope < 2 mV/day

The distribution of ΔV_{max} is shown in Fig. B.1.8 for all the channels; the temperature variation effect is not taken into account.
All the data, collected during the stability test, are inserted in a mysql database

called Redacle [96]; this database has been originally developed by the Rome Group for the ECAL construction activities performed in the INFN/ENEA Regional Center. A different version of Redacle, adapted for the High Voltage system, is used to trace the crate locations, to mantain the correspondence between boards and crates and to collect the stability test data.

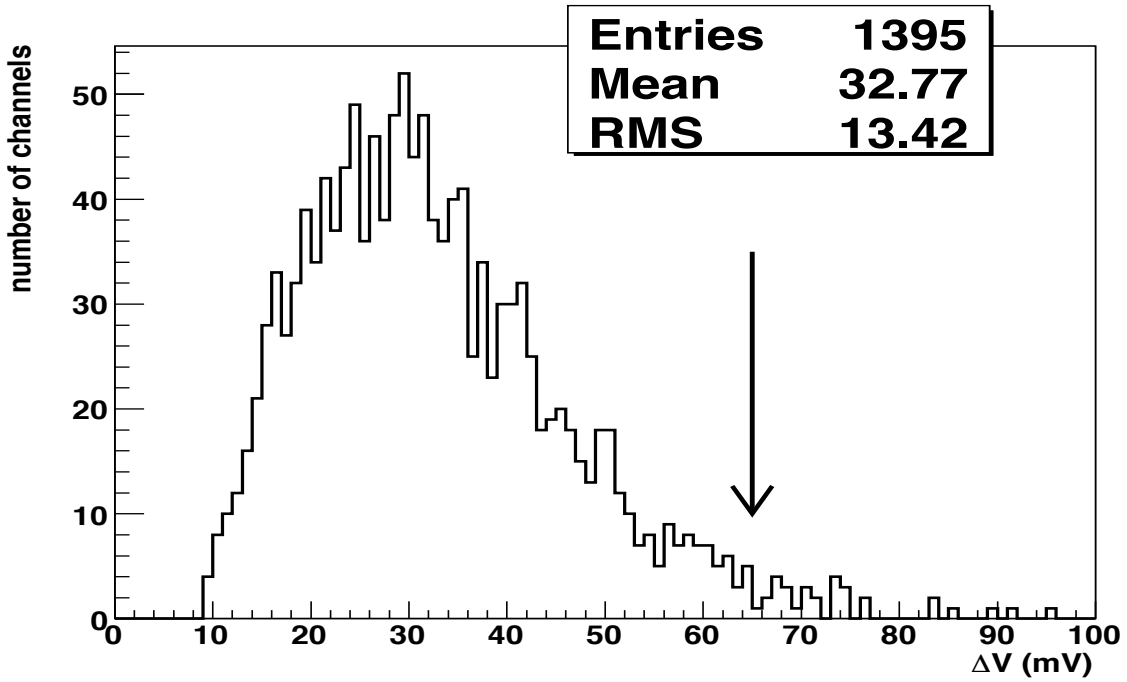

Figure B.1.8: Distribution of V_{max}, the maximum difference between measured Voltage and V_{set}; the channels having a value greater than 65 mV (shown by the black arrow) are rejected

B.1.5 Performance of the High Voltage system in CMS Test Beam

During 2004 the first full ECAL supermodule was tested for a few weeks with high energy electrons at the H4 beam line at CERN. During 2005 and 2006, the beam setup was used to take cosmic ray data with several supermodules in order to calibrate the crystals. In 2006, new beam tests were made with several supermodules. All these tests were done with the final ECAL electronics, a precise cooling system, the laser monitoring and the final HV system installed with full length cables (120 metres).
In the beam tests, the APDs were biased at nominal gain 50, while, in the cosmics calibration set-up, the APDs were biased with gain 200, to be able to select single crystal cosmics by vetoing on the surrounding ones. In all these tests the noise performance of the ECAL was very good and the average

noise was, as expected, around 40 MeV in the single crystal [91]. This noise performance meets the design goal. A test beam with high energy electrons was done, during summer 2006, on supermodule number 22 (SM22) in order to inter-calibrate the crystals. The test was repeated twice, with a delay of 45 days between the two tests. The width (σ) of the relative difference distribution between the two calibrations averaged over each HV channel, versus the HV channel number is about $\sigma \simeq 0.1\%$. The result showed that the long term stability and reproducibility of the HV system is well within the hardware specifications and requirement.

B.1.6 Old Calibration Procedure

In order to avoid the introduction of noise in the calorimeter signal measurement, the HV system was not equipped with a continuous monitoring system. Therefore, a periodic monitoring and calibration campaigns are performed every year.
The old calibration was done mainly manually in each of its steps. Each board was calibrated using another board specifically designed for this purpose. It contains 9 channels with a 33 kΩ resistor each that are latched to a HV board with a particular cable. The calibration board has to be plugged in a crate so, it takes the place of an already present HV board. This procedure takes time to unplug and plug the HV board to replace it temporally with the calibration one. These continuous movements of the HV board could damage the board or its back panel pins causing possible errors in the connection with the crate or HV channel failure that can be solved only with the channel replacement.

B.2 New Calibration Procedure

A new calibration system was deployed at the end of 2015. It consists of mechanical switches connecting the HV cables to the calibration system, guaranteeing that no additional noise is introduced. Calibration cables draw the bias to a precision multimeter through a set of multiplexers. The calibration program cycles through all the channels allowing both to measure the voltage and to recalibrate the channels one by one following an automatic customized routine.

B.2.1 HW System

The main purpose of the Calibration program is to simplify and make the High Voltage Calibration faster, so that the 3 weeks campaign of the old calibration can be reduced to 3-4 days of work and a crew of 10-12 people can be reduced to 2-3. This goal can be achieved using some hardware components that have

been installed and tested during 2015.
The calibration chain, on the hardware side is quite simple; for each EB side (plus and minus):

- One Digital MultiMeter (DMM);
- Four Cytec Mainframes;

B.2.2 Digital Multimeter

The two Digital Multimeters are already in the service cavern, located in the central racks of EB+ and EB-. They both are $8\frac{1}{2}$ digis *3458A Digital Multimeter* from Keysight Technologies^{TM}.

Figure B.2.1: 8 digis Digital Multimeter

The input of these devices is directly connected to the Cytec mainframes (Sec. B.2.3) and can monitor only one HV channel at a time.
They are programmed via visa and visacom libraries that provide tools for the communication between the PC (running Windows) and the Multimeter and the datataking (measurements). Of course their main job is to read Voltage and Current values from the channel that is going to be calibrated or just *checked*.
As a backup solution, that can be chosen from the program, there is also the possibility to use another DMM: 6 digis *34401A Digital Multimeter* always by Keysight Technologies^{TM}.
It can be used on-the-fly and it isn't present in the cavern. The program can be used without any problem with both these devices.

B.2.3 Cytec mainframes

The connection between the HV channel and the Multimeter is done using a Multiplexer device. It is an array of switches that can be latched or unlatched to a *main* connector which is the DMM input.

Figure B.2.2: Cytec Mainframe

It is a matrix (or a sum of matrices), containing many slots with a fixed number of switches. The protocol used for communication uses TCIP language and functions. For every part of the program related to these devices we followed the Cytec guidelines. After the initialization of the module and the connection (ConnectToTCPServer) a single write command (ClientTCPWrite) to prevent any possible overwriting of the commands sent.
The main logistical issue is related to the number of Cytec mainframes (four for each EB side) and the number of DMM's input (only one). The solution used is to connect all the mainframes common connector (a line that connects any board of the same mainframe) to a single board (called "star" board) in a mainframe located under the DMM. To access a single HV channel, the program will latch the corresponding cytec channel corresponding to the HV one and the channel of the "star" board corresponding to the cytec mainframe to connect the HV channel to the DMM.

The main problem is related to different switches latched at the same time. If two or more switches are latched together and at least one of the HV channels connected is On, the mainframes and the channels will be damaged as they'll be in short. To prevent this type of accidents, there is a security protection in the program that controls the DMM voltage readings before latching a new channel and that automatically open any possible connection with a single command for each mainframe until the DMM voltage readings are compatible with 0 Volts or noise-only signals.

B.2.4 Terminal Service

Before describing the real program, here is a very short outline of the framework where it is installed: the CMS' *Terminal Service*. It is a Windows™ based system which can be accessed only through the CMS P5 network to prevent any possible undesired connection to the system from outside. It is installed in a VM running on a CMS "physical" PC. Any activity regarding the Calibration program can be performed through a Visual Studio package already installed on it.

B.2.5 HV Wrapper Library

The High Voltage calibration program relies on a dedicated library. It is a tool developed by CAEN that permits communication between a Windows PC and a CAEN system that in our case is an HV crate *SY4527* equipped with *Board A1520E*.
It contains all the functions that are used in the Calibration program. Below a list of the functions mainly used:

- CAENHV_InitSystem: its inputs are the board model, a value needed to be 0, the crate IP, the username and password to access the crate and to create the handle variable which is needed for further operations
- CAENHV_GetCrateMap: this function is used to set a number of variables that identify the crate module. Its only input is the handle that have to be created before
- CAENHV_GetChParam: this function is one of the most important one in our set. Because its output is the value of an internal parameter of the CAEN board. It is mainly used to know if the channel is On, the V_{Mon} and other vital parameters of the channel
- CAENHV_SetChParam: any instruction to the channel will be sent through this command

There is a function meant for closing correctly the connection with the crate: CAENHV_Free.
Below, the sequence of the important status bits contained in the channel buffer and that can be read to know some information about it, is reported:

0	**ON /OFF**	8	External Disable
1	Ramp Up	9	Internal Trip
2	Ramp Down	10	Calibration Error
3	OverCurrent	11	**Unplugged**
4	OverVoltage	12	UnderCurrent
5	UnderVoltage	13	OverVoltage Protection
6	External Trip	14	Power Fail
7	Over HV_{max}	15	Temperature Error

The bolded bits have been used mainly for the calibration. The procedure will be described in details in the following Sections. A channel is considered ready to be calibrated when the Status variable is 2049 (in decimal units) so

when is ON (first bit = 1) and Unplugged (twelfth bit = 1): 1000000000010000.

B.2.6 Calibration Program

The program is completely written in c++ following the CAEN prescriptions and is divided in subroutines that can handle and manage any part of the calibration.
Its main purpose is to undergo each procedure to launch the calibration steps in the safest way for the user and the hardware system. The real procedure consists in an automatic sequence of readings and settings that will be described in the following and that are contained in the channel firmware.

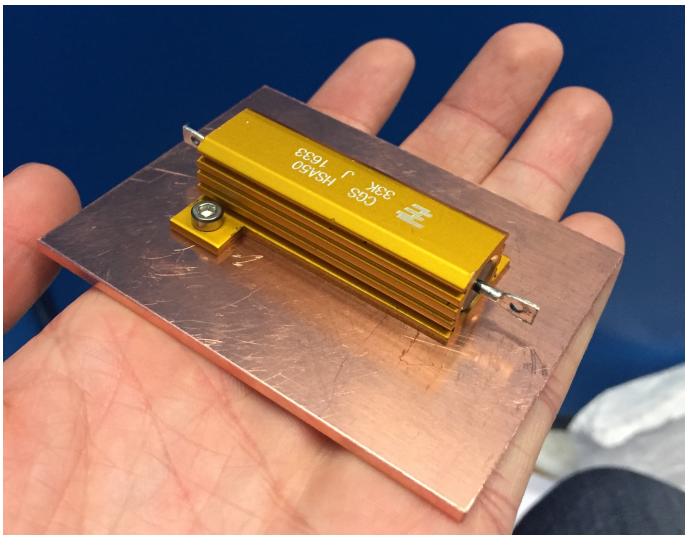

Figure B.2.3: Load used for the new Calibration procedure. The copper plate dissipates the heat generate by the current passing through the resistor preventing any possible changes of the Ω value (33 kΩ)

B.2.7 Calibration Description

The basic idea of the calibration campaign is fairly simple. Inside each HV channel there is a little Voltmeter which reads the voltage and stops the HV ramp when it reaches the right value (the one you have set). The problem is that this Voltmeter doesn't have a global scale. Moreover it actually could be uncalibrated (stopping the ramp to the wrong value meaning a wrong gain of the APD). What we need to do, once in a while, is to connect an external DMM (more accurate) and state to the channel at what voltage it is.
To keep the automatic calibration procedure safe for the whole detector, Multiboxes have been introduced. If the HV of a channel is ON, also the Low Voltage has to be ON to prevent any possible failure or damage to the photo-detectors.

However the two systems are completely separated and therefore the interventions on any of the two systems has to be agreed before with the other one. The use of the Multiboxes erased this problem. In Fig. B.2.4, they are shown during a phase of the installation. They are big switches, that can operate and bear high voltages/currents and can direct the HV from the CAEN channels to the APDs (meaning CMS) or to the Cytec mainframes.
The Multiboxes are plugged in the blue female connector that can be seen clearly in Fig B.1.3. The connection is done using 4 screws with an octagonal head to have an easier grip using a screwdriver.

Figure B.2.4: P5 HV racks during the first installation of the Multiboxes in 2015

The Multiboxes' outputs are 2. One is a big grey cable with a red line that goes down to CMS. The other one is the connector to the Cytec mainframe (Fig. B.2.6).
While the first one has been used also in the old configuration (where the HV channels were connected only and directly to CMS), the second one is completely new and has been designed for this specific purpose.

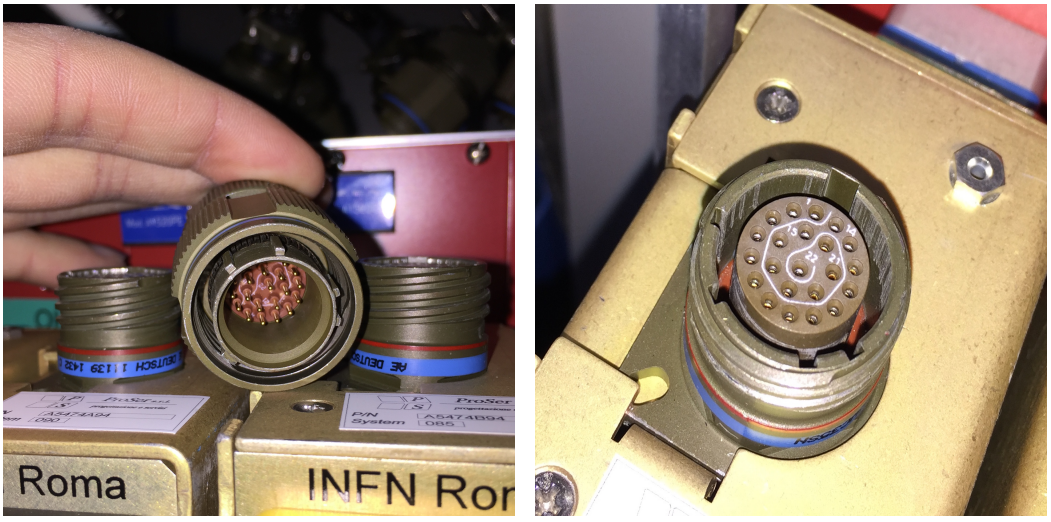

(a) (b)

Figure B.2.5: Male (a) and female (b) plugs for the channel-cytec connection

It is a quite complicated, military-derived cable (Fig. B.2.5) that provides the connection between the HV channel and the correct Cytec mainframe. Moving the lever of the Multiboxes up or down will give power to the APDs or direct the voltage to the cytec mainframes.

Figure B.2.6: MultiBoxes - front view

The plane connector brings the voltage from the Cytec (so from the HV channel) to the DMM. The polarity is very important as some decision in the program are taken in respect to the voltage read by the DMM, so if the cable is not connected properly and the DMM reads a negative voltage, the program will give an **EXIT_FAILURE** signal thinking that the channel is broken (as the DMM voltage value is very different from the Voltage *Mon* and *Set* of the HV channel).
The red line visible in Fig. B.2.7 of the plane connector corresponds to the

+ voltage and it has to be placed UP when the cable is plugged in the Cytec *main* connector.

Figure B.2.7: DMM - Cytec connection[1]

B.2.8 Calibration Procedures

The procedure itself is not under the control of the ordinary user. Once the channel is in the correct[2] state, the calibration procedure can be started.
It is prompted from an internal command sent by the Calibration program and it consists in 10 different steps. Each step is a different voltage value. The HV channel is ramped to the pre-decided value and the V_{mon} (which is the value read by the internal Voltmeter of the channel) is compared with the external DMM value. As the DMM value is considered to be more accurate with respect to the V_{mon} one, it is used[3] to calibrate the HV channel. The ten steps go from 94 Volts to more than 500 Volts to create a calibration curve that covers the operation voltages of the system (which is below 450 Volts) and extract the voltages corrections extracted internally by the board and used to calibrate the channel.

B.2.9 Calibration Advantages

In the end the most visible effect and benefit of the new calibration procedure is directly connected with the time used to perform each step for the whole central part of the calorimeter.
This great reduction in terms of time, allows the possibility to perform not

[2]working and ready to be calibrated
[3]writing it in the HV channel buffer

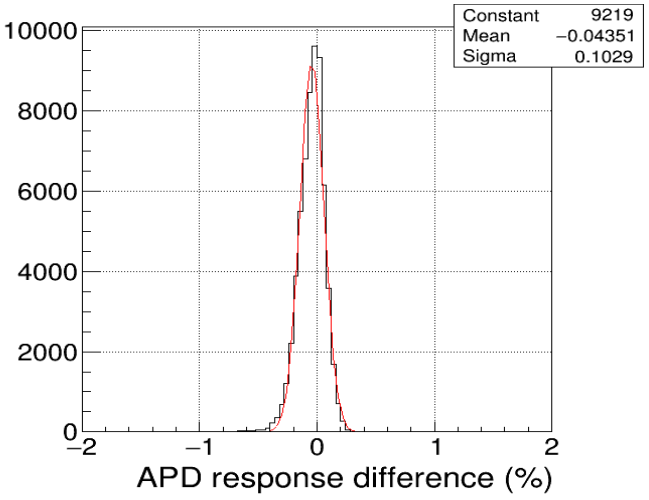

Figure B.2.8: Difference between the old and the new calibration method

only the calibration more than once in a year, but also to monitor each channel more systematically during the Technical Stops or Machine Development periods when LHC does not provide protons or collisions and the detectors are focused on repairing or upgrading issues (leaving the HV and LV free from any datataking responsibilities).
Moreover, the whole procedure can guarantee a better response and performance as it uses more sophisticated instrumentation with respect to the previous version; the old DMM with 6 digis has been replaced by a new one with $8\frac{1}{2}$ digis accuracy improving the readout of each channel.
The last thing that should not be underestimated is the crew needed for the calibration. A reduction of 50-60% is a big step forward the complete automatisation of the complete chain of monitoring and calibration, simplifying the work done by the HV crew.

Appendix C

Statistical Interpretation

In particle physics experiments especially after the discovery of the Higgs boson, often searches for processes that have been predicted but not yet seen. The statistical significance of an observed signal can be quantified by means of a p-value or its equivalent Gaussian significance [97] so it is important to characterize the sensitivity of an experiment by reporting the expected (e.g., mean or median) significance that one would obtain for a variety of signal hypotheses and extracting a limit on a particular physics variable.
Finding both the significance for a specific data set and the expected significance can involve Monte Carlo calculations that are computationally expensive. In this paper we investigate approximate methods based on results due to Wilks [98] and Wald [99] by which one can obtain both the significance for given data as well as the full sampling distribution of the significance under the hypothesis of different signal models, all without recourse to Monte Carlo. In this way one can find, for example, the median significance and also a measure of how much one would expect this to vary as a result of statistical fluctuations in the data.
A useful element of the method involves estimation of the median significance by replacing the ensemble of simulated data sets by a single representative one, called Asimov data set, which however, in this particular case, has only be used for sanity checks and not for the Zγ analysis.
For purposes of discovering a new signal process, one defines the null hypothesis, H_0, as describing only known processes, here designated as background. This is to be tested against the alternative H_1, which includes both background as well as the sought after signal. When setting limits, the model with signal plus background plays the role of H0, which is tested against the background-only hypothesis, H_1.
To summarize the outcome of such a search one quantifies the level of agreement of the observed data with a given hypothesis H by computing a p-value (a probability), under the assumption of H, of finding data of equal or greater incompatibility with the predictions of H. The measure of incompatibility can be based, for example, on the number of events found in designated regions of certain distributions or on the corresponding likelihood ratio for signal and background. One can regard the hypothesis as excluded if its p-value is ob-

served below a specified threshold. In particle physics one usually converts the p-value into an equivalent significance, Z, defined such that a Gaussian distributed variable found Z standard deviations above its mean has an upper-tail probability equal to p (a 5σ significance corresponding to p = 5.7 x 10^7). Where Z is defined as: $Z = \Phi^{-1}(1-p)$. Where Φ^{-1} is the quantile of the standard Gaussian distribution.
A widely used procedure to establish discovery (or exclusion) in particle physics is based on a frequentist significance test using a likelihood ratio as a test statistic. In addition to parameters of interest such as the rate (cross section) of the signal process, the signal and background models will contain in general nuisance parameters whose values are not taken as known a priori but rather must be fitted from the data.
To illustrate the use of the profile likelihood ratio, consider an experiment where for each selected event one measures the values of certain kinematic variables and thus the resulting data can be represented as one or more histograms. Using the method in an unbinned analysis is a straightforward extension. If for each event in the signal sample one measures a variable x and uses these values to construct a histogram $n = (n_1, \ldots, n_N)$. The expectation value of n_i can be written as $E[n_i] = \mu s_i + b_i$ where the mean number of entries for the signal is:

$$s_i = s_{tot} \int_{bin\, i} f_s(x; \Theta_s) dx \tag{C.1}$$

and the mean number of entries for the background is:

$$b_i = b_{tot} \int_{bin\, i} f_b(x; \Theta_b) dx \tag{C.2}$$

Here the parameter μ determines the strength of the signal process, with $\mu = 0$ corresponding to the background-only hypothesis and $\mu = 1$ being the nominal signal hypothesis. The functions $f_s(x; \Theta_s)$ and $f_b(x; \Theta_b)$ are the probability density functions (pdfs) of the variable x for signal and background events and Θ_s and Θ_b represent parameters that characterize the shapes of pdfs, while the quantities s_{tot} and b_{tot} are the total mean numbers of signal and background events.
The likelihood function is the product of Poisson probabilities for all bins and can be written as:

$$L(\mu, \Theta) = \prod_{j=1}^{N} \frac{(\mu s_j + b_j)^{n_j}}{n_j!} e^{-\mu s_j + b_j} \prod_{k=1}^{M} \frac{u_k^{m_k}}{m_k!} e^{-u_k} \tag{C.3}$$

Therefore, to test a hypothesized value of μ we consider the profile likelihood ratio:

$$\lambda(\mu) = \frac{L(\mu, \Theta'')}{L(\mu', \Theta')} \tag{C.4}$$

where Θ'' in the numerator is the value of Θ that maximizes the likelihood L for the specified μ (it is the conditional Maximum-Likelihood estimator of Θ).

The denominator is the maximized (unconditional) likelihood function. μ' and Θ' are their Maximum-Likelihood (ML) estimators. The presence of the nuisance parameters broadens the profile likelihood as a function of μ relative to what one would have if their values were fixed. This reflects the loss of information about μ due to the systematic uncertainties.

C.1 Test statistics for upper limits

In this brief document only this particular case will be analyzed as the Zγ search has not bee traduced into a discovery, but into upper limits.
The test statistics in this case is defined as:

$$q_\mu \begin{cases} -2ln\lambda(\mu) & \mu' \leq \mu \\ 0 & \mu' > \mu \end{cases} \tag{C.5}$$

where $\lambda(\mu)$ is the profile likelihood ratio defined in Eq. C.4. The reason for setting $q_\mu = 0$ for $\mu' > \mu$ is that when setting an upper limit, one would not regard data with $\mu' > \mu$ as representing less compatibility with μ than the data obtained and therefore this is not taken as part of the rejection region of the test. From the definition of the test statistic one sees that higher values of q represent greater incompatibility between the data and the hypothesized value of μ. One should note that q_0 is not simply a special case of q_μ with $\mu = 0$, but rather has a different definition (see Eq. C.5). That is, q_0 is zero if the data fluctuate downward ($\mu' < 0$), but q_μ is zero if the data fluctuate upward ($\mu' > \mu$). As with the case of discovery, one quantifies the level of agreement between the data and hypothesized μ with p-value. For an observed value $q_{\mu,obs}$, one has:

$$p_\mu = \int_{q_{\mu,obs}}^{\infty} f(q_\mu \mid \mu) dq_\mu \tag{C.6}$$

Which can be expressed as a significance the expression of Z written in the first part of this Section. Here $f(q_\mu \mid \mu)$ is the pdf of q_μ assuming the hypothesis μ. As a final aspect, assuming the validity of the Wald approximation, we can write the test statistic used for upper limits, Eq. C.5 as:

$$q_\mu \begin{cases} \frac{(\mu - \mu')^2}{\sigma^2} & \mu' < \mu \\ 0 & \mu' > \mu \end{cases} \tag{C.7}$$

where μ' follows a Gaussian centred about μ_m with a standard deviation σ. The pdf $f(q_\mu \mid \mu_m)$ is found to be:

$$f(q_\mu \mid \mu_m) = \Phi\left(\frac{\mu_m - \mu}{\sigma}\right)\delta(q_\mu) + \frac{1}{2}\frac{1}{\sqrt{2\pi}}\frac{1}{\sqrt{q_\mu}} exp\left[-\frac{1}{2}\left(\sqrt{q_\mu} - \frac{\mu - \mu_m}{\sigma}\right)^2\right] \tag{C.8}$$

so that if $\mu = \mu_{\rm m}$, it is a half-chi-square distribution:

$$f(q_\mu \mid \mu) = \frac{1}{2}\delta(q_\mu) + \frac{1}{2}\frac{1}{\sqrt{2\pi}}\frac{1}{\sqrt{q_\mu}}e^{-q_\mu/2} \tag{C.9}$$

the cumulative distribution can be written as:

$$F(q_\mu \mid \mu_m) = \Phi\left(\sqrt{q_\mu} - \frac{\mu - \mu_m}{\sigma}\right) \tag{C.10}$$

which for the case $\mu = \mu_{\rm m}$, is $\mathrm{F}(\mathrm{q}_\mu \mid \mu = \Phi\left(\sqrt{\mathrm{q}_\mu}\right)$.
The p-value is, for the hypothesized μ:

$$p_\mu = 1 - F(q_\mu \mid \mu) = 1 - \Phi\left(\sqrt{q_\mu}\right) \tag{C.11}$$

with the corresponding significance of:

$$Z_\mu = \Phi^{-1}(1 - p_\mu) = \sqrt{q_\mu} \tag{C.12}$$

if the p-value is found below a specified threshold α (often one takes $\alpha = 0.05$), then the value of μ is said to be excluded at a confidence level (CL) of 1 - α. The upper limit on μ is the largest μ with $\mathrm{p}_\mu \leq \alpha$. Here this can be obtained simply by setting $\mathrm{p}_\mu = \alpha$ and solving for μ finding:

$$\mu_{up} = \mu' + \sigma\Phi^{-1}(1 - \alpha) \tag{C.13}$$

For example, $\alpha = 0.05$ gives Φ^{-1}(1-α) = 1.64. Also as noted above, σ depends in general on the hypothesized μ. Thus in practice one may find the upper limit numerically as the value of μ for which $\mathrm{p}_\mu = \alpha$.

Appendix D

Analysis Addendum

In this Appendix, sanity checks and additional studies performed for the $Z/W\gamma$ analysis are presented. Further tests on the goodness of fit not reported in Chapter 6 and the synchronization done with the analyzers who developed the first $Z\gamma$ analysis is also presented.

D.1 Jet substructure selection improvement

The introduction of a new requirement based on the jet substructure variable described in Sec. 4.13 improved the sensitivity of the Zγ analysis. A preliminary study based on the expected limits is shown in Fig. D.1.1.

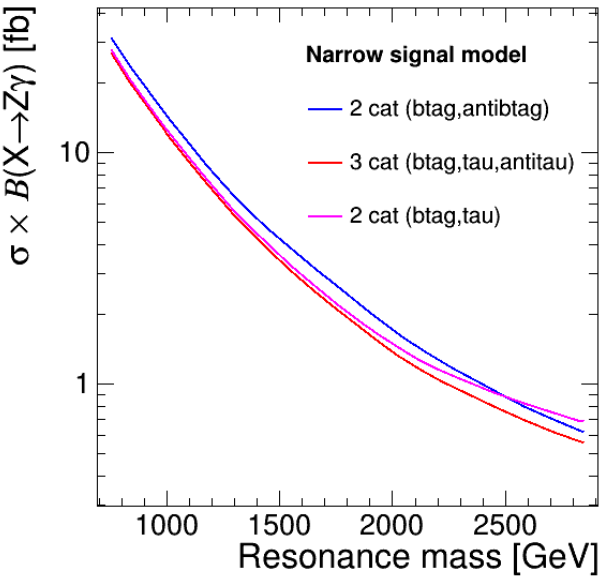

Figure D.1.1: Expected limits for 2 and 3 categories scenario for the Zγ analysis

In Fig. D.1.1, the expected limits for the 2 (blue) and 3 (red) categories are shown. As can be seen, there is a non-negligible improvement resulting in better limits of the cross section production for different masses of a Zγ resonance.

D.2 Analysis synchronization

Before performing the analysis using the Z/W framework, a validation and synchronization has been performed. Here, in Fig. D.2.1, the expected limits of the official analysis and the ones obtained with the new framework are compared and superimposed.
As a first step to prepare the combined analysis for the Z/W+γ hadronic signature, the Z+γ results have been reproduced using a different analysis framework. In Fig. D.2.1 the combined limit is reported. In blue the expected limits of the official analysis and in black the limits obtained with a different framework meant for the Z/Wγ analysis.

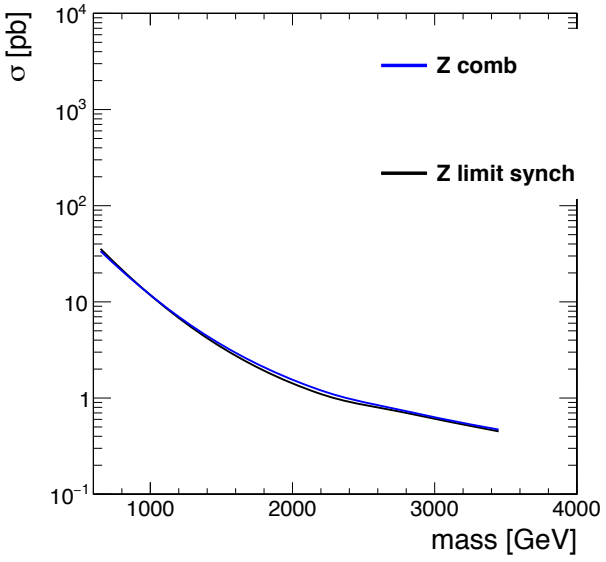

Figure D.2.1: Expected limits comparison for the Z+γ analysis with the old (blue line) and the new (black line) frameworks

As can be seen from Fig. D.2.1, the two results are comparable proving that the new framework can reproduce the old results.

D.3 B-tag requirement study

As a preliminary check, the Zγ standalone analysis has been carried on also with another requirement for the b-tag category. The previous analysis required a sort of double b-tag signature in the AK08 jet, selecting only AK08

jet with two b-tagged subjet. Another option, studied here, is to require that the AK08 itself presents a b-tag signature using the CSV directly on this wide-jet.

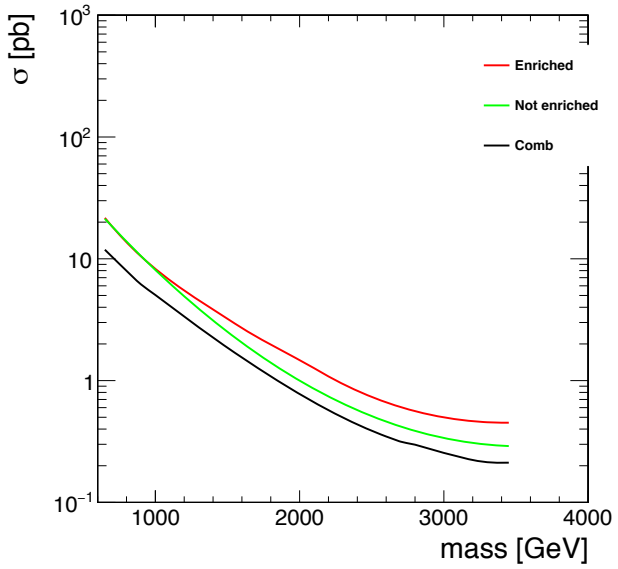

Figure D.3.1: Expected limits for the Z+γ analysis in the enrich/not enrich and combined categories using the single ak08 btag requirement

The plots in Fig. D.3.1, are obtained combining the separate results of the three categories combination for each of the two mass category. Their expected limits are shown in Fig. D.3.2 and bring a enhancement of the limit of about 50% (comparing the blue line in Fig.D.2.1 and the black line in Fig. D.3.1). The A$\times\varepsilon$ distribution, obtained in the same way as the one already reported for the Z standalone analysis is reported in Fig. 6.18. Moreover, as can be seen comparing Fig. 6.18(a) with Fig. D.3.3, the btag category in the enrich region has a higher efficiency due to the less stringent requirements on the b-tag AK08.

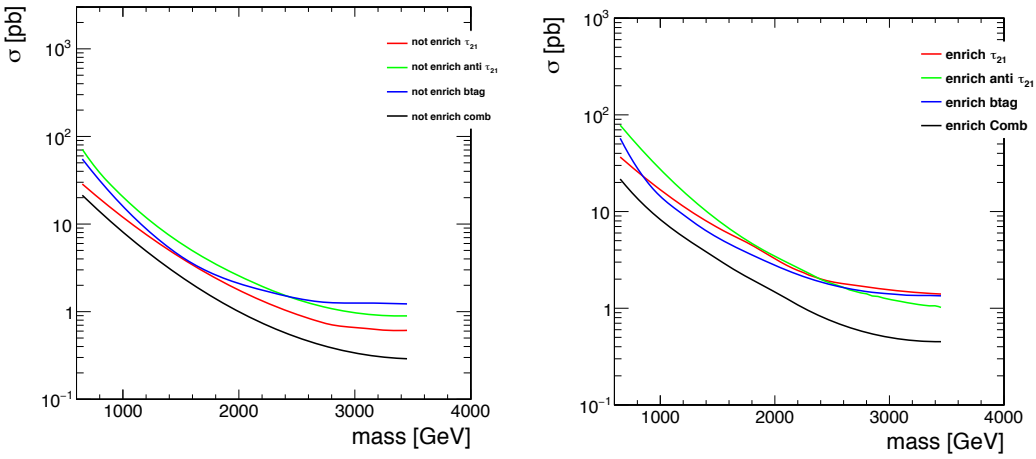

(a) Enrich category

(b) Not enrich category

Figure D.3.2: Expected limits for the Z+γ analysis using the single ak08 btag requirement and six categories

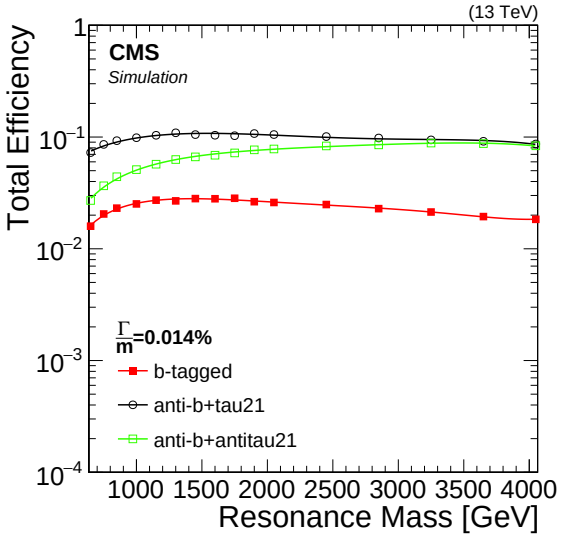

Figure D.3.3: Full selection and reconstruction A$\times\varepsilon$ of three analysis categories as a function of the resonance mass

D.4 Categories comparison (6 vs 3)

After choosing the CSV algorithm to replace the selection of the double b-tagger used in the standalone Zγ analysis, a first check regarding the number of categories has been performed.

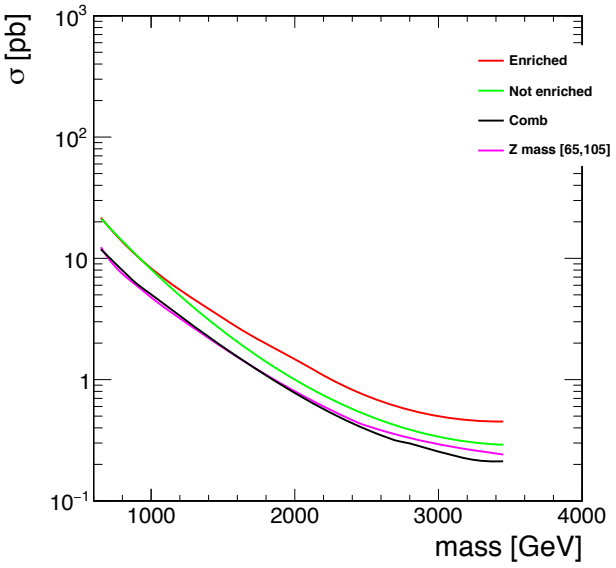

Figure D.4.1: Comparison between 3 and 6 categories for a Zγ signal

In Fig. D.4.1, the comparison between the analysis performed with 3 categories and with 6 categories (adding the mass selection) is shown. As expected, the line in magenta (3 categories) and black (6 categories) are comparable and lead to the same result having the same sensitivity.
The idea of dividing the sample into two subset of events depending on the jet mass regards the possibility of discriminate between a possible signal coming from a Zγ or a Wγ resonance which will appear in a peak in the jet+photon invariant mass spectrum. In the case of 3 categories, the two analyses will have overlapping events, while adding a mass category, the right contribution will be visible and therefore will permit to discriminate between a Zγ and a Wγ resonance signal.

D.5 N-Subjettiness selection

The jet substructure has been introduced in Sec. 4.13. Here, this variable is used to identify hadronic Z/W and discriminate them with respect to QCD or γ+Jets events. This section shows the method used to optimize the τ_{21} selection described in Sec. 6.4.
In Tab. D.5.1, the choice of the correct requirement on τ_{21} is shown. The expected limits for different selection values are reported.

As reported in Tab. D.5.1, the optimal cut for this analysis is $\tau_{21} = 0.45$, giving the lowest expected limit for different resonance masses. Although it has to be noted that for high masses, the improvement is not visible; this could be related to the topology of the hadronic Z/W at very high masses and it is an expected behaviour. The two quarks, coming from its decay are so collimated

τ_{21} cut	M_x = 1 TeV	M_x = 2.05 TeV	M_x = 2.85 TeV
0.35	10.19	1.35	0.59
0.40	10.16	1.30	0.58
0.45	10.16	1.28	0.57
0.50	10.53	1.30	0.57
0.55	10.78	1.31	0.57
0.60	11.09	1.39	0.59

Table D.5.1: Expected limits for a Zγ resonance with different τ_{21} requirements

that their signature results very similar to the one of a single quark and the substructure could be more difficult to be detected. In that region however, the presence of γ+Jet or QCD events is more rare, giving an higher signal over background ratio.

Bibliography

[1] Particle Data Group. "Review of Particle Physics". In: *Chin. Phys.* C40.10 (2016), p. 100001. DOI: 10.1088/1674-1137/40/10/100001.

[2] F. Englert and R. Brout. "Broken Symmetry and the Mass of Gauge Vector Mesons". In: *Phys. Rev. Lett.* (1964), pp. 321–323. DOI: 10.1103/PhysRevLett.13.321.

[3] P. W. Higgs. "Broken symmetries, massless particles and gauge fields". In: *Phys. Rev. Lett.* (1964), pp. 132–133. DOI: 10.1016/0031-9163(64)91136-9.

[4] The ATLAS Collaboration. "Observation of a new particle in the search for the Standard Model Higgs boson with the ATLAS detector at the LHC". In: *Phys. Lett.* B716 (2012), pp. 1–29. DOI: 10.1016/j.physletb.2012.08.020. arXiv:1207.7214 [hep-ex].

[5] The CMS Collaboration. "Observation of a new boson at a mass of 125 GeV with the CMS experiment at the LHC". In: *Phys. Lett.* B716 (2012), pp. 30–61. DOI: 10.1016/j.physletb.2012.08.021. arXiv:1207.7235 [hep-ex].

[6] Halzen and Martin. "Quarks and Leptons". In: John Wiley and Sons (1984).

[7] B. Cabrera and M. E. Peskin. "Cooper-pair mass". In: *Phys. Rev. B* 39 (10 1989), pp. 6425–6430. DOI: 10.1103/PhysRevB.39.6425. URL: https://link.aps.org/doi/10.1103/PhysRevB.39.6425.

[8] Gerald S. Guralnik. "Gauge Invariance and the Goldstone Theorem". In: *Mod. Phys. Lett.* A26 (2011), pp. 1381–1392. DOI: 10.1142/S0217732311036188. arXiv:1107.4592 [hep-th].

[9] Gerard 't Hooft and M.J.G. Veltman. "Regularization and Renormalization of Gauge Fields". In: *Nucl.Phys* (1972), B44:189–213. DOI: 10.1016/0550-3213(72)90279-9.

[10] M. Peskin. "Beyond the Standard Model". In: *Lectures notes of the 1996 European School of High-Energy Physics* (Carry-le-Rouet, France, 1996).

[11] David J. Gross and Frank Wilczek. "Ultraviolet Behavior of Nonabelian Gauge Theories". In: *Phys. Rev. Lett.* (1973), 30:1343–1346. DOI: 10.1103/PhysRevLett.30.1343.

[12] H. David Politzer. "Reliable Perturbative Results for Strong Interactions?" In: *Phys. Rev. Lett.* (1973), 30:1346–1349. DOI: 10.1103/PhysRevLett.30.1346.

[13] Vera C. Rubin and W. Kent Ford Jr. "Rotation of the Andromeda Nebula from a Spectroscopic Survey of Emission Regions". In: *Astrophys. J.* 159 (1970), pp. 379–403. DOI: 10.1086/150317.

[14] Katherine Freese. "Review of Observational Evidence for Dark Matter in the Universe and in upcoming searches for Dark Stars". In: *EAS Publ. Ser.* 36 (2009), pp. 113–126. DOI: 10.1051/eas/0936016. arXiv:0812.4005 [astro-ph].

[15] Y. Fukuda et al. "Evidence for oscillation of atmospheric neutrinos". In: *Phys. Rev. Lett.* 81 (1998), pp. 1562–1567. DOI: 10.1103/PhysRevLett.81.1562. arXiv:9807003 [hep-ex].

[16] Y. Abe et al. "Indication for the disappearance of reactor electron antineutrinos in the Double Chooz experiment". In: *Phys. Rev. Lett.* 108 (2012), p. 131801. DOI: 10.1103/PhysRevLett.108.131801. arXiv:1112.6353 [hep-ex].

[17] Stephen P. Martin. "A Supersymmetry primer". In: *Adv. Ser. Direct. High Energy Phys.18,1* (1997). DOI: 10.1142/9789812839657_0001, 10.1142/9789814307505_0001. arXiv:hep-ph/9709356 [hep-ph].

[18] Adam G. Riess et al. "Observational evidence from supernovae for an accelerating universe and a cosmological constant". In: *Astron. J.* 116 (1998), pp. 1009–1038. DOI: 10.1086/300499. arXiv:astro-ph/9805201 [astro-ph].

[19] S. Perlmutter et al. "Measurements of Omega and Lambda from 42 high redshift supernovae". In: *Astrophys. J.* 517 (1999), pp. 565–586. DOI: 10.1086/307221. arXiv:astro-ph/9812133 [astro-ph].

[20] The CMS and ATLAS Collobarations. "Measurements of the Higgs boson production and decay rates and constraints on its couplings from a combined ATLAS and CMS analysis of the LHC pp collision data at $\sqrt{s} = 7$ and 8 TeV". In: *JHEP* 08 (2016), p. 045. DOI: 10.1007/JHEP08(2016)045. arXiv:1606.02266 [hep-ex].

[21] B. Grzadkowski, P. Osland. "A Natural Two-Higgs-Doublet Model". In: *Phys.Rev.D82* 125026 (2010). DOI: 10.1103/PhysRevD.82.125026. arXiv:0910.4068.

[22] L. Randall and R. Sundrum. "A Large mass hierarchy from a small extra dimension". In: *Phys. Rev. Lett.* 83 (1999), p. 3370. DOI: 10.1103/PhysRevLett.83.3370.

[23] M. Luty J. Evans J. Galloway and R. Tacchi. "Minimal conformal technicolor and precision electroweak tests". In: *Journal of High Energy Physics* (2010). DOI: 10.1007/JHEP10(2010)086.

[24] Nima Arkani-Hamed, Raffaele Tito D'Agnolo, Matthew Low, David Pinner. "Unification and New Particles at the LHC". In: *JHEP* (2016). DOI: 10.1007/JHEP11(2016)082. arXiv:1608.01675.

[25] N. Karagiannakis, G. Lazarides, C. Pallis. "Constrained Minimal Supersymmetric Standard Model with Generalized Yukawa Quasi-Unification". In: *Phys.Rev. D87* 055001 (2012). DOI: 10.1103/PhysRevD.87.055001. arXiv:1212.0517.

[26] ATLAS Collaboration. "Search for new resonances in Wγ and Zγ Final States in pp Collisions at $\sqrt{s}$=8 TeV with the ATLAS Detector". In: *Phys.Lett. B* 738 428-447 (2014). DOI: 10.1016/j.physletb.2014.10.002. arXiv:1407.8150.

[27] ATLAS Collaboration. "Searches for the Zγ decay mode of the Higgs boson and for new high-mass resonances in pp collisions at $\sqrt{s}$=13 TeV with the ATLAS detector". In: (2017). arXiv:1708.00212.

[28] CMS Collaboration. "Search for high-mass Zγ resonances in proton-proton collisions at $\sqrt{s}$= 8 and 13 TeV using jet substructure techniques". In: *Phys.Lett. B* 772 363 (2016). arXiv:1612.09516.

[29] CMS Collaboration. "Search for high-mass Zγ resonances in $e^+e^-\gamma$ and $\mu^+\mu^-\gamma$ final states in proton-proton collisions at $\sqrt{s}$= 8 and 13 TeV". In: *JHEP* 01 076 (2016). arXiv:1610.02960.

[30] L. Evans and P. Bryant. "LHC Machine". In: *JINST* 3 (2008). DOI: 10.1088/1748-0221/3/08/S08001.

[31] The ALICE Collaboration. "The ALICE experiment at the CERN LHC". In: *JINST* 3 (2008). DOI: 10.1088/1748-0221/3/08/S08002.

[32] The ATLAS Collaboration. "The ATLAS Experiment at the CERN Large Hadron Collider". In: *JINST* 3 (2008). DOI: 10.1088/1748-0221/3/08/S08003.

[33] The CMS Collaboration. "The CMS experiment at the CERN LHC". In: *JINST* 3 (2008). DOI: 10.1088/1748-0221/3/08/S08004.

[34] The LHCb Collaboration. "The LHCb Detector at the LHC". In: *JINST* 3 (2008). DOI: 10.1088/1748-0221/3/08/S08005.

[35] The CMS Collaboration. *CMS Luminosity - Public Results*. URL: https://twiki.cern.ch/twiki/bin/view/CMSPublic/LumiPublicResults.

[36] W.J. Stirling. *Public plots*. http://www.hep.ph.ic.ac.uk/wstirlin/plots/crosssections2012_v5.pdf.

[37] Bo Andersson et al. "Parton Fragmentation and String Dynamics". In: *Phys. Rept.* 97 (1983), pp. 31–145. DOI: 10.1016/0370-1573(83)90080-7.

[38] The H1 Collaboration. "Inclusive Deep Inelastic Scattering at High Q2 with Longitudinally Polarised Lepton Beams at HERA". In: *PoS* EPS-HEP2013 (2013), p. 474. arXiv:1310.0968 [hep-ex].

[39] The H1 and ZEUS Collaborations. "Deep inelastic scattering at HERA". In: *Acta Phys. Polon. Supp.* 6 (2013), pp. 709–714. DOI: 10.5506/APhysPolBSupp.6.709.

[40] Yuri L. Dokshitzer. "Calculation of the Structure Functions for Deep Inelastic Scattering and e^+e^- Annihilation by Perturbation Theory in Quantum Chromodynamics." In: *Sov. Phys. JETP* 46 (1977), pp. 641–653.

[41] Guido Altarelli and G. Parisi. "Asymptotic Freedom in Parton Language". In: *Nucl. Phys.* B126 (1977), pp. 298–318. DOI: 10.1016/0550-3213(77)90384-4.

[42] V. N. Gribov and L. N. Lipatov. "Deep inelastic e-p scattering in perturbation theory". In: *Sov. J. Nucl. Phys.* 15 (1972), pp. 438–450.

[43] H.-L. Lai et al. "New parton distributions for collider physics". In: *Phys.Rev.* D82 (2010), 074024. DOI: 10.1103/PhysRevD.82.074024.

[44] Jonathan Pumplin et al. "New generation of parton distributions with uncertainties from global QCD analysis". In: *JHEP* 07 (2002), p. 012. DOI: 10.1088/1126-6708/2002/07/012. arXiv:0201195 [hep-ph].

[45] A. Martin, W. Stirling, R. Thorne, and G. Watt. "Parton distributions for the LHC". In: *Eur.Phys.J.* C63 (2009), p. 189. DOI: 10.1140/epjc/s10052-009-1072-5.

[46] R. D. Ball et al. "Parton distributions with LHC data". In: *Nucl.Phys.* B867 (2013), p. 244. DOI: 10.1016/j.nuclphysb.2012.10.003.

[47] *The Durham Hep-Data Project - PDF plotter*. URL: http://hepdata.cedar.ac.uk/pdf/pdf3.html.

[48] John C. Collins, Davison E. Soper, and George F. Sterman. "Factorization of Hard Processes in QCD". In: *Adv. Ser. Direct. High Energy Phys.* 5 (1989), pp. 1–91. DOI: 10.1142/9789814503266_0001. arXiv:0409313 [hep-ph].

[49] The CMS Collaboration. "CMS Physics Technical Design Report, Volume II: Physics Performance". In: *Journal of Physics G: Nuclear and Particle Physics* 34.6 (2007), p. 995. URL: http://stacks.iop.org/0954-3899/34/i=6/a=S01.

[50] Christian Piasecki. "Development of the CMS tracker and reconstruction of secondary vertices of b and c hadrons". In: *IEKP-KA-2006-7* (2006).

[51] The CMS Collaboration. *The CMS electromagnetic calorimeter project: Technical Design Report*. Geneva: CERN, 1997.

[52] A.A Annenkov, M.V Korzhik, and P Lecoq. "Lead tungstate scintillation material". In: *Nuclear Instruments and Methods in Physics Research Section A: Accelerators, Spectrometers, Detectors and Associated Equipment* 490.1–2 (2002), pp. 30 –50. ISSN: 0168-9002. DOI: 10.1016/S0168-9002(02)00916-6.

[53] The CMS Collaboration. *The CMS hadron calorimeter project: Technical Design Report*. Geneva: CERN, 1997.

[54] The CMS Collaboration. *The CMS muon project: Technical Design Report*. Geneva: CERN, 1997.

[55] M Raymond et al. "The MGPA electromagnetic calorimeter readout chip for CMS". In: *9th Workshop on Electronics for LHC Experiments* (2003). DOI: 10.5170/CERN-2003-006.83.

[56] Emanuele Di Marco. *CMS electromagnetic calorimeter calibration and timing performance during LHC Run I and future prospects*. Tech. rep. CMS-CR-2014-410. Geneva: CERN, 2014. URL: https://cds.cern.ch/record/1975982.

[57] P Adzic and E Auffray. "Reconstruction of the signal amplitude of the CMS electromagnetic calorimeter". In: *Eur. Phys. J. C* 46 S1 (2006), pp. 23–35. URL: https://cds.cern.ch/record/1062402.

[58] S Gadomski et al. "The deconvolution method of fast pulse shaping at hadron colliders". In: *Nucl. Instrum. Methods Phys. Res., A* 320.CERN-PPE-92-024 (1992), 217–227. 28 p. URL: https://cds.cern.ch/record/232960.

[59] M T Heath. *Numerical methods for large sparse linear least squares problems*. Tech. rep. ORNL-CSD-114. Oak Ridge, TN: Oak Ridge Nat. Lab., 1983. URL: https://cds.cern.ch/record/144406.

[60] The CMS Collaboration. *Energy Calibration and Resolution of the CMS Electromagnetic Calorimeter in pp Collisions at $\sqrt{s}$ = 7 TeV*. Tech. rep. P09009. JINST 8: Oak Ridge Nat. Lab., 2013.

[61] Zhang Liang Ying et al. "Monitoring light source for CMS lead tungstate crystal calorimeter at LHC". In: *IEEE Trans. Nucl. Sci.* 48.3 pt.1 (2001), pp. 372–8. URL: https://cds.cern.ch/record/521707.

[62] The CMS Collaboration. "Description and performance of track and primary-vertex reconstruction with the CMS tracker". In: *J. Instrum.* 9 (2014), P10009. DOI: 10.1088/1748-0221/9/10/P10009.

[63] Franz Hamilton, Tyrus Berry, and Timothy Sauer. "Kalman-Takens filtering in the presence of dynamical noise". In: Eur. Phys. J. C (2016). arXiv:1611.05414 [physics.data-an].

[64] Afiq A. Anuar. "Electrons and photons at High Level Trigger in CMS for Run II". In: *J. Phys. Conf. Ser.* 664.8 (2015), p. 082001. DOI: 10.1088/1742-6596/664/8/082001.

[65] K. Krajewska, C. Müller, and J. Z. Kami ński. "Bethe-Heitler pair production in ultrastrong short laser pulses". In: *Phys. Rev. A* 87 (6 2013), p. 062107. DOI: 10.1103/PhysRevA.87.062107. URL: https://link.aps.org/doi/10.1103/PhysRevA.87.062107.

[66] Livia Soffi. "Search for new exotic particles decaying to photons with the CMS experiment at the LHC". In: *The European Physical Journal Plus* 131.8 (2016), p. 283. ISSN: 2190-5444. DOI: 10.1140/epjp/i2016-16283-3. URL: http://dx.doi.org/10.1140/epjp/i2016-16283-3.

[67] CMS Collaboration. "Performance of photon reconstruction and identification with the CMS detector in proton-proton collisions at $\sqrt{s}$=8 TeV". In: *JINST* 10 P08010 (2015). DOI: 10.1088/1748-0221/10/08/P08010. arXiv:1502.02702.

[68] The CMS Collaboration. *The CMS Physics Technical Design Report.* CERN/LHCC 2006-001, CMS TDR 8.1. 2006.

[69] The CMS Collaboration. "Particle-Flow event reconstruction in CMS and performance for jets, taus and MET". In: *CMS Physics Analysis Summaries* CMS-PAS-PFT-09-001 (2009).

[70] The CMS Collaboration. "Commissioning of the particle-flow event reconstruction with leptons from J/Ψ and W decays at 7 TeV ". In: *CMS Physics Analysis Summaries* CMS-PAS-PFT-10-003 (2010).

[71] Sanmay Ganguly. *Jet Measurements In CMS.* Tech. rep. arXiv:1303.6038. 2013. URL: https://cds.cern.ch/record/1532824.

[72] Matteo Cacciari and Gavin P. Salam. "The anti-kt jet clustering algorithm". In: *LPTHE-07-03* (2008). arXiv:hep-ph/0802.1189.

[73] Matthew Low Daniele Bertolini Philip Harris and Nhan Tran. "Pileup Per Particle Identification". In: *JHEP* (2014). arXiv:1407.6013.

[74] Ivan Marchesini. *Identification of b-quark Jets in the CMS experiment.* Tech. rep. CMS-CR-2013-412. Geneva: CERN, 2013. URL: https://cds.cern.ch/record/1629516.

[75] Christopher K. Vermilion Stephen D. Ellis and Jonathan R. Walsh. "Techniques for improved heavy particle searches with jet substructure". In: (2009). arXiv:0903.5081.

[76] Gregory Soyez Andrew J. Larkoski Simone Marzani and Jesse Thaler. "Soft Drop". In: *JHEP* (2014). arXiv:1402.2657.

[77] Saranya Ghosh. "Performance of MET reconstruction and pileup mitigation techniques in CMS". In: *Nucl. Part. Phys. Proc.* 273-275.arXiv:1502.05207 (2015). Proceedings of the 37th International Conference on High Energy Physics, ICHEP 2014, 2512–2514. 3 p. URL: https://cds.cern.ch/record/1992977.

[78] J. Alwall et al. "MadGraph 5: going beyond". In: *JHEP* 06 128 (2011). DOI: 10.1007/JHEP06(2011)128. arXiv:1106.0522.

[79] J. Alwall et al. "The automated computation of tree-level and next-to-leading order differential cross sections, and their matching to parton shower simulations". In: *JHEP* 076 079 (2014). DOI: 10.1007/JHEP07(2014)079. arXiv:1405.0301.

[80] NNPDF Collaboration. "Parton distributions for the LHC Run II". In: *JHEP* 04 040 (2015). DOI: 10.1007/JHEP04(2015)040. arXiv:1410.8849.

[81] GEANT4 Collaboration. "GEANT4 — a simulation toolkit". In: *Nucl. Instrum. Meth. A* 506 250 (2003). DOI: 10.1016/S0168-9002(03)01368-8.

[82] Torbjörn Sjöstrand et al. "An Introduction to PYTHIA 8.2". In: *Comput. Phys. Commun.* 191 (2015), p. 159. DOI: 10.1016/j.cpc.2015.01.024. arXiv:1410.3012 [hep-ph].

[83] P. Skands, S. Carrazza, and J. Rojo. "Tuning PYTHIA 8.1: the Monash 2013 tune". In: *Eur. Phys. J. C* 74 3024 (2014). DOI: 10.1140/epjc/s10052-014-3024-y. arXiv:1404.5630.

[84] CMS Collaboration. "Event generator tunes obtained from underlying event and multiparton scattering measurements". In: *Eur. Phys. J. C* 76 155 (2016). DOI: 10.1140/epjc/s10052-016-3988-x. arXiv:1512.00815.

[85] R. A. Fisher. "On the interpretation of χ^2 from contingency tables, and the calculation of p". In: *J. Roy. Stat. Soc.* 85 87 (1922). DOI: 10.2307/2340521.

[86] *Procedure for the LHC Higgs boson search combination in Summer 2011*. Tech. rep. CMS-NOTE-2011-005. ATL-PHYS-PUB-2011-11. Geneva: CERN, 2011. URL: https://cds.cern.ch/record/1379837.

[87] R. Mackeprang and A. Rizzi. "Interactions of coloured heavy stable particles in matter". In: *Eur. Phys. J.* C 50 353 (2007).

[88] P. Adzic et al. "Reconstruction of the signal amplitude of the CMS electromagnetic calorimeter". In: *Eur. Phys. J.* C 46 S1 23 (2006).

[89] M. Goncharov et al. "The Timing system for the CDF electromagnetic calorimeters". In: *Nucl. Instrum. Meth.* A 565 543 (2006).

[90] CMS collaboration. "The Electromagnetic Calorimeter Project: Technical Design Report". In: *CERN-LHCC-97-33* (1997).

[91] P. Adzic et al. "Energy resolution of the barrel of the CMS electromagnetic calorimeter". In: *JINST* 2 P04004 (2007).

[92] CMS collaboration. "Measurement of the muon stopping power in lead tungstate". In: *JINST* 5 P03007 (2010).

[93] CMS Collaboration. "The Compact Muon Solenoid Technical Proposal". In: *CERN/LHCC 94-38* (1994).

[94] Z. Antunovic et al. "Radiation hard avalanche photodiodes for the CMS detector". In: *Nucl. Instr. and Meth.* A537 379 (2005).

[95] P. Adzic et al. "The detector control system for the electromagnetic calorimeter of the CMS experiment at the LHC". In: *CERN-CMS-CR-2005-028* (2005).

[96] L.M. Barone et al. "REDACLE: A flexible database for traceability and workflow management for detector construction". In: *Computer Physics Communications* 174 869 (2006).

[97] Eilam Gross Ofer Vitells Glen Cowan Kyle Cranmer. "Asymptotic formulae for likelihood-based tests of new physics". In: *Eur. Phys. J.* C71:1554,2011 (2010). DOI: 10.1140/epjc/s10052-011-1554-0. arXiv:1007.1727.

[98] S.S. Wilks. "The large-sample distribution of the likelihood ratio for testing composite hypotheses". In: *Ann. Math. Statist.* 9 60-2 (1938).

[99] A. Wald. "Tests of Statistical Hypotheses Concerning Several Parameters When the Number of Observations is Large". In: *Transactions of the American Mathematical Society* 54, No. 3 (1943).